

Silicon Nanoparticles from the Inside Out: Exploring the Internal Structure of Silicon
Nanoparticles and Its Impact on Their Photoluminescence

by

Alyxandra N. Thiessen

A thesis submitted in partial fulfillment of the requirements for the degree of

Doctor of Philosophy

Department of Chemistry
University of Alberta

© Alyxandra N. Thiessen, 2020

Abstract

Silicon nanoparticles (SiNPs) have garnered significant attention as a biologically compatible alternative to traditional quantum dots. SiNPs are well suited for a wide range of applications due to their photoluminescence (PL) and chemical properties. These advantageous properties can be controlled on the basis of the internal and surface structure of the SiNPs. The internal structure can be tuned during the synthesis of the SiNP core, while the surface typically is modified by functionalization after. This thesis examines the internal structure of SiNPs and the impact of the internal structure on the luminescence response.

Chapter 1 introduces SiNPs and the important role that the structure plays on their properties. Chapter 2 explores the internal structure of 3, 6, 9, 21, and 64 nm hydride-terminated SiNPs (H-SiNPs) using a series of characterization techniques. A graded internal structure is identified, consisting of a crystalline core, a semi-ordered subsurface, and a disordered surface. This structure breaks down for 3 and 6 nm SiNPs, in which no long-range order is observed.

The insight from Chapter 2 is used in Chapter 3 to explore the impact of the internal structure on the photoluminescence properties. Two groups of SiNPs were studied, one with a thick amorphous shell (>1 nm) and one with a thin amorphous shell (<0.8 nm), determined by the difference between the overall diameter (d_{TEM}) and the crystalline domain size (d_{XRD}). For SiNPs with a thick amorphous shell, the PL emission maximum (PL max) and lifetimes correlate better with d_{XRD} than d_{TEM} , while PL max and lifetimes correlate well with both d_{XRD} and d_{TEM} for SiNPs with a thin amorphous shell.

The impact of oxidation on the internal structure of SiNPs and their photoluminescence is outlined in Chapter 4. Upon oxidation, a decrease in d_{XRD} and an

increase in d_{TEM} are observed that appear to correlate with the SiNP size, where smaller SiNPs show a larger change in d_{XRD} and d_{TEM} . This corresponds with a size-dependent blue-shift in the PL max with increasing oxidation. A summary of the experimental chapters is provided in Chapter 5, along with future research directions.

Preface

Chapter 2 of this thesis has been published as Thiessen, A. N.; Ha, M.; Hooper, R. W.; Yu, H.; Oliynyk, A. O.; Veinot, J. G. C.; Michaelis, V. K, Silicon Nanoparticles: Are They Crystalline from the Core to the Surface? *Chem. Mater.* **2019**, *31*, 678-688. M. Ha and I contributed equally to this work. I was responsible for synthesizing the SiNPs, data collection and analysis, and manuscript preparation. M. Ha performed solid state NMR experiments and worked with me on data analysis and manuscript preparation. R. W. Hooper assisted with synthesis and NMR experiments. H. Yu assisted with XPS analysis and contributed to manuscript edits. A. O. Oliynyk assisted with analysis of XRD data and contributed to manuscript edits. J. G. C. Veinot and V. K. Michaelis were the supervisory authors and contributed to concept formation, data analysis, and manuscript preparation.

Chapter 3 of this thesis has been published as Thiessen, A. N.; Zhang, L.; Oliynyk, A. O.; Yu, H.; O'Connor, K. M.; Meldrum, A.; Veinot, J. G. C., "A Tale of Seemingly "Identical" Silicon Quantum Dot Families: Structural Insight into Silicon Quantum Dot Photoluminescence", *Chem. Mater* ASAP, DOI: 10.1021/acs.chemmater.0c00650. I was responsible for concept formation, data collection and analysis, and manuscript preparation. L. Zhang assisted with data collection. A. O. Oliynyk assisted with interpretation of XRD data. H. Yu assisted with data collection. K. M. O'Connor assisted with data collection. A. Meldrum performed modelling of size effects on photoluminescence and assisted with data analysis and manuscript preparation. J. G. C. Veinot was the supervisory author and assisted with concept formation, data analysis, and manuscript preparation. Part of the research described in this chapter was performed at the Canadian Light Source (CLS), a national research facility of the University of Saskatchewan, which is supported by the Canada Foundation for Innovation (CFI), the Natural Sciences and Engineering Research Council (NSERC), the National Research Council (NRC), the Canadian Institutes of Health Research (CIHR), the Government of Saskatchewan, and the University of Saskatchewan.

Chapter 4 is an original work. I was responsible for concept formation, data collection, and analysis. I. T. Cheong performed photoluminescence spectroscopy. S. Milliken assisted with data collection. Part of the research described in this chapter was performed at the Canadian Light Source.

Chapter 5 presents preliminary results and original work. I was responsible for synthesis, data collection, and analysis. M. Ha performed ^{29}Si NMR experiments. Some of the data presented in this chapter forms part of an international research collaboration, led by Dr. G. Drisko at the University of Bordeaux, with Dr. J. G. C. Veinot being the lead collaborator at the University of Alberta. Dr. P. Barois at the University of Boudreaux was responsible for data collection.

Appendix A of this thesis has been published as Thiessen, A. N.; Purkait, T. K.; Faramus, A.; Veinot, J. G. C., Lewis Acid Protection: A Method towards Synthesizing Phase Transferable Luminescent Silicon Nanocrystals. *Phys. Status Solidi A*. **2018**, *215*, 1700620. I was responsible for concept formation, data collection and analysis, and manuscript preparation. T. K. Purkait assisted with concept formation. A. Faramus helped with data collection. J. G. C. Veinot was the supervisory author and assisted with concept formation, data analysis, and manuscript preparation.

I dedicate this thesis to my family.

“Around here, however, we don’t look backwards for very long. We keep moving forward opening up new doors and doing new things, because we’re curious...and curiosity keeps leading us down new paths.” – Walt Disney

“Immediately Jesus reached out his hand and caught him. ‘You of little faith,’ he said, ‘why did you doubt?’” – Matthew 14:31 (NIV)

Acknowledgments

This thesis would not have been possible without the support of my friends, family, and colleagues. First, I would like to thank Dr. Jonathan Veinot for supporting me throughout my degree. Thank you for encouraging me to take risks, try new things, and push beyond what I ever thought was possible. I would also like to thank my committee members, Drs. Jillian Buriak, Mark McDermott, and Julianne Gibbs, for their time and enlightening discussions. Thank you Dr. Paola Ceroni, for serving as an external reader for my thesis.

I would like to thank the students and faculty involved in the ATUMS program for providing a supportive community to do research and enjoy our international collaborations. Specifically, I would like to thank Professor Bernhard Rieger and Dr. Markus Pschenitzka for hosting me in Germany during my research exchanges. A special thanks goes to Leah Veinot, who works tirelessly to coordinate ATUMS events and research exchanges.

A huge thank you to my collaborators, Dr. Vladimir Michaelis, Michelle Ha, Dr. Anton Oliynyk, Dr. Al Meldrum, Lijuan Zhang, Dr. Glenna Drisko, and Dr. Philippe Barois, who have contributed heavily to the work presented in this thesis. Michelle, thank you for our long discussions about research directions and life.

I would also like to acknowledge the support staff in the Chemistry Department and the Nanofab. Thank you Wayne Moffat, Jennifer Jones, Ryan Lewis (shipping my samples near and far), Dirk Kelm, Dieter Starke, Paul Crothers, Michael Barteski, Andrew Yeung, Anita Weiler, Peng Li, and Dr. Anqiang He for your support and assistance. I greatly enjoyed working with all of you. Anna Jordan, thank you very much for all your help with the completion of this thesis. It would not look nearly as well put together without your thoughtful contribution. I would like to acknowledge ATUMS, Alberta Innovates, and the Alberta government for their financial support through scholarships and awards.

Veinot group members, past and present, thank you very much for your support and friendship. The kindness that you have all showed me, whether it was teaching me how to do research or helping with experiments and characterization, always will be remembered. To the students that I have supervised, thank you for teaching me to be a good mentor and bringing life into the lab. Dr. Christina Gonzalez, Dr. Regina Sinelnikov, Dr. Maryam

Aghajamali, Haoyang Yu, Sarah Milliken, and I Teng (Emily) Cheong, thank you all for being there when I needed advice, needed to vent, or a break to chat.

My family has grown since starting my thesis, and I appreciate all of you and your unconditional love and support more than you will ever know. Quinton Thiessen, I would never have gotten through this thesis without you. You pick me up when I am down and always are there to support me. Thank you so much!

Table of Contents

Chapter 1 Introduction	1
1.1 Quantum Dots – Inorganic Semiconductor Nanoparticles	1
1.2 Silicon Nanoparticles	6
1.3 Applications of Silicon Nanoparticles	8
1.3.1 Biological Imaging.....	8
1.3.2 Sensors	10
1.3.3 Luminescent Solar Concentrators	11
1.3.4 Light-emitting Diodes	11
1.3.5 Lithium Ion Batteries	12
1.4 Synthesis and Functionalization of Silicon Nanoparticles	13
1.4.1 Synthesis of Silicon Nanoparticles.....	13
1.4.1.1 Gas Phase Synthesis.....	13
1.4.1.2 Solution Phase Synthesis	14
1.4.1.3 Solid-state Methods	15
1.4.2 Functionalization of Hydride-terminated Silicon Nanoparticles	15
1.4.2.1 Silicon—Carbon Bonds: Hydrosilylation.....	16
1.4.2.2 Silicon—Carbon Bonds: Other Methods.....	18
1.4.2.3 Silicon—Heteroatom Bonds	20
1.5 Structure of Freestanding Silicon Nanoparticles	21
1.5.1 Structure of the Silicon Nanoparticle Core	21
1.5.1.1 Impact of Structure on Optical Response	22
1.5.1.2 Impact of Structure on Applications: Beyond the Photoluminescence	25
1.5.2 Surface Structure of Silicon Nanoparticles	25
1.5.2.1 Impact of Surface on Optical Response.....	26
1.5.2.2 Impact of Surface on Applications: Beyond the Photoluminescence.....	27
1.6 Thesis Outline	28
1.7 References.....	29

Chapter 2 Silicon Nanoparticles: Are They Crystalline from Core to the Surface?	41
.....	
2.1 Introduction	41
2.2 Experimental Section.....	43
2.2.1 Materials.....	43
2.2.1.1 Starting Materials.....	43
2.2.1.2 Preparation of Hydrogen Silsesquioxane (HSQ).....	43
2.2.1.3 Preparation of the H-SiNPs.....	44
2.2.2 Characterization	45
2.2.2.1 Fourier Transform Infrared Spectroscopy (FTIR).....	45
2.2.2.2 X-ray Photoelectron Spectroscopy (XPS)	45
2.2.2.3 Transmission Electron Microscopy (TEM)	48
2.2.2.4 Powder X-ray Diffraction (XRD).....	48
2.2.2.5 Solid-State NMR Spectroscopy	49
2.3 Results and Discussion	51
2.4 Conclusions.....	63
2.5 References.....	64
Chapter 3 A Tale of Seemingly “Identical” Silicon Quantum Dot Families: Structural Insight into Silicon Quantum Dot Photoluminescence	70
3.1 Introduction	70
3.2 Experimental.....	72
3.2.1 Materials.....	72
3.2.1.1 Reagents.....	72
3.2.1.2 Preparation of Hydrogen Silsesquioxane (HSQ).....	73
3.2.1.3 Preparation of the SiQDs/SiO ₂ Composite.....	73
3.2.1.4 Preparation of Alkyl Passivated SiQDs	73
3.2.2 Characterization	74
3.2.2.1 Fourier Transform Infrared Spectroscopy	74
3.2.2.2 X-ray Photoelectron Spectroscopy	74
3.2.2.3 Electron Microscopy.....	75

3.2.2.4 Powder X-ray Diffraction	75
3.2.2.5 Photoluminescence Characterization	76
3.3 Results and Discussion	78
3.4 Conclusions.....	88
3.5 References.....	88
Chapter 4 Insights into the Structure and Optical Response of Oxidized Silicon	
Nanoparticles: A Study on the Role of Structure on Oxidation	92
4.1 Introduction	92
4.2 Experimental Section.....	94
4.2.1 Materials.....	94
4.2.1.1 Starting Materials.....	94
4.2.1.2 Preparation of Hydrogen Silsesquioxane (HSQ).....	94
4.2.1.3 Preparation of Hydride-Terminated Silicon Nanoparticles (H-SiNPs)	94
4.2.1.4 Preparation of Alkyl-Passivated SiNPs with Varied Surface Coverage...	95
4.2.1.5 Oxidation of Alkyl-Passivated SiNPs.....	95
4.2.2 Characterization	96
4.2.2.1 Thermogravimetric Analysis (TGA).....	96
4.2.2.2 X-ray Photoelectron Spectroscopy (XPS)	96
4.2.2.3 X-ray Diffraction (XRD)	96
4.2.2.4 Electron Microscopy.....	97
4.2.2.5 Photoluminescence Spectroscopy.....	97
4.3 Results and Discussion	98
4.3.1 Size Dependent Impact of Oxidation on Structure of SiNPs	98
4.3.2 Impact of Oxidation on the Optical Response of SiNPs	108
4.3.3 Internal Structure Dependent Impact of Oxidation on Structure of SiNPs.....	110
4.3.4 Influence of Internal Structure on Oxidation-based Changes in Photoluminescence	114
4.4 Conclusions and Future Work	116
4.5 References.....	116

Chapter 5 Conclusions and Future Directions	119
5.1 Conclusions.....	119
5.2 Future Directions	121
5.2.1 Expanding Insights into the Structure of SiNPs.....	121
5.2.1.1 Exploring Oxidation on H-SiNPs	121
5.2.1.2 Impact of Synthetic Methods on Internal Structure of SiNPs.....	122
5.2.2 Impact of SiNP Internal Structure on Applications	123
5.2.2.1 Impact of SiNP Internal Structure on Performance of Lithium Ion Battery Anodes.....	123
5.2.2.2 Optimization of Structure for Multimodal Imaging.....	123
5.2.3 Moving into a New Size Regime	124
5.3 References.....	126
Bibliography	128
Appendix A Lewis Acid Protection: A Method Towards Synthesizing Phase Transferable Luminescent Silicon Nanocrystals	152
A.1 Introduction.....	152
A.2 Experimental.....	154
A.2.1 Materials.....	154
A.2.1.1 Starting Materials.....	154
A.2.1.2 Preparation of N'-undec-10-enyl-N,N-dimethylacetamide	154
A.2.1.3 Preparation of the H-SiNCs	154
A.2.1.4 Synthesis of Amidine Functionalized SiNCs.....	155
A.2.2 Characterization.....	155
A.2.3 Hydrophilicity Switch Experiments	156
A.3 Results and Discussion	156
A.3.1 Synthesis of Amidine Functionalized SiNCs	156
A.3.2 Hydrophilicity Switch Experiments	159
A.4 Conclusions.....	161
A.5 References.....	161

Appendix B Calculation of Surface Coverage from TGA..... 163
**Appendix C Calculation of Si:O Ratio From High Binding Energy Components of High
Resolution Si 2p XP Spectrum..... 165**

List of Figures

- Figure 1-1.** A pictorial representation of the relative size of biological and technological objects. (Image by Guillaume Paumier, Philip Ronan, NIH, Artur Jan Fijałkowski, Jerome Walker, Michael David Jones, Tyler Heal, Mariana Ruiz, Science Primer (National Center for Biotechnology Information), Liquid_2003, Arne Nordmann & The Tango! Desktop Project and licensed under CC BY-SA 2.5) 2
- Figure 1-2.** A schematic representation of the change in band structure when going from bulk (conduction and valence bands) to nano to molecular systems (highest occupied and lowest unoccupied molecular orbitals; HOMO and LUMO). 3
- Figure 1-3.** Schematic representation of band edge alignment of materials for different types of core@shell QDs. 4
- Figure 1-4.** A schematic representation of the band edges for CdTe@CdS core@shell QDs showing the transition from a) Type I to c) Type II QDs as a function of the shell thickness and d) the relative band edges of the bulk CdTe and CdS systems. Image adapted from *Opt. Mater.* **2016**, 53, 34-38 (Ref 14). Copyright 2016 Elsevier..... 5
- Figure 1-5.** a) A schematic representation of core@shell, C@A@S, and C@GS QDs, their band structures (the black lines), and the associated wavefunctions of the carriers (blue lines). b) A comparative illustration of the interaction of the electronic wavefunction at the interface of a core@shell QD with a hard interface and a C@GS QD with a soft interface. The black lines represent the band structure, and the blue lines represent the interaction of the wavefunction. c) The ratios of the integrated areas of the PL emission from the core and the total PL emission for CdSe QDs (no shell), CdSe@ZnS (core@shell), and CdSe@Cd,Zn,S (C@GS). Reprinted with permission from *Chem. Mater.*, **2013**, 25 (23), 4731-4738 (Ref 20) and *J. Phys. Chem. C*, **2016**, 120 (34), 19409-19415 (Ref 19). Copyright 2013 and 2016 American Chemical Society..... 6

Figure 1-6. A schematic representation of the band structure of a) direct and b) indirect semiconductors. Image adapted from <i>Scientific Reports</i> , 2017 , 7, 15365 (Ref 28). Licensed under CC BY 4.0.	7
Figure 1-7. Atomic force microscopy image of a) white light, b) steady-state luminescence imaging, and c) time-gated luminescence imaging after subcutaneous injection of SiNPs. d) A comparison of the signal-to-background ratio using time-gated imaging (with a delay of 10 μ s) and steady state imaging. Reproduced from <i>Nanoscale</i> , 2020 , 12, 7921-7926 (Ref. 38) with permission from the Royal Society of Chemistry.....	9
Figure 1-8. A ^{29}Si magnetic resonance image taken of hyperpolarized silicon microparticles in an H-shaped phantom. Reprinted with permission from <i>ACS Nano</i> , 2009 , 3(12), 4003-4008 (Ref 39). Copyright 2009 American Chemical Society.....	10
Figure 1-9. a) A schematic representation of a luminescent solar concentrator based on silicon QDs. b) A plot showing the overlap of the solar spectrum (gray trace) with the absorbance (black trace) and photoluminescence emission (red trace) of 4.3 nm silicon nanoparticles. The transparency window is indicated by the gray shading. Reprinted by permission from Springer Nature: <i>Nature, Nat. Photon.</i> 2017 , 11, 177-185 (Ref 43).....	11
Figure 1-10. a) Electroluminescence and photoluminescence spectra of 1.3, 1.6 and 1.8 nm SiNPs. b) Photographs of LEDs made from SiNPs demonstrating visible luminescence taken under ambient lighting conditions. Reprinted with permission from <i>Nano Lett.</i> 2013 , 13(2), 475-480 (Ref 79). Copyright 2013 American Chemical Society.	12
Figure 1-11. SiNP synthesis from silane using the pyrolysis and plasma methods.....	13
Figure 1-12. Schematic representation of the thermal disproportionation of HSQ to make 3, 6, and 9 nm SiNPs embedded in SiO_2 and the subsequent liberation via HF etching.....	15
Figure 1-13. Schematic representation of the different hydrosilylation methods that have been used to passivate SiNP surfaces.	16

Figure 1-14. Schematic representation of silyl radical abstraction and radical propagation along the silicon surface during hydrosilylation. Reprinted with permission from <i>Chem. Mater.</i> 2015 , 27 (19), 6869-6878 (Ref 143). Copyright 2015 American Chemical Society.	18
Figure 1-15. Scheme showing the functionalization of Si surfaces with organolithium reagents. Reprinted with permission from <i>Chem. Eur J.</i> 2015 , 21, 2755-2758 (Ref. 154). Copyright 2015 Wiley-VCH Verlage GmbH&Co. KGaA, Weinheim.	19
Figure 1-16. An illustration of the aspects of a SiNP and an overview of how they can be tuned.	21
Figure 1-17. Structure of a) 2.4, b) 3.3, c) 7.9, and d) 13.6 nm SiNPs generated from Reverse Monte Carlo simulations based on experimental PDF data. Details of the modelling can be found in Ref 171. Reprinted with permission from <i>Chem. Mater.</i> 2013 , 25(11), 2365-2371 (Ref 170). Copyright 2013 American Chemical Society.	22
Figure 1-18. a) A plot of the relationship between the input power during the plasma synthesis of SiNPs and the quantum yields. b) A comparison of the PL emission spectra of crystalline (red trace) and amorphous (blue trace) SiNPs made through the plasma synthesis. c) The relationship between amorphous SiNP diameter and band gap with (red) and without (blue) exposure to H ₂ . Images a) and b) reprinted with permission from Anthony, R.; Kortshagen, U., <i>Phys. Rev. B</i> , 2009 , 80, 115407 http://dx.doi.org/10.1103/PhysRevB.80.115407 (Ref 98). Copyright 2009 by the American Physical Society. Image c) reprinted from <i>Adv. Mater.</i> , 2015 , 27, 8011-8016 (Ref 177). Licensed under CC BY.	23
Figure 1-19. Illustration outlining the influence of surface functionalization on the photoluminescence, showing tuning throughout the visible and near infrared. Image adapted from: <i>ACS Nano</i> 2014 , 8 (9), 9636-9648 (Ref 165).	26
Figure 2-1. Survey XPS data for 3 nm (black), 6 nm (red), 9 nm (blue), 21 nm (green), and 64 nm (purple); tabulated elemental composition and peak composition for C and O at% from survey.	46

Figure 2-2. Peak fitting for C and Si XPS data for 3, 6, 9, 21, and 64 nm nanoparticles.	47
Figure 2-3. Histograms showing size distributions for (a) 3 nm, (b) 6 nm, (c) 9 nm, (d) 21 nm, and (e) 64 nm H-SiNPs.	48
Figure 2-4. XRD alignment with (a) LaB ₆ (NIST) and (b) Si standards.	49
Figure 2-5. T_1 buildup curves for H-SiNPs using a mono-exponential longitudinal magnetization recovery for smaller H-SiNPs (3 and 6 nm) and a bi-exponential recovery for larger H-SiNPs (9, 21, and 64 nm).	50
Figure 2-6. FTIR spectra for H-SiNPs annealed at 1500 °C (purple), 1400 °C (green), 1300 °C (blue), 1200 °C (red), and 1100 °C (black). The spectra show peaks associated with Si-H (highlighted in gray) and Si-O (highlighted in blue).	52
Figure 2-7. (a) High-resolution Si 2p XPS showing the 2p _{3/2} and 2p _{1/2} emission for 64, 9, and 3 nm H-SiNPs. The colored traces correspond to: gray = experimental data, dotted black = complete fit, red = crystalline core Si, blue = surface Si, orange = disordered Si, and green = Si oxides. (b) Bright-field TEM images of H-SiNPs (d ~ 64 and 9 nm) and dodecyl-SiNPs (d ~ 3 nm). (c) XRD patterns for d ~ 64 (blue), 21 (red), 9 (green), 6 (cyan), and 3 (brown) nm H-SiNPs, showing characteristic Si 111, 220, 311, 400, 331, and 422 reflections.	53
Figure 2-8. XRD Peak broadening distribution for nanocrystalline materials.	54
Figure 2-9. Direct (a) and CP (b) ²⁹ Si MAS NMR spectra of H-SiNPs with varying particle diameter.	56
Figure 2-10. Contact time array for ²⁹ Si CP MAS ranging from 0.05 to 8.0 ms for 3, 9, and 64 nm H-SiNPs.	57
Figure 2-11. Silicon-29 NMR spectra for 9 nm H-SiNPs purposefully oxidized over a period of 9 months to indicate contamination of oxygen under ambient storage. Presence of Si-O species at δ_{iso} of ~ -110 ppm 4 and 9 months post-synthesis.	58
Figure 2-12. Sample of the post-NMR analysis of the H-SiNPs (6 nm) using (a) Si 2p high resolution XPS data (with only the 2p _{3/2} shown for clarity) and (b) FTIR spectra of 6 nm H-SiNPs.	58
Figure 2-13. (a) Two-dimensional ²⁹ Si[¹ H] HETCOR MAS NMR spectra of 64 nm H-SiNPs with a mixing time of 3.0 ms. (b) Overlay of direct excitation ²⁹ Si MAS NMR	

and $^{29}\text{Si}[^1\text{H}]$ CP MAS NMR with variable mixing times for 64 nm H-SiNP to illustrate NMR features corresponding to H-SiNP surface (yellow), subsurface (red), and core (blue) signatures. Red arrows indicate sharper subsurface NMR features present in the direct excitation ^{29}Si MAS NMR, as seen with $^{29}\text{Si}[^1\text{H}]$ CP MAS NMR with a mixing time of 3.0 ms. Direct excitation ^{29}Si MAS NMR with a recycle delay of 200 s was used to artificially inflate the surface resonance still present at shorter recycle delays. (c) Artistic schematic of a H-SiNP indicating the silicon surface, subsurface, and core with a model of the first ten atomic layers of H-SiNPs.....59

Figure 2-14. (a) Relationship of δ_{cgs} as a function of inverse bandgap of SiNPs. (b) Surface/subsurface area % for NMR experiments (black) and model (red) and ^{29}Si full-width at half maximum (FWHM, blue) with increasing H-SiNP size. As the H-SiNPs move from a disordered to an ordered system, the corresponding surface area % and line width decreases as NP size increases.....60

Figure 2-15. Estimated core (blue) vs surface/subsurface (gray) fractions from ^{29}Si MAS NMR (Bloch) using appropriate delay times (i.e., $5 \times T_1$). The black line is the experimental data and the red dashed line is the fitting envelope.62

Figure 3-1. A summary of representative literature data showing the relationship between SiQD peak PL emission and particle dimension.^{37, 39, 40, 52-56} Predicted relationships obtained using the effective mass approximation⁵⁷ (solid line; $E_{\text{gr}} = 1.12 + 3.77/r^2$) and linear combination of atomic orbitals^{26, 42} (dashed line; $E_{\text{gr}} = 1.12 + 3.77/r^{1.39}$) are shown for comparison.72

Figure 3-2. a) Trend subtracted STEM image highlighting lattice fringes of sample. b) Original HAADF STEM image showing full size of SiNCs. (Note: Colored lines illustrate particle measurement method.)75

Figure 3-3. Fitting of Si NIST linewidth standard (640f) measured on the Rigaku Ultima IV.76

Figure 3-4. FTIR of 1200-SiQDs (red) and 1300-SiQDs (purple).79

Figure 3-5. a) Si 2p XP spectrum with deconvolution/fitting of the data for 1200-SiQDs and 1300-SiQDs. Fitting peaks are shown as Si 2p_{1/2} and 2p_{3/2} components

corresponding to Si(0) (i.e., orange), Si(I) (i.e., green), and Si(II) (i.e., blue). The black trace is the experimental spectrum and the red dashed line represents the overall fitting envelope. b) TEM image of 1200-SiQDs and 1300-SiQDs inset: average shifted histogram with the average size and the distribution width. c) XRD data for 1200-SiQDs and 1300-SiQDs showing experimental powder pattern (black) with fitting (red for 1300-SiQDs and purple for 1200-SiQDs) and residuals (light gray).80

Figure 3-6. High annular angle dark field STEM images of a) 1200-SiQDs and b) 1300-SiQDs.81

Figure 3-7. Histograms showing the STEM determined non-crystalline shell thicknesses for a) 1200-SiQDs and b) 1300-SiQDs. Experimental data are represented by the blue bars below the x-axis. The density of these bars indicates the frequency. The line in the plot was determined using a fitting routine described in Ref #75 that is designed to minimize binning bias.82

Figure 3-8. Comparing a) the photoluminescence emission of 1300-SiQDs (purple) and 1200-SiQDs (red) as well as b) the luminescence lifetimes of 1300-SiQDs (purple fit) and 1200-SiQDs (red fit). Photoluminescence emission data were collected on an Ocean Optics 2000+ spectrometer. Luminescence lifetimes were fitted to a stretched exponential function, and then the mean time constants were calculated as described below.⁶⁶ The fitting parameters are reported in Table 3-2.82

Figure 3-9. A comparison of the relationship between quantum efficiency with d_{TEM} (blue squares) and d_{XRD} (red circles) for SiQDs with a thick amorphous layer (>2 nm; a) and a thin amorphous layer (<0.8 nm; b).83

Figure 3-10. A plot of the maximum photoluminescence energy against the lifetimes for all SiQDs in this study. A clear trend is observed that can be fit to the equation $1/\bar{\tau} = A' * e^{E/E_0}$,⁷⁰⁻⁷² where $A' = 62.5 \text{ s}^{-1}$ and $E_0 = 0.34 \text{ eV}$ (the black line).84

Figure 3-11. Plot showing d_{TEM} vs. d_{XRD} , where the line is $d_{\text{TEM}} = d_{\text{XRD}}$84

Figure 3-12. A schematic representation of Si QDs showing the thick (a) and thin (b) amorphous layers surrounding the crystalline core. A comparison of the

relationship between PL energy (c and d) and lifetimes (e and f) with d_{TEM} (blue squares) and d_{XRD} (red circles) for SiQDs with a thick amorphous layer (>1 nm; a, c, e) and a thin amorphous layer (<0.4 nm; b, d, f). The solid and dashed black lines in c) and d) represent the EMA and LCAO as in Figure 1. The solid black line in e) and f) is a fitting from all of the d_{XRD} vs. lifetime data, according to Eq.3.86

Figure 3-13. The XRD (red points) and TEM (green points) mean diameters as a function of the mean PL energy. The blue lines are model fits that incorporate the quantum efficiency, absorption cross sections, size distributions, and effective mass approximation using methods similar to those in Ref. Yu et al. 2017. The uppermost light blue line is the pure EMA; increasing the size distribution “pulls” the model downward, mainly due to the higher QY of the larger particles (darker blue lines).87

Figure 4-1. Schematic representation of a home-built relative humidity chamber. The blue box represents the plexiglass box that was taped shut, and the orange cylinders represent the vials containing toluene solutions of the silicon samples.96

Figure 4-2. Formation of different sizes of SiNP through thermal annealing of hydrogen silsesquioxane (HSQ), and subsequent liberation to form H-SiNPs of various sizes.99

Figure 4-3. Schematic representation of reaction showing different levels of functionalization obtained through different reaction times. Si-H represents all Si-H_x (x = 1–3) species. This ultimately leads to different levels of oxidation after exposure to 73% relative humidity for 30 days.99

Figure 4-4. TGA plot of dodecyl-terminated a) 3, 5, and b) 7 nm SiNPs functionalized for different lengths of time. The experiments were performed with a heating rate of 10 °C/min in an Ar atmosphere. The initial weight loss in the 7 nm 75 min sample is due to residual solvent loss. 100

Figure 4-5. High resolution Si 2p spectrum showing the 2p_{3/2} and 2p_{1/2} emissions for a) 3 nm, b) 5 nm, and c) 7 nm SiNPs with different levels of surface passivation after oxidation. The colored traces correspond as follows: black = experimental data,

dashed red = fitting envelope, orange = core Si, green = $\sim\text{SiO}_{0.5}$ or silicon-carbon species, purple = $\sim\text{SiO}$, blue = $\sim\text{SiO}_{1.5}$, and magenta = $\sim\text{SiO}_2$ 101

Figure 4-6. Plots showing the ratio of oxygen and silicon normalized to the surface area to volume ratio for the SiNPs calculated from a) the ratio of high oxidation state Si and b) the relative atm% from the survey spectrum. 102

Figure 4-7. Brightfield TEM images showing (a and b) 3, (c and d) 5, and (e and f) 7 nm SiNPs functionalized for (a,c,e) 900 and (b, d, f) 30 min after oxidation. 104

Figure 4-8. Histograms showing the size distribution of a) 3, b) 5, and c) 7 nm SiNPs functionalized for 900 min (top) and for 30 min (bottom). Sizes were determined based on brightfield TEM imaging. 104

Figure 4-9. A plot showing the difference in d_{TEM} for samples functionalized for 30 min ($d_{TEM, 30 \text{ min}}$) and 900 min ($d_{TEM, 900 \text{ min}}$) as a function of $d_{TEM, 900 \text{ min}}$. Error bars represent standard deviations based on the size distributions. 105

Figure 4-10. XRD patterns for a) 3 nm, b) 5 nm, and c) 7 nm SiNPs (nominally) functionalized for different lengths of time after oxidation, showing the experimental data (black trace), the fit (red, dashed trace), and the difference between the two (gray trace). All samples except the smallest, most oxidized SiNPs show reflections characteristic of crystalline Si (as indexed above the plots). 106

Figure 4-11. Plots comparing the a) size, b) strain, and c) lattice parameter determined from the XRD fitting for the SiNPs functionalized for different amounts of time and different functionalized TEM sizes. 107

Figure 4-12. Photoluminescence spectra for a) 3 nm, b) 5 nm, and c) 7 nm SiNPs with varying functionalization times after oxidation. 109

Figure 4-13. Comparing the PL max as a function of a) d_{XRD} for 3, 5, and 7 nm SiNPs with varying degrees of oxidation to the effective mass approximation (black trace: $E_{gr} = 1.12 + 3.77/r^2$). For further understanding, the change in photoluminescence is compared to b) d_{XRD} 110

Figure 4-14. A comparison of lifetimes as a function of $d_{XRD, 900 \text{ min}}$ with different functionalization times after oxidation. 110

Figure 4-15. Scheme showing the synthesis of hydride-terminated 3 nm SiNPs and 3 nm SiNCs from hydrogen silsesquioxane (HSQ). 111

Figure 4-16. High resolution Si 2p spectrum showing the 2p_{3/2} and 2p_{1/2} emissions for oxidized samples of a) 3 nm SiNPs and b) 3 nm SiNCs The colored traces are: black = experimental data, dashed red = fitting envelope, orange = core Si, green = ~SiO_{0.5} or silicon-carbon species, purple = ~SiO, blue = ~SiO_{1.5}, and magenta = ~SiO₂. 111

Figure 4-17. TEM images showing (a and b) 3 nm SiNPs and (c and d) 3 nm SiNCs functionalized for (a,c) 900 and (b, d) 30 min after oxidation. 112

Figure 4-18. Histograms showing the size distribution of a) 3 nm SiNPs, and b) 3 nm SiNCs that were functionalized for 900 min (top) and for 30 min (bottom). Sizes were determined based on TEM imaging of the SiNPs. 113

Figure 4-19. XRD patterns for a) 3 nm SiNPs and b) 3 nm SiNCs functionalized for 900 min and for 30 min after oxidation, showing the experimental data (black trace), the fit (red, dashed trace), and the difference between the two (gray trace). The SiNCs show reflections characteristic of crystalline Si. 114

Figure 4-20. Photoluminescence spectra for a) 3 nm SiNPs, b) 3 nm SiNCs, and c) 5 nm SiNPs with varying functionalization times after oxidation. 115

Figure 4-21. a) A plot of the PL max as a function of d_{XRD} for 3, 5, and 7 nm SiNPs, as well as 3 nm SiNCs with varying degrees of oxidation. b) The change in photoluminescence is plotted against $d_{XRD, 900 \text{ min}}$, with the 3 nm SiNCs showed in orange. 115

Figure 5-1. A schematic representation of the internal structure of SiNPs of various sizes, as outlined in Chapter 2. Blue represents the crystalline core; red, the semi-ordered subsurface; and yellow, the disordered surface. 120

Figure 5-2. An artistic rendering of SiNPs with different amorphous shell thicknesses and a demonstration of the impact on photoluminescence emission for SiNPs of the same d_{TEM} 120

Figure 5-3. ^{29}Si NMR spectra of 9 nm SiNPs functionalized with dodecene using AIBN and XeF_2 as the initiators. The spectra of 6 and 9 nm H-SiNPs are presented for comparison.	123
Figure 5-4. Purposed structure for a SiNP-based multimodal imaging agent.	124
Figure 5-5. a) Bright field TEM image, b) X-ray diffraction pattern, and c) experimental and d) simulated light scattering data for 113 ± 35 nm SiNPs. The bright field TEM image was acquired as outlined in 4.2.2.4 and the diffraction pattern was acquired at the Canadian Light Source (as described in 4.2.2.3). Static light scattering experiments and simulations were performed by Philippe Barois at the University of Bordeaux. Static light scattering experiments were performed using a custom built set-up. Colloidal solutions of the SiNPs were irradiated using a super continuum white source (SuperK EXB-6 with SuperK Split visible filter from NKT Photonics), and the scattered light is collected at 90° using a Minispectrometer (Hamamatsu C10083CA) fed with an optical fiber. Simulations were performed using software that solves the equations of Mie scattering theory (coded in Maple). The software calculates the scattering efficiency of the diagonal elements of the scattering matrix and every individual mode. Size, size distribution, porosity, and crystallinity of the SiNPs are accounted for in the simulations.	125
Figure A-1. Scheme showing amidine switching hydrophilicity in the presence of CO_2 . .	153
Figure A-2. Scheme showing the functionalization of Si-NCs with a terminal amidine group using radical initiated hydrosilylation, followed by deprotection using HCl. .	157
Figure A-3. a) Brightfield TEM image and b) photoluminescence emission spectrum of the amidine-functionalized Si-NCs. Inset: Histogram depicting measured Si-NC size.	157
Figure A-4. FTIR spectra highlighting the chemical functionalities of hydride-terminated SiNCs (blue), N'-undec-10-enyl-N,N-dimethylacetamide (red), and the amidine-functionalized Si-NCs (black).	158

- Figure A-5.** High resolution X-ray photoelectron spectroscopy (XPS) of the a) Si 2p and b) N 1s. The black trace is the experimental spectra and the red dashed line is the fit. For clarity, only the Si 2p_{3/2} are shown. 159
- Figure A-6.** Photographs depicting the hydrophilicity switch of the material irradiated under 365 nm light depicting the photoluminescence of the SiNCs a) in toluene before switching, b) after adding water, c) after bubbling through CO₂ for 1 h, and d) after bubbling Ar through the sample for 30 min at 65 °C. 160
- Figure A-7.** Comparison of normalized photoluminescence spectra of Si-NCs in toluene before the switch (black), water after bubbling CO₂ at room temperature for 1 h (red), and toluene after bubbling Ar through the sample for 30 min at 65 °C..161

List of Tables

Table 2-1. Particle Band Gap and Size Analysis from TEM and XRD	44
Table 2-2. List of Common ^{29}Si Chemical Shifts for Silicon Containing Materials	55
Table 2-3. Experimental ^{29}Si MAS NMR FWHM, Nuclear Spin-Lattice Relaxation Times (T_1) and Surface Fraction Deconvolutions of the H-SiNPs with Varying Particle Diameters	61
Table 2-4. Calculated Fraction of Surface, Sub-surface and Core Si Species Based on the Model by Zhao et al. and Avramov et al. ^{2,3}	63
Table 3-1. A Summary of Experimental Parameters and Results for All Samples.	74
Table 3-2. Lifetime Fitting Parameters for 1200-SiQDs and 1300-QDs	77
Table 4-1. Surface coverage determination using TGA.....	101
Table 4-2. Table of surface area to volume ratio (SA/V) and relative atm% of Si, C, O, and F from survey XPS spectrum	103
Table 4-3. Table of d_{TEM} obtained from TEM analysis and d_{XRD} , strain, and lattice parameter, obtained from XRD fitting of 3 nm SiNPs and 3 nm SiNC.....	114

List of Symbols, Nomenclature and Abbreviations

Å	Angstrom
°	Degree(s)
°C	Degree Celsius
ΔE	Excitation energy
δ_{cgs}	Center-of-gravity chemical shift
δ_{iso}	Isotropic chemical shift
μm	Micrometer(s)
μs	Microsecond(s)
1200-SiQD	Silicon quantum dots from hydrogen silsesquioxane annealed at 1200 °C
1300-SiQD	Silicon quantum dots from hydrogen silsesquioxane annealed at 1300 °C and subjected to extended HF etching
2D	Two dimensional
a. u.	Arbitrary unit
AIBN	Azobisisobutyronitrile
<i>a</i> -Si	Amorphous silicon
at(m)%	Atomic percent
core@shell QD	Quantum dot with a material grown epitaxially off the surface to form a shell surrounding the core
C@GS QD	Core@graded shell; a core@shell QD with a transition region that slowly changes from the core composition to the shell composition
C@A@S	Core@alloyed shell@shell; a core@shell QD with an additional layer between the core and shell of mixed composition.
CB	Conduction band
CLS	Canadian Light Source
cm^{-1}	Wavenumber(s)
CP	Cross-polarization
<i>c</i> -Si	Crystalline silicon
<i>d</i>	Diameter
DNP	Dynamic nuclear polarization
DPA	9,10-diphenylanthracene
d_{TEM}	Diameter of the nanoparticle, based upon TEM analysis
d_{XRD}	Diameter of the crystalline domain, based upon XRD analysis
E_{g}	Band gap
EMA	Effective mass approximation
ESR	Electron spin resonance
eV	Electronvolt
FTIR	Fourier transform infrared spectroscopy
FWHM	Full width half maximum
g	Gram(s)
GL	Gaussian-Lorentzian
h	Hour(s)
HAADF	High annular angle dark field

H-SiNPs	Hydride-terminated silicon nanoparticles
HSQ	Hydrogen silsesquioxane
HOMO	Highest occupied molecular orbital
<i>I</i>	Intensity
IR	Infrared
<i>k</i> space	Momentum space
kV	Kilovolt(s)
kHz	Kilohertz
LCAO	Linear combination of atomic orbitals
LED	Light-emitting diodes
LIB	Lithium-ion battery
LSC	Luminescent solar concentrator
LUMO	Lowest unoccupied molecular orbital
MAS	Magic-angle spinning
mg	Milligram(s)
MHz	Megahertz
min	Minute(s)
mL	Millilitre(s)
mmol	Millimole(s)
MRI	Magnetic resonance imaging
mW	Milliwatt(s)
NMR	Nuclear magnetic resonance
NPs	Nanoparticles
ng	Nanogram(s)
nM	Nanomolar
nm	Nanometer(s)
ns	Nanosecond(s)
PDF	Pair distribution function
PEG	Polyethylene glycol
PET	Positron emission tomography
PL	Photoluminescence
PL max	Photoluminescence emission maximum
ppm	parts per million
QD	Quantum dot
QY	Quantum yield
RH	Relative humidity
s	Second(s)
SA/V	Surface area to volume ratio
SiNC	Silicon nanocrystal
SiNP	Silicon nanoparticle
SiNP/SiO ₂	Silicon nanoparticles embedded in a silica matrix
SiQDs	Silicon quantum dots
SiQD/SiO ₂	Silicon quantum dots embedded in a silica matrix
STEM	Scanning transmission electron microscopy
<i>T</i> ₁ relaxation	Nuclear spin-lattice relaxation

TGA	Thermogravimetric analysis
TEM	Transmission electron microscopy
TMF	Toxic metal-free
TRPL	Time-resolved photoluminescence
UV	Ultraviolet
VB	Valence band
XPS	X-ray photoelectron spectroscopy
XRD	X-ray diffraction

Chapter 1

Introduction

1.1 Quantum Dots – Inorganic Semiconductor Nanoparticles

The National Nanotechnology Initiative (NNI) defines nanotechnology as *science, engineering, and technology conducted at the nanoscale, which is about 1 to 100 nanometers*.¹ Antibodies, proteins and viruses are found in this size regime (Figure 1-1). Nanomaterials are thousands of times smaller than the width of a piece of paper. When materials are prepared on the nanoscale, unique properties emerge that are not observed in bulk systems, for example, gold appears red due to plasmonic interactions with light.² Due to the extremely small size of nanomaterials, surfaces and quantum mechanics play a more pronounced role in defining material properties.³ The importance of surfaces means that the size, shape and surface all play a critical role in defining material properties. The complex nature of these systems requires an interdisciplinary approach to understand, tune, and apply nanomaterials in novel technologies.

Quantum dots (QDs) are semiconductor nanomaterials that exhibit light emission due to their nanoscale dimensions. When the dimensions of semiconductor particles are below the dimensions of a Bohr exciton in the corresponding bulk material (the diameter where the electron-hole pair is confined by the boundaries of the nanoparticle instead of Coulombic attraction),⁴ the electrons and holes become quantum mechanically confined. This confinement manifests itself through a widening of the band gap (the energy gap separating the conduction and valence bands), which enables QDs to emit light. The energy of the emitted light is dominated by the composition and dimensions of the nanoparticle.⁵ Quantum confinement in semiconductor nanomaterials manifests itself in the emergence of discrete energy levels at the band edges of the semiconductor. In a bulk semiconductor, the conduction and valence bands are comprised of pseudo continuous energy levels separated by the band gap. In shifting to the nanoscale, atomic orbitals are removed from the band structure of the material as a result of the removal of atoms (Figure 1-2).⁶

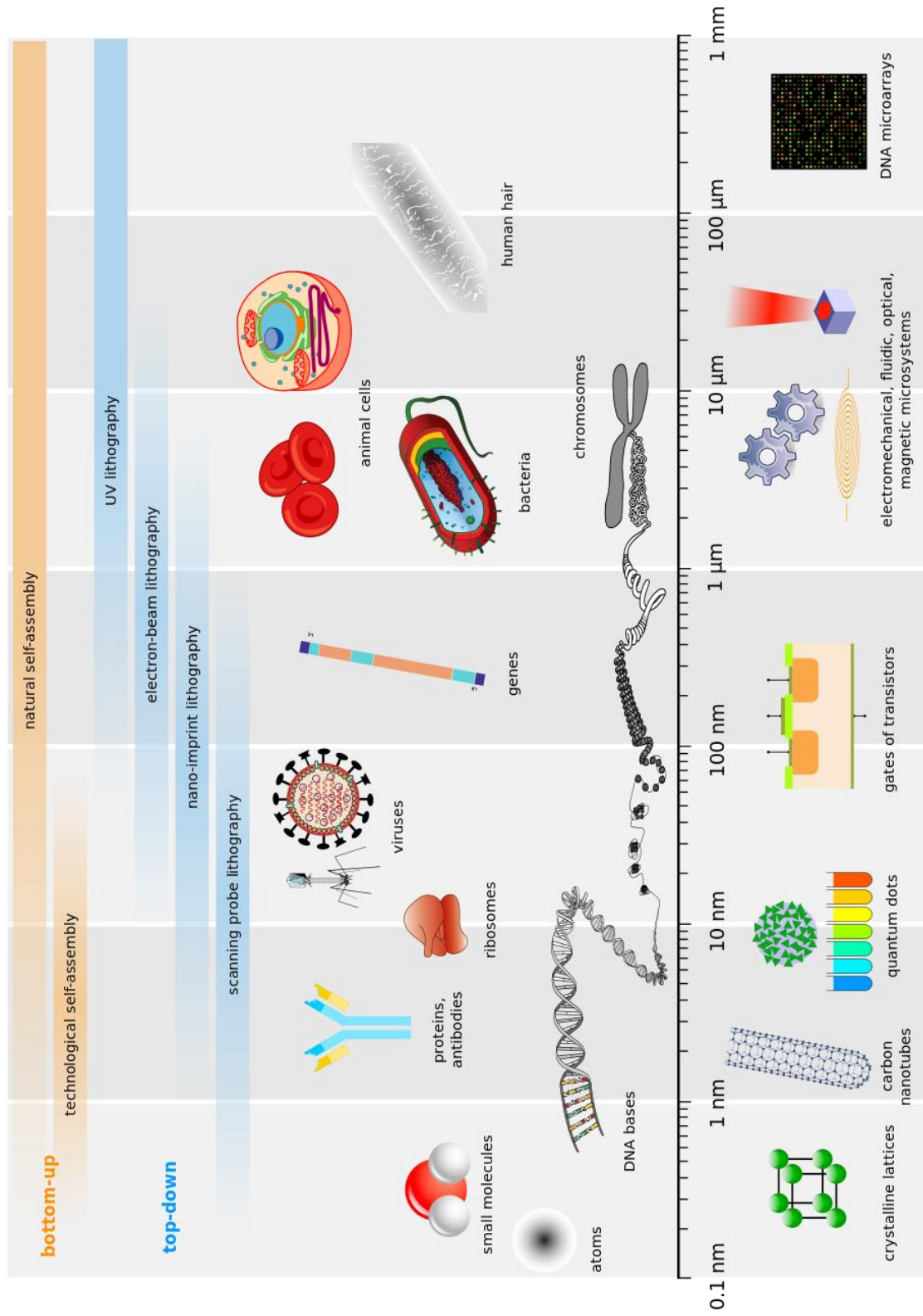


Figure 1-1. A pictorial representation of the relative size of biological and technological objects. (Image by Guillaume Paumier, Philip Ronan, NIH, Artur Jan Fijałkowski, Jerome Walker, Michael David Jones, Tyler Heal, Mariana Ruiz, Science Primer (National Center for Biotechnology Information), Liquid_2003, Arne Nordmann & The Tango! Desktop Project and licensed under CC BY-SA 2.5)

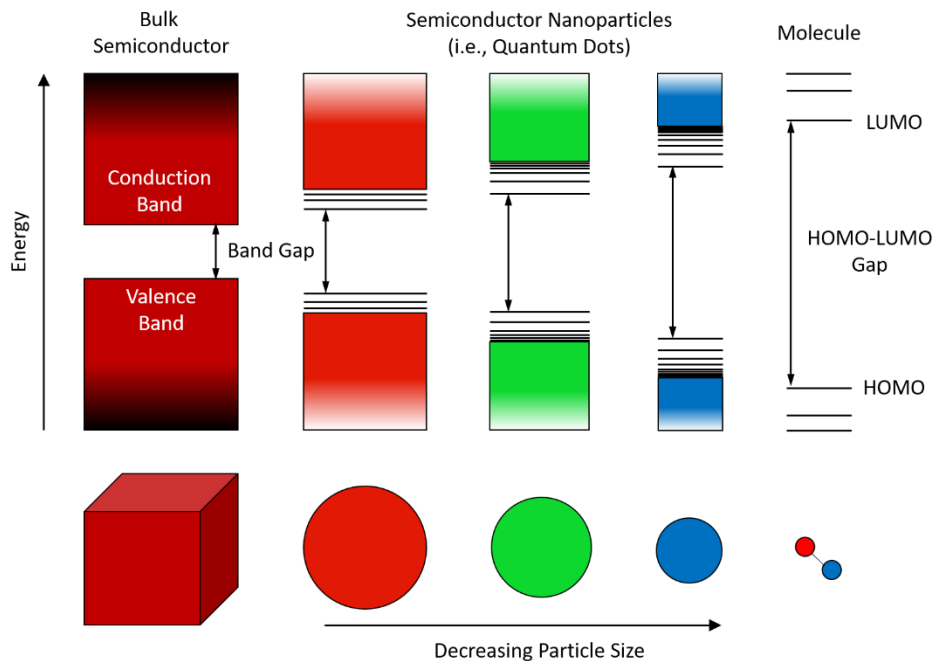


Figure 1-2. A schematic representation of the change in band structure when going from bulk (conduction and valence bands) to nano to molecular systems (highest occupied and lowest unoccupied molecular orbitals; HOMO and LUMO).

This results in a quantization of the energy levels at the band edge, similar to that observed for molecular systems. As the particle becomes smaller, more energy levels are removed from the band edge, causing the band gap to increase and resulting in a blue shift of the photoluminescence. A pictorial representation of this effect is shown in Figure 1-2.

Epitaxial growth of another material on the surface of a QD passivates the surface, yielding a core@shell QD.⁷ The composition of the core and shell can be tuned to control the confinement of the carriers within the core and/or shell.^{8, 9} These core@shell systems are separated into four categories based on the relative band positions of the core and shell material, as shown in Figure 1-3: Type I, Inverse Type I, Type II, and Inverse Type II QDs. Type I QDs are the most common; the band gap of the core falls within the band gap of the shell.⁷ This system increases trapping of the carriers within the particle core and leads to near quantitative photoluminescence quantum yields (i.e., 99.5%).¹⁰ In the Inverse Type I system, the shell band gap is smaller than and falls within the band gap of the core, as shown in Figure 1-3.¹¹ These systems confine the carriers to the shell, facilitating electron and hole transfer out of the QD.¹¹

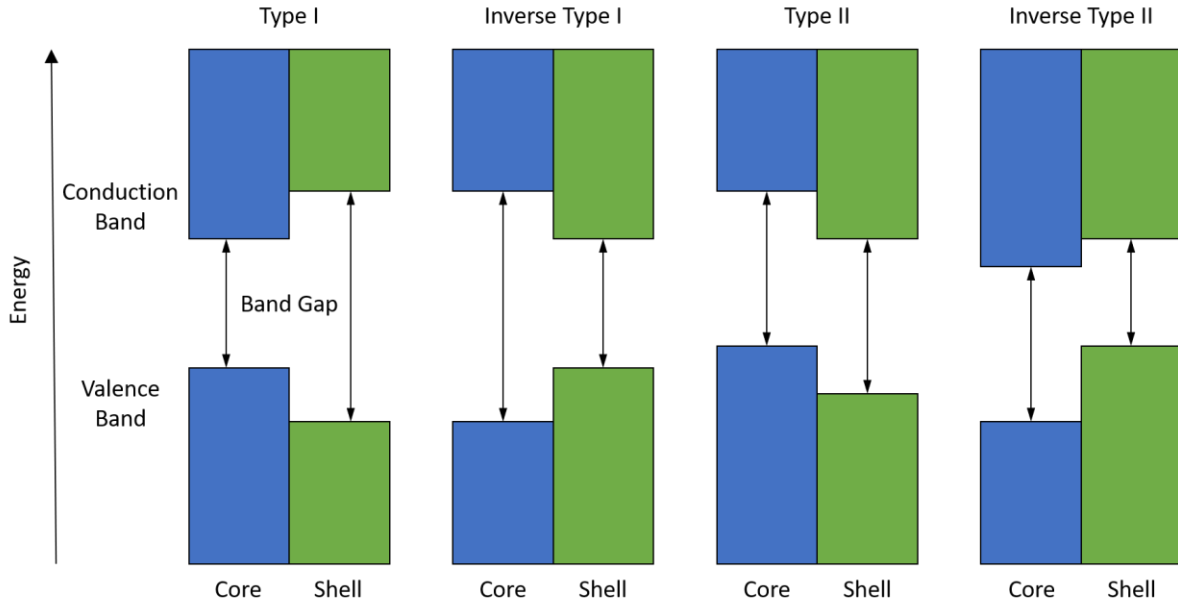


Figure 1-3. Schematic representation of band edge alignment of materials for different types of core@shell QDs.

Type II QDs are characterized by nesting of the energy bands so that they lead to the spatial separation of the electron and the hole between the core and the shell. In a Type II QD, the conduction and valence bands of the shell are of lower energy than the conduction and valence bands of the core.¹² This confines the holes to the core and the electrons to the shell. When the conduction bands are close in energy, the electrons will be delocalized over the whole QD (referred to as a Quasi-Type II QD).¹³ This system typically has a low quantum yield and is limited by insufficient carrier confinement.⁹ In the inverse Type II system, the bands are nested the opposite way, confining the electron to the core and the hole to the shell, however, delocalization of the carriers over the system is still possible.^{12, 13} This system improves quantum yields, however, not as much as Type I QDs.⁹ While the relative position of the bands typically is controlled by the composition of the core and the shell, the band structure also can be tuned by manipulating the diameter of the core and the thickness of the shell.¹⁴ For example, if a CdS shell is thin enough, then the band gap increases so that it will form a Type I system with CdTe instead of a Type II system, as shown in Figure 1-4.¹⁴

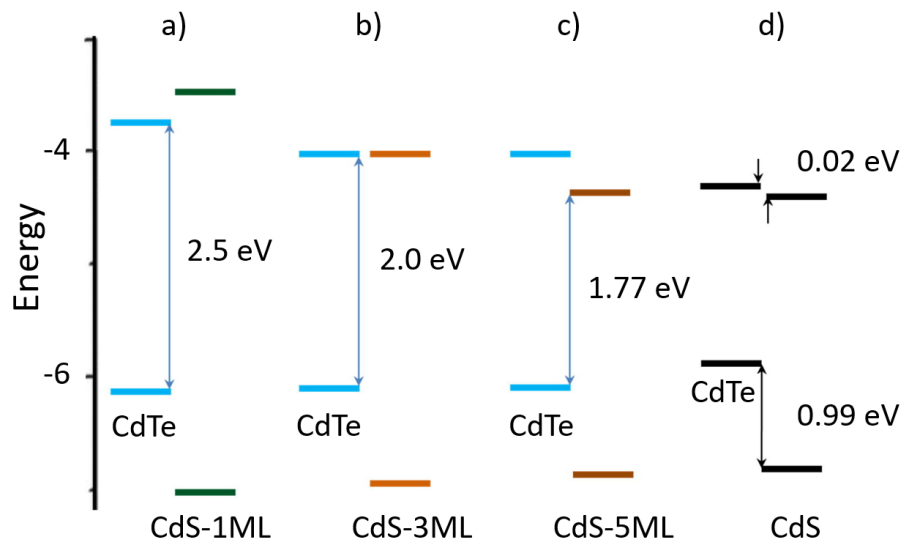


Figure 1-4. A schematic representation of the band edges for CdTe@CdS core@shell QDs showing the transition from a) Type I to c) Type II QDs as a function of the shell thickness and d) the relative band edges of the bulk CdTe and CdS systems. Image adapted from *Opt. Mater.* **2016**, 53, 34-38 (Ref 14). Copyright 2016 Elsevier.

Core@graded shell (C@GS) QDs gradually transition from the core composition to the shell in a radially graded fashion (Figure 1-5a).^{15, 16} This transition is different from the abrupt transition in the core@shell systems described above. This also is different than core@alloyed shell@shell (C@A@S) QDs where the alloyed shell adds a step in between the band edges of the core and the shell, as can be observed in Figure 1-5a.^{17, 18} In QDs, the graded shell provides unique control over the band alignment and, as a result, the carrier dynamics at the interface. Gradient shell systems emerged due to their “soft” interface dynamics relative to traditional core@shell systems (Figure 1-5b).¹⁹ It is proposed that the soft interface arises from delocalized surface states (Figure 1-5a) enabling the exciton to decay evanescently into the core, as shown in Figure 1-5b.^{19, 20} This decreases photoluminescence from surface states, as evidenced by the ratio of the PL intensity from core emission and total PL intensity shown in Figure 1-5c.¹⁹ The transition region also lowers strain, suppressing Auger recombination (a non-radiative recombination of the exciton that results in the emission of an electron), leading to increased quantum yields.^{17, 21, 22} Together, the soft interface and suppression of Auger recombination in graded shell systems make them intriguing examples of the influence of interface dynamics on QD systems.

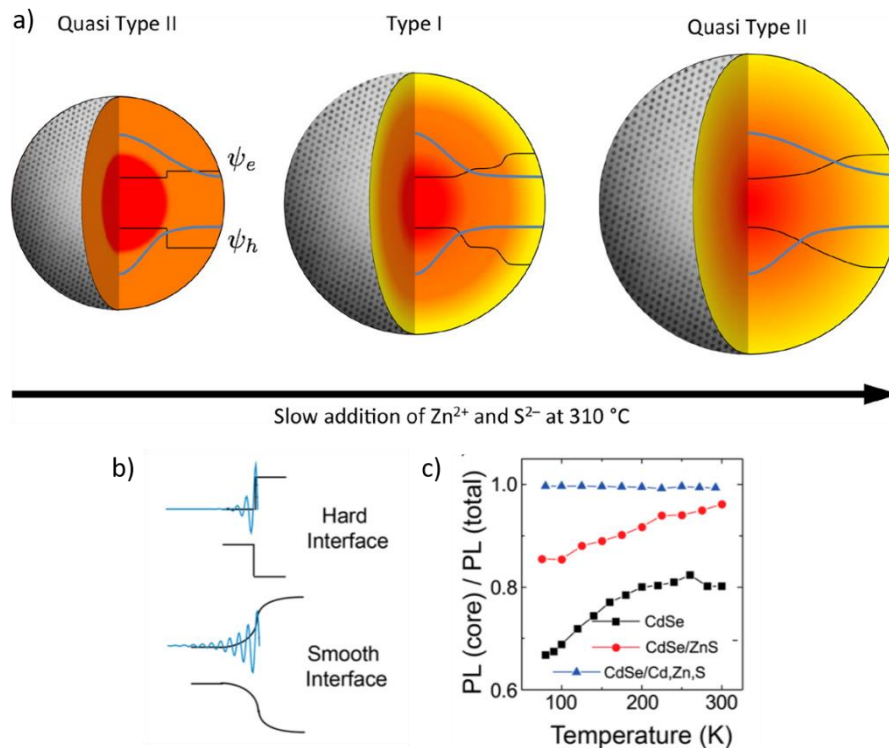


Figure 1-5. a) A schematic representation of core@shell, C@A@S, and C@GS QDs, their band structures (the black lines), and the associated wavefunctions of the carriers (blue lines). b) A comparative illustration of the interaction of the electronic wavefunction at the interface of a core@shell QD with a hard interface and a C@GS QD with a soft interface. The black lines represent the band structure, and the blue lines represent the interaction of the wavefunction. c) The ratios of the integrated areas of the PL emission from the core and the total PL emission for CdSe QDs (no shell), CdSe@ZnS (core@shell), and CdSe@Cd,Zn,S (C@GS). Reprinted with permission from *Chem. Mater.*, **2013**, 25 (23), 4731-4738 (Ref 20) and *J. Phys. Chem. C*, **2016**, 120 (34), 19409-19415 (Ref 19). Copyright 2013 and 2016 American Chemical Society.

1.2 Silicon Nanoparticles

Quantum dots in current use often rely on toxic and non-earth abundant elements (e.g., Cd and In).^{23, 24} Instead, it is desirable to use QDs based on earth abundant and biologically compatible materials, such as silicon.^{23, 25} In early studies, luminescence from silicon was demonstrated by applying current to a *p-n* junction.^{26, 27} In 1990, Leigh Canham demonstrated that silicon-based luminescence could also be achieved through quantum confinement of carriers.²⁸ Since then, applications and properties of luminescent silicon nanostructures have been explored widely.

Silicon is an indirect band gap semiconductor. In a direct band gap semiconductor, the minimum of the conduction band sits directly above the maximum of the valence band in momentum space (*k* space), as shown in Figure 1-6a. Direct transitions between the valence and conduction bands in direct band gap semiconductors conserve both momentum and

energy and, therefore, are allowed. For indirect band gap semiconductors, the minimum of the conduction band and the maximum of the valence band are offset (Figure 1-6b).^{29, 30} This offset makes direct transitions between the conduction and valence bands forbidden as the transition would not follow the Law of Conservation of Momentum; thus, it requires a change in symmetry. In order to satisfy this condition, a phonon must be released during the transition (Figure 1-6b).³¹

The forbidden vertical transition made Canham's original discovery of luminescence from silicon surprising. However, when silicon is below its Bohr exciton radius (~ 4 nm for Si), the transition occurs more readily.⁴ It is thought that these transitions are enabled by spreading of the hole and electron wavefunctions in k space due to the spatial confinement of the carriers, causing an increase in the overlap of the wavefunctions. This breaks the crystal momentum selection rules, facilitating the otherwise forbidden transition.^{32, 33} Further, when the dimensions of a silicon particle are below the Bohr exciton radius, the finite size enables the required momentum changes to come from a combination of surface scattering and phonons in the particle.^{32, 34} Together, these factors provide an explanation for the long-lived luminescence from nanostructured silicon that is typically referred to as S-band emission (emission of orange to near-infrared radiation). However, the exact origin of silicon-based photoluminescence is undoubtedly more complex. Insights into the nature of silicon-based luminescence are further complicated by the high energy emission with short-lived lifetimes (typically referred to as the F-band), which will be discussed briefly in Section 1.5.

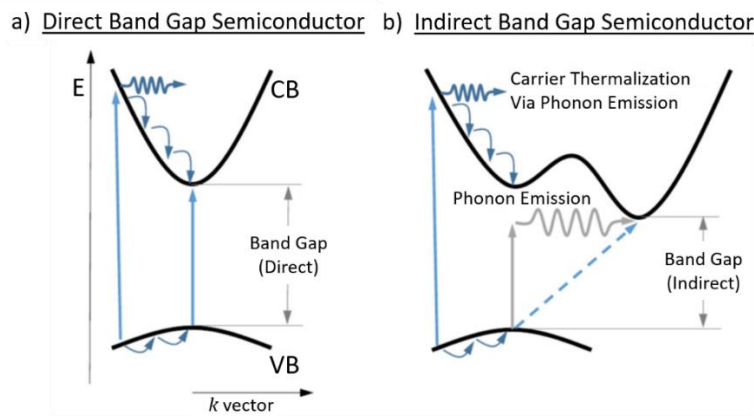


Figure 1-6. A schematic representation of the band structure of a) direct and b) indirect semiconductors. Image adapted from *Scientific Reports*, 2017, 7, 15365 (Ref 30). Licensed under CC BY 4.0.

1.3 Applications of Silicon Nanoparticles

Silicon nanoparticles (SiNPs) have been studied widely because of their unique optical and chemical properties.³⁵⁻³⁸ Applications of these materials range from medical (i.e., luminescence imaging,^{39, 40} MRI)^{41, 42} to defense (i.e., sensors for high-energy materials and neurotoxins)^{43, 44} to energy (i.e., luminescent solar concentrators,^{45, 46} light-emitting diodes,^{47, 48} and battery anode materials).^{36, 49} It is a combination of the biological compatibility, earth-abundance, long-lived excited states, large Stokes shift (the difference between the absorption and emission), and tunable luminescence, among other chemical properties that enable diverse potential applications.

1.3.1 Biological Imaging

The good biological compatibility of silicon relative to other QDs, combined with its luminescence in the near infrared (IR), makes these materials desirable for biological imaging.²³ There are many reports using silicon-based QDs for fluorescence imaging of biological systems. Efforts to synthesize water-soluble SiNPs for this application have been extensive, including direct grafting of water-soluble ligands (i.e., PEG, carboxylic acids, amines),^{25, 50-52} indirect grafting of water-soluble moieties (i.e., using Click-Chemistry),^{40, 53} and incorporation into water-soluble media (i.e., quatsomes and micelles).^{39, 54, 55}

These systems exhibit photoluminescence, ranging from blue (with nanosecond lifetimes)^{51, 53} into the near infrared region (with microsecond lifetimes),^{39, 40, 54, 55} and have been used for both *in vitro*^{39, 50, 51, 53, 55} and *in vivo* imaging.^{40, 54, 55} While many examples of photoluminescence imaging with SiNPs exist, recently, the community has worked to leverage the long-lived photoluminescence lifetimes to improve contrast over the autofluorescence of cells using time-gated imaging. Sailor first demonstrated this with porous SiNPs in a mouse model.^{56, 57} While SiNPs have a lower quantum efficiency than typical fluorescent dyes (i.e., fluorescein isothiocyanate [FITC]), time-gated imaging can remove background fluorescence, thereby enhancing the contrast.^{58, 59} In fact, by using time-gated imaging, the signal to background ratio is increased up to 3x compared to steady state imaging for SiNPs, as shown in Figure 1-7.⁴⁰

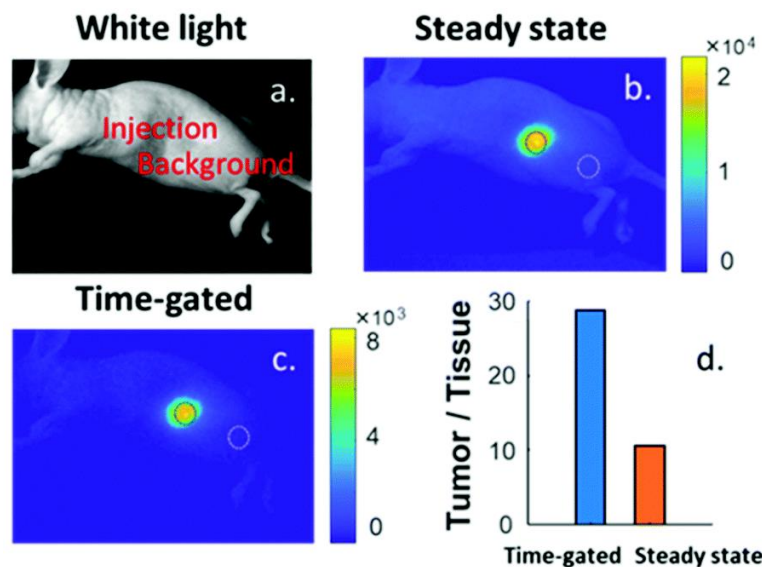


Figure 1-7. Athymic nude mouse imaged with a) white light, b) steady-state luminescence imaging, and c) time-gated luminescence imaging after subcutaneous injection of SiNPs. d) A comparison of the signal-to-background ratio using time-gated imaging (with a delay of 10 μ s) and steady state imaging. Reproduced from *Nanoscale*, **2020**, *12*, 7921-7926 (Ref. 40) with permission from the Royal Society of Chemistry.

Imaging of SiNPs has been extended beyond fluorescence and optical imaging to ²⁹Si magnetic resonance imaging (MRI). It is non-trivial to probe the ²⁹Si nuclei directly as the nuclei have a small absorption cross section, low gamma, and are not abundant, making detection of small quantities of these materials in vivo difficult.⁶⁰

In order to overcome these deficits, “hyperpolarization” using dynamic nuclear polarization (DNP) can be employed (Figure 1-8).⁴¹ This method involves the transfer of spin polarization from electrons (i.e., radicals) either directly to the nuclei of interest or to protons and then the nuclei, thus requiring a source of radicals near the SiNP.^{61, 62} A ²⁹Si MRI of large SiNPs (50 nm–2 μ m) has been achieved using both external and internal radical sources. The addition of a radical agent, such as TEMPO into the solution (an external radical), is able to provide enough enhancement to get a clear ²⁹Si MR image.⁶³ However, radicals from oxidation induced defects in large SiNPs also can be used.^{41, 42} ²⁹Si MR images can be observed for SiNPs polarized using both methods in mouse models.^{42, 63} While the use of an external radical shortens the relaxation time relative to the internal radicals (i.e., 20 vs 30 min), the improvement in signal allows clear ²⁹Si MR imaging of both after 60 min.^{42, 63} While small particles with long T_1 relaxation rates have shown potential for this application, they have not been employed for imaging.⁶⁴

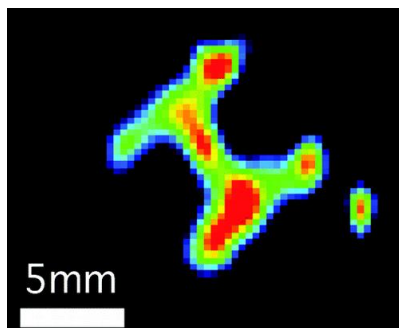


Figure 1-8. A ^{29}Si magnetic resonance image taken of hyperpolarized silicon microparticles in an H-shaped phantom. Reprinted with permission from *ACS Nano*, **2009**, 3(12), 4003-4008 (Ref 41). Copyright 2009 American Chemical Society.

The tailorable surface chemistry (vide infra) combined with time-gated fluorescence imaging and ^{29}Si MRI make these materials seemingly great candidates for multimodal imaging applications. While fluorescence imaging and ^{29}Si MRI have not been combined, SiNPs doped with Mn^{2+} exhibiting blue PL have shown promise for combined fluorescence and T_1 weighted ^1H MRI.⁶⁵ In fact, these SiNPs can be derivatized further with DOTA (1,4,7,10-tetraazacyclododecane-1,4,7,10-tetraacetic acid) to chelate the PET active ^{64}Cu ion to provide a more versatile imaging system.⁶⁶ This work was extended further to Fe-doped silicon as a similarly promising candidate for T_2 weighted ^1H MRI and fluorescence imaging.⁶⁷

1.3.2 Sensors

The visible photoluminescence of SiNPs makes them promising as luminescence-based sensors.^{37, 38} Sensor designs often are based upon photoluminescence quenching through electron transfer.³⁸ SiNPs have been used to detect high energy compounds (such as DNT, TNT RDX),^{43, 68} metal cations (Hg^{2+} ,⁶⁹ Cu^{2+} ,⁷⁰ Cr^{4+}),⁷¹ biologically relevant molecules (glucose,^{72, 73} dopamine,⁷⁴ ethanol),⁷⁵ and pesticides (carbaryl, parathion, diazinon, phorate).^{44, 76} SiNP sensors are capable of sensing DNT to 18.2 ng with oligomer alkyl passivation⁴³ and Hg^{2+} to 50 nM with amine termination.⁶⁹ To improve the visual detection, ratiometric sensors have been developed based on SiNP hybrids with green fluorescent protein.⁴⁴ This enables detection of nerve agents (paraoxon and parathion) by a clear visible change from yellow to green photoluminescence due to the quenching of the silicon nanoparticle.⁴⁴

1.3.3 Luminescent Solar Concentrators

Recently, SiNPs have been employed as emitters in luminescent solar concentrators (LSCs). LSCs take advantage of the large Stokes shift that has been attributed to the indirect band gap of silicon to turn windows into solar energy generators (Figure 1-9).⁴⁵ SiNPs absorb UV light from solar irradiation and down convert it to near infrared photoluminescence, which is absorbed more efficiently by Si-based solar cells. Then, the light is propagated along the glass pane to the edges, where the concentrated light illuminates photovoltaic (PV) cells.

Recent work has focused on reducing light scattering of the SiNP film to improve transparency by tuning the surface moieties to improve compatibility with the polymer matrix.^{46, 77} Other work has targeted shifting the absorption of the LSC system to correspond better with the solar spectrum. To accomplish this, Ceroni and co-workers mixed 9,10-diphenylanthracene (DPA) chromophores with silicon nanoparticles to capture visible light more efficiently. They found that physical mixing of DPA and SiNPs works better than covalent linking as functionalization decreases the photoluminescent quantum yields of the silicon core.⁷⁸

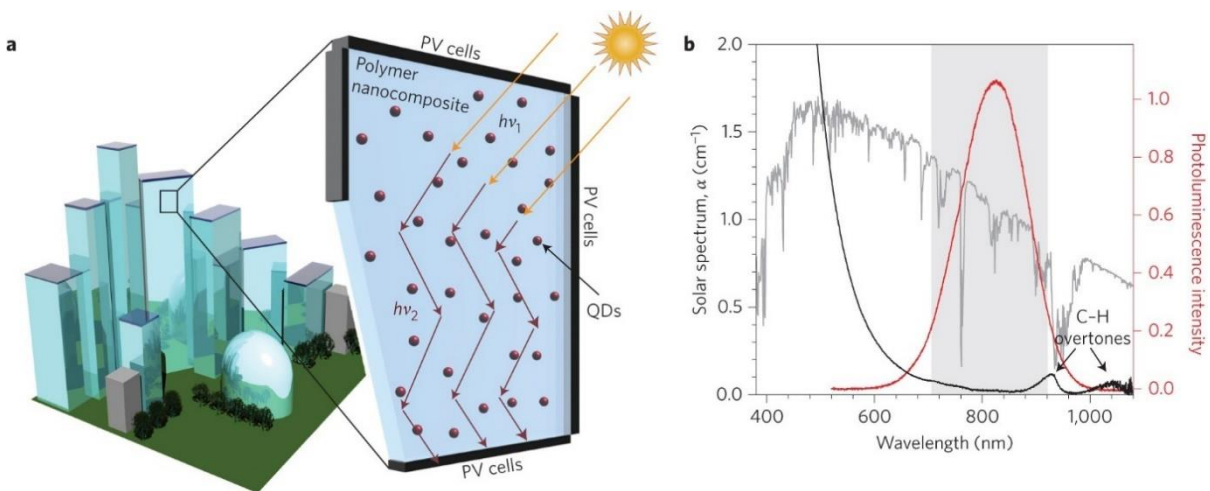


Figure 1-9. a) A schematic representation of a luminescent solar concentrator based on silicon QDs. b) A plot showing the overlap of the solar spectrum (gray trace) with the absorbance (black trace) and photoluminescence emission (red trace) of 4.3 nm silicon nanoparticles. The transparency window is indicated by the gray shading. Reprinted by permission from Springer Nature: *Nature, Nat. Photon.* **2017**, *11*, 177-185 (Ref 45).

1.3.4 Light-emitting Diodes

The emergence of QDs as highly tunable emitters for LEDs in TVs, coupled with the European Union's ban on Cd-based materials, has driven investigations into alternative QDs for LEDs.⁷⁹ While this work has focused largely on the use of InP systems, these systems

rely on In, which has limited earth abundance.⁸⁰ SiNPs provide an intriguing alternative. SiNPs of different sizes have been utilized to make LEDs with luminescence, spanning between the orange and near IR regions of the electromagnetic spectrum (Figure 1-10).^{47, 81} Despite promising luminescent properties, before commercialization for TV applications, SiNPs have several limitations that must be overcome: their wide full-width half maximum (FWHM) of the luminescence spectrum and intrinsically low quantum efficiencies.^{47, 81}

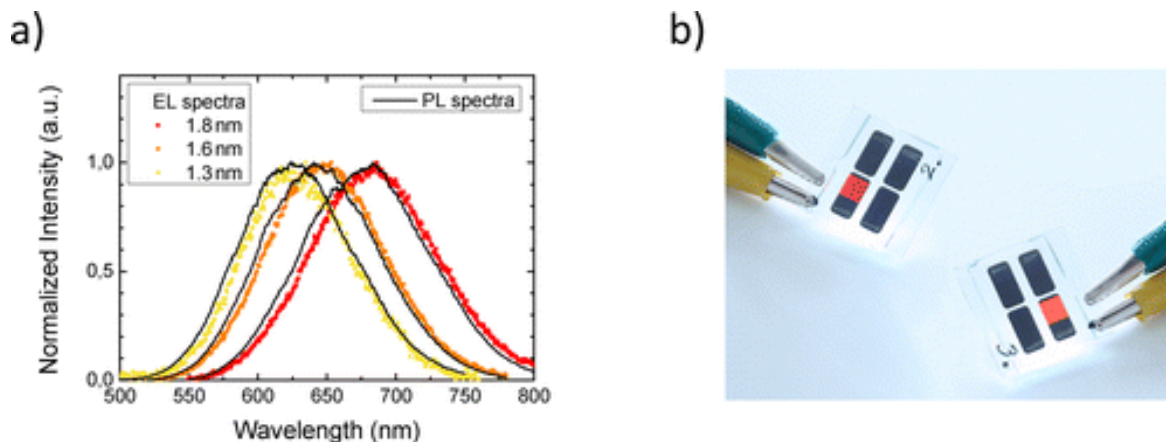


Figure 1-10. a) Electroluminescence and photoluminescence spectra of 1.3, 1.6 and 1.8 nm SiNPs. b) Photographs of LEDs made from SiNPs demonstrating visible luminescence taken under ambient lighting conditions. Reprinted with permission from *Nano Lett.* **2013**, *13*(2), 475-480 (Ref 81). Copyright 2013 American Chemical Society.

1.3.5 Lithium Ion Batteries

With the world moving toward portable energy, there is a great desire to improve the capacity of batteries, specifically lithium ion batteries (LIBs). This can be accomplished through optimization of the various components of LIBs. Silicon is a prime candidate for replacing graphite as the anode material as it has a much higher theoretical specific capacity (4200 mAh/g for Si vs. 372 mAh/g for graphite).³⁶ However, this is associated with large volume changes upon lithiation (>300%) that lead to pulverization of the silicon after several cycles and deterioration of the anode.⁸² These limitations can be overcome by shifting to nanoscale Si, which is able to accommodate the volume changes better.⁴⁹ Other limitations, including low conductivity and the formation of the solid electrolyte interphase, can be addressed by employing a conductive matrix and careful manipulation of surface chemistry.^{83, 84}

1.4 Synthesis and Functionalization of Silicon Nanoparticles

To realize these diverse applications, free-standing SiNPs first must be synthesized. The synthetic procedure can be separated broadly into two main categories: synthesis of the silicon nanoparticle core and the functionalization with surface passivating ligands. Both the nanoparticle core and surface ligands are important for determining the final properties of the silicon nanoparticles and their applications. This section explores bottom-up synthetic methods for making silicon nanoparticles and passivation of hydride-terminated silicon nanoparticle surfaces.

1.4.1 Synthesis of Silicon Nanoparticles

Synthesizing silicon nanoparticles is of great interest owing to their desirable properties outlined above. While top-down synthetic methods, such as ball-milling^{85, 86} and laser ablation,⁸⁷ often are used, this section will focus on bottom-up approaches. The bottom-up synthetic methods will be broken down into three categories: gas-, solution-, and solid-phase synthesis.

1.4.1.1 Gas Phase Synthesis

The gas phase synthesis of SiNPs typically revolves around the decomposition of silane and the subsequent clustering of silicon atoms into nanoparticles. Thermal decomposition of silane at 1100 °C was reported first by Murthy et al. in 1976 for the synthesis of large ($d = 30\text{--}80$ nm) octahedral SiNPs.⁸⁸ However, silicon in this size regime does not demonstrate luminescence, making other methods to produce small luminescent SiNPs desirable. CO₂ laser induced pyrolysis of silane forms small SiNPs (5 nm; Figure 1-11).^{89, 90} However, only after HF or HNO₃/HF etching can photoluminescence spanning the visible spectrum be observed.⁹⁰⁻⁹³

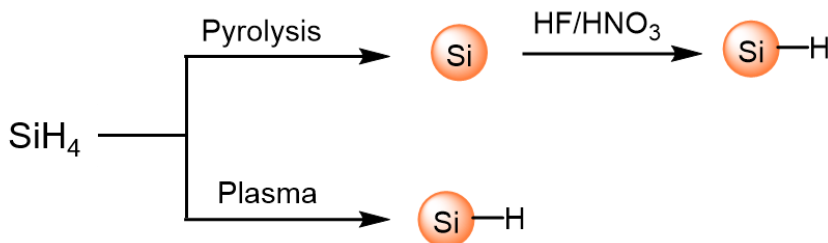


Figure 1-11. SiNP synthesis from silane using the pyrolysis and plasma methods.

Silane also decomposes to form silicon nanoparticles upon introduction into a plasma. The hot electrons in the plasma decompose molecules into highly reactive radicals and ions that can nucleate, aggregate, and grow to form nanoparticles.^{94, 95} Plasma-based synthetic methods (i.e., nonthermal,⁹⁶ RF thermal,⁹⁷ microwave,⁹⁸ etc.) yield luminescent, hydride-terminated SiNCs without the need for HF etching (Figure 1-11).⁹⁶ By using different power levels, the crystallinity of the resulting SiNPs can be controlled (from completely amorphous to highly crystalline).^{99, 100} The size of the SiNPs can be tuned by reducing the residence time of the particles in the plasma,⁹⁶ changing the silane flow rate,⁹⁶ and subsequent etching in a second plasma using CF₄ or SF₆ as the etching gas.^{101, 102} This synthetic method has been expanded further to other precursors, such as cyclohexasilane (a liquid precursor)¹⁰³ and tetrachlorosilane (which provides chloride-terminated SiNCs), demonstrating the flexibility that this method offers.¹⁰⁴

1.4.1.2 Solution Phase Synthesis

It is highly desirable to make SiNPs through solution methods, however, many of these techniques result in SiNPs with size-independent blue photoluminescence instead of the often-desired size-dependent (or band gap) emission.^{35, 105} Typically, SiCl₄ is used as a silicon source and is reduced using a variety of reducing agents (i.e., LiAlH₄,^{51, 106, 107} Na(naphthalide))^{108, 109} or decomposed at high temperature (385 °C) in the presence of trichlorosilane (or octyltrichlorosilane).¹¹⁰ The resulting SiNP surfaces vary, depending on the synthetic procedure employed (hydride,¹⁰⁷ chloride,¹⁰⁸ and mixed surfaces,).¹¹⁰

Zintl salts (an intermetallic phase where the anions or anionic network can be considered valence satisfied;¹¹¹ MSi, M = Na, K, Mg) can be used to synthesize SiNPs either as a reducing agent or a silicon source. Zintl salts were utilized first as a reducing agent for SiCl₄ to form chloride terminated SiNPs.¹¹²⁻¹¹⁴ After that, Liu et al. demonstrated that Mg₂Si could be used as the Si source and oxidized to form SiNPs using Br₂ in refluxing octane to yield SiNPs with a bromide surface.¹¹⁵ Using NaSi with NH₄Br, Kauzlarich and co-workers were able to synthesize hydrogen capped SiNPs.¹¹⁶

1.4.1.3 Solid-state Methods

In the solid-state, SiNPs are synthesized through thermally-induced disproportionation of silicon-rich oxides (i.e., silicon oxide (SiO_x ; $0 < x < 2$),¹¹⁷⁻¹²⁰ and hydrogen silsesquioxane (HSQ; $\sim\text{SiO}_{1.5}\text{H}$).^{121, 122} In this method, the oxide is heated at elevated temperatures to encourage disproportionation into Si (0) and SiO_2 . The Si is protected from thermal decomposition into SiO_2 in a nitrogen or argon atmosphere, while the addition of H_2 also is used to passivate defects.¹²³ The resulting SiNPs are embedded in a SiO_2 matrix (shown for HSQ in Figure 1-12) and can be liberated from the oxide-matrix via HF etching to produce free-standing hydride-terminated SiNPs.^{121, 122} The size of the SiNPs prepared from HSQ is controlled by the annealing temperature: 3 nm from 1100 °C, 6 nm from 1200 °C, and 9 nm from 1300 °C (Figure 1-12).^{122, 124} Faceted SiNPs often are observed after annealing for 1 h at 1400 °C,^{124, 125} and further shape control can be achieved through tuning of the annealing program (i.e., cubes, 1300 °C for 20 h;¹²⁶ cubeoctahedra, quick cycling between 1400 and 800 °C).¹²⁷

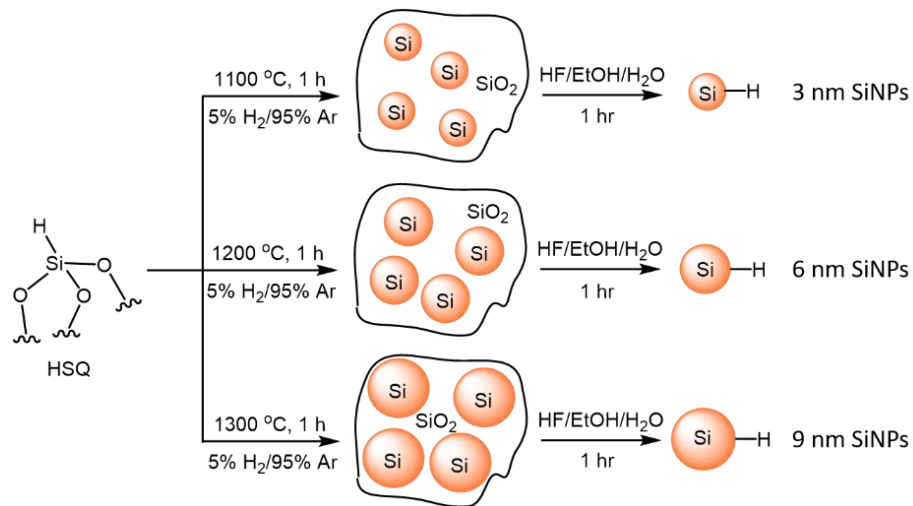


Figure 1-12. Schematic representation of the thermal disproportionation of HSQ to make 3, 6, and 9 nm SiNPs embedded in SiO_2 and the subsequent liberation via HF etching.

1.4.2 Functionalization of Hydride-terminated Silicon Nanoparticles

Many of the synthetic procedures outlined above result in either a hydride or halide surface passivation. This type of bonding on the surface of SiNPs renders them highly susceptible to surface oxidation,¹²⁸ which is undesirable as it can lead to degradation of the optical response of the material.¹²⁹ In order to minimize surface oxidation from occurring, surface

functionalization can be performed to form more stable surface bonds that help limit oxidation. These surface functional groups also can improve solubility¹³⁰ and optoelectronic properties,¹³¹ as will be discussed in Section 1.5.1.

1.4.2.1 Silicon—Carbon Bonds: Hydrosilylation

Hydrosilylation is the main method used for the functionalization of SiNPs. Starting with hydride-terminated silicon nanoparticles (H-SiNPs), Si—H bonds are added across unsaturated bonds; typical reactions on SiNPs utilizing alkenes and alkynes to form Si—C are shown in Figure 1-13.¹³²⁻¹³⁴ Covalent Si—C bonds protect the surface from oxidation, and the R-group is used improve SiNP solubility and functionality. Many hydrosilylation techniques were developed first on porous and bulk silicon substrates and transferred to SiNP surfaces.^{130, 135, 136} While many hydrosilylation methods (i.e., thermal,^{137, 138} photochemical,¹³⁹⁻¹⁴¹ radical,^{142, 143} platinum catalyzed,^{51, 107} Lewis-acid mediated,¹³⁰ and etchant initiated)^{132, 133} have been employed to passivate SiNP surfaces, this section will focus on the three most common methods: thermal, photochemical and radical-initiated.

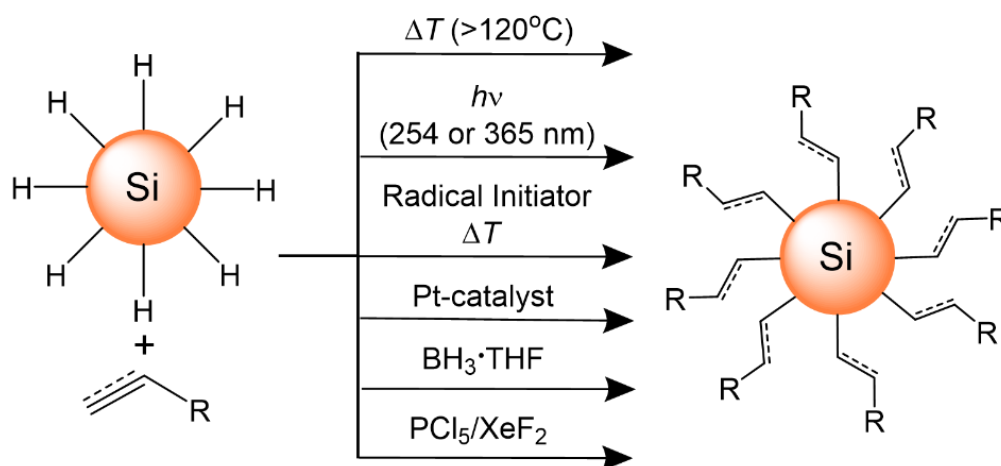


Figure 1-13. Schematic representation of the different hydrosilylation methods that have been used to passivate SiNP surfaces.

Thermal Hydrosilylation

Thermal hydrosilylation utilizes high temperatures (typically 140 °C or more) to activate the SiNP surface, forming radicals by breaking either Si—Si or Si—H bonds.^{137, 138, 144} While there is some debate about which bond breaks first to form the radical,¹⁴⁵ it is expected that the produced radical will propagate along the SiNP surface as the alkene adds to the surface,

providing an alkyl radical that is capable of abstracting a neighboring hydride.¹³⁷ However, these radicals often undergo side-reactions with other alkenes to produce oligomers off the surface.¹³⁸ While the oligomers effectively passivate the surface from oxidation, they also electronically insulate the particle. This method is robust and straightforward, with tolerance for methyl esters, carboxylic acids, and aromatic functional R groups; however, it requires high boiling point ligands that can withstand the reaction temperatures.^{146, 147} Dodecyl surface termination yields very high surface coverage (over 200%), without accounting for the formation of oligomers.¹⁴³

Photochemical Hydrosilylation

Photochemical hydrosilylation is induced by irradiating H-SiNCs under UV light (wavelengths of 365 nm^{135, 140} or 254 nm¹⁴⁸). The mechanism has been explored for porous silicon and free-standing SiNPs, illuminating diverse mechanisms for various hydride-terminated silicon systems and different wavelengths of light.^{136, 141, 149} Two wavelength dependent mechanisms are dominant on SiNP surfaces due to the energetics involved in the cleavage of the Si—H bond. At 254 nm, the light is strong enough to cleave the Si—H bond homolytically, providing a radical on the surface that can propagate and react with incoming alkenes to form Si—C bonds.^{136, 148} This radical initiated reaction leads to both the Markovnikov and anti-Markovnikov addition of the alkene to the SiNP surface, as evidenced by NMR.^{148, 150} However, 365 nm light does not contain enough energy to cleave the Si—H bond (requiring 81 kcal/mol or light with a wavelength of ~354 nm).^{136, 151} The hydrosilylation reaction with 365 nm light likely goes through an exciton mediated mechanism instead.¹³⁶ This mechanism is supported by the observed size dependent surface passivation.^{135, 152} Functionalization using UV-irradiation shows relatively strong functional group tolerance (e.g., vinyl acetate, styrene, ethyl undecylenate, 1-dodecene, 5-hexen-1-ol, and allylamine) and can be used for both alkenes and alkynes.^{140, 148, 153}

Radical-Initiated Hydrosilylation

Radical-initiated hydrosilylation takes advantage of external radical sources to initiate hydrosilylation at lower temperatures compared to thermally initiated procedures, thus enabling the use of lower boiling point ligands. This method of hydrosilylation proceeds across both alkenes and alkynes with good functional group tolerance: carboxylic acids,

methyl esters, alkyl, styrene, phenylacetylene, and vinyltrimethylsilane.^{143, 154} Many different radical-initiators have been explored (e.g., 2,2'-azobis(2-methylpropionitrile) (AIBN), benzoyl peroxide (BP), 1,1'-azobis(cyclohexanecarbonitrile) (ABCN), diazonium salts, diaryliodonium salts, etc.).^{142, 143, 145, 154} The reaction time and temperature is highly dependent on the half-life of the initiator^{143, 145} as well as synergistic effects with the SiNP surface.^{142, 154}

The reaction rate depends on the concentration of the radical initiator and the steric bulk of the alkene; however, it is independent of the monomer concentration, which suggests that the activation of the surface is the rate limiting step in this hydrosilylation method.¹⁵⁵ It follows that the surface coverage can be limited by the presence of other functional groups and bulky substituents (64% for dodecene to 34% for ester and phenylacetylene) as bulky substituents limit initiator access to the surface.¹⁴³ While initial reports explore a mechanism based on hydride abstraction, Neale and co-workers have demonstrated that a silyl radical can be abstracted from the SiNP surface, as shown in Figure 1-14.^{143, 145} Both mechanisms introduce a surface radical that can propagate along the surface as the hydride is abstracted by the adjacent alkyl radical, as explained for thermal hydrosilylation.

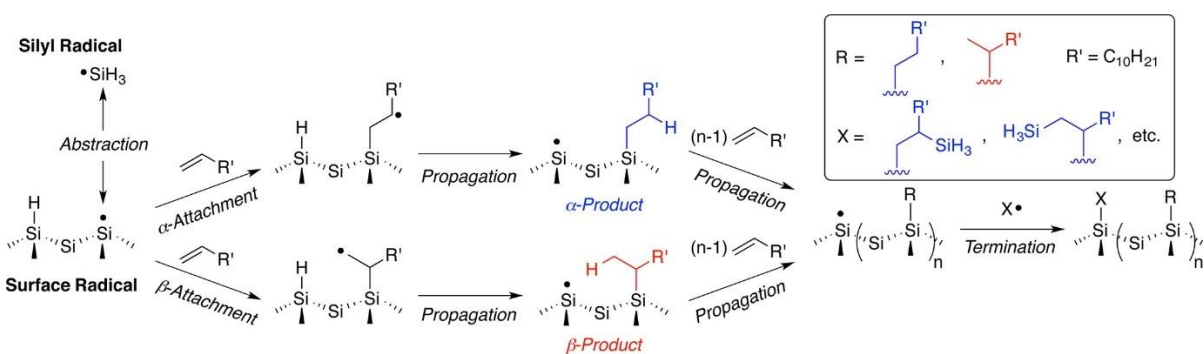


Figure 1-14. Schematic representation of silyl radical abstraction and radical propagation along the silicon surface during hydrosilylation. Reprinted with permission from *Chem. Mater.* **2015**, 27 (19), 6869-6878 (Ref 145). Copyright 2015 American Chemical Society.

1.4.2.2 Silicon—Carbon Bonds: Other Methods

Organolithium Reagents

While hydrosilylation is extremely effective for forming Si—C bonds and can be achieved using a wide-range of methods, it is limited as there is no way to have a triple bond or aromatic group directly bound to the surface. These functional bonding modalities can be

realized by utilizing organolithium reagents.¹⁵⁶ These reagents add across Si—Si bonds at room temperature forming R-Si-Si-Li groups that are readily protonated using HCl to form additional Si-H species, as shown in Figure 1-15.^{156, 157}

The addition of the lithiated species to the SiNP surface allows direct attachment to conjugated systems, such as 5-hexyl-2-thienyl, phenyl, and phenylacetylene groups.^{156, 158} Furthermore, the SiNPs functionalized with organolithium reagents have significant residual hydrogen left on the surface.¹⁵⁶ These moieties can be functionalized further via hydrosilylation to yield a mixed surface. The lithium that is remaining on the surface also can be utilized directly by functionalization with a brominated alkane or propylene oxide to yield an additional alkyl or secondary alcohol on the surface.¹⁵⁶

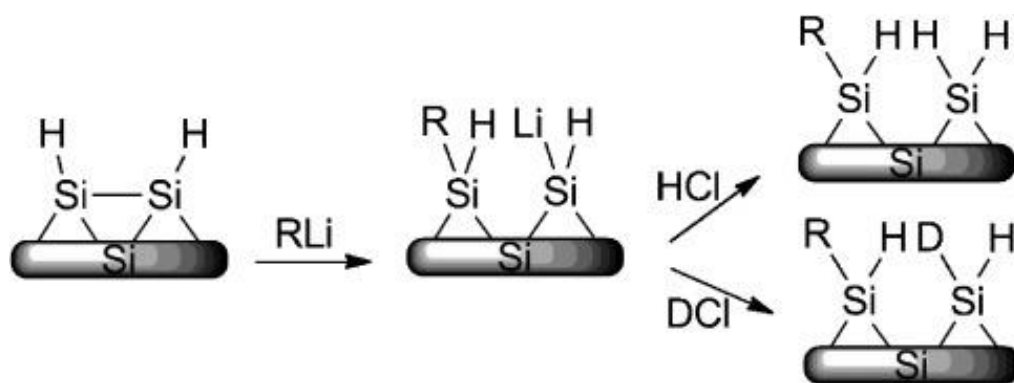


Figure 1-15. Scheme showing the functionalization of Si surfaces with organolithium reagents. Reprinted with permission from *Chem. Eur J.* **2015**, *21*, 2755-2758 (Ref. 156). Copyright 2015 Wiley-VCH Verlag GmbH&Co. KGaA, Weinheim.

Dehydrocoupling

Dehydrocoupling of organosilanes on H-SiNP surfaces passivate the surface with Si—C species by forming Si—Si bonds.^{159, 160} This reaction can be accomplished using Wilkinson's catalyst at 50 °C with a reaction time of 15 h.¹⁶⁰ While this reaction proceeds regardless of size, the photoluminescence properties of the smaller SiNPs are quenched.¹⁶⁰ This is likely due to remaining "Si-Rh-Si" impurities on the surface from the catalyst, as has been shown previously on porous silicon.^{160, 161} Dehydrocoupling on porous silicon occurs at 80 °C without requiring a catalyst and without degrading the photoluminescence, rendering a well-passivated surface.¹⁵⁹ Extension of this surface passivation method to SiNPs is desirable as an efficient, catalyst-free means of passivating the surface.

1.4.2.3 Silicon—Heteroatom Bonds

While many surface passivation reactions are focused on the formation of Si—C bonds,¹¹² bonds with other elements can also be realized when starting from H-SiNP surfaces. These bonds often heavily impact the photoluminescence of SiNPs, as outlined in Section 1.5.2.¹¹³ Exchange reactions also can be realized by replacing Si—OR and Si—SR with Si—C bonds.^{51, 114} The broad range of ligands that can be employed through heteroatom bonding to SiNP surfaces enable further tailoring of SiNPs properties for future applications.

Si—X bonds (X=Cl, Br, I)

While many synthetic schemes result in silicon nanocrystals with halide-terminated surfaces, halogenating H-SiNPs also can be achieved. Halide-passivated SiNPs are a reactive platform for functionalization of SiNPs with Grignard reagents, alcohols, and amines.¹⁶²⁻¹⁶⁶ Chloride-terminated SiNPs are particularly reactive and have been realized by reacting H-SiNPs with chlorinating agents, such as PCl_5 .^{132, 162, 163, 167} Other halide-terminated surfaces can be achieved by exposing H-SiNPs to Br_2 or I_2 .¹⁶³ Chlorination and bromination of H-SiNPs using these methods etched the particles, while complete iodination was not observed.¹⁶³

Si—O bonds

Though less common than their alkyl-terminated counterparts, alkoxy-terminated SiNPs (Si—OR) often are prepared in the literature. Typically, they are produced through reactions of halide- and hydride-terminated silicon nanoparticles with alcohols.^{75, 108, 164, 168} This is typically a spontaneous reaction involving the elimination of hydrogen,¹⁶⁸ however, it is a slow reaction for H-SiNPs.⁷⁵ The reaction can be accelerated by adding an oxidant such as ferrocenium, to activate the Si surface towards alcohols and carboxylic acids to form Si—O bonds, as evidenced by the decrease in the Si-H stretching mode in FTIR ($\sim 2100\text{ cm}^{-1}$) and increased C-H stretching at $\sim 3000\text{ cm}^{-1}$.¹⁶⁹ Si—OR bonds also can be made through hydrosilylation of ketones using microwave and etchant-based procedures.^{133, 134}

Si—N, Si—S, and Si—P bonds

Other heteroatom bonds with SiNPs also have been reported. Si—N bonds can be formed by reacting H-SiNPs with alkyl amines, tetraoctylammonium bromide, and ammonium bromide at room temperature.¹⁰⁵ Si—N bonds also can be formed by reacting H-SiNPs with alkylamines in the presence of ferrocenium, as described above for alcohols and carboxylic acids.¹⁶⁹ This oxidant-activated method also works to cap silicon nanoparticles with

disulfides and alkylphosphines to form Si—S and Si—P bonds, respectively.¹⁶⁹ Si—S bonds also have been created by reacting H-SiNPs with thiols at 190°C, however, they are extremely reactive and quickly react with moisture to quench the SiNP PL.¹⁷⁰

1.5 Structure of Freestanding Silicon Nanoparticles

The structure of nanomaterials often determines the resulting properties. For example, a core@shell nanoparticle with a graded shell exhibits a different photoluminescence response than an epitaxially grown shell, as discussed in Section 1.1. In this section, the structure of free-standing SiNPs is separated into two major components: the nanoparticle core and the surface groups that are attached to it (Figure 1-16). The size, crystallinity, and strain of the SiNP core can be controlled by the synthetic method (i.e., power used in plasma synthesis) and external forces (i.e., hydrostatic pressure), where the surface groups can be controlled by the functionalization method. Both structural components impact the optical and chemical properties and can tailor the SiNPs for desired applications. Oxidation of SiNPs plays a unique role as it can influence both the surface and the core. During oxidation, surface defects are initially passivated, however, further oxidation penetrates into the core. This unique role is explored further in Chapter 4, and only its surface influence will be outlined here.

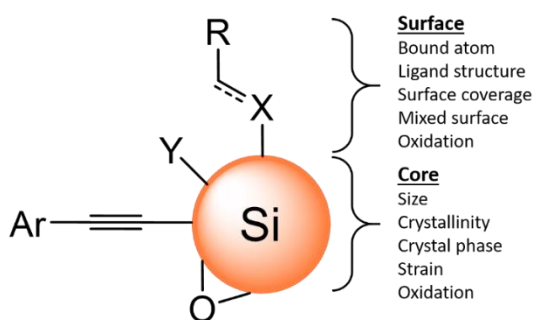


Figure 1-16. An illustration of the aspects of a SiNP and an overview of how they can be tuned.

1.5.1 Structure of the Silicon Nanoparticle Core

Control over the structure of the SiNP core can be afforded by the synthetic method used. The size of the SiNP, which is known to play a role in the luminescence and reactivity of the nanomaterial, can be tuned during SiNP synthesis^{96, 122, 171} and post-synthesis via HF or HF/HNO₃ etching.^{92, 121} In the HSQ method, the size is controlled by the annealing

temperature, and the shape is controlled by the annealing profile.^{122, 126, 127, 171} Plasma synthesis also offers considerable control over the resulting SiNPs because the size can be controlled by the precursor concentration and residence time in the plasma and the crystallinity and internal structure can be controlled by the power applied.^{96, 100, 172}

To date, much of the work in evaluating the structure of SiNPs has been focused on the impact of size, however, some work also has examined the uniformity of the internal structure. In 2013, pair distribution function (PDF) analysis examining the Si-Si-Si bond angles and structural coherence in SiNPs indicated that small particles were quite disordered. As the particle size increased, the atoms became more ordered, as evidenced by more consistent Si-Si-Si bond angles and a Si—Si coordination number closer to 4 (Figure 1-17).¹⁷³ Examination of plasma synthesized SiNPs using Raman spectroscopy combined with modelling was used to identify the thickness of a thin amorphous shell on the outer surface.¹⁷² Together, these studies point toward a complex internal structure for SiNPs.

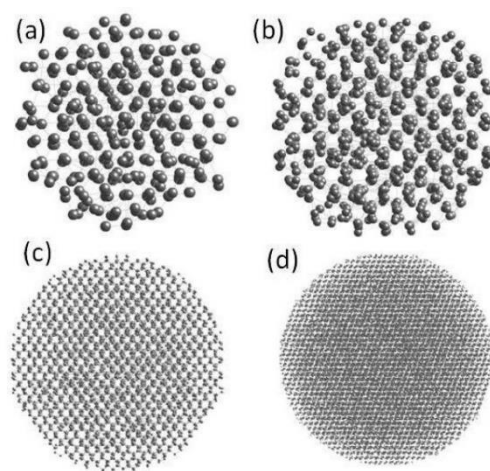


Figure 1-17. Structure of a) 2.4, b) 3.3, c) 7.9, and d) 13.6 nm SiNPs generated from Reverse Monte Carlo simulations based on experimental PDF data. Details of the modelling can be found in Ref 173. Reprinted with permission from *Chem. Mater.* **2013**, 25(11), 2365-2371 (Ref 173). Copyright 2013 American Chemical Society.

1.5.1.1 Impact of Structure on Optical Response

SiNPs often are separated broadly into two groups, based on their PL properties: one that exhibits size-dependent PL emission with long luminescent lifetimes and one that exhibits size-independent PL with short lifetimes.³⁵ The size-dependent emission often is attributed to quantum confinement of the carriers in the SiNP core, as is observed typically for QDs.^{35, 124, 145, 174} However, the relationship between size and PL emission maximum (PL max) is not as

well defined as it is for Cd-based systems.¹⁴⁵ This is thought to be related, in part, to size-dependent quantum yields, which cause a shift in the PL max, based on the size distribution of the synthesized SiNPs.¹⁷⁴ The relationship between the size and PL max is outlined in more detail in Chapter 3.

SiNPs typically are viewed as being either crystalline or amorphous, which is an important distinction since amorphous and crystalline Si have different band structures.^{175, 176} While quantum confinement is observed for both crystalline and amorphous SiNPs,¹⁷⁷ amorphous silicon nanoparticles typically show a larger band gap and a smaller Stokes shift than their crystalline counterparts.¹⁷⁸ Previously, Anthony and Kortshagen demonstrated that the quantum yields are considerably lower for freestanding amorphous SiNPs than crystalline SiNPs (Figure 1-18a and b).¹⁰⁰

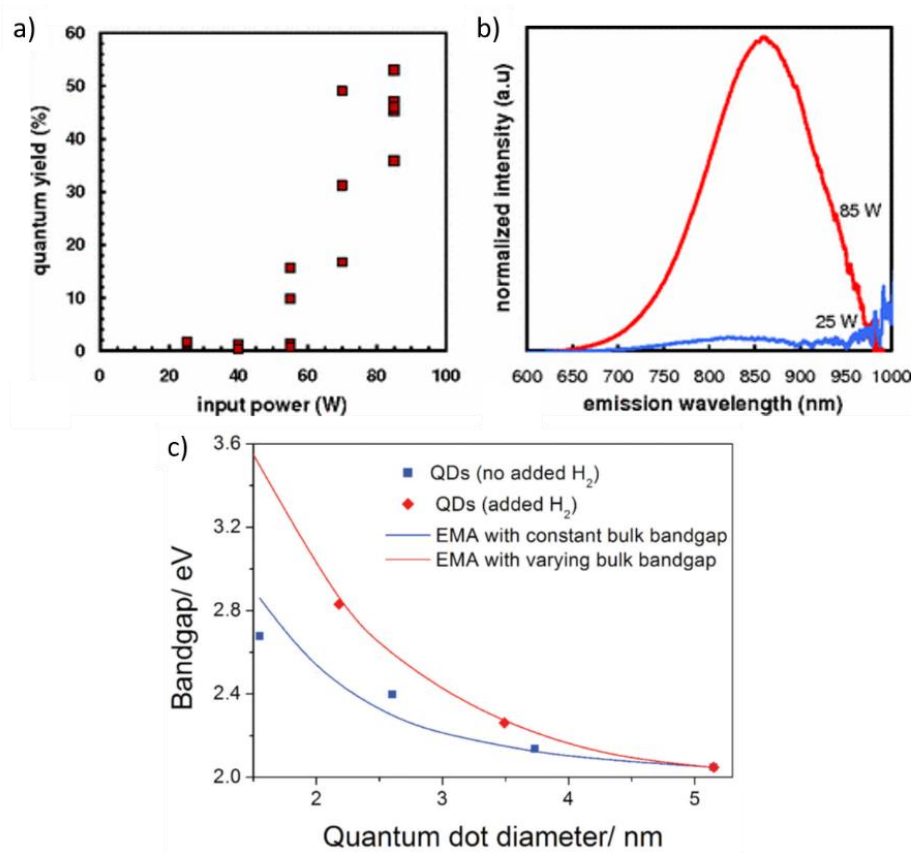


Figure 1-18. a) A plot of the relationship between the input power during the plasma synthesis of SiNPs and the quantum yields. b) A comparison of the PL emission spectra of crystalline (red trace) and amorphous (blue trace) SiNPs made through the plasma synthesis. c) The relationship between amorphous SiNP diameter and band gap with (red) and without (blue) exposure to H₂. Images a) and b) reprinted with permission from Anthony, R.; Kortshagen, U., *Phys. Rev. B*, **2009**, *80*, 115407 <http://dx.doi.org/10.1103/PhysRevB.80.115407> (Ref 100). Copyright 2009 by the American Physical Society. Image c) reprinted from *Adv. Mater.*, **2015**, *27*, 8011-8016 (Ref 179). Licensed under CC BY.

Amorphous SiNPs are intriguing because their internal composition can be altered further upon hydrogenation.¹⁷⁹ This structural change influences the band gap and, in turn, their photoluminescent response, as shown in Figure 1-18c.¹⁷⁹ The authors found that exposure to H₂ yielded different levels of hydrogenation depending on the SiNP diameter. Increasing levels of hydrogenation widen the bulk band gap, therefore, the authors employed a varying band gap when fitting the photoluminescence data for SiNPs exposed to H₂.¹⁷⁹ This work clearly shows the impact that the internal structure can have on the photoluminescence of SiNPs.

The crystalline phase also can impact the band gap of silicon and, potentially, the photoluminescence properties. Allotropes of Si with direct band gaps (0.39–1.25 eV) have been proposed,^{180, 181} as opposed to the indirect band gap (1.12 eV) of diamond-cubic Si that typically comprises SiNPs. Unfortunately, these alternate crystalline phases are difficult to access using traditional techniques, making the study of the photoluminescence properties of these phases in SiNPs difficult.

The optical response of SiNPs also is influenced by strain in the core. In a study on the impact of pressure on SiNP photoluminescence, increasing pressure caused the PL max to red-shift.¹⁸² During this study, other crystal phases of Si were accessed through further increased pressure, however, the photoluminescence of these phases was not studied. Further to this, tensile strain causes a blue shift in PL max and introduces a direct band gap.¹⁸³ By placing tensile strained SiNPs under hydrostatic pressure, the authors showed that this can be reversed, and the PL max red shift is similar to that observed in the diamond anvil study.¹⁸³

While little has been done to examine the impact of structure uniformity on the photoluminescence, one study on plasma synthesized SiNPs suggested an amorphous layer on the crystalline core as a possible source for the fast-photoluminescence band at higher energy (the F-band).¹⁷² However, it is not clear if the same conclusions hold for silicon nanoparticles synthesized through other methods.^{184, 185} In the PDF study described above, the authors reported a correlation between the SiNP structure and photoluminescence response, however, the nature of the relationship was not expanded on.¹⁷³ Further insight into the relationship between structure and photoluminescence would be valuable for tuning luminescence for various applications.

1.5.1.2 Impact of Structure on Applications: Beyond the Photoluminescence

The internal structure and size of SiNPs impact their properties beyond the photoluminescence response outlined above. In LIBs, both the size and internal structure of SiNPs influence anode performance. SiNP size is of particular importance as smaller SiNPs demonstrate improved tolerance to volume changes and increase the rate of lithiation and delithiation.^{36, 186} While smaller SiNPs exhibit better cycling performance, larger SiNPs have a higher initial capacity.^{83, 186} During the lithiation and delithiation processes, SiNPs undergo amorphization due to the breaking and reforming of Si—Si bonds from the accommodation of lithium.¹⁸⁷ By starting with amorphous Si, the SiNPs do not need to undergo this amorphization step.¹⁸⁸ This improves robustness and increases first-cycle Coulombic efficiency (92.5%) compared to their crystalline counterparts, making amorphous SiNPs more well suited for LIB anodes.¹⁸⁸

The size and internal structure of SiNPs also have implications for ²⁹Si MRI applications. ²⁹Si MRI relies on the transfer of polarization from radicals to highly polarize Si nuclei prior to imaging.^{41, 42} This typically is accomplished through radicals that exist within the SiNP.⁴² Varying the internal structure can change the radical concentration, which impacts the effectiveness of the hyperpolarization (with more internal radicals being desirable).^{128, 189} Furthermore, the SiNPs must remain polarized long enough for injection and subsequent imaging, which is related to the T_1 relaxation rates. SiNPs exhibit size dependent T_1 relaxation rates, where smaller particles have shorter relaxation times, making larger SiNPs desirable.^{41, 64} However, large SiNPs are not photoluminescent, thus, it is important to optimize the size for the desired imaging applications.

1.5.2 Surface Structure of Silicon Nanoparticles

When discussing the surface of SiNPs, this section will focus on the structure of the ligand and its bonding to the surface. As described above, surface passivation of SiNPs typically is performed to prevent oxidation and improve processability. While the surface ligands are often exploited to improve compatibility with solvents and polymer matrices,^{25, 77, 190} various ligand moieties can be utilized to improve SiNP properties for a wide-array of applications. The surface ligand influence over the optical response has been studied widely. However, the influence of the ligands on other applications should not be overlooked.

The photoluminescence also can be tuned by Si—C passivation. Si—C bonds normally do not influence the PL max of SiNPs relative to their hydride counterparts but have been shown to increase the quantum yields.^{131, 196} However, the addition of extended conjugated systems, such as phenylacetylene (grafted through the organolithium reaction), can introduce in-gaps states to the SiNP,¹⁹⁷ which narrows the band gap, red-shifting the photoluminescence.¹⁹⁷ This work was extended to 2-ethynyl-naphthalene and 2-ethynyl-5-hexylthiophene, which further red-shifted the photoluminescence (Figure 1-19).¹⁵⁸

Surface species also impact SiNP photoluminescence quantum efficiencies. Quantum yields appear to be impacted detrimentally by SiH₃ species on the surface of SiNPs. It has been shown that SiH₃ can be removed through etchant-based hydrosilylation procedures, such as XeF₂ and PCl₅, yielding SiNPs with reasonably high quantum yields.^{132, 133} The inverse relationship between F-band emission and quantum yields also points to the negative influence of surface states on the emission efficiency.¹⁰³ Further study into the nature of these surface states requires more control over the structure of SiNPs.

The F-band, though implicated in surface-dependent photoluminescence as described above, is complex and not well understood.³⁷ Though it has been suggested that it is related to quantum confinement of carriers in small SiNP,¹⁹⁸ its appearance is more often related to the presence of oxide species and changes to the SiNP surface chemistry (e.g., high levels of surface oxidation and exposure to amines and alcohols).^{162, 163, 167, 191, 199-202} The origin of the changing luminescence is still unclear but has been attributed to the silicon/oxide interface,^{199, 200} defect states in the oxide layer,²⁰¹ and contamination of the oxide layer.²⁰² Carbon-dots have also been implicated in the observation of F-band emission for a few bottom-up synthetic methods.²⁰³⁻²⁰⁵ Thus, showing that a deeper understanding of the material is required to gain significant insight into F-band emission for SiNP systems.

1.5.2.2 Impact of Surface on Applications: Beyond the Photoluminescence

Manipulation of surface ligands increases the suitability of SiNPs for a wide range of applications. Often, surface functionalities are tuned to improve compatibility with a variety of media to target a wide range of applications. For example, ester-moieties are used to improve compatibility with poly(methyl methacrylate) in order to improve transparency for

LSCs,⁷⁷ and mixed-surfaces can be used to improve water-solubility for biological imaging.²⁵ However, functional groups can also play a more active role.

In LEDs, the structure of the surface can be used to improve the transfer of carriers into the SiNPs to improve quantum efficiencies. Bulky phenylpropyl ligands have been shown to improve the optical power density over octyl ligands as the phenylpropyl passivation has less unpaired electron defects (due to increased oxidation) and improves electron transport.⁴⁸ However, the phenyl functionality hinders hole transport, thus decreasing the external quantum efficiency relative to their alkyl counterparts.⁴⁸ The surface functionalization method also impacts the efficiency of LEDs.²⁰⁶ The LED performance of hexyl-passivated SiNPs functionalized by radical-initiated hydrosilylation and with organolithium reagents were compared. Improved parameters (such as lower turn-on voltages, higher brightness, and higher external quantum efficiencies) were observed for SiNPs functionalized with organolithium reagents due to the reduced surface coverage and increased photoluminescent quantum yields.²⁰⁶

Lithium ion battery performance also is influenced by the surface of the SiNPs. One intrinsic issue with SiNPs when being employed as an anode material for LIBs is the low conductivity of Si. This can be overcome by covalent attachment of the SiNPs to a conductive matrix.²⁰⁷ Non-covalent incorporation into conductive matrices also has been explored.^{83, 208} Recently, it was shown that surface ligands can decrease lithium uptake in very small (i.e., 3 nm) SiNPs detrimentally, making them inefficient as an anode material.⁸³ However, subsequent removal of the surface groups increased the uptake and showed excellent stability over 500 cycles (when incorporated in a graphene aerogel).⁸³ Functionalization of SiNPs with other functional groups (i.e., epoxy groups) can mitigate parasitic reactions between the silicon and the electrolyte during lithiation and delithiation and improve battery performance over H-SiNPs.⁸⁴ Further studies are required to optimize SiNP surfaces for LIB applications.

1.6 Thesis Outline

This chapter highlights the importance of SiNPs for a wide array of applications. The internal and surface structure of SiNPs can be controlled via various synthetic procedures and influences their photoluminescence and chemical properties. This thesis focuses on

furthering the understanding of the internal core structure of HSQ-derived SiNPs and applying that understanding to the photoluminescent properties and oxidation of these materials.

In Chapter 2, we aim to identify the internal structure of H-SiNPs made through the thermal disproportionation of HSQ. In order to accomplish this, a combination of ^{29}Si solid-state NMR (SS NMR), transmission electron microscopy (TEM), X-ray diffraction (XRD), X-ray photoelectron spectroscopy (XPS), and Fourier transform infrared spectroscopy (FTIR) were employed. Different NMR pulse sequences were applied to study the internal structure of SiNPs of different sizes.

Armed with insight into the internal structure of SiNPs from Chapter 2, Chapter 3 aims to identify the influence of this internal structure on the photoluminescence properties. By controlling the internal structure through HF etching, SiNPs of varying degrees of crystallinity were synthesized. The size of the crystalline domain was determined using XRD and compared with the overall particle size (from TEM) to approximate the thickness of the disordered component. The photoluminescence emission and lifetimes were investigated in the context of the overall particle size and crystalline domain size.

Intrigued by the insight into the internal structure provided by XRD, Chapter 4 explores the influence of oxidation on the structure of these materials. The investigation reported in this chapter set out to understand these structural changes as they relate to the internal structure of well-passivated SiNPs and, ultimately, the impact that the structural changes have on the photoluminescence properties. Chapter 5 summarizes the main findings of Chapters 2–4 and explores relevant future research directions.

1.7 References

1. National Nanotechnology Institute. What is Nanotechnology? <https://www.nano.gov/nanotech-101/what/definition> (accessed: July 6, 2020).
2. Bayda, S.; Adeel, M.; Tuccinardi, T.; Cordani, M.; Rizzolio, F., The History of Nanoscience and Nanotechnology: From Chemical-Physical Applications to Nanomedicine. *Molecules* **2019**, *25* (1), 112.
3. Nature. Nanoscience and technology. <https://www.nature.com/subjects/nanoscience-and-technology> (accessed: July 6, 2020).
4. Wang, L.-W.; Zunger, A., Dielectric Constants of Silicon Quantum Dots. *Phys. Rev. Lett.* **1994**, *73* (7), 1039-1042.
5. Brus, L. E., Electron–electron and electron-hole interactions in small semiconductor crystallites: The size dependence of the lowest excited electronic state. *J. Chem. Phys.* **1984**, *80* (9), 4403-4409.

6. Bawendi, M. G.; Steigerwald, M. L.; Brus, L. E., The Quantum Mechanics of Larger Semiconductor Clusters ("Quantum Dots"). *Annu. Rev. Phys. Chem.* **1990**, *41* (1), 477-496.
7. Kortan, A. R.; Hull, R.; Opila, R. L.; Bawendi, M. G.; Steigerwald, M. L.; Carroll, P. J.; Brus, L. E., Nucleation and Growth of CdSe on ZnS Quantum Crystallite Seeds, and Vice Versa, in Inverse Micelle Media. *J. Am. Chem. Soc.* **1990**, *112* (4), 1327-1332.
8. Vasudevan, D.; Gaddam, R. R.; Trinchi, A.; Cole, I., Core-shell quantum dots: Properties and applications. *J. Alloys Compd.* **2015**, *636*, 395-404.
9. AbouElhamd, A. R.; Al-Sallal, K. A.; Hassan, A., Review of Core/Shell Quantum Dots Technology Integrated into Building's Glazing. *Energies* **2019**, *12* (6), 1058.
10. Hanifi, D. A.; Bronstein, N. D.; Koscher, B. A.; Nett, Z.; Swabeck, J. K.; Takano, K.; Schwartzberg, A. M.; Maserati, L.; Vandewal, K.; van de Burgt, Y.; Salleo, A.; Alivisatos, A. P., Redefining near-unity luminescence in quantum dots with photothermal threshold quantum yield. *Science* **2019**, *363* (6432), 1199-1202.
11. Pan, Z.; Zhang, H.; Cheng, K.; Hou, Y.; Hua, J.; Zhong, X., Highly Efficient Inverted Type-I CdS/CdSe Core/Shell Structure QD-Sensitized Solar Cells. *ACS Nano* **2012**, *6* (5), 3982-3991.
12. Kim, S.; Fisher, B.; Eisler, H.-J.; Bawendi, M., Type-II Quantum Dots: CdTe/CdSe(Core/Shell) and CdSe/ZnTe(Core/Shell) Heterostructures. *J. Am. Chem. Soc.* **2003**, *125* (38), 11466-11467.
13. Chuang, C.-H.; Lo, S. S.; Scholes, G. D.; Burda, C., Charge Separation and Recombination in CdTe/CdSe Core/Shell Nanocrystals as a Function of Shell Coverage: Probing the Onset of the Quasi Type-II Regime. *J. Phys. Chem. Lett.* **2010**, *1* (17), 2530-2535.
14. Thuy, U. T. D.; Tu, L. A.; Loan, N. T.; Chi, T. T. K.; Liem, N. Q., Comparative photoluminescence properties of type-I and type-II CdTe/CdS core/shell quantum dots. *Opt. Mater.* **2016**, *53*, 34-38.
15. Yarema, M.; Xing, Y.; Lechner, R. T.; Ludescher, L.; Dordevic, N.; Lin, W. M. M.; Yarema, O.; Wood, V., Mapping the Atomistic Structure of Graded Core/Shell Colloidal Nanocrystals. *Sci. Rep.* **2017**, *7*, 11718.
16. Boldt, K.; Bartlett, S.; Kirkwood, N.; Johannessen, B., Quantification of Material Gradients in Core/Shell Nanocrystals Using EXAFS Spectroscopy. *Nano Lett.* **2020**, *20* (2), 1009-1017.
17. Park, Y.-S.; Bae, W. K.; Padilha, L. A.; Pietryga, J. M.; Klimov, V. I., Effect of the Core/Shell Interface on Auger Recombination Evaluated by Single-Quantum-Dot Spectroscopy. *Nano Lett.* **2014**, *14* (2), 396-402.
18. Park, Y.-S.; Lim, J.; Makarov, N. S.; Klimov, V. I., Effect of Interfacial Alloying versus "Volume Scaling" on Auger Recombination in Compositionally Graded Semiconductor Quantum Dots. *Nano Lett.* **2017**, *17* (9), 5607-5613.
19. Walsh, B. R.; Saari, J. I.; Krause, M. M.; Mack, T. G.; Nick, R.; Coe-Sullivan, S.; Kambhampati, P., Interfacial Electronic Structure in Graded Shell Nanocrystals Dictates Their Performance for Optical Gain. *J. Phys. Chem. C* **2016**, *120* (34), 19409-19415.
20. Boldt, K.; Kirkwood, N.; Beane, G. A.; Mulvaney, P., Synthesis of Highly Luminescent and Photo-Stable, Graded Shell CdSe/CdxZn1-xS Nanoparticles by In Situ Alloying. *Chem. Mater.* **2013**, *25* (23), 4731-4738.
21. Beane, G. A.; Gong, K.; Kelley, D. F., Auger and Carrier Trapping Dynamics in Core/Shell Quantum Dots Having Sharp and Alloyed Interfaces. *ACS Nano* **2016**, *10* (3), 3755-3765.
22. Cragg, G. E.; Efros, A. L., Suppression of Auger Processes in Confined Structures. *Nano Lett.* **2010**, *10* (1), 313-317.
23. Pramanik, S.; Hill, S. K. E.; Zhi, B.; Hudson-Smith, N. V.; Wu, J. J.; White, J. N.; McIntire, E. A.; Kondeti, V. S. S. K.; Lee, A. L.; Bruggeman, P. J.; Kortshagen, U. R.; Haynes, C. L., Comparative toxicity

assessment of novel Si quantum dots and their traditional Cd-based counterparts using bacteria models *Shewanella oneidensis* and *Bacillus subtilis*. *Environ. Sci.: Nano* **2018**, *5* (8), 1890-1901.

24. Werner, T. T.; Mudd, G. M.; Jowitt, S. M., Indium: key issues in assessing mineral resources and long-term supply from recycling. *Applied Earth Science* **2015**, *124* (4), 213-226.
25. Islam, M. A.; Sinelnikov, R.; Howlader, M. A.; Faramus, A.; Veinot, J. G. C., Mixed Surface Chemistry: An Approach to Highly Luminescent Biocompatible Amphiphilic Silicon Nanocrystals. *Chem. Mater.* **2018**, *30* (24), 8925-8931.
26. Haynes, J. R.; Westphal, W. C., Radiation Resulting from Recombination of Holes and Electrons in Silicon. *Phys. Rev.* **1956**, *101* (6), 1676-1678.
27. Michaelis, W.; Pilkuhn, M. H., Radiative Recombination in Silicon p-n Junctions. *Phys. Status Solidi B* **1969**, *36* (1), 311-319.
28. Canham, L. T., Silicon quantum wire array fabrication by electrochemical and chemical dissolution of wafers. *Appl. Phys. Lett.* **1990**, *57* (10), 1046-1048.
29. Liang, D.; Bowers, J. E., Recent progress in lasers on silicon. *Nature Photon.* **2010**, *4* (8), 511-517.
30. Zelewski, S. J.; Kudrawiec, R., Photoacoustic and modulated reflectance studies of indirect and direct band gap in van der Waals crystals. *Sci. Rep.* **2017**, *7* (1), 15365.
31. Brus, L., Luminescence of Silicon Materials: Chains, Sheets, Nanocrystals, Nanowires, Microcrystals, and Porous Silicon. *J. Phys. Chem.* **1994**, *98* (14), 3575-3581.
32. Hybertsen, M. S., Absorption and emission of light in nanoscale silicon structures. *Phys. Rev. Lett.* **1994**, *72* (10), 1514-1517.
33. Hill, N. A.; Whaley, K. B., A theoretical study of light emission from nanoscale silicon. *J. Electron. Mater.* **1996**, *25* (2), 269-285.
34. Delerue, C.; Allan, G.; Lannoo, M., Electron-phonon coupling and optical transitions for indirect-gap semiconductor nanocrystals. *Phys. Rev. B* **2001**, *64* (19), 193402.
35. Mazzaro, R.; Romano, F.; Ceroni, P., Long-lived luminescence of silicon nanocrystals: from principles to applications. *Phys. Chem. Chem. Phys.* **2017**, *19* (39), 26507-26526.
36. Su, X.; Wu, Q.; Li, J.; Xiao, X.; Lott, A.; Lu, W.; Sheldon, B. W.; Wu, J., Silicon-Based Nanomaterials for Lithium-Ion Batteries: A Review. *Adv. Energy Mater.* **2014**, *4*, (1), 1300882.
37. Canham, L., Introductory lecture: origins and applications of efficient visible photoluminescence from silicon-based nanostructures. *Faraday Discuss.* **2020**, *222*, 10-81.
38. Gonzalez, C. M.; Veinot, J. G. C., Silicon nanocrystals for the development of sensing platforms. *J. Mater. Chem. C* **2016**, *4* (22), 4836-4846.
39. Erogbogbo, F.; Yong, K.-T.; Roy, I.; Xu, G.; Prasad, P. N.; Swihart, M. T., Biocompatible Luminescent Silicon Quantum Dots for Imaging of Cancer Cells. *ACS Nano* **2008**, *2* (5), 873-878.
40. Romano, F.; Angeloni, S.; Morselli, G.; Mazzaro, R.; Morandi, V.; Shell, J. R.; Cao, X.; Pogue, B. W.; Ceroni, P., Water-soluble silicon nanocrystals as NIR luminescent probes for time-gated biomedical imaging. *Nanoscale* **2020**, *12* (14), 7921-7926.
41. Aptekar, J. W.; Cassidy, M. C.; Johnson, A. C.; Barton, R. A.; Lee, M.; Ogier, A. C.; Vo, C.; Anahtar, M. N.; Ren, Y.; Bhatia, S. N.; Ramanathan, C.; Cory, D. G.; Hill, A. L.; Mair, R. W.; Rosen, M. S.; Walsworth, R. L.; Marcus, C. M., Silicon Nanoparticles as Hyperpolarized Magnetic Resonance Imaging Agents. *ACS Nano* **2009**, *3* (12), 4003-4008.
42. Cassidy, M. C.; Chan, H. R.; Ross, B. D.; Bhattacharya, P. K.; Marcus, C. M., In vivo magnetic resonance imaging of hyperpolarized silicon particles. *Nat. Nanotechnol.* **2013**, *8*, 363-368.
43. Gonzalez, C. M.; Iqbal, M.; Dasog, M.; Piercey, D. G.; Lockwood, R.; Klapotke, T. M.; Veinot, J. G. C., Detection of high-energy compounds using photoluminescent silicon nanocrystal paper based sensors. *Nanoscale* **2014**, *6* (5), 2608-2612.

44. Robidillo, C. J. T.; Wandelt, S.; Dalangin, R.; Zhang, L.; Yu, H.; Meldrum, A.; Campbell, R. E.; Veinot, J. G. C., Ratiometric Detection of Nerve Agents by Coupling Complementary Properties of Silicon-Based Quantum Dots and Green Fluorescent Protein. *ACS Appl. Mater. Interfaces* **2019**, *11* (36), 33478-33488.
45. Meinardi, F.; Ehrenberg, S.; Dharmo, L.; Carulli, F.; Mauri, M.; Bruni, F.; Simonutti, R.; Kortshagen, U.; Brovelli, S., Highly efficient luminescent solar concentrators based on earth-abundant indirect-bandgap silicon quantum dots. *Nature Photon.* **2017**, *11*, 177-185.
46. Hill, S. K. E.; Connell, R.; Peterson, C.; Hollinger, J.; Hillmyer, M. A.; Kortshagen, U.; Ferry, V. E., Silicon Quantum Dot–Poly(methyl methacrylate) Nanocomposites with Reduced Light Scattering for Luminescent Solar Concentrators. *ACS Photonics* **2019**, *6* (1), 170-180.
47. Cheng, K.-Y.; Anthony, R.; Kortshagen, U. R.; Holmes, R. J., High-Efficiency Silicon Nanocrystal Light-Emitting Devices. *Nano Lett.* **2011**, *11* (5), 1952-1956.
48. Liu, X.; Zhao, S.; Gu, W.; Zhang, Y.; Qiao, X.; Ni, Z.; Pi, X.; Yang, D., Light-Emitting Diodes Based on Colloidal Silicon Quantum Dots with Octyl and Phenylpropyl Ligands. *ACS Appl. Mater. Interfaces* **2018**, *10* (6), 5959-5966.
49. Choi, J. W.; Aurbach, D., Promise and reality of post-lithium-ion batteries with high energy densities. *Nat. Rev. Mater.* **2016**, *1* (4), 16013.
50. Li, Z. F.; Ruckenstein, E., Water-Soluble Poly(acrylic acid) Grafted Luminescent Silicon Nanoparticles and Their Use as Fluorescent Biological Staining Labels. *Nano Lett.* **2004**, *4* (8), 1463-1467.
51. Warner, J. H.; Hoshino, A.; Yamamoto, K.; Tilley, R. D., Water-soluble photoluminescent silicon quantum dots. *Angew. Chem. Int. Ed.* **2005**, *44* (29), 4550-4.
52. Sato, S.; Swihart, M. T., Propionic-Acid-Terminated Silicon Nanoparticles: Synthesis and Optical Characterization. *Chem. Mater.* **2006**, *18* (17), 4083-4088.
53. Cheng, X.; Lowe, S. B.; Ciampi, S.; Magenau, A.; Gaus, K.; Reece, P. J.; Gooding, J. J., Versatile “Click Chemistry” Approach to Functionalizing Silicon Quantum Dots: Applications toward Fluorescent Cellular Imaging. *Langmuir* **2014**, *30* (18), 5209-5216.
54. Erogbogbo, F.; Yong, K.-T.; Roy, I.; Hu, R.; Law, W.-C.; Zhao, W.; Ding, H.; Wu, F.; Kumar, R.; Swihart, M. T.; Prasad, P. N., In Vivo Targeted Cancer Imaging, Sentinel Lymph Node Mapping and Multi-Channel Imaging with Biocompatible Silicon Nanocrystals. *ACS Nano* **2011**, *5* (1), 413-423.
55. Erogbogbo, F.; Yong, K.-T.; Hu, R.; Law, W.-C.; Ding, H.; Chang, C.-W.; Prasad, P. N.; Swihart, M. T., Biocompatible Magnetofluorescent Probes: Luminescent Silicon Quantum Dots Coupled with Superparamagnetic Iron(III) Oxide. *ACS Nano* **2010**, *4* (9), 5131-5138.
56. Joo, J.; Liu, X.; Kotamraju, V. R.; Ruoslahti, E.; Nam, Y.; Sailor, M. J., Gated Luminescence Imaging of Silicon Nanoparticles. *ACS Nano* **2015**, *9* (6), 6233-6241.
57. Gu, L.; Hall, D. J.; Qin, Z.; Anglin, E.; Joo, J.; Mooney, D. J.; Howell, S. B.; Sailor, M. J., In vivo time-gated fluorescence imaging with biodegradable luminescent porous silicon nanoparticles. *Nat. Commun.* **2013**, *4* (1), 2326.
58. Tu, C.-C.; Awasthi, K.; Chen, K.-P.; Lin, C.-H.; Hamada, M.; Ohta, N.; Li, Y.-K., Time-Gated Imaging on Live Cancer Cells Using Silicon Quantum Dot Nanoparticles with Long-Lived Fluorescence. *ACS Photonics* **2017**, *4* (6), 1306-1315.
59. Yang, W.; Srivastava, P. K.; Han, S.; Jing, L.; Tu, C.-C.; Chen, S.-L., Optomechanical Time-Gated Fluorescence Imaging Using Long-Lived Silicon Quantum Dot Nanoparticles. *Anal. Chem.* **2019**, *91* (9), 5499-5503.
60. Uhlig, F., ²⁹Si NMR Spectroscopy. In *Organosilicon Compounds*; Lee, V. Y., Ed. Academic Press: 2017; Chapter 2, pp 59-77.

61. Ha, M.; Michaelis, V. K., High-Frequency Dynamic Nuclear Polarization NMR for Solids: Part 1 – An Introduction. In *Modern Magnetic Resonance*, Webb, G. A., Ed. Springer International Publishing: 2017; pp 1-24.
62. Hooper, R. W.; Klein, B. A.; Michaelis, V. K., Dynamic Nuclear Polarization (DNP) 101: A New Era for Materials. *Chem. Mater.* **2020**, *32* (11), 4425-4430.
63. Hu, J.; Whiting, N.; Bhattacharya, P., Hyperpolarization of Silicon Nanoparticles with TEMPO Radicals. *J. Phys. Chem. C* **2018**, *122* (19), 10575-10581.
64. Atkins, T. M.; Cassidy, M. C.; Lee, M.; Ganguly, S.; Marcus, C. M.; Kauzlarich, S. M., Synthesis of Long T₁ Silicon Nanoparticles for Hyperpolarized ²⁹Si Magnetic Resonance Imaging. *ACS Nano* **2013**, *7* (2), 1609-1617.
65. Tu, C.; Ma, X.; Pantazis, P.; Kauzlarich, S. M.; Louie, A. Y., Paramagnetic, Silicon Quantum Dots for Magnetic Resonance and Two-Photon Imaging of Macrophages. *J. Am. Chem. Soc.* **2010**, *132* (6), 2016-2023.
66. Tu, C.; Ma, X.; House, A.; Kauzlarich, S. M.; Louie, A. Y., PET Imaging and Biodistribution of Silicon Quantum Dots in Mice. *ACS Med. Chem. Lett.* **2011**, *2* (4), 285-288.
67. Singh, M. P.; Atkins, T. M.; Muthuswamy, E.; Kamali, S.; Tu, C.; Louie, A. Y.; Kauzlarich, S. M., Development of Iron-Doped Silicon Nanoparticles As Bimodal Imaging Agents. *ACS Nano* **2012**, *6* (6), 5596-5604.
68. Ban, R.; Zheng, F.; Zhang, J., A highly sensitive fluorescence assay for 2,4,6-trinitrotoluene using amine-capped silicon quantum dots as a probe. *Anal. Methods* **2015**, *7* (5), 1732-1737.
69. Zhang, J.; Yu, S.-H., Highly photoluminescent silicon nanocrystals for rapid, label-free and recyclable detection of mercuric ions. *Nanoscale* **2014**, *6* (8), 4096-4101.
70. Liao, B.; Wang, W.; Deng, X.; He, B.; Zeng, W.; Tang, Z.; Liu, Q., A facile one-step synthesis of fluorescent silicon quantum dots and their application for detecting Cu²⁺. *RSC Adv.* **2016**, *6* (18), 14465-14467.
71. Campos, B. B.; Algarra, M.; Alonso, B.; Casado, C. M.; Jiménez-Jiménez, J.; Rodríguez-Castellón, E.; Esteves da Silva, J. C. G., Fluorescent sensor for Cr(VI) based in functionalized silicon quantum dots with dendrimers. *Talanta* **2015**, *144*, 862-867.
72. Yi, Y.; Deng, J.; Zhang, Y.; Li, H.; Yao, S., Label-free Si quantum dots as photoluminescence probes for glucose detection. *Chem. Commun.* **2013**, *49* (6), 612-614.
73. Chen, Q.; Liu, M.; Zhao, J.; Peng, X.; Chen, X.; Mi, N.; Yin, B.; Li, H.; Zhang, Y.; Yao, S., Water-dispersible silicon dots as a peroxidase mimetic for the highly-sensitive colorimetric detection of glucose. *Chem. Commun.* **2014**, *50* (51), 6771-6774.
74. Zhang, X.; Chen, X.; Kai, S.; Wang, H.-Y.; Yang, J.; Wu, F.-G.; Chen, Z., Highly Sensitive and Selective Detection of Dopamine Using One-Pot Synthesized Highly Photoluminescent Silicon Nanoparticles. *Anal. Chem.* **2015**, *87* (6), 3360-3365.
75. Zhang, Z. H.; Lockwood, R.; Veinot, J. G. C.; Meldrum, A., Detection of ethanol and water vapor with silicon quantum dots coupled to an optical fiber. *Sensor. Actuat. B: Chem.* **2013**, *181*, 523-528.
76. Yi, Y.; Zhu, G.; Liu, C.; Huang, Y.; Zhang, Y.; Li, H.; Zhao, J.; Yao, S., A Label-Free Silicon Quantum Dots-Based Photoluminescence Sensor for Ultrasensitive Detection of Pesticides. *Anal. Chem.* **2013**, *85* (23), 11464-11470.
77. Hill, S. K. E.; Connell, R.; Held, J.; Peterson, C.; Francis, L.; Hillmyer, M. A.; Ferry, V. E.; Kortshagen, U., Poly(methyl methacrylate) Films with High Concentrations of Silicon Quantum Dots for Visibly Transparent Luminescent Solar Concentrators. *ACS Appl. Mater. Interfaces* **2020**, *12* (4), 4572-4578.
78. Mazzaro, R.; Gradone, A.; Angeloni, S.; Morselli, G.; Cozzi, P. G.; Romano, F.; Vomiero, A.; Ceroni, P., Hybrid Silicon Nanocrystals for Color-Neutral and Transparent Luminescent Solar Concentrators. *ACS Photonics* **2019**, *6* (9), 2303-2311.

79. Union, T. E., Ed. *Publications Office of the European Union: Official Journal of the European Union*, 2017; Vol. 2017/1975, p 3.
80. Jang, E.; Kim, Y.; Won, Y.-H.; Jang, H.; Choi, S.-M., Environmentally Friendly InP-Based Quantum Dots for Efficient Wide Color Gamut Displays. *ACS Energy Lett.* **2020**, *5* (4), 1316-1327.
81. Maier-Flaig, F.; Rinck, J.; Stephan, M.; Bocksrocker, T.; Bruns, M.; Kübel, C.; Powell, A. K.; Ozin, G. A.; Lemmer, U., Multicolor Silicon Light-Emitting Diodes (SiLEDs). *Nano Lett.* **2013**, *13* (2), 475-480.
82. Wu, H.; Cui, Y., Designing nanostructured Si anodes for high energy lithium ion batteries. *Nano Today* **2012**, *7* (5), 414-429.
83. Aghajamali, M.; Xie, H.; Javadi, M.; Kalisvaart, W. P.; Buriak, J. M.; Veinot, J. G. C., Size and Surface Effects of Silicon Nanocrystals in Graphene Aerogel Composite Anodes for Lithium Ion Batteries. *Chem. Mater.* **2018**, *30* (21), 7782-7792.
84. Jiang, S.; Hu, B.; Sahore, R.; Liu, H.; Pach, G. F.; Carroll, G. M.; Zhang, L.; Zhao, B.; Neale, N. R.; Zhang, Z., Tailoring the Surface of Silicon Nanoparticles for Enhanced Chemical and Electrochemical Stability for Li-Ion Batteries. *ACS Appl. Energy Mater.* **2019**, *2* (9), 6176-6183.
85. Shen, T. D.; Koch, C. C.; McCormick, T. L.; Nemanich, R. J.; Huang, J. Y.; Huang, J. G., The structure and property characteristics of amorphous/nanocrystalline silicon produced by ball milling. *J. Mater. Res.* **1995**, *10* (1), 139-148.
86. Chaudhary, A.-L.; Sheppard, D. A.; Paskevicius, M.; Saunders, M.; Buckley, C. E., Mechanochemical synthesis of amorphous silicon nanoparticles. *RSC Adv.* **2014**, *4* (42), 21979-21983.
87. Tan, D.; Ma, Z.; Xu, B.; Dai, Y.; Ma, G.; He, M.; Jin, Z.; Qiu, J., Surface passivated silicon nanocrystals with stable luminescence synthesized by femtosecond laser ablation in solution. *Phys. Chem. Chem. Phys.* **2011**, *13* (45), 20255-20261.
88. Murthy, T. U. M. S.; Miyamoto, N.; Shimbo, M.; Nishizawa, J., Gas-phase nucleation during the thermal decomposition of silane in hydrogen. *J. Cryst. Growth* **1976**, *33* (1), 1-7.
89. Hofmeister, H.; Huiskens, F.; Kohn, B. Lattice contraction in nanosized silicon particles produced by laser pyrolysis of silane. In *The European Physical Journal D*; Châtelain, A., Bonard, J. M., Eds.; Springer Berlin Heidelberg: 1999; pp 137-140.
90. Li, X.; He, Y.; Talukdar, S. S.; Swihart, M. T., Preparation of luminescent silicon nanoparticles by photothermal aerosol synthesis followed by acid etching. *Phase Transit.* **2004**, *77*, 131-137.
91. Huiskens, F.; Ledoux, G.; Guillois, O.; Reynaud, C., Light-Emitting Silicon Nanocrystals from Laser Pyrolysis. *Adv. Mater.* **2002**, *14* (24), 1861-1865.
92. Li, X.; He, Y.; Talukdar, S. S.; Swihart, M. T., Process for Preparing Macroscopic Quantities of Brightly Photoluminescent Silicon Nanoparticles with Emission Spanning the Visible Spectrum. *Langmuir* **2003**, *19* (20), 8490-8496.
93. Li, X.; He, Y.; Swihart, M. T., Surface Functionalization of Silicon Nanoparticles Produced by Laser-Driven Pyrolysis of Silane followed by HF-HNO₃ Etching. *Langmuir* **2004**, *20* (11), 4720-4727.
94. Kortshagen, U. R.; Sankaran, R. M.; Pereira, R. N.; Girshick, S. L.; Wu, J. J.; Aydil, E. S., Nonthermal Plasma Synthesis of Nanocrystals: Fundamental Principles, Materials, and Applications. *Chem. Rev.* **2016**, *116* (18), 11061-11127.
95. Gorla, C. R.; Liang, S.; Tompa, G. S.; Mayo, W. E.; Lu, Y., Silicon and germanium nanoparticle formation in an inductively coupled plasma reactor. *J. Vac. Sci. Technol. A* **1997**, *15* (3), 860-864.
96. Mangolini, L.; Thimsen, E.; Kortshagen, U., High-Yield Plasma Synthesis of Luminescent Silicon Nanocrystals. *Nano Lett.* **2005**, *5* (4), 655-659.
97. So, K.-S.; Lee, H.; Kim, T.-H.; Choi, S.; Park, D.-W., Synthesis of silicon nanopowder from silane gas by RF thermal plasma. *Phys. Status Solidi A* **2014**, *211*, 310-315.

98. Gupta, A.; Swihart, M. T.; Wiggers, H., Luminescent Colloidal Dispersion of Silicon Quantum Dots from Microwave Plasma Synthesis: Exploring the Photoluminescence Behavior Across the Visible Spectrum. *Adv. Funct. Mater.* **2009**, *19* (5), 696-703.
99. Mangolini, L.; Kortshagen, U., Plasma-assisted synthesis of silicon nanocrystal inks. *Adv. Mater.* **2007**, *19* (18), 2513-2519.
100. Anthony, R.; Kortshagen, U., Photoluminescence quantum yields of amorphous and crystalline silicon nanoparticles. *Phys. Rev. B* **2009**, *80* (11), 115407.
101. Pi, X. D.; Liptak, R. W.; Deneen Nowak, J.; Wells, N. P.; Carter, C. B.; Campbell, S. A.; Kortshagen, U., Air-stable full-visible-spectrum emission from silicon nanocrystals synthesized by an all-gas-phase plasma approach. *Nanotechnology* **2008**, *19* (24), 245603.
102. Liptak, R. W.; Yang, J.; Kramer, N. J.; Kortshagen, U.; Campbell, S. A., Environmental photostability of SF₆-etched silicon nanocrystals. *Nanotechnology* **2012**, *23* (39), 395205.
103. Pringle, T. A.; Hunter, K. I.; Brumberg, A.; Anderson, K. J.; Fagan, J. A.; Thomas, S. A.; Petersen, R. J.; Sefannaser, M.; Han, Y.; Brown, S. L.; Kilin, D. S.; Schaller, R. D.; Kortshagen, U. R.; Boudjouk, P. R.; Hobbie, E. K., Bright Silicon Nanocrystals from a Liquid Precursor: Quasi-Direct Recombination with High Quantum Yield. *ACS Nano* **2020**, *14* (4), 3858-3867.
104. Yasar-Inceoglu, O.; Lopez, T.; Farshihagro, E.; Mangolini, L., Silicon nanocrystal production through non-thermal plasma synthesis: a comparative study between silicon tetrachloride and silane precursors. *Nanotechnology* **2012**, *23* (25), 255604.
105. Dasog, M.; Yang, Z. Y.; Regli, S.; Atkins, T. M.; Faramus, A.; Singh, M. P.; Muthuswamy, E.; Kauzlarich, S. M.; Tilley, R. D.; Veinot, J. G. C., Chemical Insight into the Origin of Red and Blue Photoluminescence Arising from Freestanding Silicon Nanocrystals. *ACS Nano* **2013**, *7* (3), 2676-2685.
106. Rosso-Vasic, M.; Spruijt, E.; van Lagen, B.; De Cola, L.; Zuilhof, H., Alkyl-functionalized oxide-free silicon nanoparticles: synthesis and optical properties. *Small* **2008**, *4* (10), 1835-1841.
107. Tilley, R. D.; Warner, J. H.; Yamamoto, K.; Matsui, I.; Fujimori, H., Micro-emulsion synthesis of monodisperse surface stabilized silicon nanocrystals. *Chem. Commun.* **2005**, *14*, 1833-1835.
108. Baldwin, R. K.; Pettigrew, K. A.; Ratai, E.; Augustine, M. P.; Kauzlarich, S. M., Solution reduction synthesis of surface stabilized silicon nanoparticles. *Chem. Commun.* **2002**, *17*, 1822-1823.
109. Zou, J.; Baldwin, R. K.; Pettigrew, K. A.; Kauzlarich, S. M., Solution synthesis of ultrastable luminescent siloxane-coated silicon nanoparticles. *Nano Lett.* **2004**, *4* (7), 1181-1186.
110. Heath, J. R., A liquid-solution-phase synthesis of crystalline silicon. *Science* **1992**, *258* (5085), 1131-1133.
111. Janka, O.; Kauzlarich, S. M. Zintl Compounds. In *Encyclopedia of Inorganic and Bioinorganic Chemistry*; Scott, R. A., Ed.; John Wiley & Sons: 2014; pp 1-14.
112. Bley, R. A.; Kauzlarich, S. M., A Low-Temperature Solution Phase Route for the Synthesis of Silicon Nanoclusters. *J. Am. Chem. Soc.* **1996**, *118* (49), 12461-12462.
113. Yang, C.-S.; Bley, R. A.; Kauzlarich, S. M.; Lee, H. W. H.; Delgado, G. R., Synthesis of Alkyl-Terminated Silicon Nanoclusters by a Solution Route. *J. Am. Chem. Soc.* **1999**, *121* (22), 5191-5195.
114. Mayeri, D.; Phillips, B. L.; Augustine, M. P.; Kauzlarich, S. M., NMR Study of the Synthesis of Alkyl-Terminated Silicon Nanoparticles from the Reaction of SiCl₄ with the Zintl Salt, NaSi. *Chem. Mater.* **2001**, *13* (3), 765-770.
115. Pettigrew, K. A.; Liu, Q.; Power, P. P.; Kauzlarich, S. M., Solution Synthesis of Alkyl- and Alkyl/Alkoxy-Capped Silicon Nanoparticles via Oxidation of Mg₂Si. *Chem. Mater.* **2003**, *15* (21), 4005-4011.
116. Zhang, X.; Neiner, D.; Wang, S.; Louie, A. Y.; Kauzlarich, S. M., A new solution route to hydrogen-terminated silicon nanoparticles: synthesis, functionalization and water stability. *Nanotechnology* **2007**, *18* (9), 095601.

117. Nesheva, D.; Raptis, C.; Perakis, A.; Bineva, I.; Aneva, Z.; Levi, Z.; Alexandrova, S.; Hofmeister, H., Raman scattering and photoluminescence from Si nanoparticles in annealed SiO_x thin films. *J. Appl. Phys.* **2002**, *92* (8), 4678-4683.
118. Hao, X. J.; Podhorodecki, A. P.; Shen, Y. S.; Zatoryb, G.; Misiewicz, J.; Green, M. A., Effects of Si-rich oxide layer stoichiometry on the structural and optical properties of Si QD/SiO₂ multilayer films. *Nanotechnology* **2009**, *20* (48), 485703.
119. Sun, W.; Qian, C.; Cui, X. S.; Wang, L.; Wei, M.; Casillas, G.; Helmy, A. S.; Ozin, G. A., Silicon monoxide – a convenient precursor for large scale synthesis of near infrared emitting monodisperse silicon nanocrystals. *Nanoscale* **2016**, *8*, (6), 3678-3684.
120. Liu, S.-M.; Yang; Sato, S.; Kimura, K., Enhanced Photoluminescence from Si Nano-organosols by Functionalization with Alkenes and Their Size Evolution. *Chem. Mater.* **2006**, *18* (3), 637-642.
121. Hessel, C. M.; Henderson, E. J.; Veinot, J. G. C., Hydrogen Silsesquioxane: A Molecular Precursor for Nanocrystalline Si–SiO₂ Composites and Freestanding Hydride-Surface-Terminated Silicon Nanoparticles. *Chem. Mater.* **2006**, *18* (26), 6139-6146.
122. Clark, R. J.; Aghajamali, M.; Gonzalez, C. M.; Hadidi, L.; Islam, M. A.; Javadi, M.; Mobarok, M. H.; Purkait, T. K.; Robidillo, C. J. T.; Sinelnikov, R.; Thiessen, A. N.; Washington, J.; Yu, H.; Veinot, J. G. C., From Hydrogen Silsesquioxane to Functionalized Silicon Nanocrystals. *Chem. Mater.* **2017**, *29* (1), 80-89.
123. Wilkinson, A. R.; Elliman, R. G., The effect of annealing environment on the luminescence of silicon nanocrystals in silica. *J. Appl. Phys.* **2004**, *96* (7), 4018-4020.
124. Hessel, C. M.; Reid, D.; Panthani, M. G.; Rasch, M. R.; Goodfellow, B. W.; Wei, J.; Fujii, H.; Akhavan, V.; Korgel, B. A., Synthesis of Ligand-Stabilized Silicon Nanocrystals with Size-Dependent Photoluminescence Spanning Visible to Near-Infrared Wavelengths. *Chem. Mater.* **2012**, *24* (2), 393-401.
125. Yang, Z.; Dobbie, A. R.; Veinot, J. G. C., Shape Evolution of Faceted Silicon Nanocrystals upon Thermal Annealing in an Oxide Matrix. *MRS Proceedings* **2013**, *1536*, 207-212.
126. Yang, Z.; Dobbie, A. R.; Cui, K.; Veinot, J. G. C., A Convenient Method for Preparing Alkyl-Functionalized Silicon Nanocubes. *J. Am. Chem. Soc.* **2012**, *134* (34), 13958-13961.
127. Yu, Y.; Lu, X.; Guillaussier, A.; Voggu, V. R.; Pineros, W.; de la Mata, M.; Arbiol, J.; Smilgies, D.-M.; Truskett, T. M.; Korgel, B. A., Orientationally Ordered Silicon Nanocrystal Cuboctahedra in Superlattices. *Nano Lett.* **2016**, *16* (12), 7814-7821.
128. Pereira, R. N.; Rowe, D. J.; Anthony, R. J.; Kortshagen, U., Oxidation of freestanding silicon nanocrystals probed with electron spin resonance of interfacial dangling bonds. *Phys. Rev. B* **2011**, *83* (15), 155327.
129. Rinck, J.; Schray, D.; Kübel, C.; Powell, A. K.; Ozin, G. A., Size-Dependent Oxidation of Monodisperse Silicon Nanocrystals with Allylphenylsulfide Surfaces. *Small* **2015**, *11* (3), 335-340.
130. Purkait, T. K.; Iqbal, M.; Wahl, M. H.; Gottschling, K.; Gonzalez, C. M.; Islam, M. A.; Veinot, J. G. C., Borane-catalyzed room-temperature hydrosilylation of alkenes/alkynes on silicon nanocrystal surfaces. *J. Am. Chem. Soc.* **2014**, *136* (52), 17914-17917.
131. Ghosh, B.; Masuda, Y.; Wakayama, Y.; Imanaka, Y.; Inoue, J.-i.; Hashi, K.; Deguchi, K.; Yamada, H.; Sakka, Y.; Ohki, S.; Shimizu, T.; Shirahata, N., Hybrid White Light Emitting Diode Based on Silicon Nanocrystals. *Adv. Funct. Mater.* **2014**, *24* (45), 7151-7160.
132. Islam, M. A.; Mobarok, M. H.; Sinelnikov, R.; Purkait, T. K.; Veinot, J. G. C., Phosphorus Pentachloride Initiated Functionalization of Silicon Nanocrystals. *Langmuir* **2017**, *33* (35), 8766-8773.
133. Mobarok, M. H.; Purkait, T. K.; Islam, M. A.; Miskolzie, M.; Veinot, J. G. C., Instantaneous Functionalization of Chemically Etched Silicon Nanocrystal Surfaces. *Angew. Chem. Int. Ed.* **2017**, *56* (22), 6073-6077.

134. Purkait, T. K.; Iqbal, M.; Islam, M. A.; Mobarok, M. H.; Gonzalez, C. M.; Hadidi, L.; Veinot, J. G. C., Alkoxy-Terminated Si Surfaces: A New Reactive Platform for the Functionalization and Derivatization of Silicon Quantum Dots. *J. Am. Chem. Soc.* **2016**, *138* (22), 7114-7120.
135. Kelly, J. A.; Shukaliak, A. M.; Fleischauer, M. D.; Veinot, J. G. C., Size-dependent reactivity in hydrosilylation of silicon nanocrystals. *J. Am. Chem. Soc.* **2011**, *133* (24), 9564-9571.
136. Buriak, J. M., Illuminating Silicon Surface Hydrosilylation: An Unexpected Plurality of Mechanisms. *Chem. Mater.* **2014**, *26* (1), 763-772.
137. Holm, J.; Roberts, J. T., Thermally Induced Hydrosilylation at Deuterium-Terminated Silicon Nanoparticles: An Investigation of the Radical Chain Propagation Mechanism. *Langmuir* **2009**, *25* (12), 7050-7056.
138. Yang, Z.; Iqbal, M.; Dobbie, A. R.; Veinot, J. G. C., Surface-Induced Alkene Oligomerization: Does Thermal Hydrosilylation Really Lead to Monolayer Protected Silicon Nanocrystals? *J. Am. Chem. Soc.* **2013**, *135* (46), 17595-17601.
139. Rosso-Vasic, M.; Spruijt, E.; van Lagen, B.; De Cola, L.; Zuilhof, H., Alkyl-Functionalized Oxide-Free Silicon Nanoparticles: Synthesis and Optical Properties. *Small* **2008**, *4* (10), 1835-1841.
140. Kelly, J. A.; Veinot, J. G. C., An Investigation into Near-UV Hydrosilylation of Freestanding Silicon Nanocrystals. *ACS Nano* **2010**, *4* (8), 4645-4656.
141. Huck, L. A.; Buriak, J. M., Toward a mechanistic understanding of exciton-mediated hydrosilylation on nanocrystalline silicon. *J. Am. Chem. Soc.* **2012**, *134* (1), 489-497.
142. Hohlein, I. M.; Kehrle, J.; Helbich, T.; Yang, Z.; Veinot, J. G.; Rieger, B., Diazonium salts as grafting agents and efficient radical-hydrosilylation initiators for freestanding photoluminescent silicon nanocrystals. *Chem. Eur. J.* **2014**, *20* (15), 4212-4216.
143. Yang, Z.; Gonzalez, C. M.; Purkait, T. K.; Iqbal, M.; Meldrum, A.; Veinot, J. G. C., Radical Initiated Hydrosilylation on Silicon Nanocrystal Surfaces: An Evaluation of Functional Group Tolerance and Mechanistic Study. *Langmuir* **2015**, *31* (38), 10540-10548.
144. Sun, W.; Qian, C.; Mastronardi, M. L.; Wei, M.; Ozin, G. A., Hydrosilylation kinetics of silicon nanocrystals. *Chem. Commun.* **2013**, *49* (97), 11361-11363.
145. Wheeler, L. M.; Anderson, N. C.; Palomaki, P. K. B.; Blackburn, J. L.; Johnson, J. C.; Neale, N. R., Silyl Radical Abstraction in the Functionalization of Plasma-Synthesized Silicon Nanocrystals. *Chem. Mater.* **2015**, *27* (19), 6869-6878.
146. Rogozhina, E. V.; Eckhoff, D. A.; Gratton, E.; Braun, P. V., Carboxyl functionalization of ultrasmall luminescent silicon nanoparticles through thermal hydrosilylation. *J. Mater. Chem.* **2006**, *16* (15), 1421-1430.
147. Yang, Z. Y.; Dasog, M.; Dobbie, A. R.; Lockwood, R.; Zhi, Y. Y.; Meldrum, A.; Veinot, J. G. C., Highly Luminescent Covalently Linked Silicon Nanocrystal/Polystyrene Hybrid Functional Materials: Synthesis, Properties, and Processability. *Adv. Funct. Mater.* **2014**, *24* (10), 1345-1353.
148. Hua, F.; Swihart, M. T.; Ruckenstein, E., Efficient surface grafting of luminescent silicon quantum dots by photoinitiated hydrosilylation. *Langmuir* **2005**, *21* (13), 6054-62.
149. Stewart, M. P.; Buriak, J. M., Exciton-mediated hydrosilylation on photoluminescent nanocrystalline silicon. *J. Am. Chem. Soc.* **2001**, *123* (32), 7821-7830.
150. Calder, S.; Boies, A.; Lei, P. Y.; Girshick, S.; Roberts, J., Photo-Assisted Hydrosilylation of Silicon Nanoparticles: Dependence of Particle Size on Grafting Chemistry. *Chem. Mater.* **2011**, *23* (11), 2917-2921.
151. Wu, Y.-D.; Wong, C.-L., Substituent Effect on the Dissociation Energy of the Si-H Bond: A Density Functional Study. *J. Org. Chem.* **1995**, *60* (4), 821-828.
152. Yang, Z.; De los Reyes, G. B.; Titova, L. V.; Sychugov, I.; Dasog, M.; Linnros, J.; Hegmann, F. A.; Veinot, J. G. C., Evolution of the Ultrafast Photoluminescence of Colloidal Silicon Nanocrystals with Changing Surface Chemistry. *ACS Photonics* **2015**, *2* (5), 595-605.

153. Shiohara, A.; Prabakar, S.; Faramus, A.; Hsu, C. Y.; Lai, P. S.; Northcote, P. T.; Tilley, R. D., Sized controlled synthesis, purification, and cell studies with silicon quantum dots. *Nanoscale* **2011**, *3* (8), 3364-3370.
154. Helbich, T.; Kloberg, M. J.; Sinelnikov, R.; Lyuleeva, A.; Veinot, J. G. C.; Rieger, B., Diaryliodonium salts as hydrosilylation initiators for the surface functionalization of silicon nanomaterials and their collaborative effect as ring opening polymerization initiators. *Nanoscale* **2017**, *9* (23), 7739-7744.
155. Kehrle, J.; Kaiser, S.; Purkait, T. K.; Winnacker, M.; Helbich, T.; Vagin, S.; Veinot, J. G. C.; Rieger, B., In situ IR-spectroscopy as a tool for monitoring the radical hydrosilylation process on silicon nanocrystal surfaces. *Nanoscale* **2017**, *9* (24), 8489-8495.
156. Hohlein, I. M.; Angi, A.; Sinelnikov, R.; Veinot, J. G.; Rieger, B., Functionalization of Hydride Terminated Photoluminescent Silicon Nanocrystals with Organolithium Reagents. *Chem. Eur. J.* **2015**, *21* (7), 2755-2758.
157. Song, J. H.; Sailor, M. J., Functionalization of Nanocrystalline Porous Silicon Surfaces with Aryllithium Reagents: Formation of Silicon–Carbon Bonds by Cleavage of Silicon–Silicon Bonds. *J. Am. Chem. Soc.* **1998**, *120* (10), 2376-2381.
158. Angi, A.; Sinelnikov, R.; Heenen, H. H.; Meldrum, A.; Veinot, J. G. C.; Scheurer, C.; Reuter, K.; Ashkenazy, O.; Azulay, D.; Balberg, I.; Millo, O.; Rieger, B., The influence of conjugated alkynyl(aryl) surface groups on the optical properties of silicon nanocrystals: photoluminescence through in-gap states. *Nanotechnology* **2018**, *29* (35), 355705.
159. Kim, D.; Joo, J.; Pan, Y.; Boarino, A.; Jun, Y. W.; Ahn, K. H.; Arkles, B.; Sailor, M. J., Thermally Induced Silane Dehydrocoupling on Silicon Nanostructures. *Angew. Chem. Int. Ed.* **2016**, *55* (22), 6423-6427.
160. Yang, Z.; Wahl, M. H.; Veinot, J. G. C., Size-independent organosilane functionalization of silicon nanocrystals using Wilkinson's catalyst. *Can. J. Chem.* **2014**, *92* (10), 951-957.
161. Holland, J. M.; Stewart, M. P.; Allen, M. J.; Buriak, J. M., Metal Mediated Reactions on Porous Silicon Surfaces. *J. Solid State Chem.* **1999**, *147* (1), 251-258.
162. Dasog, M.; Veinot, J. G. C., Size independent blue luminescence in nitrogen passivated silicon nanocrystals. *Phys. Status Solidi A* **2012**, *209* (10), 1844-1846.
163. Dasog, M.; Bader, K.; Veinot, J. G. C., Influence of Halides on the Optical Properties of Silicon Quantum Dots. *Chem. Mater.* **2015**, *27* (4), 1153-1156.
164. Wang, R.; Pi, X.; Yang, D., Surface modification of chlorine-passivated silicon nanocrystals. *Phys. Chem. Chem. Phys.* **2013**, *15* (6), 1815-1820.
165. Zhai, Y.; Dasog, M.; Snitynsky, R. B.; Purkait, T. K.; Aghajamali, M.; Hahn, A. H.; Sturdy, C. B.; Lowary, T. L.; Veinot, J. G. C., Water-soluble photoluminescent d-mannose and l-alanine functionalized silicon nanocrystals and their application to cancer cell imaging. *J. Mater. Chem. B* **2014**, *2* (47), 8427-8433.
166. Baldwin, R. K.; Pettigrew, K. A.; Ratai, E.; Augustine, M. P.; Kauzlarich, S. M., Solution reduction synthesis of surface stabilized silicon nanoparticles. *Chem. Commun.* **2002**, *17*, 1822-1823.
167. Dasog, M.; De los Reyes, G. B.; Titova, L. V.; Hegmann, F. A.; Veinot, J. G., Size vs surface: tuning the photoluminescence of freestanding silicon nanocrystals across the visible spectrum via surface groups. *ACS Nano* **2014**, *8* (9), 9636-9648.
168. El-Demellawi, J. K.; Holt, C. R.; Abou-Hamad, E.; Al-Talla, Z. A.; Saih, Y.; Chaieb, S., Room-Temperature Reactivity Of Silicon Nanocrystals With Solvents: The Case Of Ketone And Hydrogen Production From Secondary Alcohols: Catalysis? *ACS Appl. Mater. Interfaces* **2015**, *7* (25), 13794-13800.
169. Dasog, M.; Thompson, J. R.; Lewis, N. S., Oxidant-Activated Reactions of Nucleophiles with Silicon Nanocrystals. *Chem. Mater.* **2017**, *29* (16), 7002-7013.
170. Yu, Y.; Rowland, C. E.; Schaller, R. D.; Korgel, B. A., Synthesis and Ligand Exchange of Thiol-Capped Silicon Nanocrystals. *Langmuir* **2015**, *31* (24), 6886-6893.

171. Hessel, C. M.; Henderson, E. J.; Veinot, J. G. C., An Investigation of the Formation and Growth of Oxide-Embedded Silicon Nanocrystals in Hydrogen Silsesquioxane-Derived Nanocomposites. *J. Phys. Chem. C* **2007**, *111* (19), 6956-6961.
172. Hannah, D. C.; Yang, J.; Kramer, N. J.; Schatz, G. C.; Kortshagen, U. R.; Schaller, R. D., Ultrafast Photoluminescence in Quantum-Confined Silicon Nanocrystals Arises from an Amorphous Surface Layer. *ACS Photonics* **2014**, *1* (10), 960-967.
173. Petkov, V.; Hessel, C. M.; Ovtchinnikov, J.; Guillaussier, A.; Korgel, B. A.; Liu, X.; Giordano, C., Structure-Properties Correlation in Si Nanoparticles by Total Scattering and Computer Simulations. *Chem. Mater.* **2013**, *25* (11), 2365-2371.
174. Yu, Y.; Fan, G.; Fermi, A.; Mazzaro, R.; Morandi, V.; Ceroni, P.; Smilgies, D.-M.; Korgel, B. A., Size-Dependent Photoluminescence Efficiency of Silicon Nanocrystal Quantum Dots. *J. Phys. Chem. C* **2017**, *121* (41), 23240-23248.
175. Vatan Meidanshahi, R.; Bowden, S.; Goodnick, S. M., Electronic structure and localized states in amorphous Si and hydrogenated amorphous Si. *Phys. Chem. Chem. Phys.* **2019**, *21* (24), 13248-13257.
176. Jarolimek, K.; Hazrati, E.; de Groot, R. A.; de Wijs, G. A., Band Offsets at the Interface between Crystalline and Amorphous Silicon from First Principles. *Phys. Rev. Appl.* **2017**, *8* (1), 014026.
177. Park, N.-M.; Kim, T.-S.; Park, S.-J., Band gap engineering of amorphous silicon quantum dots for light-emitting diodes. *Appl. Phys. Lett.* **2001**, *78* (17), 2575-2577.
178. Park, N.-M.; Choi, C.-J.; Seong, T.-Y.; Park, S.-J., Quantum Confinement in Amorphous Silicon Quantum Dots Embedded in Silicon Nitride. *Phys. Rev. Lett.* **2001**, *86* (7), 1355-1357.
179. Askari, S.; Svrcek, V.; Maguire, P.; Mariotti, D., The Interplay of Quantum Confinement and Hydrogenation in Amorphous Silicon Quantum Dots. *Adv. Mater.* **2015**, *27* (48), 8011-8016.
180. Guo, Y.; Wang, Q.; Kawazoe, Y.; Jena, P., A New Silicon Phase with Direct Band Gap and Novel Optoelectronic Properties. *Sci. Rep.* **2015**, *5* (1), 14342.
181. Wang, Q.; Xu, B.; Sun, J.; Liu, H.; Zhao, Z.; Yu, D.; Fan, C.; He, J., Direct Band Gap Silicon Allotropes. *J. Am. Chem. Soc.* **2014**, *136* (28), 9826-9829.
182. Hannah, D. C.; Yang, J.; Podsiadlo, P.; Chan, M. K. Y.; Demortière, A.; Gosztola, D. J.; Prakapenka, V. B.; Schatz, G. C.; Kortshagen, U.; Schaller, R. D., On the Origin of Photoluminescence in Silicon Nanocrystals: Pressure-Dependent Structural and Optical Studies. *Nano Lett.* **2012**, *12* (8), 4200-4205.
183. Kůsová, K.; Hapala, P.; Valenta, J.; Jelinek, P.; Cibulka, O.; Ondič, L.; Pelant, I., Direct Bandgap Silicon: Tensile-Strained Silicon Nanocrystals. *Adv. Mater. Interfaces* **2014**, *1* (2), 1300042.
184. Kůsová, K.; Ondič, L.; Pelant, I., Comment on “Ultrafast Photoluminescence in Quantum-Confined Silicon Nanocrystals Arises from an Amorphous Surface Layer”. *ACS Photonics* **2015**, *2* (3), 454-455.
185. Hannah, D. C.; Yang, J.; Kramer, N. J.; Schatz, G. C.; Kortshagen, U. R.; Schaller, R. D., Reply to “Comment on ‘Ultrafast Photoluminescence in Quantum-Confined Silicon Nanocrystals Arises from an Amorphous Surface Layer’”. *ACS Photonics* **2015**, *2* (3), 456-458.
186. Kim, H.; Seo, M.; Park, M. H.; Cho, J., A critical size of silicon nano-anodes for lithium rechargeable batteries. *Angew. Chem. Int. Ed.* **2010**, *49* (12), 2146-2149.
187. Chan, C. K.; Peng, H. L.; Liu, G.; McIlwrath, K.; Zhang, X. F.; Huggins, R. A.; Cui, Y., High-performance lithium battery anodes using silicon nanowires. *Nat. Nanotechnol.* **2008**, *3* (1), 31-35.
188. Ko, M.; Chae, S.; Jeong, S.; Oh, P.; Cho, J., Elastic α -Silicon Nanoparticle Backboned Graphene Hybrid as a Self-Compacting Anode for High-Rate Lithium Ion Batteries. *ACS Nano* **2014**, *8* (8), 8591-8599.
189. Lockwood, R.; Yang, Z.; Sammynaiken, R.; Veinot, J. G. C.; Meldrum, A., Light-Induced Evolution of Silicon Quantum Dot Surface Chemistry—Implications for Photoluminescence, Sensing, and Reactivity. *Chem. Mater.* **2014**, *26* (19), 5467-5474.

190. Aghajamali, M.; Iqbal, M.; Purkait, T. K.; Hadidi, L.; Sinelnikov, R.; Veinot, J. G. C., Synthesis and Properties of Luminescent Silicon Nanocrystal/Silica Aerogel Hybrid Materials. *Chem. Mater.* **2016**, *28* (11), 3877-3886.
191. DeBenedetti, W. J. I.; Chiu, S.-K.; Radlinger, C. M.; Ellison, R. J.; Manhat, B. A.; Zhang, J. Z.; Shi, J.; Goforth, A. M., Conversion from Red to Blue Photoluminescence in Alcohol Dispersions of Alkyl-Capped Silicon Nanoparticles: Insight into the Origins of Visible Photoluminescence in Colloidal Nanocrystalline Silicon. *J. Phys. Chem. C* **2015**, *119* (17), 9595-9608.
192. Sinelnikov, R.; Dasog, M.; Beamish, J.; Meldrum, A.; Veinot, J. G. C., Revisiting an Ongoing Debate: What Role Do Surface Groups Play in Silicon Nanocrystal Photoluminescence? *ACS Photonics* **2017**, *4* (8), 1920-1929.
193. Kang, Z.; Liu, Y.; Tsang, C. H. A.; Ma, D. D. D.; Fan, X.; Wong, N.-B.; Lee, S.-T., Water-Soluble Silicon Quantum Dots with Wavelength-Tunable Photoluminescence. *Adv. Mater.* **2009**, *21* (6), 661-664.
194. Martin, J.; Cichos, F.; Huisken, F.; von Borczyskowski, C., Electron-Phonon Coupling and Localization of Excitons in Single Silicon Nanocrystals. *Nano Lett.* **2008**, *8* (2), 656-660.
195. Botas, A. M. P.; Ferreira, R. A. S.; Pereira, R. N.; Anthony, R. J.; Moura, T.; Rowe, D. J.; Kortshagen, U., High Quantum Yield Dual Emission from Gas-Phase Grown Crystalline Si Nanoparticles. *J. Phys. Chem. C* **2014**, *118* (19), 10375-10383.
196. Reboredo, F. A.; Galli, G., Theory of Alkyl-Terminated Silicon Quantum Dots. *J. Phys. Chem. B* **2005**, *109* (3), 1072-1078.
197. Angl, A.; Sinelnikov, R.; Meldrum, A.; Veinot, J. G. C.; Balberg, I.; Azulay, D.; Millo, O.; Rieger, B., Photoluminescence through in-gap states in phenylacetylene functionalized silicon nanocrystals. *Nanoscale* **2016**, *8* (15), 7849-7853.
198. Valenta, J.; Fucikova, A.; Pelant, I.; Kůsová, K.; Dohnalová, K.; Aleknavičius, A.; Cibulka, O.; Fojtík, A.; Kada, G., On the origin of the fast photoluminescence band in small silicon nanoparticles. *New J. Phys.* **2008**, *10* (7), 073022.
199. Yang, S.; Li, W.; Cao, B.; Zeng, H.; Cai, W., Origin of Blue Emission from Silicon Nanoparticles: Direct Transition and Interface Recombination. *J. Phys. Chem. C* **2011**, *115* (43), 21056-21062.
200. Gupta, A.; Wiggers, H., Freestanding silicon quantum dots: origin of red and blue luminescence. *Nanotechnology* **2010**, *22* (5), 055707.
201. Uchino, T.; Kurumoto, N.; Sagawa, N., Structure and formation mechanism of blue-light-emitting centers in silicon and silica-based nanostructured materials. *Phys. Rev. B* **2006**, *73* (23), 233203.
202. Loni, A.; Simons, A. J.; Calcott, P. D. J.; Canham, L. T., Blue photoluminescence from rapid thermally oxidized porous silicon following storage in ambient air. *J. Appl. Phys.* **1995**, *77* (7), 3557-3559.
203. Ddungu, J. L. Z.; Silvestrini, S.; Tassoni, A.; De Cola, L., Shedding light on the aqueous synthesis of silicon nanoparticles by reduction of silanes with citrates. *Faraday Discuss.* **2020**, *222*, 350-361.
204. Wilbrink, Jonathan L.; Huang, C.-C.; Dohnalova, K.; Paulusse, J. M. J., Critical assessment of wet-chemical oxidation synthesis of silicon quantum dots. *Faraday Discuss.* **2020**, *222*, 149-165.
205. Oliinyk, B. V.; Korytko, D.; Lysenko, V.; Alekseev, S., Are Fluorescent Silicon Nanoparticles Formed in a One-Pot Aqueous Synthesis? *Chem. Mater.* **2019**, *31* (18), 7167-7172.
206. Angl, A.; Loch, M.; Sinelnikov, R.; Veinot, J. G. C.; Becherer, M.; Lugli, P.; Rieger, B., The influence of surface functionalization methods on the performance of silicon nanocrystal LEDs. *Nanoscale* **2018**, *10* (22), 10337-10342.
207. Yang, S.; Li, G.; Zhu, Q.; Pan, Q., Covalent binding of Si nanoparticles to graphene sheets and its influence on lithium storage properties of Si negative electrode. *J. Mater. Chem.* **2012**, *22* (8), 3420-3425.
208. Lee, J. K.; Smith, K. B.; Hayner, C. M.; Kung, H. H., Silicon nanoparticles-graphene paper composites for Li ion battery anodes. *Chem. Commun.* **2010**, *46* (12), 2025-2027.

Chapter 2

Silicon Nanoparticles: Are They Crystalline from Core to the Surface?^a

2.1 Introduction

Semiconductor nanoparticles (i.e., quantum dots, QDs) exhibit exquisitely tunable optoelectronic properties, making them useful for a variety of applications, including displays, photovoltaics, and sensors. Unfortunately, many QDs are based upon toxic constituents (e.g., Cd) that are regulated in many jurisdictions.¹ In this context, identifying, preparing, and tailoring the properties of toxic metal-free (TMF) QDs is of paramount importance. Silicon nanoparticles (SiNPs) are TMF QDs that are prepared readily using abundant materials;^{2,3} they possess tailorable surface chemistry, exhibit size- and surface chemistry-tunable photoluminescence that spans the visible and near-infrared spectral regions with absolute quantum yields that compete with their CdSe-based counterparts,^{4,5} possess long-lived (microsecond) excited states,⁶ are biologically compatible,^{2,7} and reversibly alloy with lithium. As such, SiNPs are being explored as functional materials in luminescence-based biological imaging,^{3,8} medical imaging,^{9,10} light-emitting diodes, photovoltaics,¹²⁻¹⁴ sensors,¹⁵ solar concentrators,¹⁶ and lithium ion battery anodes.¹⁷⁻¹⁹ For many of these applications, SiNP size and surface profoundly impact material performance.²⁰

For example, when employed in lithium ion battery anodes, the SiNP surface has been implicated in the formation of the solid electrolyte interphase layer that drastically impacts device performance.^{19,21} Similarly, the SiNP surface plays an important role in defining their optical properties (e.g., luminescent color, brightness, photoluminescence (PL) quantum yield, excited state lifetime); by defining the surface bonded moiety, the SiNPs PL can be tuned through the visible range, and the excited state lifetime can be defined within the micro- to nanosecond regime.²²⁻²⁴ Furthermore, various ill-defined surfaces (e.g., defects, oxidation, etc.) have been implicated in low SiNP PL quantum yields.^{5,25}

^a The contents of this chapter have been adapted with permission from the following publication: Thiessen, A. N.; Ha, M.; Hooper, R. W.; Yu, H.; Oliynyk, A. O.; Veinot, J. G. C.; Michaelis, V. K., Silicon Nanoparticles: Are They Crystalline from the Core to the Surface? *Chem. Mater.* **2019**, *31*, 678-688. Copyright © 2019 American Chemical Society.

In light of their key roles in material properties, establishing an understanding of the SiNP surface and internal structure is of paramount importance. Approaches to probing SiNP surfaces have been multifaceted. Quantum chemical calculations provide insight into the nature of the SiNP-oxide interface for oxide-embedded NPs.²⁶⁻²⁸ These modeling studies suggest that, when embedded in oxides, SiNPs possess a strained structure that leads to the formation of species such as distorted (i.e., elongated or shortened) Si—Si bonds, dangling bonds, coordination defects, and Si—O—Si bridging species.^{26, 27, 29} The surfaces of SiNPs also have been interrogated directly using various spectroscopic methods. Raman spectroscopy provides direct probing of Si—Si bonds;³⁰⁻³² multiple Si—Si species have been identified for small particles ($d \sim 3$ nm), and as the particle size is increased, features associated with surface species disappear.³⁰ Fourier transform infrared spectroscopy (FTIR) also provides information regarding bonding in SiNP surface species, including different Si—H_x, Si—O, and Si—R (R = alkyl, aryl, etc.);³³⁻³⁶ however, due to dipole considerations, FTIR does not probe Si—Si bonding directly.

Nuclear magnetic resonance (NMR) spectroscopy is a workhorse method for molecular and materials characterization; ¹H NMR spectroscopy has been applied, in combination with other methods (e.g., Raman, FTIR, etc.), to evaluate SiNP surface derivatization.^{4, 37-46} It, as well as ¹⁹F NMR spectroscopy, also have been used to probe the speciation of surface functionalities on hydride-terminated SiNPs (H-SiNPs) indirectly via the evaluation of reaction byproducts.⁴ Solid-state NMR spectroscopy is a powerful analytical method that provides data related to atomic-level short- and medium-range structural differences within nanomaterials.⁴⁷ Despite suffering from a low natural abundance (4.7%), ²⁹Si is an NMR-active nucleus, with a nuclear spin $I = 1/2$, a moderate Larmor frequency (19.9% that of ¹H), and a moderate chemical shift range. These combined properties result in relatively narrow line widths and good resolution for solids when using magic-angle spinning (MAS) and allow for identification of a variety of silicon species. To date, applications of solid-state NMR spectroscopy for SiNP evaluation have been confined largely to functionalized,^{37-43, 45, 48} ammonium/chloride capped,^{44, 49} doped,⁵⁰ porous,^{46, 51} nanoclusters,⁵² or micrometer-sized high polarization studies,^{9, 53} while nondoped hydride-terminated studies are less prevalent⁵⁴⁻⁵⁶ due, in part, to their reactivity and limited solution processability. Previously, a combination of cross-

polarization and single-pulse methods with strategic wetting aided in decoding various Si-based surface species on SiNPs of $d \sim 50$ nm;⁵⁴ this approach was expanded quickly to assess the impact of surface functionalization.⁵⁵ These examples and others⁵⁷⁻⁶⁵ demonstrate the wide-ranging utility of NMR spectroscopy and its applicability to a diverse array of Si-based nanomaterials.

In this regard, size-dependent ²⁹Si NMR analyses of SiNPs are expected to provide invaluable insight into their structure, which may be used to optimize material performance in far reaching applications. In this work, we describe a methodical investigation of H-SiNPs with predefined dimensions ranging from 3 to 64 nm, employing a complementary suite of characterization methods: X-ray photoelectron spectroscopy (XPS), Fourier transform infrared (FTIR) spectroscopy, bright-field transmission electron microscopy (TEM), powder X-ray diffraction (XRD), and ²⁹Si solid-state NMR spectroscopy that together reveal the size dependent order/disorder within the NPs. We further elucidate an intermediate layer, denoted here as the *subsurface*, using cross-polarization NMR spectroscopy and SiNP size dependent nuclear spin-lattice relaxation behavior.

2.2 Experimental Section

2.2.1 Materials

2.2.1.1 Starting Materials

Hydrofluoric (Electronic grade, 48–50%) and sulfuric (reagent grade, 95–98%) acids were purchased from Fisher Scientific and Caledon Laboratory Chemicals, respectively. Fuming sulfuric acid (reagent grade, 20% free SO₃ bases), trichlorosilane (99%), and toluene (HPLC grade) were purchased from Sigma-Aldrich. Toluene was purified using a Pure-Solv purification system and collected immediately prior to use. Benzene was purchased from EMD Millipore (now MilliporeSigma). All reagents and solvents were used as received unless otherwise specified.

2.2.1.2 Preparation of Hydrogen Silsesquioxane (HSQ)

HSQ was synthesized following a modified literature procedure.⁶⁶ Briefly, dry toluene (45.0 mL) was added to a mixture of concentrated (15.0 mL) and fuming (7.2 mL) sulfuric acid under an inert atmosphere. A second solution of dry toluene (110 mL) and trichlorosilane

(16 mL) was prepared and added dropwise to the sulfuric acid mixture over a few hours. The toluene layer was isolated and washed with a sulfuric acid solution. After drying the organic layer over MgSO₄ (neutralized with CaCO₃ overnight), the volume was reduced initially using a rotary evaporator and then evaporated to dryness in vacuo to yield the desired product as a white solid that was stored under vacuum until use.

2.2.1.3 Preparation of the H-SiNPs

Thermally induced disproportionation of the HSQ was exploited to produce the well-defined SiNPs used in this study.⁶⁷ Briefly, 6 g of HSQ were processed thermally in a standard tube furnace under flowing 5% H₂/95% Ar at 1100, 1200, 1300, 1400, or 1500 °C. This procedure yielded oxide composites containing SiNPs of predefined sizes (See Table 2-1).

The resulting composites containing SiNPs were ground using an agate mortar and pestle, followed by shaking in a wrist action shaker with high purity glass beads for 6 h. The resulting powder was etched using a 1:1:1 solution of ethanol:deionized water:HF to liberate the H-SiNPs; a typical etching procedure employed ~1 g and 30 mL of composite and etching solution, respectively. The composite was exposed to the etching solution for 1 h after which the H-SiNPs were extracted into toluene and isolated by centrifugation. Next, the H-SiNPs were subjected to two suspension/centrifugation cycles in toluene, followed by dispersion in benzene for freeze-drying. The benzene suspension was freeze-dried to obtain a free flowing H-SiNP powder. Samples were packed into ZrO₂ NMR rotors and sealed with Kel-F drive caps. Identical samples also were evaluated using FTIR, XPS, and bright-field TEM. All material manipulations were performed in a nitrogen filled drybox to ensure negligible surface oxidation or reaction with water.

Table 2-1. Particle Band Gap and Size Analysis from TEM and XRD

Nominal (nm)	Annealing Temp. (°C)	Band Gap (eV) ^b	TEM (nm)	XRD (nm) ^c
3	1100	1.57	3.5 ± 0.9	1.2 ± 0.1
6	1200	1.33	5.5 ± 1.2	2.5 ± 0.1
9	1300	1.22	8.7 ± 1.2	4.7 ± 0.2
21	1400	1.14	20.7 ± 4.0	10.2 ± 0.3
64	1500	1.12	64.0 ± 16.9	22.4 ± 0.2
microcrystalline ^a	-	1.12	44 × 10 ³	-

^a Bulk microcrystalline (44 μm) silicon (Aldrich). ^b Band gap determined from Wheeler et al.²⁵

^c Values determined from powder X-ray diffraction using the integral breadth method.⁶⁸

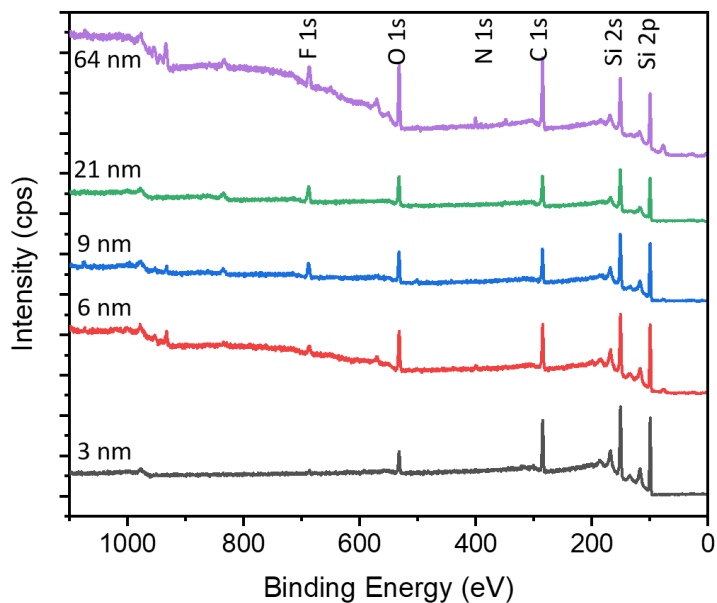
2.2.2 Characterization

2.2.2.1 Fourier Transform Infrared Spectroscopy (FTIR)

FTIR was performed on a Thermo Nicolet Continuum FT-IR microscope by drop casting SiNPs onto a silicon wafer from dry toluene suspensions.

2.2.2.2 X-ray Photoelectron Spectroscopy (XPS)

XPS was measured using a Kratos Axis 165 Ultra X-ray photoelectron spectrometer. A monochromatic Al K α source operating at 140 W with an energy $h\nu = 1486.6$ eV was used. Survey spectra were collected with an analyzer pass energy of 160 eV and a step of 0.3 eV (Figure 2-1). For high-resolution spectra, the pass energy was 20 eV and the step was 0.1 eV, with a dwell time of 200 ms. Samples were prepared by drop-coating a dry toluene dispersion of SiNPs onto a copper foil. Spectra were calibrated to the aliphatic C component of the C 1s binding energy of adventitious carbon (284.8 eV)^{69, 70} and fitted to appropriate spin-orbit pairs using CasaXPS (VAMAS) software taking into account a Shirley-type background. To fit the Si 2p high-resolution spectrum, the spin-orbit couple doublet area ratio was fixed at 2:1 and the peak-to-peak separation was defined to be 0.62 eV (Figure 2-2). The spectral window was fit using a variant of a literature procedure.⁷¹ Briefly, the spectral components (i.e., spin-orbit couple doublet) arising from elemental Si (near 99.4–99.5 eV here) were fitted first using a symmetric Gaussian–Lorentzian line shape for small-size particles. When splitting was observed in the envelope shape (i.e., $d \sim 9, 21, \text{ and } 64$ nm), a Lorentzian asymmetric (LA) line shape was applied ($LA = 1.93, 3.2, n$; where n defines the Gaussian width).⁷² To account for the decrease in structural order with SiNPs arising from a decreased particle size, the full-width at half maximum (FWHM) of the spectral components used to fit the elemental Si features were constrained as follows: d , FWHM: 3nm, 1.13 eV; 6 nm, 0.93 eV; 9 nm, 0.63 eV; 21 nm, 0.6 eV; 64 nm, 0.58 eV. The residual area always was fitted using a Gaussian–Lorentzian line shape with the same doublet relationship noted above. The fitting was evaluated by examination of the residuals.

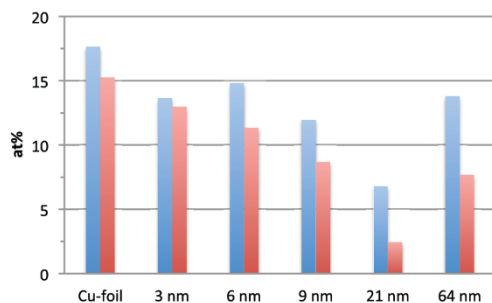


Elemental composition from survey

Sample	C at%	O at%	Si at%	F at%	Cu at%
Cu foil	72.08	17.65	0	0	5.79
3 nm	40.48	13.64	38.08	7.8	0
6 nm	36.66	14.81	44.27	4.25	0
9 nm	36.23	11.97	44.88	6.53	0.39
21 nm	42.07	6.79	50.25	0.88	0
64 nm	40.25	13.79	42.56	2.76	0.63

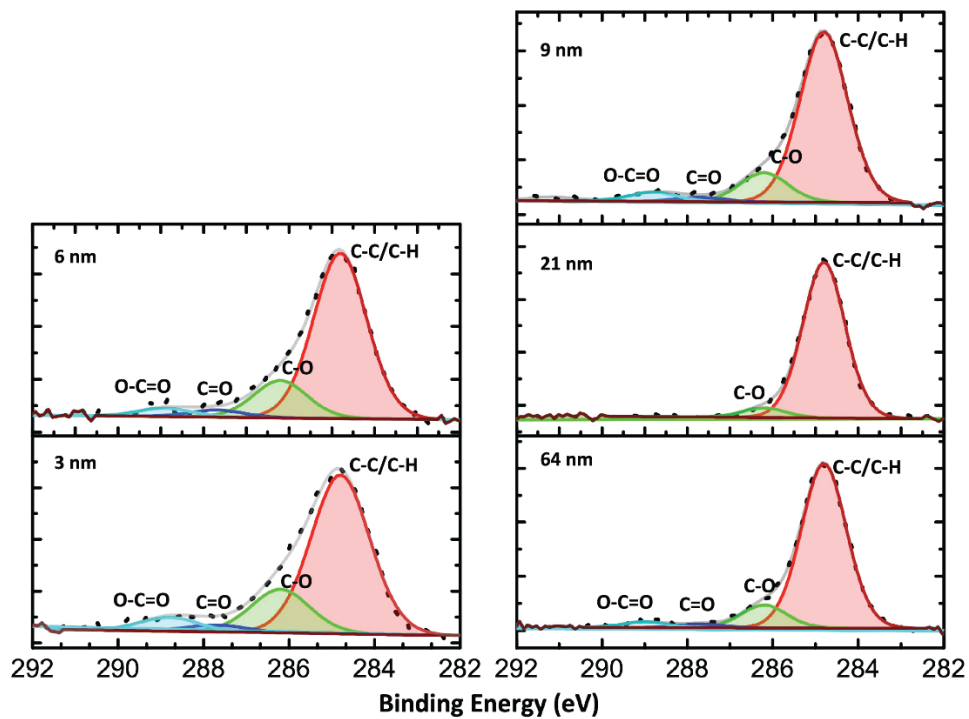
Peak composition from C 1s

C 1s	C 1s				Si 2p	
	C-C/C-H	C-O	C=O	O-C=O	eV	
Cu foil	87.37	8.74	3.35	4.54	3 nm	99.43
3 nm	74.01	17.88	2.01	6.1	6 nm	99.48
6 nm	74.07	17.1	3.88	4.95	9 nm	99.37
9 nm	78.46	13.53	2.04	4.2	21 nm	99.42
21 nm	94.17	5.83	0	0	64 nm	99.43
64 nm	83.72	11.59	1.87	2.82		99.57 (10%)



	O at% from survey	O at% from C 1s
Cu-foil	17.65	15.26
3 nm	13.64	12.99
6 nm	14.81	11.32
9 nm	11.97	8.68
21 nm	6.79	2.45
64 nm	13.79	7.69

Figure 2-1. Survey XPS data for 3 nm (black), 6 nm (red), 9 nm (blue), 21 nm (green), and 64 nm (purple); tabulated elemental composition and peak composition for C and O at% from survey.



Red= crystalline core
Blue= surface Si atoms
Orange= disordered Si network
Green= Si oxides

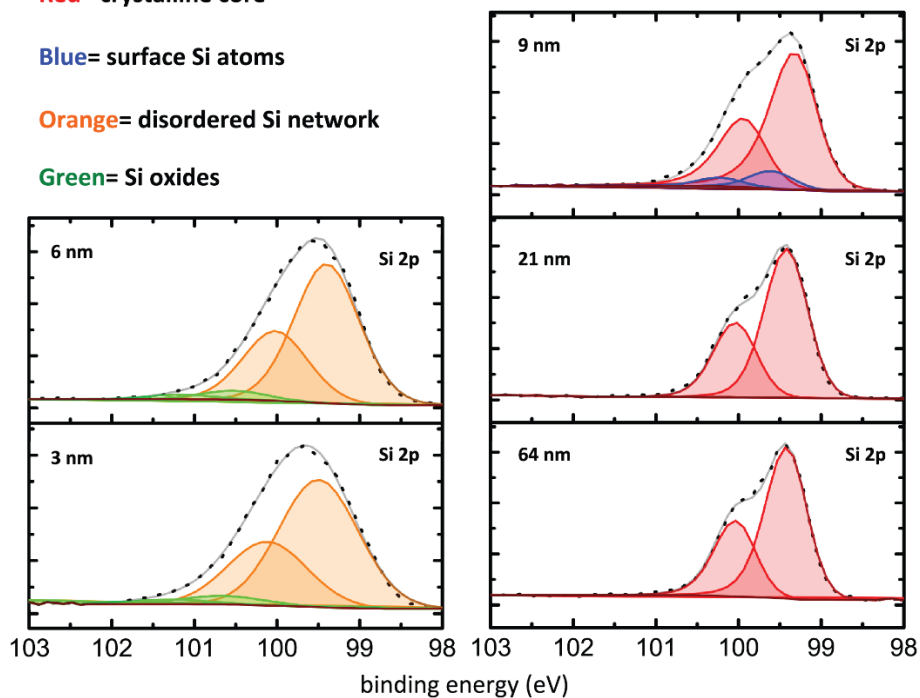


Figure 2-2. Peak fitting for C and Si XPS data for 3, 6, 9, 21, and 64 nm nanoparticles.

2.2.2.3 Transmission Electron Microscopy (TEM)

TEM imaging was performed using a JEOL-2010 electron microscope equipped with a LaB₆ source and an accelerating voltage of 200 kV. Specimens were prepared by drop-casting toluene suspensions of H-SiNPs onto carbon-coated copper grids. The NP size was determined by averaging the size of 300 particles using ImageJ software (Version 1.51j8), Figure 2-3. Bright field images of $d \sim 3$ nm SiNPs showed substantial aggregation, making imaging impractical for sizing the material. To overcome this, $d \sim 3$ nm H-SiNPs were functionalized with dodecene using established thermally induced hydrosilylation and then imaged.⁷³

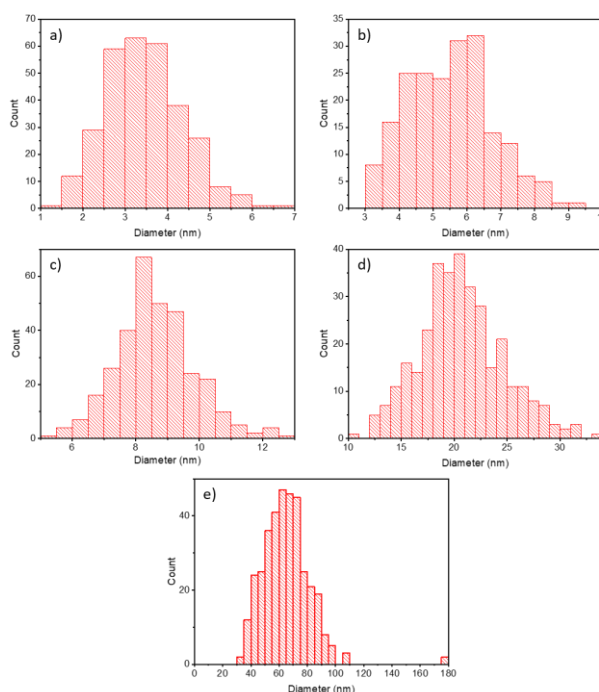


Figure 2-3. Histograms showing size distributions for (a) 3 nm, (b) 6 nm, (c) 9 nm, (d) 21 nm, and (e) 64 nm H-SiNPs.

2.2.2.4 Powder X-ray Diffraction (XRD)

Lyophilized samples were placed on a zero-background Si wafer. XRD data were acquired using a Rigaku XRD Ultima IV equipped with a Cu K α radiation source. Data for H-SiNPs with TEM-determined sizes 64, 21, 9, 6, and 3 nm were analyzed using a series of diffraction line-broadening methods (i.e., integral breadth, FWHM, and Lorentzian broadening) to determine crystallite sizes. Material properties as well as instrumental factors contribute to diffraction peak line broadening. Instrumental effects were accounted for by refining a NIST

LaB₆ standard to ensure instrument alignment, and a Si standard was used as an infinitely large crystallite size reference (Figure 2-4). After subtraction of instrumental contributions, line broadening was assumed to result only from size/strain effects. The patterns were analyzed and fitted using the TOPAS Academic software package.⁷⁴

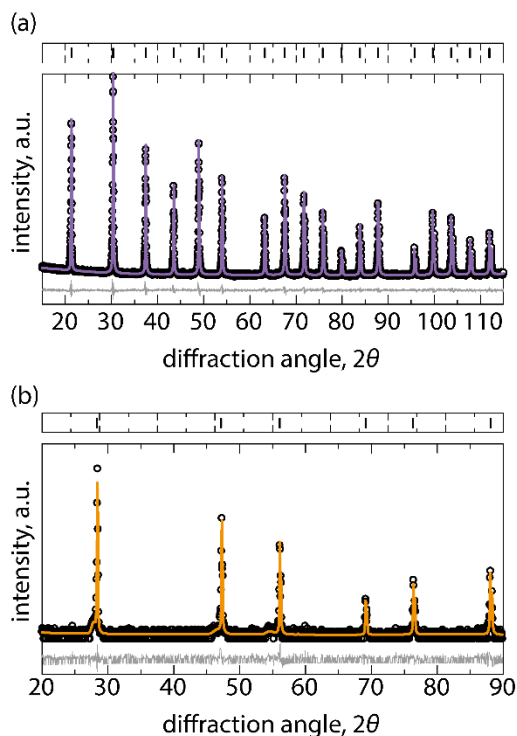


Figure 2-4. XRD alignment with (a) LaB₆ (NIST) and (b) Si standards. The black traces are the experimental data, the colored traces are the fitted data and the grey is the residuals.

2.2.2.5 Solid-State NMR Spectroscopy

Silicon-29 NMR spectra were obtained at 9.39 T (ν_0 (¹H) = 399.95 MHz, ν_0 (²⁹Si) = 79.46 MHz) on a Bruker Avance III HD 400 NMR spectrometer. All data were acquired using a 4 mm double-resonance (H-X) MAS Bruker probe. To ensure that samples had not degraded during analysis, all samples were checked pre- and post-NMR analysis using XPS and FTIR. All NMR data were acquired under magic-angle spinning conditions at ambient temperature, with a spinning frequency of 10 ± 0.002 kHz. The data for all experiments were acquired using TPPM⁷⁵ ¹H decoupling ($\gamma B_1/2\pi = 62.5$ kHz). ²⁹Si NMR data were referenced to TMS ($\delta = 0$) by setting the high frequency peak of tetrakis(trimethylsilyl)silane to -9.8 ppm.⁷⁶ All spectral deconvolutions were performed within Origin 2018, T_1 data were fitted within MATLAB 2017 assuming mono- or biexponential recoveries, and NMR data were processed within TOPSPIN

using between 50 and 200 Hz Lorentzian broadening. Unless otherwise noted, data were collected with at least $5 \times T_1$ of the longest measured T_1 time.

Analysis of H-SiNP Surface and Core: Direct excitation ^{29}Si MAS NMR data were acquired using a Bloch⁷⁷ pulse with a $4 \mu\text{s}$ $\pi/2$ pulse ($\gamma B_1/2\pi = 62.5$ kHz), optimized recycle delays (below) between 3.3 min and 24 h, and between 4 and 2048 co-added transients.

Analysis of the H-SiNP Surface: Cross-polarization⁷⁸ (CP) $^{29}\text{Si}[^1\text{H}]$ MAS NMR data were acquired with a $4 \mu\text{s}$ $\pi/2$ pulse ($\gamma B_1/2\pi = 62.5$ kHz) on ^1H , ramped Hartman–Hahn match on ^{29}Si , 5 ms contact time, 10 s recycle delay and between 7776 and 10240 co-added transients.

Deconvolution of H-SiNP Surface/Subsurface: The contact time was varied from 0.05 to 8 ms to elucidate spectral changes in the CP MAS data, as longer contact times provide time for nuclear spin diffusion to propagate further into the particle. A two-dimensional $^{29}\text{Si}[^1\text{H}]$ HETCOR experiment was obtained on the 64 nm particle using 1024 co-added transients, 3 ms contact time (conditions identical to CP experiments above), and 16 t_2 increments.

Nuclear Spin-Lattice Relaxation: Spin-lattice ^{29}Si relaxation data were acquired using the saturation recovery⁷⁹ experiment, with a pre-saturation train of 16 pulses and a $4 \mu\text{s}$ $\pi/2$ pulse ($\gamma B_1/2\pi = 62.5$ kHz), 1–1024 co-added transients; the relaxation delay was varied from 0.5 to 1000 s (Table 2-1 and Figure 2-5). Note: Due to the large H-SiNPs ($d \sim 21$ and 64 nm) exhibiting long nuclear T_1 , additional data points were collected (up to 144 h).

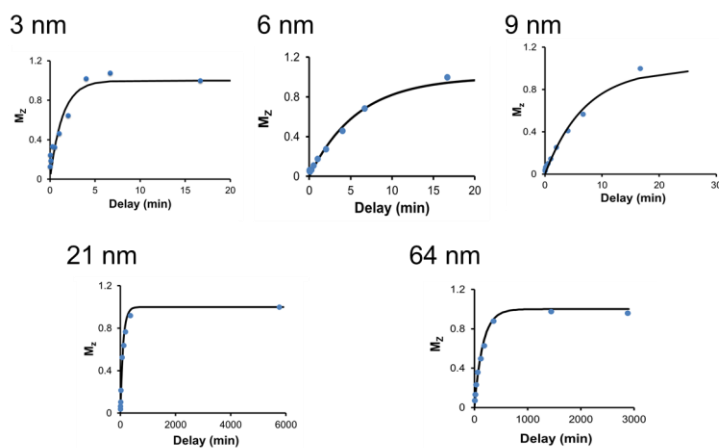


Figure 2-5. T_1 buildup curves for H-SiNPs using a mono-exponential longitudinal magnetization recovery for smaller H-SiNPs (3 and 6 nm) and a bi-exponential recovery for larger H-SiNPs (9, 21, and 64 nm).

2.3 Results and Discussion

Solid-state NMR spectroscopy is an ensemble technique that probes comparatively large quantities of material (i.e., tens to hundreds of milligrams) and provides information regarding local structure and dynamics. If nanomaterial structural property relationships are to be elucidated from such investigations, it is imperative that the NP size, shape, and composition be as uniform as possible to allow effective differentiation/identification of the nuclear environments that are present. To achieve this for SiNPs, we have prepared SiNP/SiO₂ composites that contain nanoscale inclusions of silicon with predefined sizes using a well-established, scalable method involving the thermal processing of HSQ;^{6, 67, 80} high-quality freestanding H-SiNPs are liberated routinely from these composites via alcoholic HF etching. In most cases, H-SiNPs are rendered solution processable and oxidation resistant upon surface derivatization using various approaches (e.g., hydrosilylation).^{40, 81-86} The focus of this study is to investigate the internal SiNP structure free from the influences of surface functionalities; H-SiNPs provide the nearest approximation to “naked” SiNPs available outside ultrahigh vacuum environments.

X-ray photoelectron spectroscopy is an information rich method that provides data related to material composition and constituent element chemical environment (e.g., oxidation state, nearest neighbor bonding environment, etc.). The survey spectra of the present H-SiNPs were calibrated to the aliphatic C1s signal of adventitious carbon. These data indicate that all specimens contain only Si, C, O, and F (Figure 2-1). Fluorine impurities arise from the alcoholic HF etching procedure that liberates H-SiNPs from the composite and cannot be avoided. Close examination of the C1s high-resolution XP spectra shows evidence of substantial oxygen containing carbon species (i.e., C–O, C=O, O–C=O, etc.; Figure 2-2). The relative ratios of these carbon-containing components are consistent for all sizes of H-SiNPs and are correlated with the amount of oxygen detected in the respective samples (Figure 2-1). From these analyses we conclude that the majority of the oxygen within the present H-SiNP specimens resides within the adventitious carbon species and is not associated with H-SiNP oxidation. This conclusion is supported further by FTIR analyses (Figure 2-6) and the high-resolution Si 2p spectra (Figures 2-2 and 2-7a) that are deconvolved readily into Si 2p 3/2 and Si 2p 1/2 spin-orbit couples. For all H-SiNPs, the energy separation of these doublets was fixed at 0.62 eV, and the Si 2p 1/2 to Si 2p 3/2 area

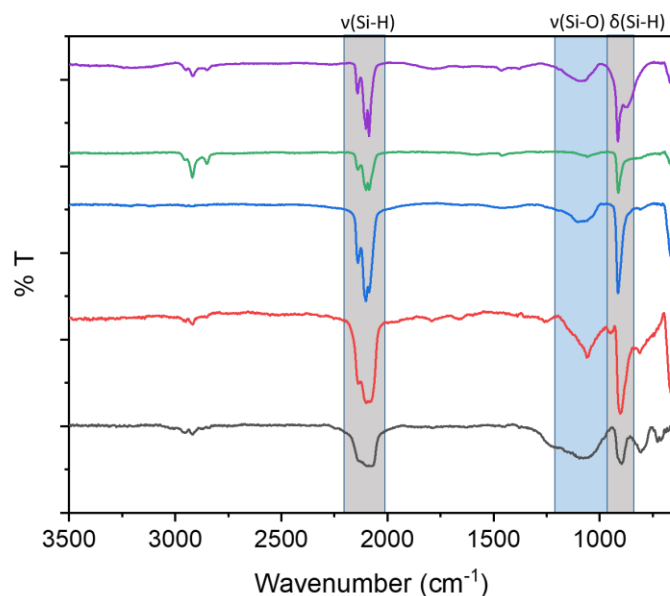


Figure 2-6. FTIR spectra for H-SiNPs annealed at 1500 °C (purple), 1400 °C (green), 1300 °C (blue), 1200 °C (red), and 1100 °C (black). The spectra show peaks associated with Si-H (highlighted in gray) and Si-O (highlighted in blue).

was fixed at 0.50. For small H-SiNPs ($d \sim 3$ and 6 nm), all components (including minor oxide contributions denoted in green) were fitted to a Voigt GL(30) line shape (70% Gaussian; 30% Lorentzian). The rationale for applying this fitting procedure lies in the nature of the NP sizes investigated. If NPs are small enough (<9 nm for the present SiNPs), a considerable number of atoms experience slightly different (disordered) chemical environments (See NMR discussion below) that lead to a distribution of binding energies and symmetric broadening that is Lorentzian in nature. As a result, the overall observed signal is dominated by a symmetric Gaussian/Lorentzian line shape. For the largest SiNPs ($d \sim 21$ and 64 nm), which represent bulk silicon (See XRD and NMR below), the spectral envelope was fitted using a Lorentzian asymmetric line shape $LA(a,b,n)$, where a and b define the asymmetry and n defines the Gaussian width. Similar procedures have been employed when fitting the Si 2p data of bulk crystalline silicon.⁷² The $d \sim 9$ nm H-SiNPs lie within an intermediate size regime, where it is possible to isolate the surface and core Si contributions to the Si 2p emission. The Si 2p spectrum of these H-SiNPs was fitted effectively by first applying the procedure noted for large NPs (highlighted in red in Figures 2-2 and 2-7a), and the remaining residual signal arising from surface atoms was fitted using a GL (30) line shape (highlighted in blue). Of important note,

the binding energy of the surface silicon species is shifted to higher energy as a result of electronegativity considerations arising because of bonding interactions with surface hydride moieties (i.e., SiH_x).

TEM imaging of H-SiNPs can be exceptionally challenging because of their limited electron contrast and poor solution processability. NP dimensions determined from bright-field TEM imaging (Figure 2-3 and 2-7) are summarized in Table 2-1. All H-SiNPs were imaged readily, with the exception of $d \sim 3$ nm H-SiNPs, which were agglomerated heavily. To determine the size of these NPs, it was necessary to render them solution processable by

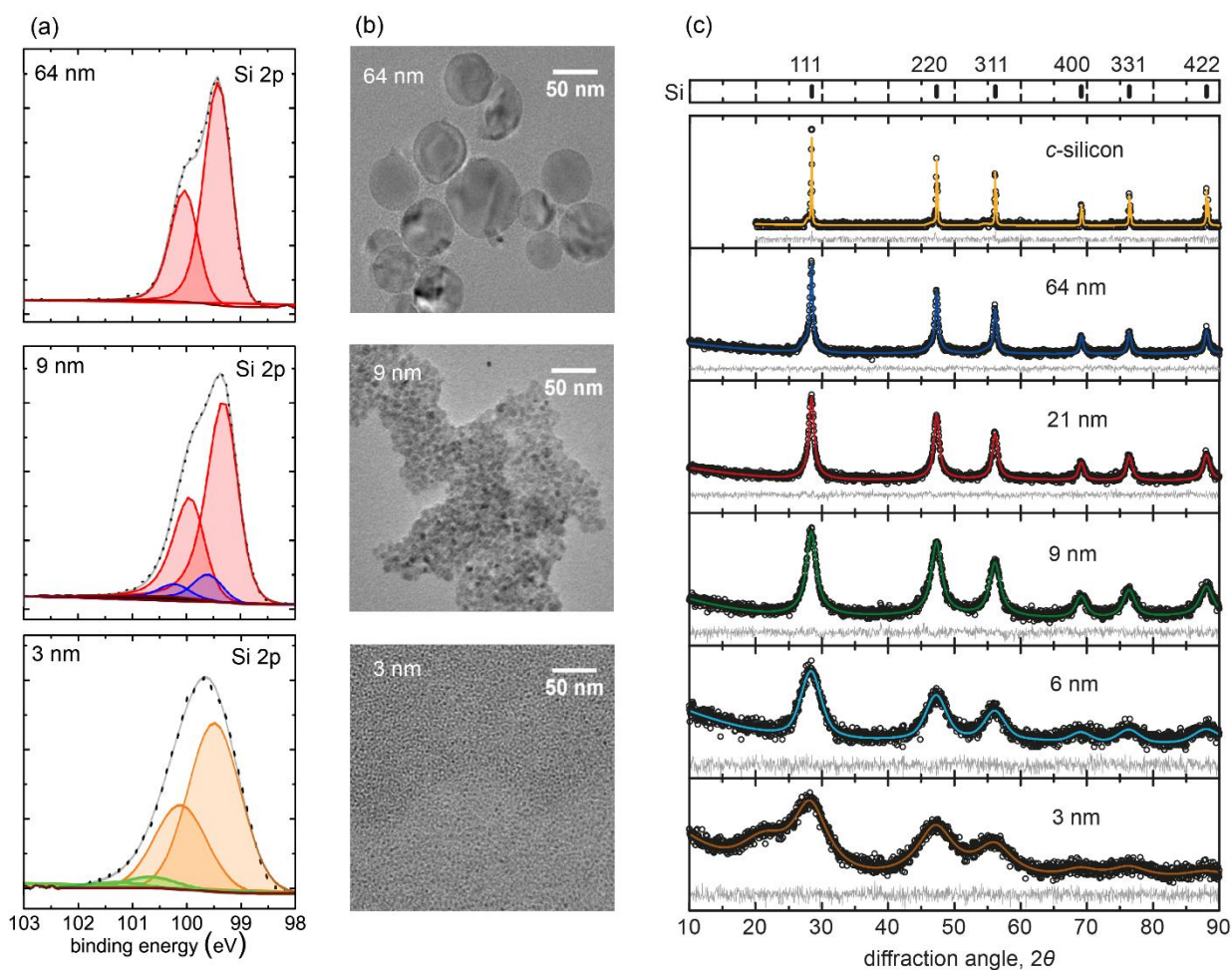


Figure 2-7. (a) High-resolution Si 2p XPS showing the $2p_{3/2}$ and $2p_{1/2}$ emission for 64, 9, and 3 nm H-SiNPs. The colored traces correspond to: gray = experimental data, dotted black = complete fit, red = crystalline core Si, blue = surface Si, orange = disordered Si, and green = Si oxides. (b) Bright-field TEM images of H-SiNPs ($d \sim 64$ and 9 nm) and dodecyl-SiNPs ($d \sim 3$ nm). (c) XRD patterns for $d \sim 64$ (blue), 21 (red), 9 (green), 6 (cyan), and 3 (brown) nm H-SiNPs, showing characteristic Si 111, 220, 311, 400, 331, and 422 reflections.

modifying their surfaces with dodecyl moieties using standard nonsize selective thermally induced hydrosilylation (Figure 2-7b); functionalized NPs obtained from the identical composites used to prepare those evaluated in our NMR studies showed a TEM-derived diameter of 3.5 ± 0.9 nm.

It is well-established that X-ray powder diffraction peak broadening provides an indirect method for approximating the nanocrystal/crystallite size, complementary to direct TEM imaging. After instrumental contributions are accounted for, only size and strain factors remain. It is possible to identify these contributions qualitatively by considering the dependence of peak broadening on diffraction angle; size-induced broadening follows a $1/\cos \theta$ relationship, while strain-induced broadening follows a $\tan \theta$ trend. For the present NPs, the broadening distribution (i.e., full-width at half maximum, FWHM) shows what is expected for size-induced broadening (Figure 2-8), with deviations arising from strain contributions being noted for smaller particles ($d \sim 3$ and 6 nm). In this context, the peak fits were refined appropriately by taking into account size-dependent strain contributions. The diffraction peak geometry was fitted successfully using a pseudo-Voigt function. A polynomial background also was included, and no overfitting (absolute correlation) was found for all polynomial terms. In addition, it was necessary to include a synthetic peak at 22° to describe effectively the peak shapes of the 3 nm particle diffraction pattern.

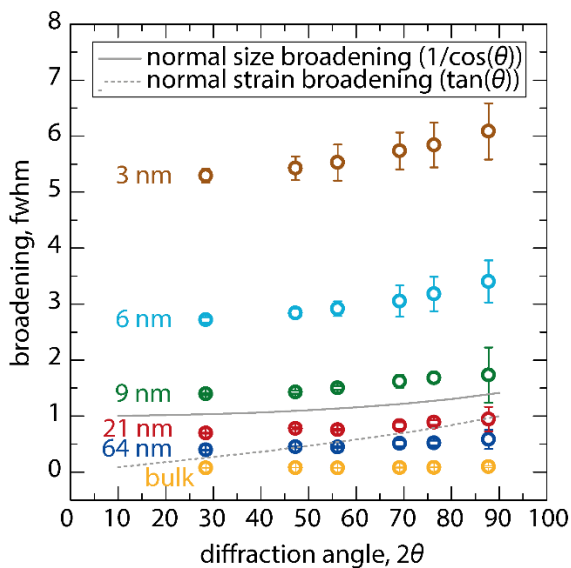


Figure 2-8. XRD Peak broadening distribution for nanocrystalline materials.

Finally, all diffraction data were analyzed using integral breadth, FWHM, and Lorentzian broadening methods (Table 2-1) that all assume a normal distribution of spherical crystallites.⁶⁸ A straightforward comparison of TEM and XRD derived data (Figure 2-7, Table 2-1) shows that the TEM determined dimensions of H-SiNPs are consistently larger; this is not surprising and is consistent with present XPS and NMR analyses, given that XRD peak broadening only gives a volume-average distribution of crystallite sizes that are routinely smaller than the size of the entire NP (i.e., XRD analyses only probe the crystalline portion of NPs).

To evaluate the H-SiNPs further, direct excitation (surface and core) and cross polarization (surface) ²⁹Si MAS NMR spectroscopy was employed. Figure 2-9 shows the direct ²⁹Si MAS NMR data, revealing a considerable evolution from ultrahigh resolution (1 ppm, FWHM) for microcrystalline silicon to a broad resonance spanning nearly 40 ppm, from -75 to -120 ppm, as the particle size shrinks to 3 nm. Peak positions and line widths in the ²⁹Si NMR spectra are consistent with size-dependent changes in the atomic and/or electronic structure of the NPs. The center-of-gravity chemical shift (δ_{cgs}) of amorphous silicon (*a*-Si) has been reported to be -41 ± 3 ppm (with a Gaussian-like resonance that spans 40 to -130 ppm); crystalline (*c*-Si) silicon appears at lower frequency (isotropic chemical shift, $\delta_{iso} = -80.9 \pm 1$ ppm; 1 ppm FWHM).⁸⁷⁻⁹⁰ In this context, we attribute the sharp resonance appearing at -81 ppm to *c*-Si (i.e., the material possesses a highly ordered structure); this feature shifts to lower frequency with decreasing particle dimensions from 44 μ m to 21 nm. As the NP size decreases to below 10 nm, a broad resonance emerges,

Table 2-2. List of Common ²⁹Si Chemical Shifts for Silicon Containing Materials

Bonding Environment	Chemical Shift (ppm)	Ref
Amorphous – SiO ₂	-110	4, 5
Quartz – SiO ₂	-107	
Cristobalite – SiO ₂	-109	
SiO ₅ / SiO ₆	-150 / -200	4
SiN ₄	-49 (⁴ Si) / -225 (⁶ Si)	4, 6
SiC ₄	-18	4
OSi-H _x / HO-Si(-OSiH _x) _x	-89 to -109	7, 8, 9
-SiH ₃ / -SiH ₂ / -SiH	-90 to -110	10,11
Molecular – H ₃ Si-SiH ₃ ; H ₂ Si(-SiH ₃) ₂ ; HSi(-SiH ₃) ₃ ; Si(-SiH ₃) ₄	-103 to -165	9, 12

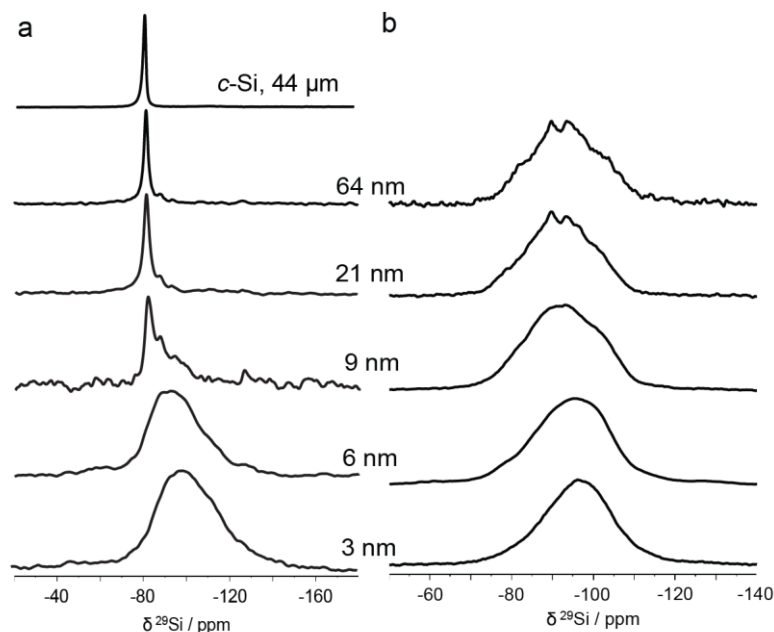


Figure 2-9. Direct (a) and CP (b) ^{29}Si MAS NMR spectra of H-SiNPs with varying particle diameter.

eventually replacing the sharp *c*-Si resonance that would be associated with highly-ordered silicon. We attribute this change in peak shape and breadth to an increased influence of surface states with decreasing NP size. Since the total surface areas of the NP increase as the dimensions decrease, the fraction of silicon atoms residing in disordered atomic positions increases (see below). These NP structural changes are manifested in the NMR because of the sensitivity of the ^{29}Si magnetic shielding to local atomic structure, such as variations in bond angles and lengths, defects caused by dangling bonds, variations in surface species (e.g., SiH_n , where $n = 1$ to 3), and/or combinations thereof, consistent with previous Raman³⁰ spectroscopy results. Magnetic shielding also can be influenced by the local electronic structure, which is discussed further below. These effects are not unique to SiNPs and have been reported for numerous nanomaterials, including InP, Zn_3P_2 , ZnSe, Cd, Na, Ag, Pb, etc.^{47, 91-99}

To elucidate further the origin of the apparent NP size dependent ^{29}Si chemical shift, line width, and shape, we employed a $^{29}\text{Si}[^1\text{H}]$ CP MAS NMR to interrogate silicon atoms selectively at the NP surface.^{78, 100} This experiment depends on dipole interactions between ^{29}Si and ^1H nuclei and enhances signals arising from ^{29}Si nuclei in close proximity to hydrogen atoms (i.e., directly bonded or through space; $\sim <10$ Å). All CP MAS NMR spectra (Figure 2-9b, Figure 2-10) are broad (i.e., -80 to -120 ppm) and featureless for the smallest

nanoparticles; features emerge as the NP size increases. Knowing that hydride moieties are present on the SiNP surfaces (FTIR; Figure 2-6), we attribute the main broad resonances to surface Si-H_x species that experience substantial structural variability (local disorder). It is reasonable to assume that the Si atomic positions at the NP surfaces are ill-defined (i.e., the structure lacks long-range periodicity) and exist in a distribution of chemical environments (vide supra); doubtless, the number of Si nuclei chemical environments is compounded by the presence of a distribution, however small it may be, of NP sizes in every sample (Table 2-1).^{54-56, 101-104}

Closer examination of the spectra obtained for the smallest NPs (d ~ 3 and 6 nm) reveals a broad, featureless, slightly asymmetric resonance centered at ~ -96 ppm. While crystalline and amorphous SiO₂ could appear within a similar chemical shift range ($\delta_{\text{iso}} \sim -110$ ppm),^{62, 105} our complementary XP analysis confirms that oxygen bonded silicon is small (~ 0.7 to 6 at%), and FTIR shows no evidence of Si-bonded hydroxyl groups (e.g., Si-OH). Hence, if present, we contend that surface oxides contribute negligibly to the NMR spectra (d ~ 6 to 64 nm), and these features result from SiH_x species (Table 2-2 provides a summary of common ²⁹Si chemical shifts). One interesting feature worth noting is the

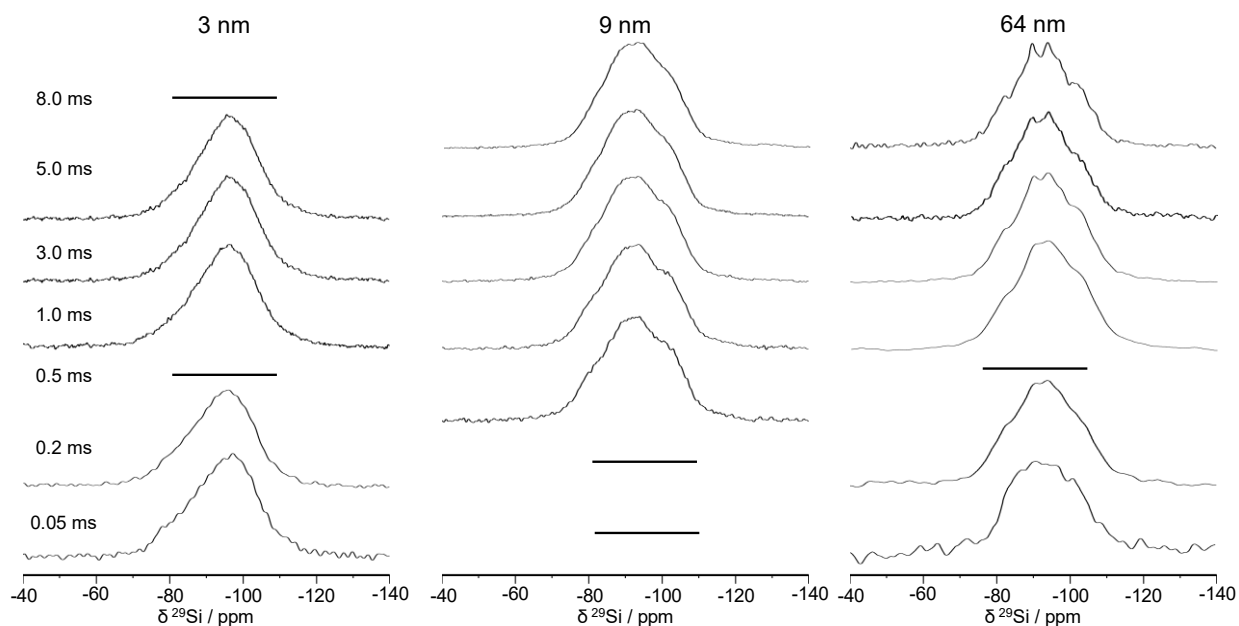


Figure 2-10. Contact time array for ²⁹Si CP MAS ranging from 0.05 to 8.0 ms for 3, 9, and 64 nm H-SiNPs.

slightly different features of the 3 nm particle when overlaying the direct and CP ^{29}Si NMR data. An extra signal from the direct ^{29}Si NMR spectrum appears between -100 and -120 ppm that does not have 1H 's nearby. This may be due to a small amount of the Si surface being oxidized ($<7\%$, SiO_x) or the electronic structure further impacting the chemical shift of these high surface area particles which have a bandgap of ~ 1.6 eV. As a control illustrating the impact of oxygen on the spectra of H-SiNPs, we purposefully oxidized a sample over a period of months, revealing the formation of SiO_2 (Figure 2-11), and analyzed the SiNPs pre- and post-NMR analysis using XPS and FTIR (Figure 2-12).

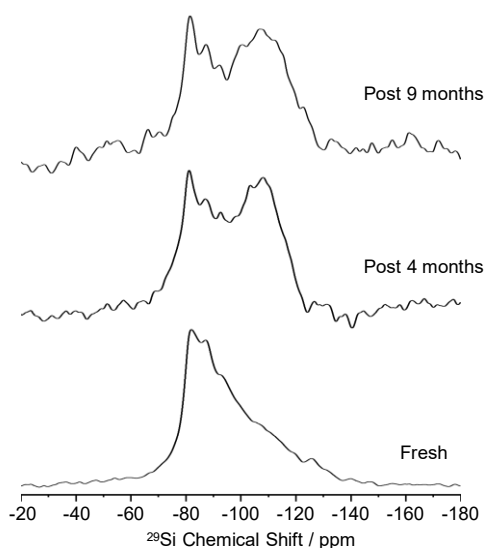


Figure 2-11. Silicon-29 NMR spectra for 9 nm H-SiNPs purposefully oxidized over a period of 9 months to indicate contamination of oxygen under ambient storage. Presence of Si-O species at δ_{iso} of ~ -110 ppm 4 and 9 months post-synthesis.

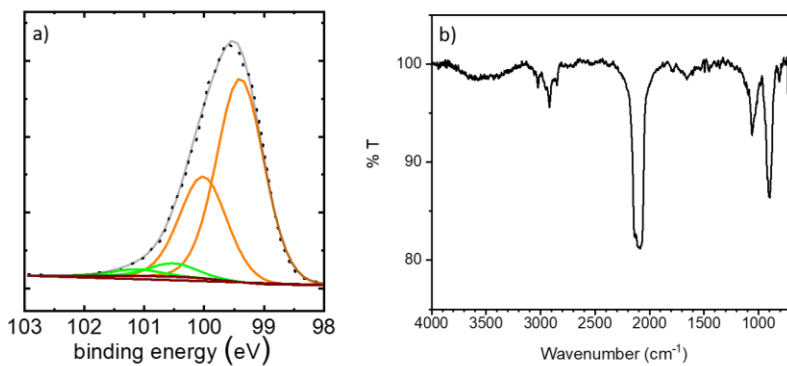


Figure 2-12. Sample of the post-NMR analysis of the H-SiNPs (6 nm) using (a) Si 2p high resolution XPS data (with only the $2p_{3/2}$ shown for clarity) and (b) FTIR spectra of 6 nm H-SiNPs.

Turning our attention to the largest NPs considered here ($d \sim 21$ and 64 nm), they too exhibit a broad resonance with two superimposed sharp features. These features emerge in the 2D $^{29}\text{Si}[^1\text{H}]$ HETCOR spectrum (Figure 2-13a) and in the CP MAS NMR data (Figures 2-13b and 2-10) with longer contact times. Closer examination of the ^{29}Si MAS NMR data (Figures 2-13b and 2-9a) also confirms two new features in low intensity. Their appearance and increased intensity, with longer mixing times, suggests the presence of an intermediate or sub-surface of quasi-ordered Si atoms. The ^{29}Si MAS NMR spectra of intermediate dimension of H-SiNPs ($d \sim 9$ nm) show evidence of these two extremes (Figures 2-9a), consistent with the presence of three structural regimes within the NPs: a crystalline core, a quasi-crystalline sub-surface, and a disordered surface (Figure 2-13c). Similar effects have been reported in other NPs, including CeO_2 and noble metal nanomaterials.^{99, 106}

Building on our understanding of the underlying structure of the presented H-SiNPs, we turned our attention to the NP size-dependence of the ^{29}Si chemical shift. A disturbance of the local nuclear electronic environment about a given nucleus typically manifests itself in a change of the observed chemical shift. The magnetic shielding interaction¹⁰⁷⁻¹⁰⁹ (chemical and/or Knight shift) could be responsible for the observed effect, depending upon the nanomaterial studied. Knight shifts dominate in metallic systems, while SiNP

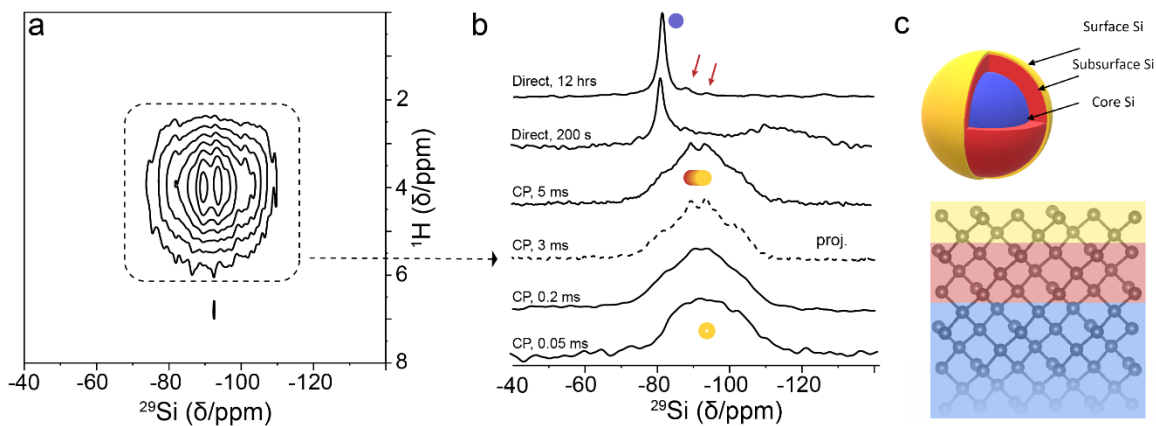


Figure 2-13. (a) Two-dimensional $^{29}\text{Si}[^1\text{H}]$ HETCOR MAS NMR spectra of 64 nm H-SiNPs with a mixing time of 3.0 ms. (b) Overlay of direct excitation ^{29}Si MAS NMR and $^{29}\text{Si}[^1\text{H}]$ CP MAS NMR with variable mixing times for 64 nm H-SiNP to illustrate NMR features corresponding to H-SiNP surface (yellow), subsurface (red), and core (blue) signatures. Red arrows indicate sharper subsurface NMR features present in the direct excitation ^{29}Si MAS NMR, as seen with $^{29}\text{Si}[^1\text{H}]$ CP MAS NMR with a mixing time of 3.0 ms. Direct excitation ^{29}Si MAS NMR with a recycle delay of 200 s was used to artificially inflate the surface resonance still present at shorter recycle delays. (c) Artistic schematic of a H-SiNP indicating the silicon surface, subsurface, and core with a model of the first ten atomic layers of H-SiNPs.

semiconductors are impacted by diamagnetic and paramagnetic chemical shielding contributions.^{47, 109} Changes in the paramagnetic contributions can be rationalized by the size-dependence of the electronic excitation energy (ΔE),^{98, 109} whereby decreasing the NP size causes an increase in band gap (as the case for the SiNPs considered here). An increase in ΔE causes greater magnetic shielding and the ^{29}Si chemical shifts appearing at lower frequencies (Figure 2-14a).^{47, 95, 98, 109-111} This general reasoning is invoked often when considering the NMR spectra of nanomaterials originating from molecular systems that have appropriate molecular orbital symmetries.^{107, 108} Therefore, the changes in δ_{cgs} observed for the samples studied here appear to be related to the size-dependent electronic properties of SiNPs and are expected to be continuous until the band gap reaches its bulk value of 1.12 eV (δ_{iso} of $d \sim 64$ nm \approx bulk c -Si).

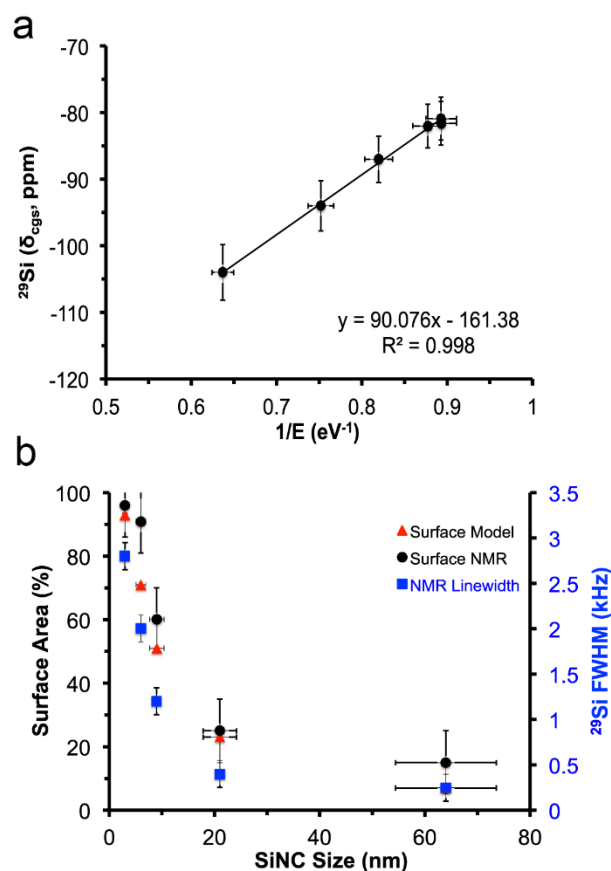


Figure 2-14. (a) Relationship of δ_{cgs} as a function of inverse bandgap of SiNPs. (b) Surface/subsurface area % for NMR experiments (black) and model (red) and ^{29}Si full-width at half maximum (FWHM, blue) with increasing H-SiNP size. As the H-SiNPs move from a disordered to an ordered system, the corresponding surface area % and line width decreases as NP size increases.

Another notable feature of the presented ^{29}Si NMR spectra is the broad underlying feature, whose intensity is inversely related to NP size for dimensions ≤ 21 nm (Table 2-3). With decreasing NP diameter, the relative contribution from surface nuclei increases such that the contribution from the ordered core becomes minor (even negligible) for the smallest NPs; long-range order simply is not possible within the confines of such small NP. Nevertheless, the factors discussed previously still are expected to play a role and give rise to a range of chemical shifts for nuclei at or near the surface. These observations are consistent with the XRD data (Figure 2-7c): reflections broaden with decreasing size, as expected with a reduction in the number of repeating units in the NP, which results in structural strain and poorer coherence in the diffraction of the material.¹¹⁴

To investigate the impact of local structure on line width, we modeled and estimated (from the ^{29}Si MAS NMR data, Figure 2-15) the surface/subsurface volume as a function of particle size (Figure 2-14b and Table 2-3). The number of surface Si atoms on the H-SiNPs was calculated as a function of size based on an assumed icosahedral shape for all sizes except the 64 nm (where a spherical shape was invoked).^{112, 113} This allowed us to estimate the number of surface/sub-surface atoms, assuming four layers (five layers total, including the surface), by removing one layer at a time from the surface; the values determined from this analysis are summarized in Table 2-4. Combining these estimates with the XRD data allows an assessment of the reduction in the size of the ordered bulk lattice with the formation of a disordered surface. With increasing surface area (decreasing NP size), the

Table 2-3. Experimental ^{29}Si MAS NMR FWHM, Nuclear Spin-Lattice Relaxation Times (T_1) and Surface Fraction Deconvolutions of the H-SiNPs with Varying Particle Diameters

Particle Size /nm	FWHM ($\pm 10\%$) [†] kHz	H-SiNC, T_1 /min		^{29}Si Surface Fraction /%	
		Surface	Core	NMR ^a ($\pm 10\%$)	Model ^b
64	0.3	0.9 ± 0.1	158.2 ± 15.0	15	7
21	0.5	3.8 ± 0.4	102.1 ± 10.1	25	23
9	1.2	1.3 ± 0.1	6.9 ± 0.7	60	51
6	2.1	$5.8 \pm 0.6^*$		91	71
3	2.8	$1.4 \pm 0.1^*$		96	93

[†] FWHM reported for the most intense resonances * Experimental data were best represented using a single exponential (i.e., only a single T_1 to describe the 3 and 6 nm H-SiNPs). ^a NMR surface fraction estimates were based on fitting of direct NMR data (Figure 2-15). ^b Model surface fraction estimates using geometric calculations based on the SiNP structure described by Zhao et al. and Avramov et al. and informed by Si lattice parameters.^{112, 113}

relative contribution of the ordered core atoms to the NMR spectra at ~ -81 ppm is reduced and no longer resolved for 3 and 6 nm NPs. These observations are consistent with the XRD and TEM particle size determination. Considering that the unit cell length for crystalline silicon is 5.4 Å and the smallest particle investigated here has a diameter of 35 Å, only about six unit cell lengths would be needed for the particle cross section. This reinforces the complementary nature of both XRD (long-range) and NMR (short-range) for materials that exhibit both structural order and local disorder. While we cannot discount the influence of quantum confinement, computational studies show that oxide-embedded 3 nm SiNPs have significant strain throughout the particle.²⁷ It would follow that this strain would manifest itself as defects, including distorted Si—Si bonds, dangling bonds, and coordination defects that are delocalized around the surface of the SiNP, as outlined by Lee et al.²⁶ These defects limit long-range order in the nanoparticle, as is evidenced by the extreme broadening of the XRD reflections and NMR spectra. A Scherrer analysis of the XRD reveals an average crystallite size of 1.2 nm for 3 nm SiNPs, which correlates to just under three Si unit cell lengths¹¹⁵, lacking long-range structure.

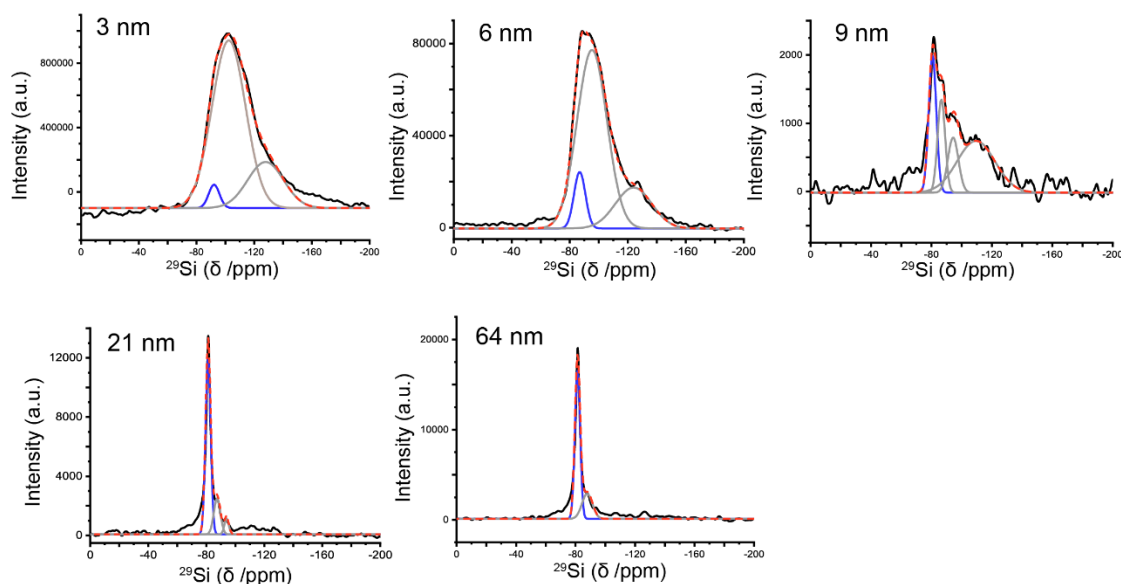


Figure 2-15. Estimated core (blue) vs surface/subsurface (gray) fractions from ^{29}Si MAS NMR (Bloch) using appropriate delay times (i.e., $5 \times T_1$). The black line is the experimental data and the red dashed line is the fitting envelope.

Table 2-4. Calculated Fraction of Surface, Sub-surface and Core Si Species Based on the Model by Zhao et al. and Avramov et al.^{2,3}

Particle Size /nm	Estimated % Fraction of atoms in each structural component		
	Surface	Subsurface	Core
64	1	4	95
21	5	17	78
9	11	37	52
6	17	50	33
3	27	62	11

Further exemplifying the combined benefits of preparing well-defined H-SiNPs and evaluating them using NMR spectroscopy, the determination of the nuclear spin lattice relaxation yields an intriguing size dependence (Table 2-3). As expected, smaller NPs ($d \sim 3$ and 6 nm) exhibit shorter T_1 values,^{9, 48, 53} with a monoexponential longitudinal magnetization recovery; larger H-SiNPs ($d \sim 9, 21,$ and 64 nm) show biexponential recovery (Figure 2-5). We assign the rapid (i.e., minutes) and slow (i.e., hours) T_1 components of the large NPs to surface and core ^{29}Si species, respectively. To elucidate the surface of the larger particles further, one may select a relaxation time (~ 200 s) that enhances the signal from the surface/subsurface nuclei that have a much shorter T_1 relaxation time (on the order of minutes) than the core nuclei. The differences in regard to surface vs. core arise due to the two chemically distinct environments: the surface being disordered allows for the ability of more motion and larger distribution of Si environments, improving the efficiency in relaxation; while the core aligns itself into a diamond-like structure with a rigid lattice, impeding relaxation as the particle size increases. The presence of unpaired electrons on the surface (i.e., dangling bonds) would cause a reduction in ^{29}Si spin-lattice relaxation, therefore, as the size of the NP increases, the core nuclei become increasingly distant from the surface, resulting in an increase in the experimentally determined nuclear T_1 .

2.4 Conclusions

In this work, we present a state-of-the-art multifaceted approach to characterizing and understanding the atomic-level structure of H-SiNPs. Using a combination of XPS, bright field TEM, XRD, FTIR, and ^{29}Si MAS NMR spectroscopy, we probe the complex surface and core

structure of H-SiNPs. Solid-state NMR methods allowed us to interrogate further a series of H-SiNPs with dimensions in the range of 3 to 64 nm, where three unique structural environments (surface, subsurface, and core) were identified. The surface silicon atoms are found between -80 to -120 ppm, while core Si, which becomes observable in H-SiNPs > 6 nm, exhibits chemical shifts similar to that for bulk silicon. Based upon the present experimental data, strain in the long-range periodicity emerges below 9 nm particles, suggesting a critical size-junction; however, the NMR chemical shifts are dominated by changes to the electronic structure of H-SiNPs. Are SiNPs crystalline to the core? Generally yes, but below 3 nm, the definition of order vs disorder becomes unclear since the number of repeating unit cells becomes limited, further straining the surface structure that makes up the bulk of the particle. The structural insight provided by this investigation provides invaluable information, key to the rational design and development of SiNP-based applications, including but not limited to, sensors, battery electrodes, optical materials, and contrast agents.

2.5 References

1. Union, T. E., Ed. Publications Office of the European Union: Official Journal of the European Union, 2017; Vol. 2017/1975, p 3.
2. Liu, J.; Erogbogbo, F.; Yong, K.-T.; Ye, L.; Liu, J.; Hu, R.; Chen, H.; Hu, Y.; Yang, Y.; Yang, J.; Roy, I.; Karker, N. A.; Swihart, M. T.; Prasad, P. N., Assessing Clinical Prospects of Silicon Quantum Dots: Studies in Mice and Monkeys. *ACS Nano* **2013**, *7*, 7303-7310.
3. Park, J. H.; Gu, L.; von Maltzahn, G.; Ruoslahti, E.; Bhatia, S. N.; Sailor, M. J., Biodegradable Luminescent Porous Silicon Nanoparticles for in vivo Applications. *Nature Mater* **2009**, *8*, 331-6.
4. Mobarok, M. H.; Purkait, T. K.; Islam, M. A.; Miskolzie, M.; Veinot, J. G. C., Instantaneous Functionalization of Chemically Etched Silicon Nanocrystal Surfaces. *Angew. Chem., Int. Ed.* **2017**, *56*, 6073-6077.
5. Islam, M. A.; Mobarok, M. H.; Sinelnikov, R.; Purkait, T. K.; Veinot, J. G. C., Phosphorus Pentachloride Initiated Functionalization of Silicon Nanocrystals. *Langmuir* **2017**, *33*, 8766-8773.
6. Mastrorardi, M. L.; Maier-Flaig, F.; Faulkner, D.; Henderson, E. J.; Kübel, C.; Lemmer, U.; Ozin, G. A., Size-Dependent Absolute Quantum Yields for Size-Separated Colloidally-Stable Silicon Nanocrystals. *Nano Lett* **2012**, *12*, 337-342.
7. Bhattacharjee, S.; Rietjens, I. M. C. M.; Singh, M. P.; Atkins, T. M.; Purkait, T. K.; Xu, Z.; Regli, S.; Shukaliak, A.; Clark, R. J.; Mitchell, B. S.; Alink, G. M.; Marcelis, A. T. M.; Fink, M. J.; Veinot, J. G. C.; Kauzlarich, S. M.; Zuilhof, H., Cytotoxicity of Surface-Functionalized Silicon and Germanium Nanoparticles: The Dominant Role of Surface Charges. *Nanoscale* **2013**, *5*, 4870-4883.
8. Erogbogbo, F.; Yong, K.-T.; Roy, I.; Hu, R.; Law, W.-C.; Zhao, W.; Ding, H.; Wu, F.; Kumar, R.; Swihart, M. T.; Prasad, P. N., In vivo Targeted Cancer Imaging, Sentinel Lymph Node Mapping and Multi-Channel Imaging with Biocompatible Silicon Nanocrystals. *ACS Nano* **2011**, *5*, 413-423.
9. Cassidy, M. C.; Chan, H. R.; Ross, B. D.; Bhattacharya, P. K.; Marcus, C. M., In vivo Magnetic Resonance Imaging of Hyperpolarized Silicon Particles. *Nature Nanotechnol.* **2013**, *8*, 363.
10. Tu, C.; Ma, X.; House, A.; Kauzlarich, S. M.; Louie, A. Y., PET Imaging and Biodistribution of Silicon Quantum Dots in Mice. *ACS Med. Chem. Lett.* **2011**, *2*, 285-288.

11. Liu, X.; Zhao, S.; Gu, W.; Zhang, Y.; Qiao, X.; Ni, Z.; Pi, X.; Yang, D., Light-Emitting Diodes Based on Colloidal Silicon Quantum Dots with Octyl and Phenylpropyl Ligands. *ACS Appl. Mater. Interfaces* **2018**, *10*, 5959-5966.
12. Dutta, M.; Thirugnanam, L.; Van Trinh, P.; Fukata, N., High Efficiency Hybrid Solar Cells Using Nanocrystalline Si Quantum Dots and Si Nanowires. *ACS Nano* **2015**, *9*, 6891-6899.
13. Svrcek, V.; McDonald, C.; Lozac'h, M.; Tayagaki, T.; Koganezawa, T.; Miyadera, T.; Mariotti, D.; Matsubara, K., Stable Ultrathin Surfactant-Free Surface-Engineered Silicon Nanocrystal Solar Cells Deposited at Room Temperature. *Energy Sci. Eng.* **2017**, *5*, 184-193.
14. Zhao, S.; Pi, X., Colloidal Silicon Quantum Dots and Solar Cells. In *Handbook of Photovoltaic Silicon*, Yang, D., Ed. Springer Berlin Heidelberg: Berlin, Heidelberg, 2017; pp 1-27.
15. Gonzalez, C. M.; Veinot, J. G. C., Silicon Nanocrystals for the Development of Sensing Platforms. *J. Mater. Chem. C* **2016**, *4*, 4836-4846.
16. Meinardi, F.; Ehrenberg, S.; Dharmo, L.; Carulli, F.; Mauri, M.; Bruni, F.; Simonutti, R.; Kortshagen, U.; Brovelli, S., Highly Efficient Luminescent Solar Concentrators based on Earth-Abundant Indirect-Bandgap Silicon Quantum Dots. *Nature Photonics* **2017**, *11*, 177.
17. Chan, C. K.; Peng, H. L.; Liu, G.; McIlwrath, K.; Zhang, X. F.; Huggins, R. A.; Cui, Y., High-Performance Lithium Battery Anodes using Silicon Nanowires. *Nature Nanotechnol* **2008**, *3*, 31-35.
18. Kim, H.; Seo, M.; Park, M. H.; Cho, J., A Critical Size of Silicon Nano-Anodes for Lithium Rechargeable Batteries. *Angew. Chem., Int. Ed.* **2010**, *49*, 2146-9.
19. Su, X.; Wu, Q.; Li, J.; Xiao, X.; Lott, A.; Lu, W.; Sheldon Brian, W.; Wu, J., Silicon-Based Nanomaterials for Lithium-Ion Batteries: A Review. *Adv. Energy Mater.* **2014**, *4*, 1300882.
20. Dohnalova, K.; Gregorkiewicz, T.; Kusova, K., Silicon Quantum Dots: Surface Matters. *J Phys Condens Matter* **2014**, *26*, 173201.
21. Chan, C. K.; Ruffo, R.; Hong, S. S.; Cui, Y., Surface Chemistry and Morphology of the Solid Electrolyte Interphase on Silicon Nanowire Lithium-ion Battery Anodes. *J Power Sources* **2009**, *189*, 1132-1140.
22. Dasog, M.; Yang, Z. Y.; Regli, S.; Atkins, T. M.; Faramus, A.; Singh, M. P.; Muthuswamy, E.; Kauzlarich, S. M.; Tilley, R. D.; Veinot, J. G. C., Chemical Insight into the Origin of Red and Blue Photoluminescence Arising from Freestanding Silicon Nanocrystals. *ACS Nano* **2013**, *7*, 2676-2685.
23. Dasog, M.; De los Reyes, G. B.; Titova, L. V.; Hegmann, F. A.; Veinot, J. G., Size vs Surface: Tuning the Photoluminescence of Freestanding Silicon Nanocrystals across the Visible Spectrum via Surface Groups. *ACS Nano* **2014**, *8*, 9636-48.
24. Dasog, M.; Bader, K.; Veinot, J. G. C., Influence of Halides on the Optical Properties of Silicon Quantum Dots. *Chem. Mater.* **2015**, *27*, 1153-1156.
25. Wheeler, L. M.; Anderson, N. C.; Palomaki, P. K. B.; Blackburn, J. L.; Johnson, J. C.; Neale, N. R., Silyl Radical Abstraction in the Functionalization of Plasma-Synthesized Silicon Nanocrystals. *Chem. Mater.* **2015**, *27*, 6869-6878.
26. Lee, B. G.; Hiller, D.; Luo, J. W.; Semonin, O. E.; Beard, M. C.; Zacharias, M.; Stradins, P., Strained Interface Defects in Silicon Nanocrystals. *Adv. Funct. Mater.* **2012**, *22*, 3223-3232.
27. Kleovoulou, K.; Kelires, P. C., Stress State of Embedded Si Nanocrystals. *Phys. Rev. B* **2013**, *88*, 085424.
28. Zhou, Z. Y.; Brus, L.; Friesner, R., Electronic Structure and Luminescence of 1.1- and 1.4-nm Silicon Nanocrystals: Oxide Shell Versus Hydrogen Passivation. *Nano Lett.* **2003**, *3*, 163-167.
29. Shu, Y. N.; Kortshagen, U. R.; Levine, B. G.; Anthony, R. J., Surface Structure and Silicon Nanocrystal Photoluminescence: The Role of Hypervalent Silyl Groups. *J. Phys. Chem. C* **2015**, *119*, 26683-26691.
30. Veprek, S.; Sarott, F.; Iqbal, Z., Effect of Grain Boundaries on the Raman Spectra, Optical Absorption, and Elastic Light Scattering in Nanometer-sized Crystalline Silicon. *Phys. Rev. B Condens. Matter* **1987**, *36*, 3344-3350.
31. Nikitin, T.; Khriachtchev, L., Optical and Structural Properties of Si Nanocrystals in SiO₂ Films. *Nanomaterials* **2015**, *5*, 614-655.
32. Yogi, P.; Tanwar, M.; Saxena, S. K.; Mishra, S.; Pathak, D. K.; Chaudhary, A.; Sagdeo, P. R.; Kumar, R., Quantifying the Short-Range Order in Amorphous Silicon by Raman Scattering. *Anal. Chem.* **2018**, *90*, 8123-8129.
33. Marra, D. C.; Edelberg, E. A.; Naone, R. L.; Aydil, E. S., Silicon Hydride Composition of Plasma-Deposited Hydrogenated Amorphous and Nanocrystalline Silicon Films and Surfaces. *J. Vac. Sci. Technol. A* **1998**, *16*, 3199-3210.

34. Mangolini, L.; Kortshagen, U., Plasma-Assisted Synthesis of Silicon Nanocrystal Inks. *Adv. Mater.* **2007**, *19*, 2513-2519.
35. Jariwala, B. N.; Kramer, N. J.; Petcu, M. C.; Bobela, D. C.; Sanden, M. C. M. v. d.; Stradins, P.; Ciobanu, C. V.; Agarwal, S., Surface Hydride Composition of Plasma-Synthesized Si Nanoparticles. *J. Phys. Chem. C* **2011**, *115*, 20375-20379.
36. Zipoli, F.; Bernasconi, M., Ab initio Simulation of the Grafting of Phenylacetylene on Hydrogenated Surfaces of Crystalline Silicon Catalyzed by a Lewis Acid. *J. Phys. Chem. B* **2006**, *110*, 23403-23409.
37. Hua, F.; Swihart, M. T.; Ruckenstein, E., Efficient Surface Grafting of Luminescent Silicon Quantum Dots by Photoinitiated Hydrosilylation. *Langmuir* **2005**, *21*, 6054-6062.
38. Hua, F.; Erogbogbo, F.; Swihart, M. T.; Ruckenstein, E., Organically Capped Silicon Nanoparticles with Blue Photoluminescence Prepared by Hydrosilylation Followed by Oxidation. *Langmuir* **2006**, *22*, 4363-4370.
39. Giuliani, J. R.; Harley, S. J.; Carter, R. S.; Power, P. P.; Augustine, M. P., Using Liquid and Solid-State NMR and Photoluminescence to Study the Synthesis and Solubility Properties of Amine Capped Silicon Nanoparticles. *Solid State Nucl. Magnet. Reson.* **2007**, *32*, 1-10.
40. Shiohara, A.; Prabakar, S.; Faramus, A.; Hsu, C. Y.; Lai, P. S.; Northcote, P. T.; Tilley, R. D., Sized Controlled Synthesis, Purification, and Cell Studies with Silicon Quantum Dots. *Nanoscale* **2011**, *3*, 3364-3370.
41. Zou, J.; Kauzlarich, S. M., Functionalization of Silicon Nanoparticles via Silanization: Alkyl, Halide and Ester. *J. Cluster Sci.* **2008**, *19*, 341-355.
42. Ahire, J. H.; Wang, Q.; Coxon, P. R.; Malhotra, G.; Brydson, R.; Chen, R.; Chao, Y., Highly Luminescent and Nontoxic Amine-Capped Nanoparticles from Porous Silicon: Synthesis and their use in Biomedical Imaging. *ACS Applied Mater. & Inter.* **2012**, *4*, 3285-3292.
43. Biesta, W.; van Lagen, B.; Gevaert, V. S.; Marcelis, A. T. M.; Paulusse, J. M. J.; Nielen, M. W. F.; Zuilhof, H., Preparation, Characterization, and Surface Modification of Trifluoroethyl Ester-Terminated Silicon Nanoparticles. *Chem. Mater.* **2012**, *24*, 4311-4318.
44. Mayeri, D.; Phillips, B. L.; Augustine, M. P.; Kauzlarich, S. M., NMR Study of the Synthesis of Alkyl-Terminated Silicon Nanoparticles from the Reaction of SiCl₄ with the Zintl Salt, NaSi. *Chem. Mater.* **2001**, *13*, 765-770.
45. Baldwin, R. K.; Pettigrew, K. A.; Ratai, E.; Augustine, M. P.; Kauzlarich, S. M., Solution Reduction Synthesis of Surface Stabilized Silicon Nanoparticles. *Chem. Commun.* **2002**, *17*, 1822-1823.
46. Carter, R. S.; Harley, S. J.; Power, P. P.; Augustine, M. P., Use of NMR Spectroscopy in the Synthesis and Characterization of Air- and Water-Stable Silicon Nanoparticles from Porous Silicon. *Chem. Mater.* **2005**, *17*, 2932-2939.
47. Yesinowski, J. P., Solid-State NMR of Inorganic Semiconductors. In *Solid State NMR*, Chan, J. C. C., Ed. Springer Berlin Heidelberg: Berlin, Heidelberg, 2012; pp 229-312.
48. Atkins, T. M.; Cassidy, M. C.; Lee, M.; Ganguly, S.; Marcus, C. M.; Kauzlarich, S. M., Synthesis of Long T₁ Silicon Nanoparticles for Hyperpolarized ²⁹Si Magnetic Resonance Imaging. *ACS Nano* **2013**, *7*, (2), 1609-1617.
49. Neiner, D.; Kauzlarich, S. M., Hydrogen-Capped Silicon Nanoparticles as a Potential Hydrogen Storage Material: Synthesis, Characterization, and Hydrogen Release. *Chem. Mater.* **2010**, *22*, (2), 487-493.
50. El-Demellawi, J. K.; Holt, C. R.; Abou-Hamad, E.; Al-Talla, Z. A.; Saih, Y.; Chaieb, S., Room-Temperature Reactivity Of Silicon Nanocrystals With Solvents: The Case of Ketone and Hydrogen Production From Secondary Alcohols: Catalysis? *ACS Applied Mater. Inter.* **2015**, *7*, 13794-13800.
51. Kravitz, K.; Kamyshny, A.; Gedanken, A.; Magdassi, S., Solid State Synthesis of Water-Dispersible Silicon Nanoparticles from Silica Nanoparticles. *J. Solid State Chem.* **2010**, *183*, 1442-1447.
52. Kolyagin, Y. G.; Zakharov, V. N.; Yatsenko, A. V.; Aslanov, L. A., Studies of Silicon Nanocluster Ligand Coating by Solid-State NMR. *Russian Chem. Bulle.* **2015**, *64*, 1829-1832.
53. Aptekar, J. W.; Cassidy, M. C.; Johnson, A. C.; Barton, R. A.; Lee, M.; Ogier, A. C.; Vo, C.; Anahtar, M. N.; Ren, Y.; Bhatia, S. N.; Ramanathan, C.; Cory, D. G.; Hill, A. L.; Mair, R. W.; Rosen, M. S.; Walsworth, R. L.; Marcus, C. M., Silicon Nanoparticles as Hyperpolarized Magnetic Resonance Imaging Agents. *ACS Nano* **2009**, *3*, 4003-4008.
54. Faulkner, A. R.; DiVerdi, A. J.; Yang, Y.; Kobayashi, T.; Maciel, E. G., The Surface of Nanoparticle Silicon as Studied by Solid-State NMR. *Materials* **2013**, *6*, 18-46.
55. Lee, D.; Kaushik, M.; Coustel, R.; Chenavier, Y.; Chanal, M.; Bardet, M.; Dubois, L.; Okuno, H.; Rochat, N.; Duclairor, F.; Mouesca, J. M.; De Paëpe, G., Solid-State NMR and DFT Combined for the Surface Study of Functionalized Silicon Nanoparticles. *Chemistry – A European Journal* **2015**, *21*, 16047-16058.

56. Hanrahan, M. P.; Fought, E. L.; Windus, T. L.; Wheeler, L. M.; Anderson, N. C.; Neale, N. R.; Rossini, A. J., Characterization of Silicon Nanocrystal Surfaces by Multidimensional Solid-State NMR Spectroscopy. *Chem. Mater.* **2017**, *29*, 10339-10351.
57. Coleman, N. R. B.; Morris, M. A.; Spalding, T. R.; Holmes, J. D., The Formation of Dimensionally Ordered Silicon Nanowires within Mesoporous Silica. *J. Amer. Chem. Soc.* **2001**, *123*, 187-188.
58. Davidowski, S. K.; Holland, G. P., Solid-State NMR Characterization of Mixed Phosphonic Acid Ligand Binding and Organization on Silica Nanoparticles. *Langmuir* **2016**, *32*, 3253-3261.
59. Lafon, O.; Thankamony, A. S. L.; Kobayashi, T.; Carnevale, D.; Vitzthum, V.; Slowing, I. I.; Kandel, K.; Vezin, H.; Amoureux, J.-P.; Bodenhausen, G.; Pruski, M., Mesoporous Silica Nanoparticles Loaded with Surfactant: Low Temperature Magic Angle Spinning ^{13}C and ^{29}Si NMR Enhanced by Dynamic Nuclear Polarization. *J. Phys. Chem. C* **2013**, *117*, 1375-1382.
60. Sugiyama, Y.; Okamoto, H.; Mitsuoka, T.; Morikawa, T.; Nakanishi, K.; Ohta, T.; Nakano, H., Synthesis and Optical Properties of Monolayer Organosilicon Nanosheets. *J. Amer. Chem. Soc.* **2010**, *132*, 5946-5947.
61. Helbich, T.; Lyuleeva, A.; Höhle, I. M. D.; Marx, P.; Scherf, L. M.; Kehrle, J.; Fässler, T. F.; Lugli, P.; Rieger, B., Radical-Induced Hydrosilylation Reactions for the Functionalization of Two-Dimensional Hydride Terminated Silicon Nanosheets. *Chem. – A Euro. J.* **2016**, *22*, 6194-6198.
62. Mackenzie, K.; Smith, M., Chapter 4 - ^{29}Si NMR. In *Pergamon Materials Series*, MacKenzie, K. J. D.; Smith, M. E., Eds. Pergamon: 2002; Vol. 6, pp 201-268.
63. Takeuchi, Y.; Takayama, T., ^{29}Si NMR Spectroscopy of Organosilicon Compounds. In *The Chemistry of Organic Silicon Compounds*, 2003; pp 267-354.
64. Wrackmeyer, B., Applications of ^{29}Si NMR Parameters. In *Annual Reports on NMR Spectroscopy*, Webb, G. A., Ed. Academic Press: 2006; Vol. 57, pp 1-49.
65. Harris, R. K.; Kimber, B. J., ^{29}Si NMR as a Tool for Studying Silicones. *Applied Spectroscopy Reviews* **2007**, *10*, 117-137.
66. Collins, W. T. F., C. L. Condensed Soluble Hydrogensilsesquioxane Resin. US3615272A, 1971.
67. Hessel, C. M.; Henderson, E. J.; Veinot, J. G. C., Hydrogen Silsesquioxane: A Molecular Precursor for Nanocrystalline Si-SiO₂ Composites and Freestanding Hydride-Surface-Terminated Silicon Nanoparticles. *Chem. Mater.* **2006**, *18*, (26), 6139-6146.
68. Barr, T. L.; Seal, S., Nature of the use of Adventitious Carbon as a Binding Energy Standard. *J. Vac. Sci. Tech. A* **1995**, *13*, 1239-1246.
69. Payne, B. P.; Biesinger, M. C.; McIntyre, N. S., The Study of Polycrystalline Nickel Metal Oxidation by Water Vapour. *J. Elec. Spectros. Rel. Phen.* **2009**, *175*, 55-65.
70. Sublemontier, O.; Nicolas, C.; Aureau, D.; Patanen, M.; Kintz, H.; Liu, X.; Gaveau, M.-A.; Le Garrec, J.-L.; Robert, E.; Barreda, F.-A.; Etcheberry, A.; Reynaud, C.; Mitchell, J. B.; Miron, C., X-Ray Photoelectron Spectroscopy of Isolated Nanoparticles. *J. Phys. Chem. Lett.* **2014**, *5*, 3399-3403.
71. Plymale, N. T.; Dasog, M.; Brunschwig, B. S.; Lewis, N. S., A Mechanistic Study of the Oxidative Reaction of Hydrogen-Terminated Si(111) Surfaces with Liquid Methanol. *J. Phys. Chem. C* **2017**, *121*, 4270-4282.
72. Yang, Z. Y.; Iqbal, M.; Dobbie, A. R.; Veinot, J. G. C., Surface-Induced Alkene Oligomerization: Does Thermal Hydrosilylation Really Lead to Monolayer Protected Silicon Nanocrystals? *J. Amer. Chem. Soc.* **2013**, *135*, 17595-17601.
73. Bruker AXS (2008): TOPAS V4: General Profile and Structure Analysis Software for Powder Diffraction Data. - User's Manual, Bruker AXS, Karlsruhe, Germany.
74. Bennett, A. E.; Rienstra, C. M.; Auger, M.; Lakshmi, K. V.; Griffin, R. G., Heteronuclear Decoupling in Rotating Solids. *J. Chem. Phys.* **1995**, *103*, 6951-6958.
75. Hayashi, S.; Hayamizu, K., Chemical Shift Standards in High-Resolution Solid-State NMR ^{13}C , ^{29}Si , and ^1H Nuclei. *Bull. Chem. Soc. Japan* **1991**, *64*, 685-687.
76. Bloch, F., Nuclear Induction. *Phys. Rev.* **1946**, *70*, 460-474.
77. Pines, A.; Gibby, M. G.; Waugh, J. S., Proton-Enhanced Nuclear Induction Spectroscopy. A Method for High Resolution NMR of Dilute Spins in Solids. *J. Chem. Phys.* **1972**, *56*, 1776-1777.
78. Freeman, R.; Hill, H. D. W., Fourier Transform Study of NMR Spin-Lattice Relaxation by "Progressive Saturation". *J. Chem. Phys.* **1971**, *54*, 3367-3377.
79. Hessel, C. M.; Reid, D.; Panthani, M. G.; Rasch, M. R.; Goodfellow, B. W.; Wei, J.; Fujii, H.; Akhavan, V.; Korgel, B. A., Synthesis of Ligand-Stabilized Silicon Nanocrystals with Size-Dependent Photoluminescence Spanning Visible to Near-Infrared Wavelengths. *Chem. Mater.* **2012**, *24*, 393-401.

80. Yu, Y.; Hessel, C. M.; Bogart, T. D.; Panthani, M. G.; Rasch, M. R.; Korgel, B. A., Room Temperature Hydrosilylation of Silicon Nanocrystals with Bifunctional Terminal Alkenes. *Langmuir* **2013**, *29*, 1533-1540.
81. Buriak, J. M., Illuminating Silicon Surface Hydrosilylation: An Unexpected Plurality of Mechanisms. *Chem. Mater.* **2014**, *26*, 763-772.
82. Weeks, S. L.; Macco, B.; van de Sanden, M. C.; Agarwal, S., Gas-phase Hydrosilylation of Plasma-synthesized Silicon Nanocrystals with Short- and Long-chain Alkynes. *Langmuir* **2012**, *28*, 17295-301.
83. Nelles, J.; Sendor, D.; Ebberts, A.; Petrat, F. M.; Wiggers, H.; Schulz, C.; Simon, U., Functionalization of Silicon Nanoparticles via Hydrosilylation with 1-Alkenes. *Colloid. Poly. Sci.* **2007**, *285*, 729-736.
84. Hohlein, I. M.; Kehrlé, J.; Helbich, T.; Yang, Z.; Veinot, J. G.; Rieger, B., Diazonium Salts as Grafting Agents and Efficient Radical-Hydrosilylation Initiators for Freestanding Photoluminescent Silicon Nanocrystals. *Chem. Eur. J.* **2014**, *20*, 4212-6.
85. Purkait, T. K.; Iqbal, M.; Wahl, M. H.; Gottschling, K.; Gonzalez, C. M.; Islam, M. A.; Veinot, J. G., Borane-Catalyzed Room-Temperature Hydrosilylation of Alkenes/Alkynes on Silicon Nanocrystal Surfaces. *J. Am. Chem. Soc.* **2014**, *136*, 17914-7.
86. Balzar, D.; Audebrand, N.; Daymond, M. R.; Fitch, A.; Hewat, A.; Langford, J. I.; Le Bail, A.; Louer, D.; Masson, O.; McCowan, C. N.; Popa, N. C.; Stephens, P. W.; Toby, B. H., Size-Strain Line-Broadening Analysis of the Ceria Round-Robin Sample. *J. Appl. Cryst.* **2004**, *37*, 911-924.
87. Hartman, J. S.; Richardson, M. F.; Sherriff, B. L.; Winsborrow, B. G., Magic Angle Spinning NMR Studies of Silicon Carbide: Polytypes, Impurities, and Highly Inefficient Spin-Lattice Relaxation. *J. Amer. Chem. Soc.* **1987**, *109*, 6059-6067.
88. Holzman, G. R.; Lauterbur, P. C.; Anderson, J. H.; Koth, W., Nuclear Magnetic Resonance Field Shifts of Si-29 in Various Materials. *J. Chem. Phys.* **1956**, *25*, 172-173.
89. Reimer, J. A.; Dubois Murphy, P.; Gerstein, B. C.; Knights, J. C., Silicon-29 Cross-Polarization Magic-Angle Sample Spinning Spectra in Amorphous Silicon-Hydrogen Films. *J. Chem. Phys.* **1981**, *74*, 1501.
90. Shao, W.-L.; Shinar, J.; Gerstein, B. C.; Li, F.; Lannin, J. S., Magic-Angle Spinning ²⁹Si NMR Study of Short-Range Order in a-Si. *Phys Rev B* **1990**, *41*, 9491-9494.
91. Bercier, J. J.; Jirousek, M.; Graetzel, M.; Klink, J. J. v. d., Evidence from NMR for Temperature-Dependent Bardeen-Friedel Oscillations in Nanometre-Sized Silver Particles. *J. Phys.: Condens. Matter* **1993**, *5*, L571.
92. Charles, R. J.; Harrison, W. A., Size Effect in Nuclear Magnetic Resonance. *Phys. Rev. Lett.* **1963**, *11*, 75-77.
93. Terskikh, V. V.; Moudrakovski, I. L.; Ratcliffe, C. I.; Ripmeester, J. A.; Reinhold, C. J.; Anderson, P. A.; Edwards, P. P., Size Effects on the Nuclear Magnetic Resonance of Sodium Metal Confined in Controlled Pore Glasses. In *Magnetic Resonance in Colloid and Interface Science*, Fraissard, J.; Lapina, O., Eds. Springer Netherlands: Dordrecht, 2002; pp 469-475.
94. Javadi, M.; Michaelis, V. K.; Veinot, J. G. C., Thermally-Induced Evolution of 'Ge(OH)₂': Controlling the Formation of Oxide-Embedded Ge Nanocrystals. *J. Phys. Chem. C* **2018**, *122*, 17518-17525.
95. Cadars, S.; Smith, B. J.; Epping, J. D.; Acharya, S.; Belman, N.; Golan, Y.; Chmelka, B. F., Atomic Positional Versus Electronic Order in Semiconducting ZnSe Nanoparticles. *Phys. Rev. Lett.* **2009**, *103*, 136802.
96. Mobarok, M. H.; Luber, E. J.; Bernard, G. M.; Peng, L.; Wasylshen, R. E.; Buriak, J. M., Phase-Pure Crystalline Zinc Phosphide Nanoparticles: Synthetic Approaches and Characterization. *Chem. Mater.* **2014**, *26*, 1925-1935.
97. Ratcliffe, C. I.; Yu, K.; Ripmeester, J. A.; Badruz Zaman, M.; Badarau, C.; Singh, S., Solid State NMR Studies of Photoluminescent Cadmium Chalcogenide Nanoparticles. *Phys. Chem. Chem. Phys.* **2006**, *8*, 3510-3519.
98. Tomaselli, M.; Yarger, J. L.; Bruchez, M.; Havlin, R. H.; deGraw, D.; Pines, A.; Alivisatos, A. P., NMR Study of InP Quantum Dots: Surface Structure and Size Effects. *J. Chem. Phys.* **1999**, *110*, 8861-8864.
99. Marbella, L. E.; Millstone, J. E., NMR Techniques for Noble Metal Nanoparticles. *Chem. Mater.* **2015**, *27*, 2721-2739.
100. Maciel, G. E.; Sindorf, D. W., Silicon-29 NMR Study of the Surface of Silica Gel by Cross Polarization and Magic-Angle Spinning. *J. Amer. Chem. Soc.* **1980**, *102*, 7606-7607.
101. Hayashi, S.; Hayamizu, K.; Yamasaki, S.; Matsuda, A.; Tanaka, K., Interpretation of ²⁹Si Nuclear Magnetic Resonance Spectra of Amorphous Hydrogenated Silicon. *J. Appl. Phys.* **1986**, *60*, 1839-1841.
102. Hayashi, S.; Hayamizu, K.; Yamasaki, S.; Matsuda, A.; Tanaka, K., ²⁹Si Nuclear Magnetic Resonance of Amorphous Hydrogenated Silicon and Amorphous Microcrystalline Mixed-Phase Hydrogenated Silicon. *Phys. Rev. B* **1987**, *35*, 4581-4590.

103. Pietraß, T.; Bifone, A.; Roth, R. D.; Koch, V. P.; Alivisatos, A. P.; Pines, A., ²⁹Si High Resolution Solid State Nuclear Magnetic Resonance Spectroscopy of Porous Silicon. *J. Non-Cryst. Solids* **1996**, *202*, 68-76.
104. Shigenobu, H.; Kikuko, H.; Satoshi, Y.; Akihisa, M.; Kazunobu, T., Silicon-29 Nuclear Magnetic Resonance Study of Amorphous-Microcrystalline Mixed-Phase Hydrogenated Silicon. *Japanese J. Applied Phys.* **1986**, *25*, L313.
105. Smith, J. V.; Blackwell, C. S., Nuclear Magnetic Resonance of Silica Polymorphs. *Nature* **1983**, *303*, 223-225.
106. Wang, M.; Wu, X.-P.; Zheng, S.; Zhao, L.; Li, L.; Shen, L.; Gao, Y.; Xue, N.; Guo, X.; Huang, W.; Gan, Z.; Blanc, F.; Yu, Z.; Ke, X.; Ding, W.; Gong, X.-Q.; Grey, C. P.; Peng, L., Identification of Different Oxygen Species in Oxide Nanostructures with ¹⁷O Solid-State NMR Spectroscopy. *Sci. Advances* **2015**, *1*, e1400133.
107. Jameson, C. J.; Gutowsky, H. S., Calculation of Chemical Shifts. I. General Formulation and the Z Dependence. *J. Chem. Phys.* **1964**, *40*, 1714-1724.
108. Ramsey, N. F., Magnetic Shielding of Nuclei in Molecules. *Phys. Rev.* **1950**, *78*, 699-703.
109. Thayer, A. M.; Steigerwald, M. L.; Duncan, T. M.; Douglass, D. C., NMR Study of Semiconductor Molecular Clusters. *Phys. Rev. Lett.* **1988**, *60*, 2673-2676.
110. Bawendi, M. G.; Carroll, P. J.; Wilson, W. L.; Brus, L. E., Luminescence Properties of CdSe Quantum Crystallites: Resonance Between Interior and Surface Localized States. *J. Chem. Phys.* **1992**, *96*, 946-954.
111. Colvin, V. L.; Alivisatos, A. P.; Tobin, J. G., Valence-Band Photoemission from a Quantum-Dot System. *Phys. Rev. Lett.* **1991**, *66*, 2786-2789.
112. Comedi, D.; Zalloum, O. H. Y.; Irving, E. A.; Wojcik, J.; Roschuk, T.; Flynn, M. J.; Mascher, P., X-Ray Diffraction Study of Crystalline Si Nanocluster Formation in Annealed Silicon-Rich Silicon Oxides. *J. Appl. Phys.* **2006**, *99*, 023518.
113. Zhao, Y.; Kim, Y.-H.; Du, M.-H.; Zhang, S. B., First-Principles Prediction of Icosahedral Quantum Dots for Tetravalent Semiconductors. *Phys. Rev. Lett.* **2004**, *93*, 015502.
114. Avramov, P. V. F., D. G.; Sorokin, P. B.; Chernozatonskii, L. A.; Gordon, M. S., New Symmetric Families of Silicon Quantum Dots and Their Conglomerates as a Tunable Source of Photoluminescence in Nanodevices. *Los Alamos Natl. Lab, Prepr. Arch., Condens. Matter* **2007**, 1-19.
115. Okada, Y.; Tokumaru, Y., Precise Determination of Lattice Parameter and Thermal Expansion Coefficient of Silicon Between 300 and 1500 K. *J Appl Phys* **1984**, *56*, 314-320.

Chapter 3

A Tale of Seemingly “Identical” Silicon Quantum Dot Families: Structural Insight into Silicon Quantum Dot Photoluminescence.^a

3.1 Introduction

Semiconductor nanoparticles (quantum dots; QDs) are fascinating structures that exhibit size- and shape-dependent optoelectronic properties. Prototypical CdSe@ZnSQDs have been studied widely, are generally well understood, and many reports of prototype applications have appeared; in fact, InP-based QDs are revolutionizing consumer electronics as active systems in QLED-TV™ displays.^{1,2} Unfortunately, legislation limits use of heavy metals in consumer products and curtails widespread implementation of many QDs;³ furthermore, alternative QD materials, such as InP, contain costly non-earth abundant elements and exhibit ‘*clear evidence of carcinogenic activity*’ in animal models.⁴ In this context, QDs comprised of abundant, non-toxic elements must be prepared, manipulated, understood, and deployed.⁵

Silicon-based QDs are attractive for many applications because they are heavy metal-free, comprised of earth-abundant elements, and biologically compatible. In this context, a variety of methods have been developed to prepare and functionalize these promising materials⁶⁻¹¹ and prototype applications, including light-emitting diodes,¹² luminescent solar concentrators (LSCs),^{13, 14} biological imaging agents,^{15, 16} sensors,^{17, 18} and lithium ion battery anodes,^{19, 20} have appeared. Many of these uses rely on the unique tailorable optical properties of SiQDs; for example, LSCs take advantage of the large Stokes shift (i.e., the energy difference between excitation and photoluminescence maxima) that arises, in part, because of the indirect nature of the Si band gap.^{13, 14} Despite impressive advances, including spectral tuning throughout the full visible region and photoluminescence (PL) quantum yields rivaling that of compound semiconductor QDs, challenges remain,²¹⁻²⁵ paramount

^a The contents of this chapter have been adapted from the following submitted manuscript: Thiessen, A. N.; Zhang, L.; Oliynyk, A. O.; Yu, H.; O’Connor, K. M.; Meldrum, A.; Veinot, J. G. C., A Tale of Seemingly “Identical” Silicon Quantum Dot Families: Structural Insight into Silicon Quantum Dot Photoluminescence. *Chem. Mater* **2020**, *32* (16), 6838 - 6846.

among these is the limited predictability of the PL maximum size dependence that appears throughout the literature.²⁶

The origin of SiQD PL is clearly complex;²⁷⁻³² for convenience, SiQDs can be categorized into two broad groupings based upon PL properties and associated excited-state lifetimes.²⁸ The first involves SiQDs exhibiting PL characterized by short-lived excited states (i.e., τ = nanoseconds); in these cases the PL maximum that often appears in the blue spectral region (i.e., 390–500 nm), is dependent on the excitation wavelength and is largely independent of particle size. Such behavior previously has been attributed to surface-state mediated relaxation processes involving heteroatom containing species (e.g., N, Cl, O, etc.).^{21, 28, 29, 33-35} Other SiQDs show PL throughout the yellow/orange to near-IR regions with long-lived excited states (i.e., τ = microseconds), consistent with the indirect band gap of silicon; the proposal that this luminescence arises from band gap-based processes is supported further by the fact that the PL maximum generally *trends* with particle size and is broadly consistent with carrier quantum confinement.^{25, 29, 33, 36}

A comprehensive review of SiQDs exhibiting microsecond lifetimes has appeared, and a detailed discussion is beyond the scope of the present contribution.³³ However, it is useful to consider that, while the PL response of these QDs has been attributed to carrier confinement, the PL maximum of seemingly identical particles can vary greatly, and its energy frequently does not correlate well with effective mass approximation (EMA) predictions (Figure 3-1).^{26, 37-39} Numerous explanations for these deviations have appeared, broad particle size distributions,⁴⁰ among others.^{38, 41} Alternative strategies, such as empirical pseudopotential approximations (linear combination of atomic orbitals),^{42, 43} empirical tight binding band theory,^{44, 45} and ab-initio local density approximations,⁴⁶ for correlating PL maximum to SiQD dimensions have been proposed.^{26, 38, 39, 42}

It is well-established that many challenges as well as intriguing properties associated with preparing and exploiting SiQDs arise from the extended covalent bonding manifested within the Si diamond-like crystal structure. While amorphous surface layers have been implicated in ultra-fast SiQD photoluminescence,⁴⁷⁻⁵⁰ the uniformity of the SiQD internal structure often has been overlooked.⁵¹ We previously demonstrated that the Si core of *large* ($d_{\text{TEM}} \sim 9\text{--}64$ nm) SiQDs exhibits a radially graded structure consisting of a highly disordered

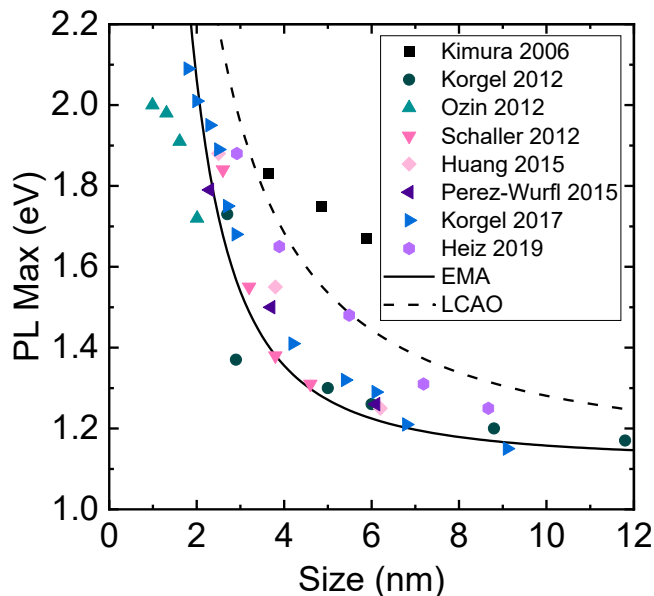


Figure 3-1. A summary of representative literature data showing the relationship between SiQD peak PL emission and particle dimension.^{37, 39, 40, 52-56} Predicted relationships obtained using the effective mass approximation⁵⁷ (solid line; $E_{gr} = 1.12 + 3.77/r^2$) and linear combination of atomic orbitals^{26, 42} (dashed line; $E_{gr} = 1.12 + 3.77/r^{1.39}$) are shown for comparison.

surface that transitions to a crystalline core; in contrast, the structure of *small* SiQDs ($d_{TEM} \sim 3$ nm) is dominated by disorder and it only possesses very small crystallite regions (i.e., $d_{XRD} \sim 1.2$ nm).⁵¹ Knowing that the electronic structure of bulk silicon strongly depends on crystallinity (e.g., amorphous Si $E_{g,optical} = 1.6\text{--}1.7$ eV; bulk crystalline Si $E_g = 1.1$ eV),⁵⁸ we endeavored to explore the impact of internal structure on SiQD optical response. Herein, we describe an evaluation of the size dependence of SiQD PL maximum and excited-state lifetime, while systematically varying particle and crystallite sizes, as determined by transmission electron microscopy (TEM) and X-ray powder diffraction (XRD), respectively.

3.2 Experimental

3.2.1 Materials

3.2.1.1 Reagents

Hydrofluoric acid (Electronic grade, 48–50%) was purchased from Fischer Scientific. Sulfuric acid (reagent grade, 95–98%) was purchased from Caledon Laboratory Chemicals. Fuming sulfuric acid (reagent grade, 20% free SO_3 bases) and trichlorosilane (99%) were purchased from Sigma (now MilliporeSigma). All reagents were used as received, unless otherwise

specified. All solvents were reagent grade and used as received. Toluene was collected from a Pure-Solv purification system immediately prior to use. Benzene was purchased from EMD Millipore (now Millipore Sigma).

3.2.1.2 Preparation of Hydrogen Silsesquioxane (HSQ)

HSQ was synthesized via known literature procedures where sulfuric acid is used to selectively oxidize trichlorosilane. Dry toluene (45.0 mL) was added to a mixture of concentrated (15.0 mL) and fuming (7.2 mL) sulfuric acid under an inert atmosphere. Once the addition was complete, 110 mL of dry toluene were added to 16 mL of trichlorosilane and this mixture was added dropwise to the sulfuric acid solution over a few hours. The product dissolved in the organic layer was washed with a sulfuric acid solution. After drying the organic layer, most of the toluene was removed via rotary evaporation, and the rest was removed in vacuo. The resulting white solid was stored under vacuum until use.

3.2.1.3 Preparation of the SiQDs/SiO₂ Composite

Thermal decomposition of the HSQ, as previously reported, was used to produce the SiQDs used in this study. Six grams of HSQ were annealed in a tube furnace under a 5% H₂/Ar atmosphere at 1100, 1200, and 1300 °C to get various sizes of nanocrystals (the sizes associated with each temperature can be seen in Table 3-1). The composite was ground using an agate mortar and pestle then shaken for 6 h to prepare a fine powder.

3.2.1.4 Preparation of Alkyl Passivated SiQDs

The composite was etched using a 1:1:1 solution of ethanol:DI water:HF to remove the SiO₂ matrix from the particles using 0.5 g of composite per etch and 15 mL total etching solution. The composite was etched as described in the supporting information (Table 3-1), and the resulting particles were extracted in toluene. The hydride-terminates SiQDs (H-SiQDs) were centrifuged twice in toluene and redispersed in 10 mL dry toluene with 6 mL of dodecene and 300 mg AIBN. The reaction mixture was degassed using three freeze-pump-thaw cycles and placed in an oil bath at 70 °C overnight (~17 h). The resulting SiQDs were purified via centrifugation using 10 mL of toluene and 20 mL of methanol thrice to remove any unreacted dodecene and AIBN. The purified SiQDs were redispersed in toluene for subsequent characterization.

Table 3-1. A Summary of Experimental Parameters and Results for All Samples.

Sample #	Anneal T ^a (°C)	Etch time ^b (min)	d_{TEM} (nm)	d_{XRD} (nm)	PL Max (nm)	Lifetime ^c (μs)	QE ^d (%)
1300-SiQD ^e	1300	240 ^g	5.5	4.69	955	546.8	N/A
1200-SiQD ^f	1200	60	5.4	3.24	837	266.6	19.7
1 ^f	1200	90	4.1	2.07	715	98.8	21.5
2 ^f	1200	60	4.7	2.62	826	190.4	33.6
3 ^f	1300	135	5.8	2.99	782	135.7	19.0
4 ^e	1200	165	3.1	2.33	701	97.0	9.4
5 ^e	1200	75	3.2	2.64	815	218.7	20
6 ^e	1300	240	3.3	3.13	800	208.1	14.9
7 ^e	1100	30	2.8	1.71	659	73.6	8.8
8 ^e	1200	60	3.4	2.64	823	172.1	33.0
9 ^e	1200	130	2.5	2.21	675	81.6	7.3
10 ^e	1200	120	2.8	2.45	700	98.5	10.1
11 ^e	1100	45	2.8	2.05	684	107.3	4.3
12 ^f	1300	210	5.3	3.06	819	159.0	15.6
13 ^f	1200	105	4.8	1.63	641	63.1	10.0
14 ^f	1200	40	4.7	2.67	860	205.7	24.5

^a Temperature used for annealing HSQ to make the composite. ^b Time used for HF etching. ^c Mean lifetimes were calculated as described above. ^d Quantum efficiency. ^e “Thin” amorphous shell samples (Figure 4 b and d). ^f “Thick” amorphous shell samples (Figure 4 a and c). ^g 5 mL of 49% HF added halfway through etch.

3.2.2 Characterization

3.2.2.1 Fourier Transform Infrared Spectroscopy

Fourier transform infrared spectroscopy (FTIR) was performed on a Thermo Nicolet Continuum FT-IR microscope by drop casting SiQDs onto a silicon wafer from dry toluene solutions.

3.2.2.2 X-ray Photoelectron Spectroscopy

X-ray photoelectron spectroscopy (XPS) was measured using a Kratos Axis 165 Ultra X-ray photoelectron spectrometer. A monochromatic Al K α source operating at 210 W with an energy $h\nu = 1486.6$ eV was used. Survey spectra were collected with an analyzer pass energy of 160 eV and a step of 0.3 eV. For high-resolution spectra, the pass energy was 20 eV and the step was 0.1 eV with dwell time of 200 ms. XPS samples were prepared by drop-coating a dispersion of SiQDs in dry toluene onto a copper foil. Spectra were calibrated to the C 1s (284.8 eV) and fitted to appropriate spin-orbit pairs using CasaXPS (VAMAS) software with a Shirley-type background. To fit the Si 2p high resolution spectrum, the doublet area ratio was fixed at 2:1 and the separation was set at 0.6.

3.2.2.3 Electron Microscopy

Transmission electron microscopy (TEM) and HR-TEM were performed on a JEOL JEM-ARM200CF S/TEM (Cold Field Emission Gun) electron microscope with an accelerating voltage of 200 kV using SiQDs drop-coated from a toluene solution onto a holey carbon-coated copper grid. The SiQD size was determined by averaging the size of 300 particles using ImageJ software (version 1.51j8) and plotted as an average shifted histogram, as outlined previously by Buriak and co-workers.⁵⁹

HAADF-STEM was performed using the same instrument and sample grids. Subsequently, images were processed using a Radial Wiener Filter in the Gatan Microscopy Suite 3.0 and subjected to trend subtraction (Figure 3-2).⁶⁰ The thickness of the amorphous layer was determined using ImageJ by overlaying two perpendicular lines span the diameter of the crystalline domain (Fig 3-2a filtered image) and total particle diameter (Fig. 3-2b) and calculating the difference. This procedure was repeated for no fewer than 20 particles for each sample.

3.2.2.4 Powder X-ray Diffraction

Powder X-ray diffraction was measured using a Rigaku Ultima IV multipurpose X-ray diffraction system equipped with a Cu K α source for most of the samples. Samples were drop cast on a zero-background Si wafer, and data was collected in a thin film orientation.

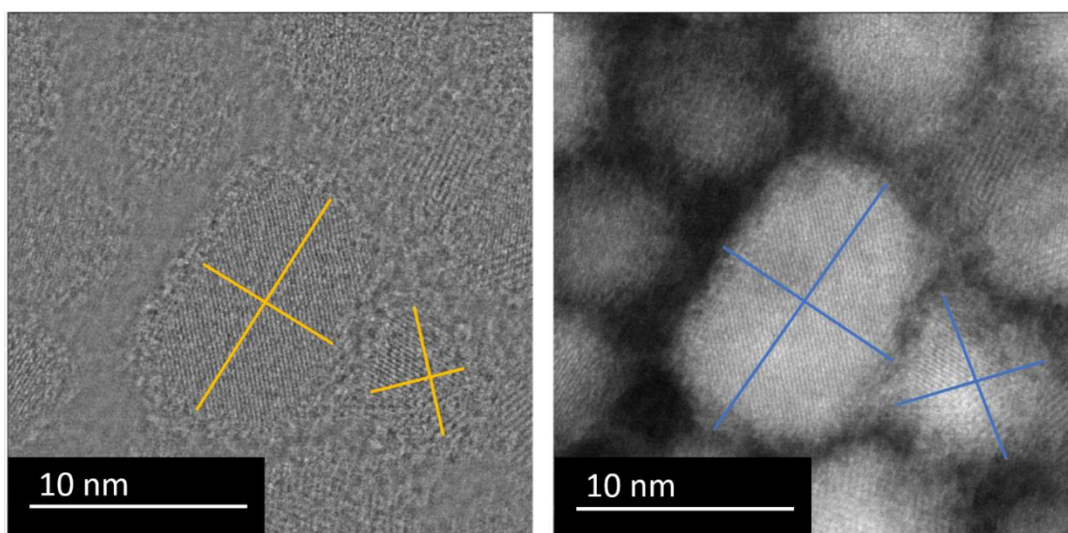


Figure 3-2. a) Trend subtracted STEM image highlighting lattice fringes of sample. b) Original HAADF STEM image showing full size of SiNCs. (Note: Colored lines illustrate particle measurement method.)

For thin film diffraction, a parallel beam was used with a glancing angle of 0.5° . Some data also was collected at the Canadian Light Source (CLS) synchrotron with a wavelength of 0.6892 \AA , using transmission mode. These methods gave equivalent data within the errors associated with the techniques and fitting parameters. To account for instrumental effects, a diffraction pattern for the NIST Si line shape standard (640f) was acquired using the identical conditions (i.e., sample holder, size step, calibration file, etc.) employed for SiQD analyses. The standards were analyzed by fitting the width of the reflections, taking into account $K\alpha_1$ and $K\alpha_2$ contributions. The fit can be found in Figure 3-3. Pawley fitting of powder patterns was performed using the TOPAS software package to determine the crystallite domain size using the integral breadth, FWHM, and Lorentzian broadening methods.⁶³ A sample-independent synthetic peak was required at $\sim 22^\circ$ for all measurements on the laboratory instrument, which is believed to originate from the sample holder imperfections or amorphous products/unreacted materials. Synchrotron diffraction data required corrections of other small peaks (8, 9, 11, 14, 16, and 19°) due to imperfections in the background subtraction from the Kapton tube (sample holder).

3.2.2.5 Photoluminescence Characterization

Photoluminescence spectroscopy measurements were performed on a solution of silicon nanocrystals dispersed in toluene in a quartz cuvette. Silicon nanoparticles were excited using an argon ion laser with a 351 nm emission wavelength.

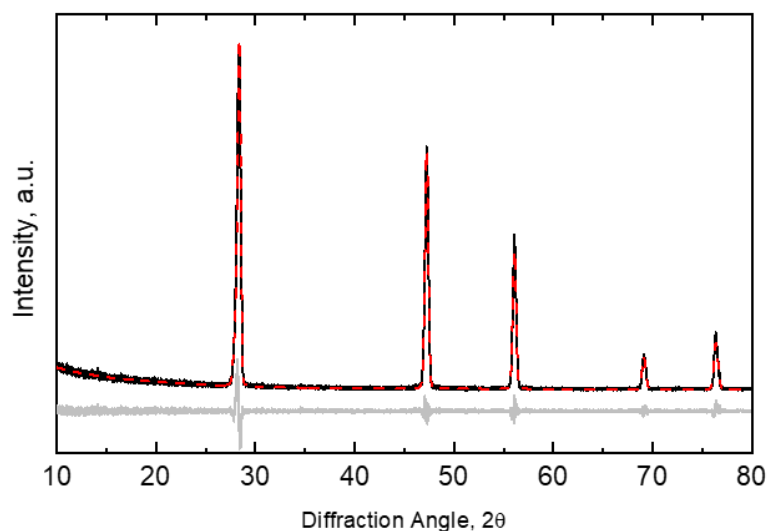


Figure 3-3. Fitting of Si NIST linewidth standard (640f) measured on the Rigaku Ultima IV.

The resulting photoluminescence was collected by an optic fibre, passed through a 500 nm long-pass filter to eliminate scattered light from the excitation source, and fed into an Ocean Optics USB2000+ spectrometer with a spectral range of 300–1000 nm and a sensitivity of 41 photons per count at 600 nm. The spectral response was calibrated using a reference light source from Ocean Optics. Photoluminescence lifetime measurements were acquired using an argon ion laser (351 nm, ~20 mW) modulated by an acousto-optic modulator (~50 ns response time) operated at a frequency of 200 Hz with a 50% duty cycle. The photoluminescence was fed into an optic fiber and passed through a 500 nm long-pass filter, which then was incident on a Hamamatsu H7422P-50 photomultiplier tube (PMT) interfaced with a Becker-Hickl PMS-400A gated photon counter. The photoluminescence data was collected with a total of 10 000 sweeps for good signal-to-noise ratio and using 1 μ s time steps. A log-normal fitting of the data in MatLab was used to calculate the luminescence decay, and the fitting parameters are shown in Table 3-2. The lifetimes were measured for each sample individually, with peak emissions at different energies (no wavelength selection was performed).

Table 3-2. Lifetime Fitting Parameters for 1200-SiQDs and 1300-QDs

	A	β	Dc
1200-SiQDs	1.031	0.8608	0.00091
1300-SiQDs	1.024	0.8346	0.0053

Quantum efficiency measurements were performed using a homemade integrating sphere with a 365 nm light emitting diode excitation source. Sample solutions were diluted to have an absorbance between 0.1 and 0.15 at 405 nm, then they were transferred into a cuvette that was lowered into the integrating sphere on a magnetic holder, as was a distilled water blank. The photoluminescence and excitation intensities were captured through a fibre attached to the sphere and analyzed with a calibrated Ocean Optics spectrometer. The equation $QE = (I_{PL, sample} - I_{PL, blank}) / (I_{ex, blank} - I_{ex, sample})$ was used to calculate the absolute quantum efficiency, where I_{PL} is the integrated photoluminescence intensity and I_{ex} is the excitation intensity recorded inside the sphere. The measurements were performed in quintuplicates.

3.3 Results and Discussion

To probe the impact of an internally graded crystal structure on SiQD optical properties, it was necessary to prepare QDs with the same *particle* (determined using TEM; d_{TEM}) and different *crystallite* (determined using XRD, d_{XRD}) sizes, while maintaining all other contributing factors (e.g., surface chemistry/oxidation) the same. Drawing on our intimate knowledge of the hydrogen silsesquioxane (HSQ)-based procedure and the structure of the resulting SiQDs,^{51, 61-63} we prepared two different composites consisting of nanocrystalline silicon domains encased within an SiO₂-like matrix via HSQ reductive thermal processing at 1200 and 1300 °C. Evaluation of the Si domain sizes using TEM was precluded by the oxide matrix; however, consistent with expectation,^{37, 62} XRD revealed reflections attributable to nanocrystalline Si domains and, as expected, it revealed larger domains for products processed at higher temperature (i.e., $d_{\text{XRD}, 1200} \sim 3.7$ nm; $d_{\text{XRD}, 1300} \sim 6.1$ nm).

Freestanding SiQDs were liberated from an HSQ-derived SiO₂-like matrix upon etching with alcoholic aqueous hydrofluoric acid. Drawing on the reasonable expectation that amorphous/disordered silicon is more susceptible to this etching process, definition of the etching time allowed isolation of SiQDs from the composites that possess statistically identical d_{TEM} but different d_{XRD} dimensions (i.e., different thicknesses of disordered Si shells). As a result of experimental variations of the SiQD/SiO₂ composite, it is important to monitor the appearance/colour of the etching mixture qualitatively. Doing so provides a qualitative indication of SiQD size (i.e., $d \sim 2.5$ nm, yellow; $d \sim 3$ nm, yellow/orange; $d \sim 5$ nm, orange; not freestanding, brown/black), however, the exact etching time depends on the specific composite, and all SiQDs must be characterized following surface functionalization using quantitative methods (vide infra) to confirm dimensions.

Following isolation, the SiQDs were surface functionalized using size independent radical-induced hydrosilylation to render them solution processable and minimize reactions (e.g., oxidation) that are known to deleteriously impact optical response.¹¹ Fourier Transform Infrared spectra of the resulting materials are consistent with successful functionalization and show the features expected for surface-bonded dodecyl-moieties (Figure 3-4).¹¹

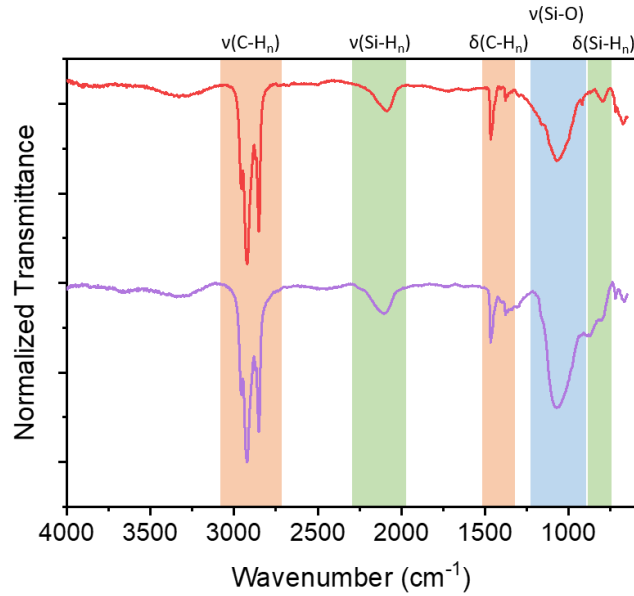


Figure 3-4. FTIR of 1200-SiQDs (red) and 1300-SiQDs (purple).

For the following discussion, SiQDs resulting from composites prepared at 1200 and 1300 °C will be referred to as 1200-SiQD and 1300-SiQD, respectively. Prior to evaluating the size and optical properties of the SiQDs, it is essential to confirm that the degree and speciation of surface oxidation is consistent across the samples because these factors also can impact SiQD PL response.^{29, 64} To do so, the Si 2p XP spectra of the 1200- and 1300-SiQDs (Figure 3-5a) were deconvoluted into component spin-orbit couples (Si 2p_{1/2} and 2p_{3/2}) corresponding to Si(0) (i.e., orange), Si(I) (i.e., green), and Si(II) (i.e., blue).⁵¹ Integrating the total area of the Si (I) and Si(II) components and comparing it to the integrated area of the Si(0) component provided an estimation of the ratio of oxidized surface silicon species to elemental silicon. For the present samples, the total integrated signal of the Si(I) and Si(II) components corresponds to 21% for 1300-SiQDs and 27% for 1200-SiQDs of the total Si 2p signal intensity. This, combined with the reasonable assumption that the degree of surface functionalization (i.e., surface density of Si-C bonds) is equivalent for both samples, indicates that the 1200- and 1300-SiQDs have similar amounts of oxidation. Furthermore, closer inspection of the O and Si spectral envelopes indicates that the speciation of the oxides is near identical. In this context, we expect the influence, if any, of surface oxide species on the optical properties of 1200- and 1300-SiQDs to be similar.

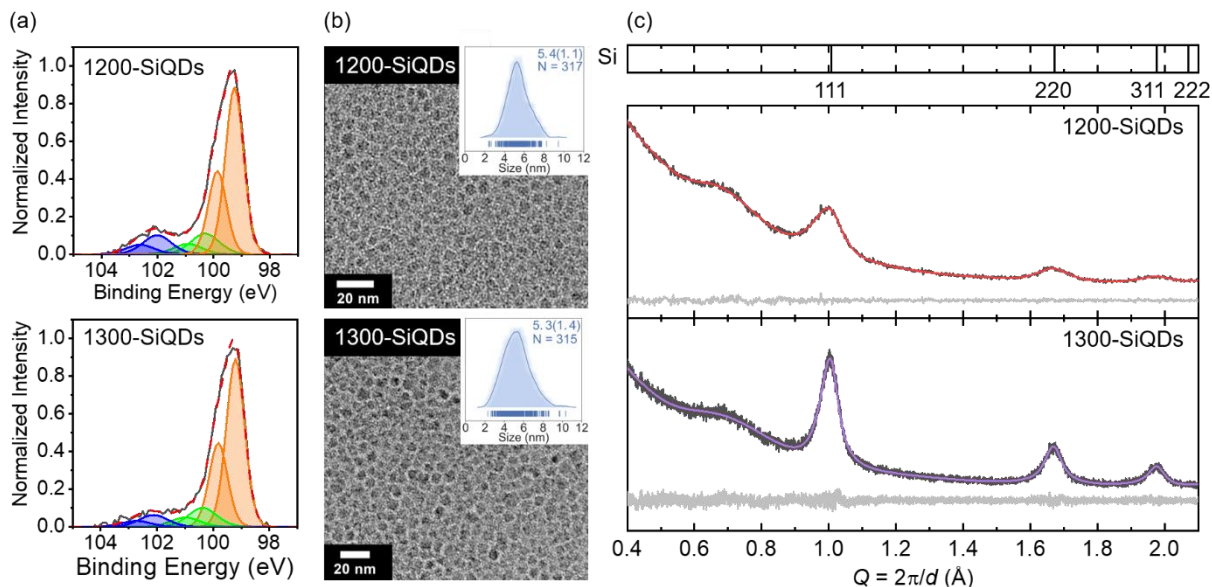


Figure 3-5. a) Si 2p XP spectrum with deconvolution/fitting of the data for 1200-SiQDs and 1300-SiQDs. Fitting peaks are shown as Si 2p_{1/2} and 2p_{3/2} components corresponding to Si(0) (i.e., orange), Si(I) (i.e., green), and Si(II) (i.e., blue). The black trace is the experimental spectrum and the red dashed line represents the overall fitting envelope. b) TEM image of 1200-SiQDs and 1300-SiQDs inset: average shifted histogram with the average size and the distribution width. c) XRD data for 1200-SiQDs and 1300-SiQDs showing experimental powder pattern (black) with fitting (red for 1300-SiQDs and purple for 1200-SiQDs) and residuals (light gray).

Turning to the evaluation of QD particle and crystallite sizes, bright-field TEM analyses of the liberated dodecyl-functionalized particles afforded d_{TEM} of 5.4 ± 1.1 and 5.3 ± 1.4 nm (Figure 3-5b) for the 1200- and 1300-SiQDs, respectively, and are statistically similar to a 95% confidence interval. To complement the TEM analyses, crystallite sizes of the identical samples were determined using XRD. Diffraction data were fitted to the NIST Si line shape standard (640f) as an “infinite” crystallite reference to account for instrumental broadening and line shape. Having accounted for instrumental broadening, Gaussian and Lorentzian peak shape parameters, with the assumption that atomic displacement parameters and crystallographic site deficiencies do not play a role, only size and strain contributions to line broadening remain; they can be accounted for qualitatively based on their diffraction angle dependence.^{51, 65} In contrast to the d_{TEM} , which were statistically identical, the d_{XRD} (i.e., crystallite sizes) determined from diffraction data (Figures 3-5e and f) were 3.2 ± 1.2 and 4.7 ± 0.4 nm for 1200-SiQDs and 1300-SiQDs, respectively. A straightforward comparison of the d_{TEM} and d_{XRD} clearly shows that, despite having the same physical dimensions, 1200-SiQDs have a smaller crystallite size and, by extension, a thicker disordered Si shell. This is supported

further by high annular angle dark field scanning transmission electron microscopy (HAADF-STEM) that shows thicker disordered layers on 1200-SiQDs (1.7 nm 1200-SiQDs vs. 1.0 nm for 1300-SiQDs; Figure 3-6 and 3-7). Our data analyses reasonably assume that the bright area in the HAADF-STEM images is representative of the overall SiQD size without the organic ligand, which has a lower Z -contrast compared to the silicon, and that the lattice fringes are representative of the dimensions of the crystalline core. With these caveats, the difference in the dimensions of these particles indicates a thicker disordered layer on the 1200-SiQDs.

Having shown that 1200-SiQDs and 1300-SiQDs exhibit near-identical physical size (i.e., d_{TEM}) as well as composition (i.e., degree of oxidation, oxidation speciation, surface functionalization) and differ only in the size of the crystalline core (i.e., d_{XRD}), we endeavored to evaluate the impact of the disordered Si shell on the SiQD optical properties. The PL spectra of SiQD toluene solutions (Fig. 3-8) were evaluated using the 351 and 364 nm lines of an Ar ion laser and show maxima of 837 and 955 nm for 1200-SiQDs and 1300-SiQDs, respectively. The marked red-shift in PL maximum with increased d_{XRD} suggests that the dimensions of the nanocrystalline domain dominate the SiQD PL and band gap; there is no demonstrable indication of a contribution from the disordered surface silicon species to these properties.

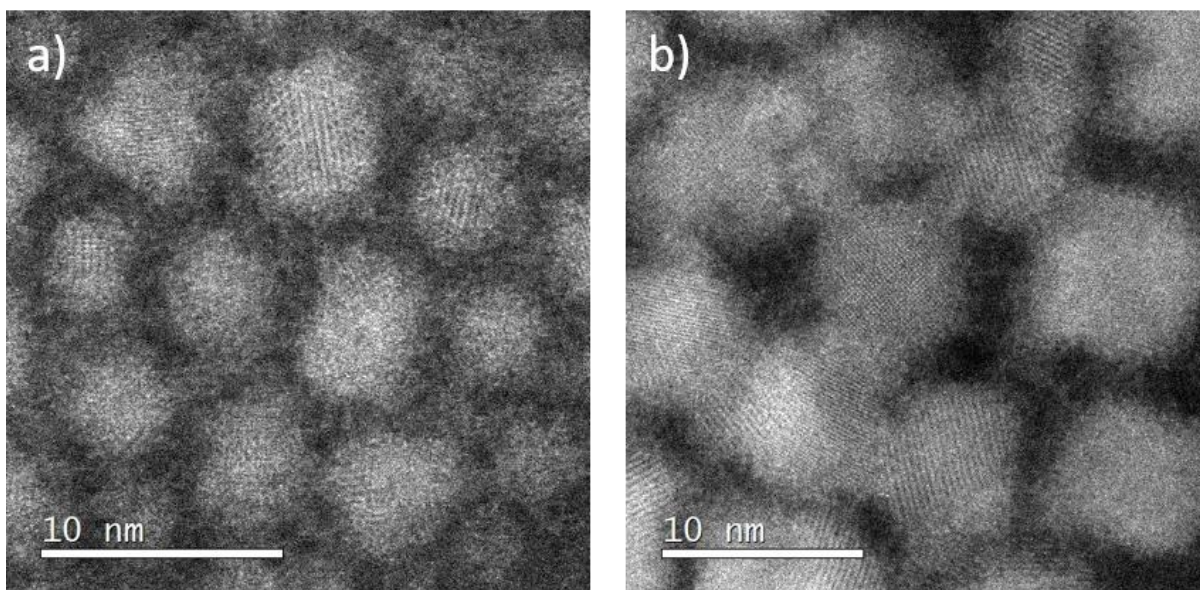


Figure 3-6. High annular angle dark field STEM images of a) 1200-SiQDs and b) 1300-SiQDs.

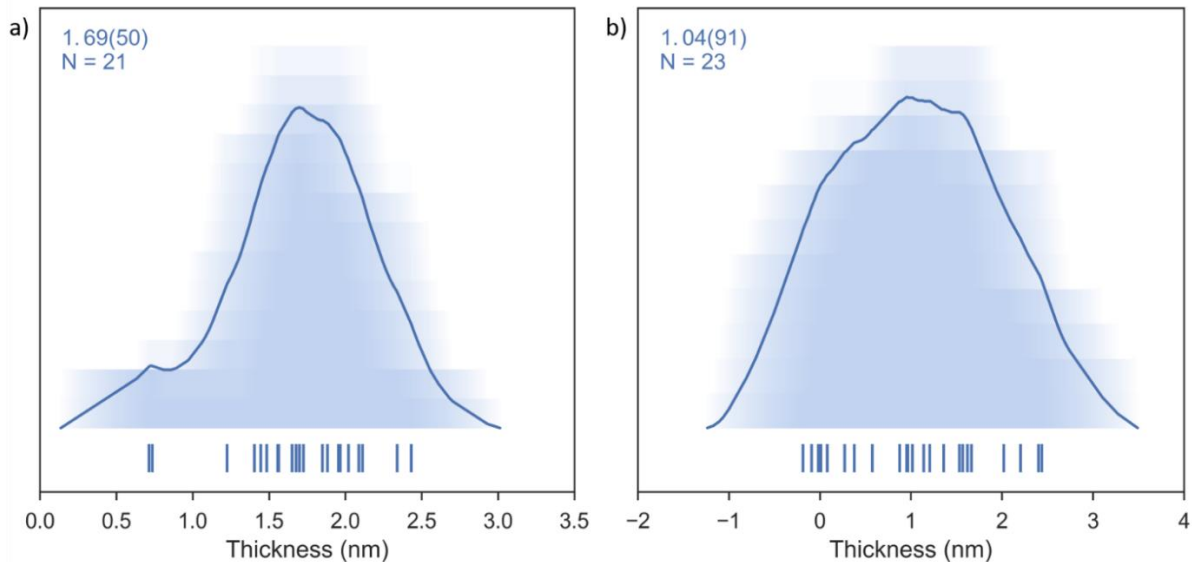


Figure 3-7. Histograms showing the STEM determined non-crystalline shell thicknesses for a) 1200-SiQDs and b) 1300-SiQDs. Experimental data are represented by the blue bars below the x-axis. The density of these bars indicates the frequency. The line in the plot was determined using a fitting routine described in Ref 59 that is designed to minimize binning bias.

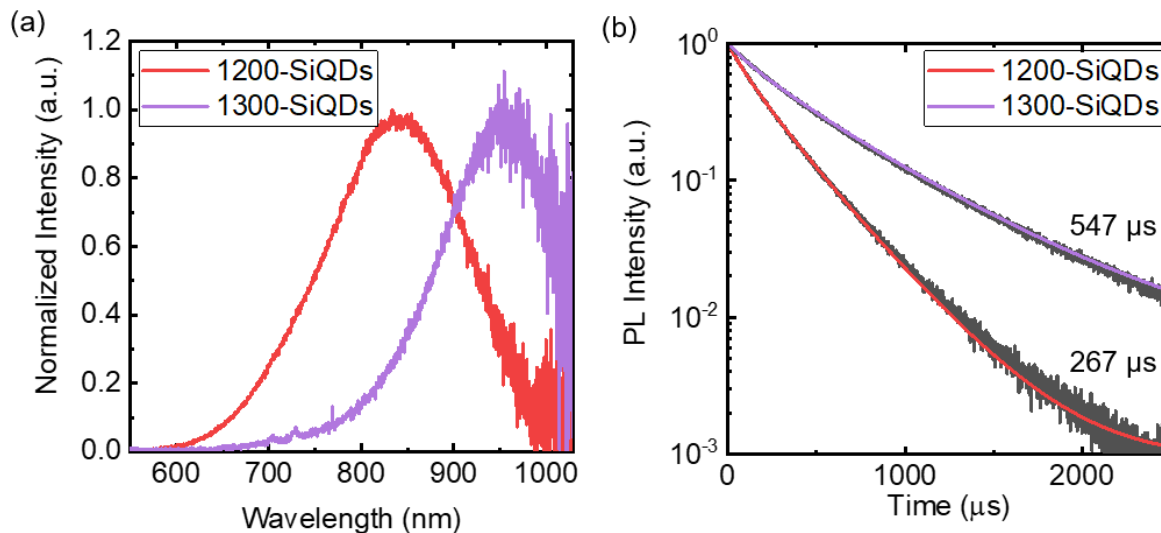


Figure 3-8. Comparing a) the photoluminescence emission of 1300-SiQDs (purple) and 1200-SiQDs (red) as well as b) the luminescence lifetimes of 1300-SiQDs (purple fit) and 1200-SiQDs (red fit). Photoluminescence emission data were collected on an Ocean Optics 2000+ spectrometer. Luminescence lifetimes were fitted to a stretched exponential function, and then the mean time constants were calculated as described below.⁶⁶ The fitting parameters are reported in Table 3-2.

This observation is also consistent with the amorphous silicon shell having wider band gap than the crystalline core, providing a core@shell structure similar to that of more commonly studied CdSe@ZnS systems (i.e., Type I QDs).⁶⁷ Contrary to the CdSe@ZnS QD

case, in which the ZnS shell grows epitaxially on the CdSe core to reduce interfacial dark defects and increase the PL QY, the graded interface between the crystalline and amorphous components of the present SiQDs can be expected to be ill-defined.^{51, 68, 69} As such, there is no obvious trend in the present PL QY data for the core@shell systems (Figure 3-9).

Time-resolved photoluminescence (TRPL) traces were fitted with a stretched exponential model given by:

$$I_t = A \exp[-(t/\tau)^\beta] + dc \quad (1)$$

where t is time and dc is a fitting parameter. From the β and τ fitting parameters, the mean time constant (referred to henceforth as the mean lifetime) was obtained according to:

$$\bar{\tau} = \tau[\Gamma(2/\beta)/\Gamma(1/\beta)] \quad (2)$$

This model has been applied widely to SiQDs and tends to fit the TRPL data quite well for the purposes of extracting a mean lifetime.⁶⁶ The 1300-SiQDs exhibit a longer mean lifetimes (i.e., 547 μ s for 1300-SiQDs vs. 267 μ s for 1200-SiQDs), consistent with experimental reports⁵³ and models⁷² showing longer lifetimes for larger SiQDs. Upon examining the mean lifetimes of all of the SiQDs here studied as a function of PL energy, an obvious trend was observed, where $1/\bar{\tau} = A' * e^{E/E_0}$ (Figure 3-10). This trend is consistent across literature;^{70, 71} it is independent of the synthetic method and has been implicated with the indirect band gap of silicon.⁷²

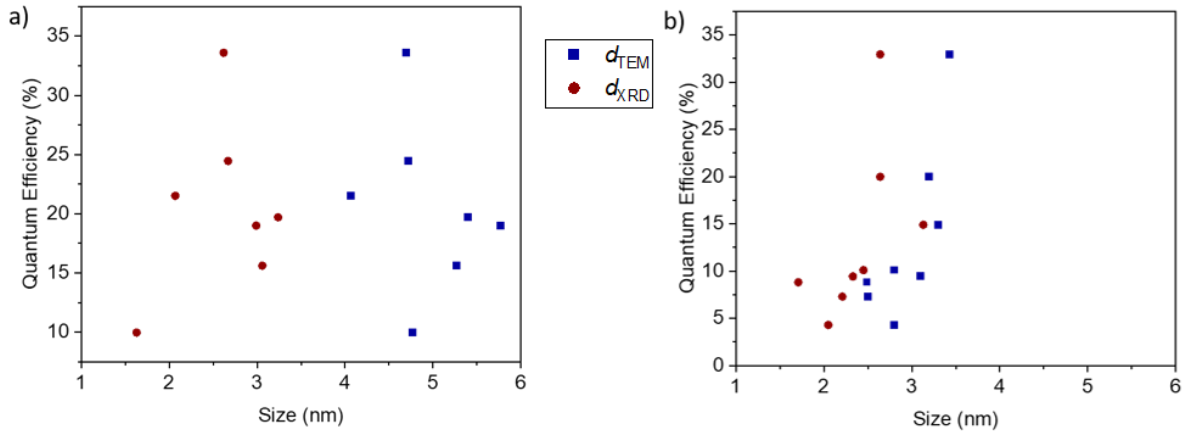


Figure 3-9. A comparison of the relationship between quantum efficiency with d_{TEM} (blue squares) and d_{XRD} (red circles) for SiQDs with a thick amorphous layer (>2 nm; a) and a thin amorphous layer (<0.8 nm; b).

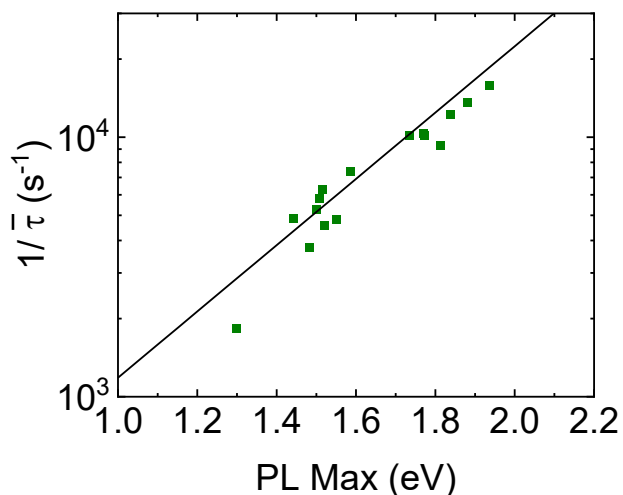


Figure 3-10. A plot of the maximum photoluminescence energy against the lifetimes for all SiQDs in this study. A clear trend is observed that can be fit to the equation $1/\bar{\tau} = A' * e^{E/E_0}$,⁷⁰⁻⁷² where $A' = 62.5 \text{ s}^{-1}$ and $E_0 = 0.34 \text{ eV}$ (the black line).

To explore the broader scope of the relationship between SiQD optical properties with d_{XRD} further, SiQD/SiO₂ composites were prepared via reductive thermal processing of HSQ at 1100, 1200, and 1300 °C, in order to have a wider range of Si crystallite sizes.^{37, 62} SiQDs were liberated upon alcoholic HF etching for pre-determined times (See Table 3-1) and surface functionalized with Si-C tethered 1-dodecyl surface groups via AIBN radical-initiated hydrosilylation. Subsequently, the d_{TEM} , d_{XRD} , and PL properties were evaluated and compared. This method yielded SiQDs with varying disordered layer thicknesses, where in all cases the d_{TEM} is larger than d_{XRD} (Figure 3-11).

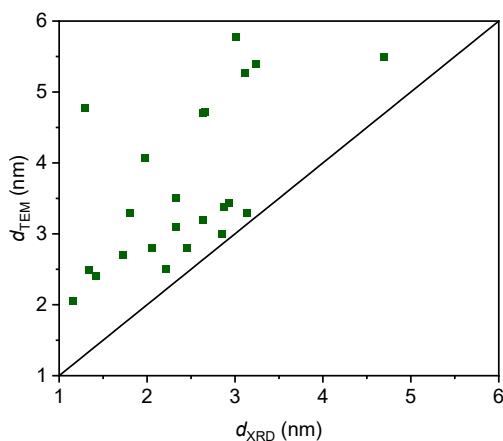


Figure 3-11. Plot showing d_{TEM} vs. d_{XRD} , where the line is $d_{\text{TEM}} = d_{\text{XRD}}$.

To illustrate/understand the relationship between SiQD dimensions and optical properties better, we categorized the present data into two groupings. **1.** Samples in which the d_{TEM} is substantially larger than d_{XRD} (i.e., $d_{\text{TEM}} - d_{\text{XRD}} > 2$ nm); these particles possess comparatively thick amorphous/disordered Si layers on their surfaces. **2.** Samples for which d_{TEM} and d_{XRD} are similar (i.e., $d_{\text{TEM}} - d_{\text{XRD}} < 0.8$ nm); these particles possess a thin amorphous/disordered Si layer on their surfaces. The data were plotted and compared with the predictions of the effective mass approximation (EMA; Figures 3-12c and d).

Consistent with our previous observations (see above), there is a clear correlation between d_{XRD} and EMA predictions for the photoluminescence of SiQDs in Group 1 (i.e., $d_{\text{TEM}} - d_{\text{XRD}} > 2$ nm; Figure 3-12c) – this is not the case for d_{TEM} . We also note that the EMA consistently overestimates particle size when comparing to d_{XRD} . In contrast, for Group 2 SiQDs that bear a thin amorphous Si layer, the PL emission energy is related closely to d_{XRD} and d_{TEM} (Figure 3-12d); furthermore, the EMA appears to agree better with the data. We also note similar relationships when evaluating time-resolved photoluminescence data in the context of d_{TEM} and d_{XRD} .

To investigate the effect of size distribution on the mean luminescence energies, we tested a model similar to that reported in Ref. 39. For particles with the same annealing temperature, and thus presumably similar defect distributions and shell thickness, we find that a somewhat better match to the XRD data can be obtained if the size distribution is factored into the analysis (Fig. 3-13). It is important to note that the impact of size distribution is not as obvious for the materials presented here when compared to those reported in Ref. 39 because the SiQDs reported previously were isolated through size selected precipitation (i.e. they have narrow size distributions) and likely have no disordered shell due to the extended etching process employed.

Theory predicts that the radiative lifetime of a silicon nanocrystal scales approximately as the inverse cube of the radius.^{73, 74} Thus, the mean lifetime data were fit to an inverse cubic function of the XRD radius given by:

$$1/\bar{\tau} = A''(1/d_{\text{XRD}})^3 + C \quad (3)$$

which appeared to yield a good fit to the experimental data (Figure 3-12e and f). Of course, there is also a strong non-radiative contribution, which cannot be measured directly; however,

under certain specific conditions (i.e., for a single defect), the dominant non-radiative decay rate also scales inversely with the crystallite volume.⁷⁵ Obviously, the actual nonradiative rate depends on the abundance and types of defects present in the samples, which may differ and likely explains some of the differences between the data and the model shown in Figure 3-12e and f.

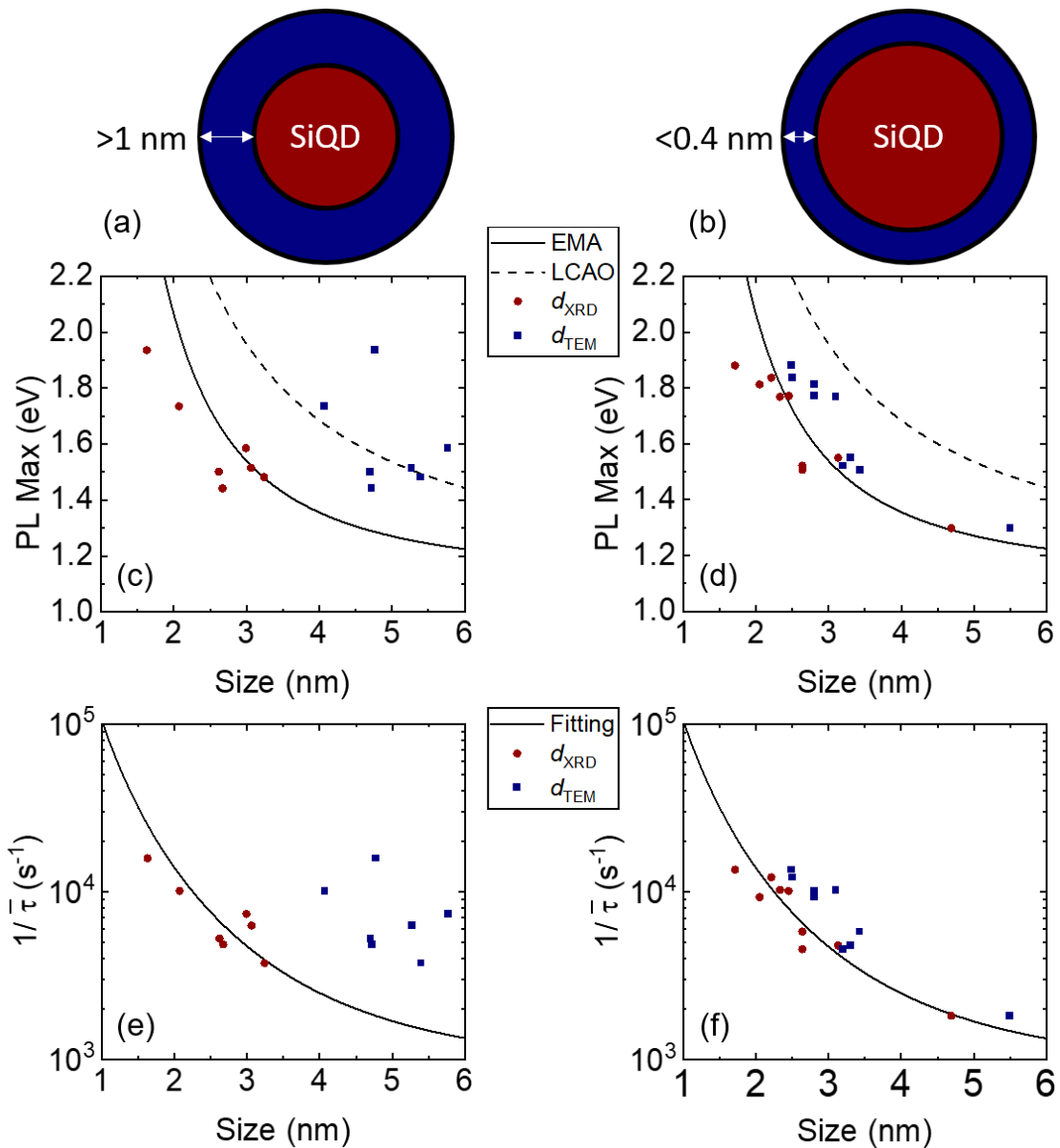


Figure 3-12. A schematic representation of Si QDs showing the thick (a) and thin (b) amorphous layers surrounding the crystalline core. A comparison of the relationship between PL energy (c and d) and lifetimes (e and f) with d_{TEM} (blue squares) and d_{XRD} (red circles) for SiQDs with a thick amorphous layer ($>1 \text{ nm}$; a, c, e) and a thin amorphous layer ($<0.4 \text{ nm}$; b, d, f). The solid and dashed black lines in (c) and (d) represent the EMA and LCAO as in Figure 1. The solid black line in (e) and (f) is a fitting from all of the d_{XRD} vs. lifetime data, according to Eq.3.

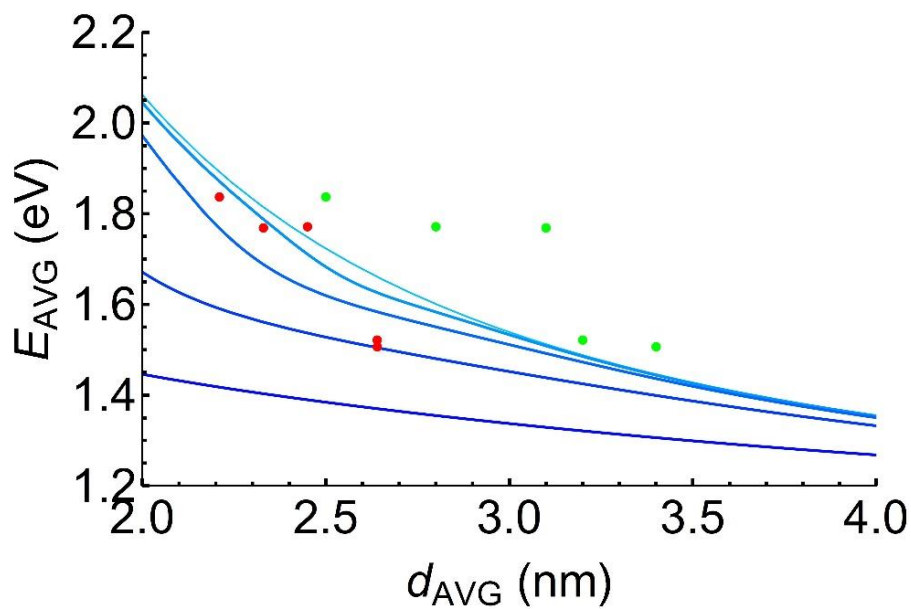


Figure 3-13. The XRD (red points) and TEM (green points) mean diameters as a function of the mean PL energy. The blue lines are model fits that incorporate the quantum efficiency, absorption cross sections, size distributions, and effective mass approximation using methods similar to those in Ref. Yu et al. 2017. The uppermost light blue line is the pure EMA; increasing the size distribution “pulls” the model downward, mainly due to the higher QY of the larger particles (darker blue lines).

The direct relationship between theoretical PL energy and lifetimes and the crystallite diameter of these SiQDs, especially when they have a thin amorphous layer (Group 2), suggests that the crystalline core controls the optical response. However, the relationships between SiQD luminescence, graded structure, and size presented for Group 1 are similar to those previously noted for CdSe@CdSe_xS_{1-x}@CdS QDs, in which the confinement of carriers (i.e., electrons and holes) depends upon a radially varied structure.⁷⁶ A detailed study of the interplay of these factors in the SiQD optical behavior obviously is complicated by the poorly-defined nature of the transitional region between the crystalline core and the amorphous shell; however, one can expect that the confinement should be stronger when the shell is thinner, as implied by the results in Fig. 3-12. This clearly highlights the importance and promise of establishing methods for controlling the uniformity of the internal SiQD structure, as well as preparing well-defined core@shell SiQD systems.

3.4 Conclusions

In conclusion, the photoluminescence of functionalized SiQDs has been evaluated in the context of internal crystallinity by examining crystallite and particle dimensions using X-ray diffraction and transmission electron microscopy. For SiQDs prepared via the widely employed “HSQ method”, the d_{XRD} provides a better representation of the optically active QD dimensions, regardless of the presence of an amorphous overlayer. In cases in which a thick Si amorphous layer is present, no obvious correlation between d_{TEM} and the photoluminescence is noted. However, EMA estimates derived from d_{TEM} and d_{XRD} dimensions agree reasonably well with the data when thin amorphous Si layers are present. This fundamental understanding of SiQD structure and its influence on their luminescence properties illuminates a foundation on which future efforts to better control SiQD optical response can be constructed.

3.5 References

1. Samsung Newsroom. [NEXT for QLED] Part 1: Samsung Dominates the Large Screen TV Market. <https://news.samsung.com/global/next-for-qled-part-1-samsung-dominates-the-large-screen-tv-market> (01/02),
2. Halford, B., Quantum dot LEDs go cadmium-free. In American Chemical Society: Chemical and Engineering News, 2019; Vol. 97.
3. Union, T. E., Ed. *Publications Office of the European Union: Official Journal of the European Union*, 2017; Vol. 2017/1975, p 3.
4. Program, N. T. *NTP Technical Report on the Toxicology and Carcinogenesis Studies of Indium Phosphide in F344/N Rats and B6C3F1 Mice (Inhalation Studies)*; U.S. Department of Health and Human Services: July 2001, 2001.
5. Nanoco <https://www.nanocotechnologies.com/> (01/02),
6. Veinot, J. G. C., Synthesis, surface functionalization, and properties of freestanding silicon nanocrystals. *Chem. Commun.* **2006**, *40*, 4160-4168.
7. Mangolini, L.; Kortshagen, U., Plasma-assisted synthesis of silicon nanocrystal inks. *Adv. Mater.* **2007**, *19* (18), 2513-2519.
8. Tilley, R. D.; Warner, J. H.; Yamamoto, K.; Matsui, I.; Fujimori, H., Micro-emulsion synthesis of monodisperse surface stabilized silicon nanocrystals. *Chem. Commun.* **2005**, *14*, 1833-1835.
9. Baldwin, R. K.; Pettigrew, K. A.; Ratai, E.; Augustine, M. P.; Kauzlarich, S. M., Solution reduction synthesis of surface stabilized silicon nanoparticles. *Chem. Commun.* **2002**, *17*, 1822-1823.
10. Zou, J.; Kauzlarich, S. M., Functionalization of Silicon Nanoparticles via Silanization: Alkyl, Halide and Ester. *J. Clust. Sci.* **2008**, *19* (2), 341-355.
11. Yang, Z.; Gonzalez, C. M.; Purkait, T. K.; Iqbal, M.; Meldrum, A.; Veinot, J. G., Radical Initiated Hydrosilylation on Silicon Nanocrystal Surfaces: An Evaluation of Functional Group Tolerance and Mechanistic Study. *Langmuir* **2015**, *31* (38), 10540-10548.
12. Liu, X.; Zhao, S.; Gu, W.; Zhang, Y.; Qiao, X.; Ni, Z.; Pi, X.; Yang, D., Light-Emitting Diodes Based on Colloidal Silicon Quantum Dots with Octyl and Phenylpropyl Ligands. *ACS Appl. Mater. Interfaces* **2018**, *10* (6), 5959-5966.
13. Meinardi, F.; Ehrenberg, S.; Dharmo, L.; Carulli, F.; Mauri, M.; Bruni, F.; Simonutti, R.; Kortshagen, U.; Brovelli, S., Highly efficient luminescent solar concentrators based on earth-abundant indirect-bandgap silicon quantum dots. *Nature Photon.* **2017**, *11*, 177-185.
14. Mazzaro, R.; Gradone, A.; Angeloni, S.; Morselli, G.; Cozzi, P. G.; Romano, F.; Vomiero, A.; Ceroni, P., Hybrid Silicon Nanocrystals for Color-Neutral and Transparent Luminescent Solar Concentrators. *ACS Photonics* **2019**, *6* (9), 2303-2311.

15. Erogbogbo, F.; Yong, K.-T.; Roy, I.; Hu, R.; Law, W.-C.; Zhao, W.; Ding, H.; Wu, F.; Kumar, R.; Swihart, M. T.; Prasad, P. N., In Vivo Targeted Cancer Imaging, Sentinel Lymph Node Mapping and Multi-Channel Imaging with Biocompatible Silicon Nanocrystals. *ACS Nano* **2011**, *5* (1), 413-423.
16. Tu, C.; Ma, X.; House, A.; Kauzlarich, S. M.; Louie, A. Y., PET Imaging and Biodistribution of Silicon Quantum Dots in Mice. *ACS Med. Chem. Lett.* **2011**, *2* (4), 285-288.
17. Gonzalez, C. M.; Iqbal, M.; Dasog, M.; Piercey, D. G.; Lockwood, R.; Klapotke, T. M.; Veinot, J. G. C., Detection of high-energy compounds using photoluminescent silicon nanocrystal paper based sensors. *Nanoscale* **2014**, *6* (5), 2608-2612.
18. Gonzalez, C.M.; Veinot, J. G. C., Silicon nanocrystals for the development of sensing platforms. *J. Mater. Chem. C* **2016**, *4* (22), 4836-4846.
19. Kim, H.; Seo, M.; Park, M. H.; Cho, J., A critical size of silicon nano-anodes for lithium rechargeable batteries. *Angew. Chem. Int. Ed.* **2010**, *49* (12), 2146-2149.
20. Su, X.; Wu, Q.; Li, J.; Xiao, X.; Lott, A.; Lu, W.; Sheldon Brian, W.; Wu, J., Silicon-Based Nanomaterials for Lithium-Ion Batteries: A Review. *Adv. Energy Mater.* **2014**, *4* (1), 1300882.
21. Dasog, M.; De los Reyes, G. B.; Titova, L. V.; Hegmann, F. A.; Veinot, J. G. C., Size vs surface: tuning the photoluminescence of freestanding silicon nanocrystals across the visible spectrum via surface groups. *ACS Nano* **2014**, *8* (9), 9636-48.
22. Mobarok, M. H.; Purkait, T. K.; Islam, M. A.; Miskolzie, M.; Veinot, J. G. C., Instantaneous Functionalization of Chemically Etched Silicon Nanocrystal Surfaces. *Angew. Chem. Int. Ed.* **2017**, *56* (22), 6073-6077.
23. Islam, M. A.; Mobarok, M. H.; Sinelnikov, R.; Purkait, T. K.; Veinot, J. G. C., Phosphorus Pentachloride Initiated Functionalization of Silicon Nanocrystals. *Langmuir* **2017**, *33* (35), 8766-8773.
24. Sanghaleh, F.; Sychugov, I.; Yang, Z.; Veinot, J. G. C.; Linnros, J., Near-Unity Internal Quantum Efficiency of Luminescent Silicon Nanocrystals with Ligand Passivation. *ACS Nano* **2015**, *9* (7), 7097-7104.
25. Jurbergs, D.; Rogojina, E.; Mangolini, L.; Kortshagen, U., Silicon nanocrystals with ensemble quantum yields exceeding 60%. *Appl. Phys. Lett.* **2006**, *88* (23), 233116.
26. Wheeler, L. M.; Anderson, N. C.; Palomaki, P. K. B.; Blackburn, J. L.; Johnson, J. C.; Neale, N. R., Silyl Radical Abstraction in the Functionalization of Plasma-Synthesized Silicon Nanocrystals. *Chem. Mater.* **2015**, *27* (19), 6869-6878.
27. Ddungu, J. L. Z.; Silvestrini, S.; Tassoni, A.; De Cola, L., Shedding Light on the Aqueous Synthesis of Silicon Nanoparticles by Reduction of Silanes with Citrates. *Faraday Discussions* **2020**. Accepted Manuscript DOI:10.1039/C9FD00127A
28. Dasog, M.; Yang, Z. Y.; Regli, S.; Atkins, T. M.; Faramus, A.; Singh, M. P.; Muthuswamy, E.; Kauzlarich, S. M.; Tilley, R. D.; Veinot, J. G. C., Chemical Insight into the Origin of Red and Blue Photoluminescence Arising from Freestanding Silicon Nanocrystals. *ACS Nano* **2013**, *7* (3), 2676-2685.
29. Sinelnikov, R.; Dasog, M.; Beamish, J.; Meldrum, A.; Veinot, J. G. C., Revisiting an Ongoing Debate: What Role Do Surface Groups Play in Silicon Nanocrystal Photoluminescence? *ACS Photonics* **2017**, *4* (8), 1920-1929.
30. Rodríguez, J. A.; Vásquez-Agustín, M. A.; Morales-Sánchez, A.; Aceves-Mijares, M., Emission Mechanisms of Si Nanocrystals and Defects in SiO₂ Materials. *J. Nanomater.* **2014**, *2014*, 409482.
31. Canham, L. T., Luminescence Bands and their Proposed Origins In Highly Porous Silicon. *phys. stat. sol. (b)* **1995**, *190*, 9-14.
32. Lee, B. G.; Luo, J.-W.; Neale, N. R.; Beard, M. C.; Hiller, D.; Zacharias, M.; Stradins, P.; Zunger, A., Quasi-Direct Optical Transitions in Silicon Nanocrystals with Intensity Exceeding the Bulk. *Nano Lett.* **2016**, *16* (3), 1583-1589.
33. Mazzaro, R.; Romano, F.; Ceroni, P., Long-lived Luminescence of Silicon Nanocrystals: From Principles to Applications. *Phys. Chem. Chem. Phys.* **2017**, *19* (39), 26507-26526.
34. DeBenedetti, W. J. I.; Chiu, S.-K.; Radlinger, C. M.; Ellison, R. J.; Manhat, B. A.; Zhang, J. Z.; Shi, J.; Goforth, A. M., Conversion from Red to Blue Photoluminescence in Alcohol Dispersions of Alkyl-Capped Silicon Nanoparticles: Insight into the Origins of Visible Photoluminescence in Colloidal Nanocrystalline Silicon. *J. Phys. Chem. C* **2015**, *119* (17), 9595-9608.
35. Dasog, M.; Bader, K.; Veinot, J. G. C., Influence of Halides on the Optical Properties of Silicon Quantum Dots. *Chem. Mater.* **2015**, *27* (4), 1153-1156.
36. Li, X.; He, Y.; Talukdar, S. S.; Swihart, M. T., Process for Preparing Macroscopic Quantities of Brightly Photoluminescent Silicon Nanoparticles with Emission Spanning the Visible Spectrum. *Langmuir* **2003**, *19* (20), 8490-8496.

37. Hessel, C. M.; Reid, D.; Panthani, M. G.; Rasch, M. R.; Goodfellow, B. W.; Wei, J.; Fujii, H.; Akhavan, V.; Korgel, B. A., Synthesis of Ligand-Stabilized Silicon Nanocrystals with Size-Dependent Photoluminescence Spanning Visible to Near-Infrared Wavelengths. *Chem. Mater.* **2012**, *24* (2), 393-401.
38. Niquet, Y. M.; Delerue, C.; Allan, G.; Lannoo, M., Method for Tight-binding Parametrization: Application to Silicon Nanostructures. *Phys. Rev. B* **2000**, *62* (8), 5109-5116.
39. Yu, Y.; Fan, G.; Fermi, A.; Mazzaro, R.; Morandi, V.; Ceroni, P.; Smilgies, D.-M.; Korgel, B. A., Size-Dependent Photoluminescence Efficiency of Silicon Nanocrystal Quantum Dots. *J. Phys. Chem. C* **2017**, *121* (41), 23240-23248.
40. Jia, X.; Zhang, P.; Lin, Z.; Anthony, R.; Kortshagen, U.; Huang, S.; Puthen-Veetil, B.; Conibeer, G.; Perez-Wurfl, I., Accurate Determination of the Size Distribution of Si Nanocrystals from PL Spectra. *RSC Adv.* **2015**, *5* (68), 55119-55125.
41. de Boer, W. D. A. M.; Timmerman, D.; Dohnalová, K.; Yassievich, I. N.; Zhang, H.; Buma, W. J.; Gregorkiewicz, T., Red Spectral Shift and Enhanced Quantum Efficiency in Phonon-Free Photoluminescence from Silicon Nanocrystals. *Nat. Nanotechnol.* **2010**, *5* (12), 878-884.
42. Delerue, C.; Allan, G.; Lannoo, M., Theoretical Aspects of the Luminescence of Porous Silicon. *Phys. Rev. B* **1993**, *48* (15), 11024-11036.
43. Wang, L. W.; Zunger, A., Electronic Structure Pseudopotential Calculations of Large (approx.1000 Atoms) Si Quantum Dots. *J. Phys. Chem.* **1994**, *98* (8), 2158-2165.
44. Hill, N. A.; Whaley, K. B., Size Dependence of Excitons in Silicon Nanocrystals. *Phys. Rev. Lett.* **1995**, *75* (6), 1130-1133.
45. Hill, N. A.; Whaley, K. B., A Theoretical Study of Light Emission from Nanoscale Silicon. *J. Electron. Mater.* **1996**, *25* (2), 269-285.
46. Ögüt, S.; Chelikowsky, J. R.; Louie, S. G., Quantum Confinement and Optical Gaps in Si Nanocrystals. *Phys. Rev. Lett.* **1997**, *79* (9), 1770-1773.
47. Hannah, D. C.; Yang, J.; Kramer, N. J.; Schatz, G. C.; Kortshagen, U. R.; Schaller, R. D., Ultrafast Photoluminescence in Quantum-Confined Silicon Nanocrystals Arises from an Amorphous Surface Layer. *ACS Photonics* **2014**, *1*, (10), 960-967.
48. Kúsová, K.; Ondič, L.; Pelant, I., Comment on “Ultrafast Photoluminescence in Quantum-Confined Silicon Nanocrystals Arises from an Amorphous Surface Layer”. *ACS Photonics* **2015**, *2* (3), 454-455.
49. Hannah, D. C.; Yang, J.; Kramer, N. J.; Schatz, G. C.; Kortshagen, U. R.; Schaller, R. D., Reply to “Comment on ‘Ultrafast Photoluminescence in Quantum-Confined Silicon Nanocrystals Arises from an Amorphous Surface Layer’”. *ACS Photonics* **2015**, *2* (3), 456-458.
50. Brown, S. L.; Miller, J. B.; Anthony, R. J.; Kortshagen, U. R.; Kryjevski, A.; Hobbie, E. K., Abrupt Size Partitioning of Multimodal Photoluminescence Relaxation in Monodisperse Silicon Nanocrystals. *ACS Nano* **2017**, *11* (2), 1597-1603.
51. Thiessen, A. N.; Ha, M.; Hooper, R. W.; Yu, H.; Oliynyk, A. O.; Veinot, J. G. C.; Michaelis, V. K., Silicon Nanoparticles: Are They Crystalline from the Core to the Surface? *Chem. Mater.* **2019**, *31* (3), 678-688.
52. Liu, S.-M.; Yang, S.; Sato, S.; Kimura, K., Enhanced Photoluminescence from Si Nano-organosols by Functionalization with Alkenes and Their Size Evolution. *Chem. Mater.* **2006**, *18* (3), 637-642.
53. Mastrorardi, M. L.; Maier-Flaig, F.; Faulkner, D.; Henderson, E. J.; Kübel, C.; Lemmer, U.; Ozin, G. A., Size-Dependent Absolute Quantum Yields for Size-Separated Colloidally-Stable Silicon Nanocrystals. *Nano Lett.* **2012**, *12* (1), 337-342.
54. Hannah, D. C.; Yang, J.; Podsiadlo, P.; Chan, M. K. Y.; Demortière, A.; Gosztola, D. J.; Prakapenka, V. B.; Schatz, G. C.; Kortshagen, U.; Schaller, R. D., On the Origin of Photoluminescence in Silicon Nanocrystals: Pressure-Dependent Structural and Optical Studies. *Nano Lett.* **2012**, *12* (8), 4200-4205.
55. Wen, X.; Zhang, P.; Smith, T. A.; Anthony, R. J.; Kortshagen, U. R.; Yu, P.; Feng, Y.; Shrestha, S.; Coniber, G.; Huang, S., Tunability Limit of Photoluminescence in Colloidal Silicon Nanocrystals. *Sci. Rep.* **2015**, *5* (1), 12469.
56. Jakob, M.; Javadi, M.; Veinot, J. G. C.; Meldrum, A.; Kartouzian, A.; Heiz, U., Ensemble Effects in the Temperature-Dependent Photoluminescence of Silicon Nanocrystals. *Chem. Eur. J.* **2019**, *25* (12), 3061-3067.
57. Breitenacker, M.; Sexl, R.; Thirring, W., On the effective mass approximation. *Z. Physik* **1964**, *182* (2), 123-129.
58. Jarolimek, K.; Hazrati, E.; de Groot, R. A.; de Wijs, G. A., Band Offsets at the Interface between Crystalline and Amorphous Silicon from First Principles. *Phys. Rev. Applied* **2017**, *8* (1), 014026.
59. Anderson, S. L.; Lubber, E. J.; Olsen, B. C.; Buriak, J. M., Substance over Subjectivity: Moving beyond the Histogram. *Chem. Mater.* **2016**, *28* (17), 5973-5975.

60. Kilaas, R., Optimal and near-optimal filters in high-resolution electron microscopy. *Journal of Microscopy* **1998**, *190*, 45-51.
61. Hessel, C. M.; Henderson, E. J.; Veinot, J. G. C., Hydrogen Silsesquioxane: A Molecular Precursor for Nanocrystalline Si-SiO₂ Composites and Freestanding Hydride-Surface-Terminated Silicon Nanoparticles. *Chem. Mater.* **2006**, *18* (26), 6139-6146.
62. Hessel, C. M.; Henderson, E. J.; Veinot, J. G. C., An Investigation of the Formation and Growth of Oxide-Embedded Silicon Nanocrystals in Hydrogen Silsesquioxane-Derived Nanocomposites. *J. Phys. Chem. C* **2007**, *111* (19), 6956-6961.
63. Clark, R. J.; Aghajamali, M.; Gonzalez, C. M.; Hadidi, L.; Islam, M. A.; Javadi, M.; Mobarok, M. H.; Purkait, T. K.; Robidillo, C. J. T.; Sinelnikov, R.; Thiessen, A. N.; Washington, J.; Yu, H.; Veinot, J. G. C., From Hydrogen Silsesquioxane to Functionalized Silicon Nanocrystals. *Chem. Mater.* **2017**, *29* (1), 80-89.
64. Dohnalova, K.; Gregorkiewicz, T.; Kusova, K., Silicon quantum dots: surface matters. *J. Phys. Condens. Matter* **2014**, *26* (17), 173201.
65. Balzar, D.; Audebrand, N.; Daymond, M. R.; Fitch, A.; Hewat, A.; Langford, J. I.; Le Bail, A.; Louër, D.; Masson, O.; McCowan, C. N.; Popa, N. C.; Stephens, P. W.; Toby, B. H., Size-strain line-broadening analysis of the ceria round-robin sample. *J. Appl. Cryst.* **2004**, *37* (6), 911-924.
66. Jakob, M.; Aissiou, A.; Morrish, W.; Marsiglio, F.; Islam, M.; Kartouzian, A.; Meldrum, A., Reappraising the Luminescence Lifetime Distributions in Silicon Nanocrystals. *Nanoscale Res. Lett.* **2018**, *13* (1), 383.
67. Dabbousi, B. O.; Rodriguez-Viejo, J.; Mikulec, F. V.; Heine, J. R.; Mattoussi, H.; Ober, R.; Jensen, K. F.; Bawendi, M. G., (CdSe)ZnS Core-Shell Quantum Dots: Synthesis and Characterization of a Size Series of Highly Luminescent Nanocrystallites. *J. Phys. Chem. B* **1997**, *101* (46), 9463-9475.
68. Lee, B. G.; Hiller, D.; Luo, J. W.; Semonin, O. E.; Beard, M. C.; Zacharias, M.; Stradins, P., Strained Interface Defects in Silicon Nanocrystals. *Adv. Funct. Mater.* **2012**, *22* (15), 3223-3232.
69. Kleovoulou, K.; Kelires, P. C., Stress state of embedded Si nanocrystals. *Phys. Rev. B* **2013**, *88*, 085424.
70. Miller, J. B.; Van Sickle, A. R.; Anthony, R. J.; Kroll, D. M.; Kortshagen, U. R.; Hobbie, E. K., Ensemble Brightening and Enhanced Quantum Yield in Size-Purified Silicon Nanocrystals. *ACS Nano* **2012**, *6* (8), 7389-7396.
71. Huisken, F.; Ledoux, G.; Guillois, O.; Reynaud, C., Light-Emitting Silicon Nanocrystals from Laser Pyrolysis. *Adv. Mater.* **2002**, *14* (24), 1861-1865.
72. Delerue, C.; Allan, G.; Reynaud, C.; Guillois, O.; Ledoux, G.; Huisken, F., Multiexponential Photoluminescence Decay in Indirect-Gap Semiconductor Nanocrystals. *Phys. Rev. B* **2006**, *73* (23), 235318.
73. Belyakov, V. A.; Burdov, V. A.; Gaponova, D. M.; Mikhaylov, A. N.; Tetelbaum, D. I.; Trushin, S. A., Phonon-Assisted Radiative Electron-Hole Recombination in Silicon Quantum Dots. *Phys. Solid State* **2004**, *46*, 27-31.
74. Belyakov, V. A.; Burdov, V. A.; Lockwood, R.; Meldrum, A., Silicon Nanocrystals: Fundamental Theory and Implications for Stimulated Emission. *Adv. Opt. Technol.* **2008**, *2008*, 279502.
75. Lannoo, M.; Delerue, C.; Allan, G., Nonradiative Recombination on Dangling Bonds in Silicon Crystallites. *J. Lumin.* **1993**, *57* (1), 243-247.
76. Bae, W. K.; Padilha, L. A.; Park, Y.-S.; McDaniel, H.; Robel, I.; Pietryga, J. M.; Klimov, V. I., Controlled Alloying of the Core-Shell Interface in CdSe/CdS Quantum Dots for Suppression of Auger Recombination. *ACS Nano* **2013**, *7* (4), 3411-3419.

Chapter 4

Insights into the Structure and Optical Response of Oxidized Silicon Nanoparticles: A Study on the Role of Structure on Oxidation

4.1 Introduction

The photoluminescent properties of silicon-based materials has been of great interest to researchers since first demonstrated for porous silicon by Leigh Canham in 1990.¹ Silicon nanomaterials exhibit photoluminescence across the visible spectrum,²⁻⁴ which makes them particularly useful for application as fluorescent probes,^{5, 6} sensors,⁷ luminescent solar concentrators,^{8, 9} and light-emitting diodes.^{10, 11} Orange to near infrared photoluminescence typically is ascribed to quantum confinement and exhibits microsecond luminescent lifetimes that are attributed to the indirect band gap of silicon.¹²

The desirable photoluminescent properties of silicon nanoparticles (SiNPs) can be impacted deleteriously by oxidation of the silicon to form SiO_x ,¹² however, the exact role of the oxygen species is still unclear. In porous silicon and SiNPs, silicon oxidation can introduce a new radiative decay at high energy (i.e. 400–500 nm), known as the F-band due to its short photoluminescence lifetimes.^{13, 14} It is speculated that the F-band arises from intrinsic core emission from small SiNPs¹⁵ or oxygen defects,¹⁶ but strong luminescence from the band often is observed for highly oxidized systems.¹⁴ In addition to its influence over the F-band, oxidation of colloidal systems also leads to a shift in the S-band (the longer-lived excited state associated with quantum confinement in the silicon core).¹⁷ A handful of theories on the origin of this shift exist in the literature. One theory suggests that this band is comprised of two components: one with a longer lifetime (due to the quantum confinement of the core) and one with a shorter lifetime (attributed to donor–acceptor recombination within states associated with the native oxide shell).¹⁸ Another theory suggests that electron–phonon coupling between excitons in the SiNPs and Si-O-Si phonons in the shell limits the photoluminescence tunability of these materials.¹⁹ The blue shift also has been attributed to shrinking of the crystalline core, consistent with quantum confinement of the carriers.²⁰ Beyond the photoluminescence emission wavelengths, the impact of oxidation on the photoluminescence quantum yields is varied in the literature, with

reports showing both quenching (for H-terminated SiNPs)²¹ and enhancement of the S-band (for dodecyl-passivated SiNPs).²² Insight into structural changes that occur in SiNPs during oxidation may illuminate the evolving photoluminescence properties during oxidation.

Structural changes during oxidation of hydride-terminated SiNPs (H-SiNPs), including an examination of the change in surface structure, crystalline core size, and radical concentration, have been explored.²³ Examination of the oxidation process using electron spin resonance (ESR) shows an initial decrease in unpaired electron defect density for plasma synthesized H-SiNCs that is attributed to the formation of surface Si-O-Si bonds, following the Cabrera–Mott oxidation theory. As more oxidation occurs, the defect density begins to increase due to introduction of interfacial defects, with further formation of Si-O-Si bridges.^{23, 24} During this process, surface Si–H species are replaced with Si-O-Si, as evidenced by FTIR, and the crystalline core decreases.²³⁻²⁵ The strain within the nanoparticle also changes, though the exact nature of this strain is debated.^{26, 27} A recent report exploring the impact of oxidation on strain in plasma synthesized H-SiNPs showed that oxidation causes the initially unstrained SiNPs to become compressively strained.²⁸ Size dependence of the structural changes associated with oxidation and their impact on the photoluminescence of SiNPs have not been studied comprehensively .

The goal of this work was to make SiNPs of different sizes with varying degrees of oxidation to investigate the influence of oxidation on the internal structure and photoluminescence response. Understanding the size-dependent structural changes that SiNPs undergo as they oxidize may help identify if the blue-shift in the photoluminescence occurs primarily due to the shrinking of the core,²⁰ if other factors (such as trap-states) play a role,^{18, 19} or combinations thereof.

To accomplish this, we aimed to control the oxidation of SiNPs by varying the degree of surface functionalization, drawing on our established understanding of radical-initiated hydrosilylation reactions on SiNP surfaces, and to limit their progression.^{22, 29} To ensure that the starting SiNPs were identical (apart from the varied level of surface functionalization), aliquots were removed from hydrosilylation reaction mixtures. The resulting materials were purified via centrifugation, then stored in a home-built relative humidity chamber at $73 \pm 5\%$ humidity for 30 days to ensure uniform oxidation. The resulting materials were characterized using XPS,

synchrotron XRD, and brightfield TEM to identify changes in the structure and photoluminescence spectroscopy (steady-state and time-resolved) in order to identify changes in the optical response.

4.2 Experimental Section

4.2.1 Materials

4.2.1.1 Starting Materials

Hydrofluoric acid (Electronic grade, 48–50%) was purchased from Fischer Scientific. sulfuric acid (reagent grade, 95–98%) was purchased from Caledon Laboratory Chemicals. Fuming sulfuric acid (reagent grade, 20% free SO₃ bases), ethanol (reagent grade, 100%), 1-dodecene (95%), azobisisobutyronitrile (AIBN), and trichlorosilane (99%) were purchased from Sigma (now MilliporeSigma). All reagents were used as received, unless otherwise specified. All solvents were reagent grade and used as received. Toluene was collected from a Pure-Solv purification system immediately prior to use. Benzene was purchased from EMD Millipore (now Millipore Sigma).

4.2.1.2 Preparation of Hydrogen Silsesquioxane (HSQ)

HSQ was prepared as outlined in Section 2.2.1.2.

4.2.1.3 Preparation of Hydride-Terminated Silicon Nanoparticles (H-SiNPs)

Silicon nanoparticles were prepared via the thermal disproportionation of HSQ under a slightly reducing atmosphere (5% H₂/95% Ar) at 1100, 1200, and 1300 °C, as previously reported.³ This yielded SiNP/SiO₂ composites that were ground using an agate mortar and pestle, followed by shaking in a wrist action shaker with high purity glass beads for 6 h. The resulting powder was dried using vacuum filtration and the resulting powder was stored.

Subsequently, 1.5 g of the ground SiNP/SiO₂ composite was etched using 45 mL of 1:1:1 mixture of ethanol:DI water:HF for 1 h to remove the SiO₂ surface. Longer etching times were used to remove a portion of the amorphous layer: the composite annealed at 1200 °C was etched for 2 h, and the composite annealed at 1300 °C was etched for 4 h. The resulting particles were extracted with three aliquots of ~10 mL of toluene and purified via centrifugation with toluene at 5000 rpm three times. The resulting H-SiNPs were functionalized immediately as follows.

4.2.1.4 Preparation of Alkyl-Passivated SiNPs with Varied Surface Coverage

The H-SiNCs obtained from the etching procedure were redispersed in dry toluene (~15 mL) and transferred into an oven-dried Schlenk flask with a teflon-coated magnetic stir bar and attached to an argon-charged Schlenk line. Then, 1-dodecene (~15 mL) and AIBN (~0.19 mmol) were added, and the reaction mixture was subjected to three freeze-pump-thaw cycles. The reaction was heated and maintained at 70 °C for 900 min, with aliquots removed after 30, 45, and 75 min to yield SiNPs with varied surface coverage. Reaction times were chosen based on in situ IR studies previously reported for this functionalization method.²⁹ Reaction aliquots were placed in PTFE centrifuge tubes with 2 mL of acetonitrile and 30 mL of ethanol and stored for the duration of the reaction (i.e. 900 min) at -20 °C.

Once the reaction was completed (i.e., after 900 min), the remaining SiNPs also were placed into a PTFE centrifuge tube with approximately equal volumes of acetonitrile and ethanol. The four mixtures were centrifuged at 12,000 rpm for 1 h to isolate the SiNPs. The supernatant was decanted, and the precipitate was redispersed in ~5 mL of toluene. A small amount of acetonitrile (~2 mL) was added, and the centrifuge tube was filled to ~50 mL with ethanol. This solvent/antisolvent precipitation method was repeated twice, and the resulting particles were redispersed in toluene for storage.

4.2.1.5 Oxidation of Alkyl-Passivated SiNPs

To oxidize the SiNPs bearing varied surface coverage, open 4 dram glass vials containing the SiNPs dispersed in ~5 mL of toluene were stored in a home-built humidity chamber at $73 \pm 5\%$ relative humidity for 30 days. These oxidized SiNPs subsequently were characterized. A schematic representation of the humidity chamber, whose temperature was maintained at room temperature (293 ± 1 K), can be found in Figure 4-1.³⁰ The set-up did not allow for monitoring the flow rate.

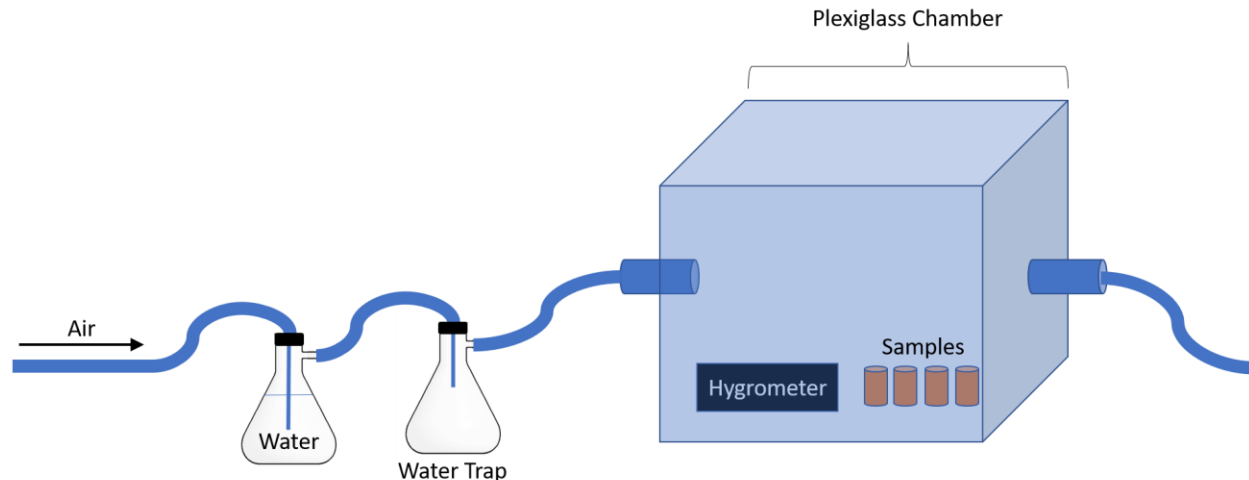


Figure 4-1. Schematic representation of a home-built relative humidity chamber. The blue box represents the plexiglass box that was taped shut, and the orange cylinders represent the vials containing toluene solutions of the silicon samples.

4.2.2 Characterization

4.2.2.1 Thermogravimetric Analysis (TGA)

TGA was performed using a Mettler Toledo Star TGA/DSC system. SiNP samples were lyophilized from benzene and then placed into a Pt pan and heated under an Ar atmosphere from 25 to 800 °C at a rate of 10 °C/min.

4.2.2.2 X-ray Photoelectron Spectroscopy (XPS)

Samples were prepared by drop casting silicon nanoparticles from toluene solutions onto copper foil. All XPS data were collected using a Kratos (Manchester, UK) AXIS Supra system at the Saskatchewan Structural Sciences Centre. This system is equipped with a 500 mm Rowland circle monochromated Al K- α (1486.6 eV) source and combined hemi-spherical analyzer and spherical mirror analyzer. A spot size of hybrid slot (300x700) microns was used. All survey scan spectra were collected in the 0–1275 binding energy range using 1 eV steps, with a pass energy of 160 eV. High resolution scans of multiple regions also were conducted using 0.05 eV steps, with a pass energy of 20 eV. An accelerating voltage of 15 keV and an emission current of 15 mA were used for the high-resolution analysis.

4.2.2.3 X-ray Diffraction (XRD)

Powder diffraction data was collected at the Canadian Light Source using the CMCF beamline. Samples were loaded in polyimide Kapton tubes, with an inner diameter of 0.488 mm and outer

diameter of 0.538 mm, purchased from Cole-Parmer. The samples were loaded into the set up using a magnetic sample holder in transmission mode. Powder data was collected using a Rayonix MX300HE 2D detector, with a detector distance of 150 mm. The beam energy was set to 18 keV, with a spot size of 150 microns. The synchrotron radiation wavelength was calibrated using a LaB₆ standard and found to be 0.68745 Å. The powder data was integrated using GSAS-II using the LaB₆ calibration to identify the integration area and radiation wavelength. The background from the empty Kapton also was subtracted prior to integration.

Pawley fitting of the powder pattern was performed using TOPAS³¹ to determine the crystallite domain size with integral breadth, FWHM, and Lorentzian broadening methods. Instrumental effects were accounted for by refining a NIST Si line shape standard (640f) to ensure instrument alignment and pattern line shape. A sample-independent synthetic peak was required at ~8.4° as well as other small peaks (8, 9, 11, 14, 16, and 19°) due to imperfections in the background subtraction from the Kapton tube (sample holder).

4.2.2.4 Electron Microscopy

Transmission electron microscopy (TEM) and HR-TEM were performed on a JEOL JEM-ARM200CF S/TEM (Cold Field Emission Gun) electron microscope, with an accelerating voltage of 200 kV using SiQDs drop-coated from a toluene solution onto a holey carbon-coated copper grid. The SiQD size was determined by averaging the size of 300 particles using ImageJ software (version 1.51j8) and plotted as an average-shifted histogram, as outlined previously.³²

4.2.2.5 Photoluminescence Spectroscopy

Photoluminescence spectroscopy measurements were performed for toluene dispersions of silicon nanoparticles in a 1 mL quartz cuvette. Silicon nanoparticles were excited using the 351 nm line of an Ar ion laser (20 mW). The resulting photoluminescence was collected by an optical fiber, passed through a 500 nm long-pass filter to eliminate scattered light from the excitation source, and fed into an Ocean Optics USB2000 spectrometer. The spectral response of the spectrometer was calibrated using a blackbody radiator (Ocean Optics LS1). Photoluminescence lifetimes were acquired using an Ar ion laser (351 nm, 20 mW), modulated by an acousto-optic modulator (50 ns response time) and operated at a frequency of 200 Hz with a 50% duty cycle. The emitted light was fed into an optical fiber and passed through a 500 nm

long-pass filter; it was then incident on a Hamamatsu H7422P-50 photomultiplier tube (PMT) interfaced with a Becker-Hickl PMS-400A gated photon counter. The photoluminescence data were collected with a total of 10,000 sweeps for good signal-to-noise ratio and using 1 μ s time steps. A log-normal fitting of the data in MatLab was used to determine the luminescence decay rate.

4.3 Results and Discussion

4.3.1 Size Dependent Impact of Oxidation on Structure of SiNPs

To determine the impact of the oxidation on SiNP structure and photoluminescence, we first must establish that the SiNPs that were originally identical were functionalized and, by extension, oxidized to different extents. In this work, this was accomplished by functionalizing H-SiNPs of different sizes (nominally 3, 5, and 7 nm SiNPs based on TEM derived diameter, d_{TEM} ; Figure 4-2) to varying degrees using the well-established radical-initiated hydrosilylation approach.³³ Following previous work by our group, we set out to make SiNPs with varying degrees of functionalization by controlling the time for which radical-initiated hydrosilylation reactions proceeded.²⁹ Based on this work, three reaction times (30, 45, and 75 min; Figure 4-3) were chosen, and aliquots were extracted from the reaction mixture at these time intervals while maintaining stirring. This approach relies on the assumptions that removing aliquots does not influence the reaction progression, that the reaction mixture is homogenous, and that materials within these aliquots are representative of the reaction mixture at that time. The remaining reaction mixture was left to react for 900 min to achieve maximal functionalization (i.e., ~40% surface coverage). Aliquots were stored at -20 °C until isolation of the final sample (i.e., the long-term overnight reaction, 900 min). Subsequently, the reaction mixtures were purified, and the products were collected and stored in toluene in a home-built humidity chamber at $73 \pm 5\%$ humidity for 30 days to allow further oxidation of the SiNPs.²³ This work assumes that oxidation due to purification and oxidation due to the storage in the humidity chamber are equivalent (i.e., similar oxidation species).

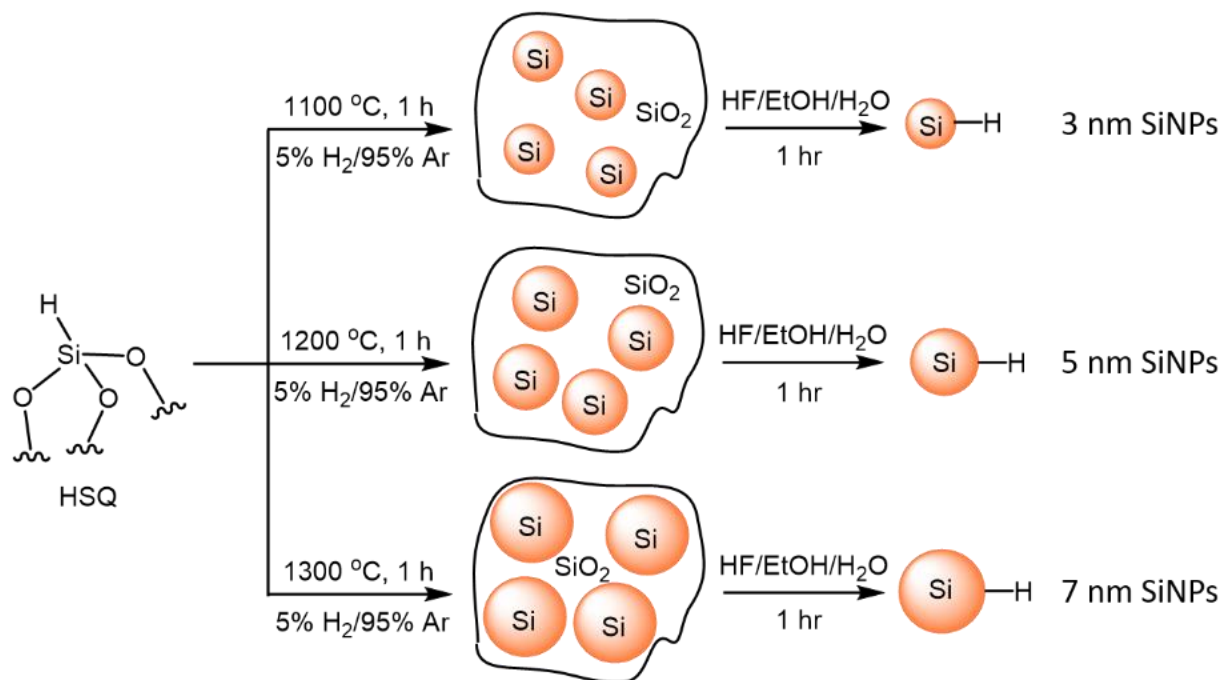


Figure 4-2. Formation of different sizes of SiNP through thermal annealing of hydrogen silsesquioxane (HSQ), and subsequent liberation to form H-SiNPs of various sizes.

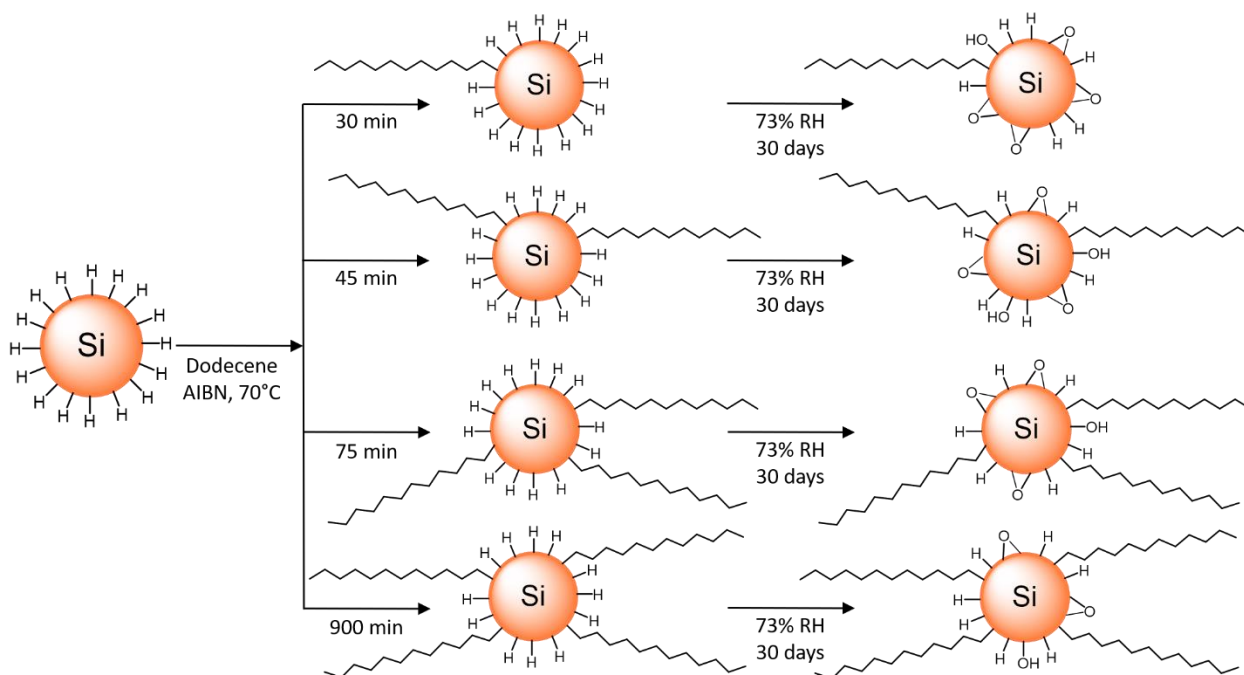


Figure 4-3. Schematic representation of reaction showing different levels of functionalization obtained through different reaction times. Si-H represents all Si-H_x ($x = 1-3$) species. This ultimately leads to different levels of oxidation after exposure to 73% relative humidity for 30 days.

To estimate the degree of surface coverage for the samples investigated here, thermogravimetric analysis (TGA) was performed. TGA for 3, 5, and 7 nm SiNPs (d_{TEM}) are shown in Figure 4-4. Using the weight loss from the thermal degradation, the surface coverage of the ligand can be approximated, as shown in Table 4-1.^{33, 34} This method of surface coverage determination assumes that the surface coverage is homogeneous throughout the samples and that all weight loss observed between 200 and 550 °C arises from the release of covalently bonded dodecyl ligands. The results of the surface coverage analysis for 7 nm SiNPs indicate that SiNPs isolated after 30 min reaction have less surface passivation than those isolated after 900 min. Samples functionalized for 45 and 75 min showed the same surface coverage within the error of the measurement. The 3 nm SiNPs also showed less surface coverage for samples functionalized for 30 min compared to 900 min. Overall, as the d_{TEM} increases, the surface coverage is less for SiNPs functionalized for 900 min, as shown in Table 4-1.

X-ray photoelectron spectroscopy (XPS) was employed to probe the degree of surface oxidation for the present samples. High resolution Si 2p XPS was used to help evaluate the relative surface oxidation of the samples. The Si 2p spectra were deconvoluted into component spin-orbit couples (Si 2p_{1/2} and 2p_{3/2}) corresponding to Si (0) (i.e., orange), Si (I) (i.e., green), Si (II) (i.e., purple), Si (III) (i.e., blue), and Si (IV) (i.e., magenta), as shown in Figure 4-5.

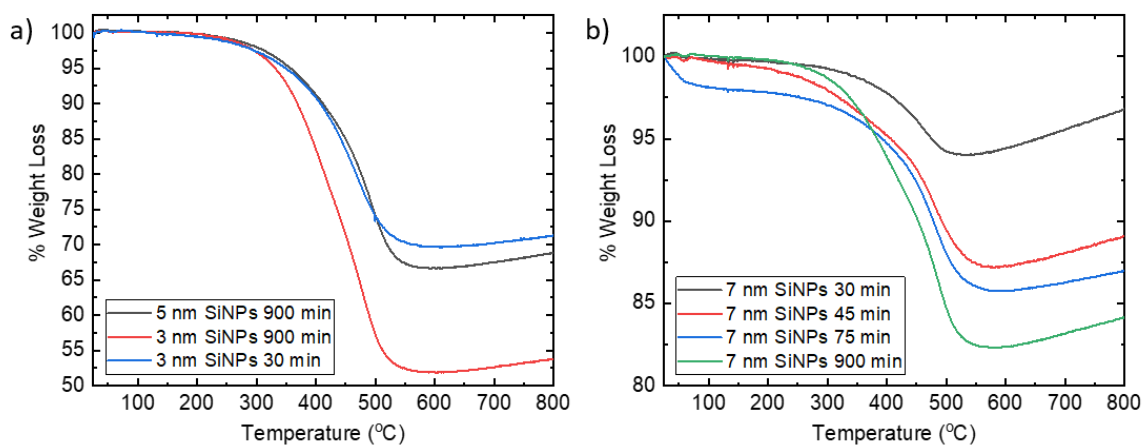


Figure 4-4. TGA plot of dodecyl-terminated a) 3, 5, and b) 7 nm SiNPs functionalized for different lengths of time. The experiments were performed with a heating rate of 10 °C/min in an Ar atmosphere. The initial weight loss in the 7 nm 75 min sample is due to residual solvent loss.

Table 4-1. Surface coverage determination using TGA

Sample	Funct. Time (min)	% wt. loss	% mole of ligand	% mole of Si atoms	Ligands per SiNP	% Surface Coverage ^a
7 nm SiNPs	30	5.9	0.03	3.4	106	7
7 nm SiNPs	45	12.8	0.08	3.1	244	17
7 nm SiNPs	75	12.8	0.08	3.1	243	17
7 nm SiNPs	900	17.6	0.10	2.9	356	25
5 nm SiNPs	900	33.4	0.20	2.4	267	40
3 nm SiNPs	30	30.3	0.18	2.5	43	20
3 nm SiNPs	900	48.1	0.28	1.8	92	42

^a Methods used to calculate surface coverage are summarized in Appendix B.

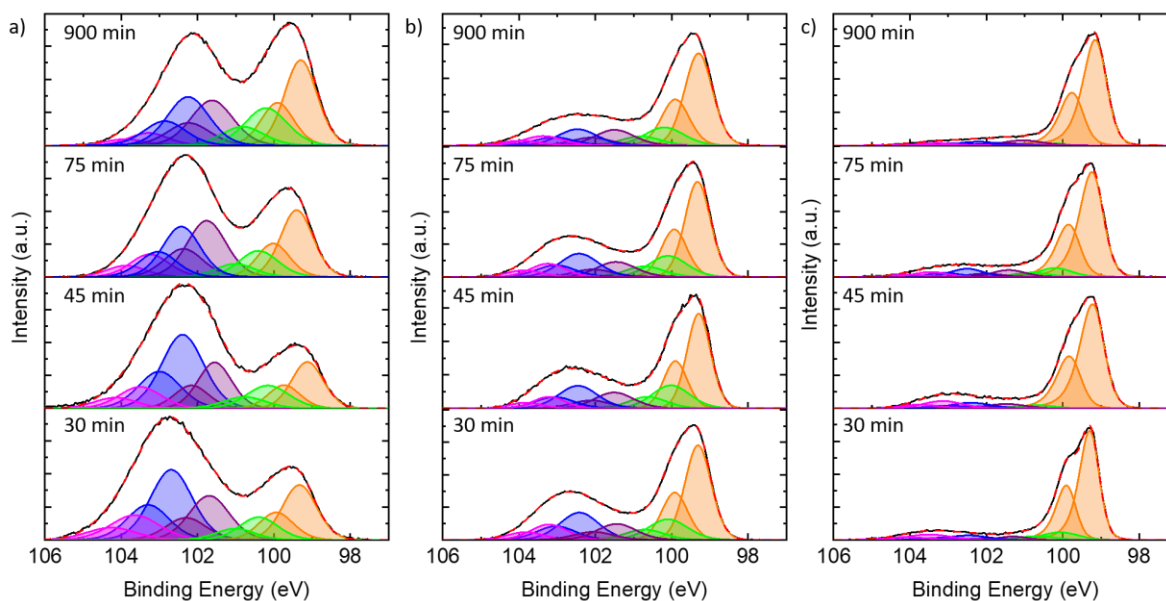


Figure 4-5. High resolution Si 2p spectrum showing the $2p_{3/2}$ and $2p_{1/2}$ emissions for a) 3 nm, b) 5 nm, and c) 7 nm SiNPs with different levels of surface passivation after oxidation. The colored traces correspond as follows: black = experimental data, dashed red = fitting envelope, orange = core Si, green = $\sim\text{SiO}_{0.5}$ or silicon-carbon species, purple = $\sim\text{SiO}$, blue = $\sim\text{SiO}_{1.5}$, and magenta = $\sim\text{SiO}_2$.

The spin-orbit couples were fitted with a Voigt GL(30) lineshape (70% Gaussian, 30% Lorentzian); the only exception was fitting the Si (0) emission for samples with a crystallite size >5 nm (vide infra), where a Lorentzian asymmetric line shape $LA(a, b, n)$ was employed (see Chapter 2, page 51 for detailed discussion). Samples functionalized for 900 min consistently have the least amount of higher binding energy (i.e., Si (I), (II), (III), (IV)) Si, based on deconvolution of Si 2p XP spectra; these species can be attributed to increased oxidation (though Si-F species contribute to emissions in this spectral region) and that the samples functionalized for shorter periods have more of these higher oxidation state species.

To investigate this characteristic further, the intensity of high binding energy Si components was used to estimate the O to Si ratio within the SiNPs (See: Appendix C) and compared to the functionalization time. To account for differences in particle size, the calculation was normalized to the surface area to volume ratio (SA/V), as found in Figure 4-6a. The SA/V was estimated from d_{TEM} assuming a simple spherical model. Generally, the O:Si ratio is lower for SiNPs functionalized for longer (i.e. 900 min vs. 30 min). The results were compared to the ratio of the atm% O and Si found in the survey XPS scan (Table 4-2); it was found that similar trends in the O:Si ratio emerged (Figure 4-6b). The higher ratio of O:Si obtained from the XPS survey scan can be attributed to carbon–oxygen species that typically are found in adventitious carbon.³⁵ Smaller particles (i.e., $d_{TEM} = 3$ nm) functionalized for 30 min have more oxidation, even when normalized to the surface area to volume ratio, than their larger counterparts, as demonstrated by Figure 4-5. This is reasonable as the higher surface area to volume ratio is also likely to make them more reactive.

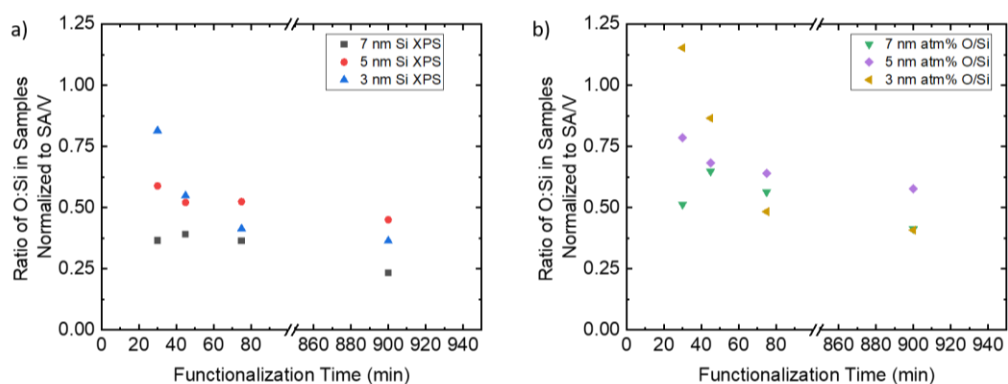


Figure 4-6. Plots showing the ratio of oxygen and silicon normalized to the surface area to volume ratio for the SiNPs calculated from a) the ratio of high oxidation state Si and b) the relative atm% from the survey spectrum.

Table 4-2. Table of surface area to volume ratio (SA/V) and relative atm% of Si, C, O, and F from survey XPS spectrum

Sample	Funct. Time	SA/V	Si (atm%)	C (atm%)	O (atm%)	F (atm %)
7 nm SiNPs	30 min	0.83	45	35	19	1.2
	45 min	0.82	40	37	22	1.3
	75 min	0.82	38	43	18	1.0
	900 min	0.82	34	53	12	1.4
5 nm SiNPs	30 min	1.05	26	51	22	0.5
	45 min	1.20	26	52	21	0.4
	75 min	1.20	26	54	20	0.5
	900 min	1.20	22	62	15	0.9
3 nm SiNPs	30 min	1.28	16	59	24	0.6
	45 min	1.94	11	70	19	0.0
	75 min	2.17	18	62	19	0.2
	900 min	2.10	15	71	13	0.5

While XPS provides a measure of particle oxidation, it provides limited quantification of the surface oxide due to the presence of adventitious and passivating hydrocarbons.³⁶ The presence of the hydrocarbons impacts the photoelectron attenuation length (attenuation length of Si2p electron travelling through an alkyl monolayer on silicon is 3.24 nm, and the attenuation length through silicon is 1.8 nm),³⁶ thus limiting the depth that can be probed within the SiNP. This dampening effect of the carbonaceous species (from increased adventitious carbon or increased surface coverage) will differ from sample to sample because each SiNP system was functionalized differently purposefully for the present study.³⁶ The influence of the dampening is expected to be the greatest for more completely functionalized samples obtained from longer reaction times; this implies that XPS analyses will probe the surface of these SiNPs more effectively. For the present study, samples functionalized for 900 min showed the lowest amount of oxidation and should be the most surface limited. Hence, it is reasonable that they are less oxidized than the samples functionalized for the shortest length of time.

To evaluate the impact of oxidation on the internal SiNP structure, we examined the overall nanoparticle size (d_{TEM}) and compared it to the size of the crystalline domain (d_{XRD}). We used brightfield TEM (Figure 4-7) to evaluate the change in size with increased oxidation and found that d_{TEM} generally increased with oxidation.

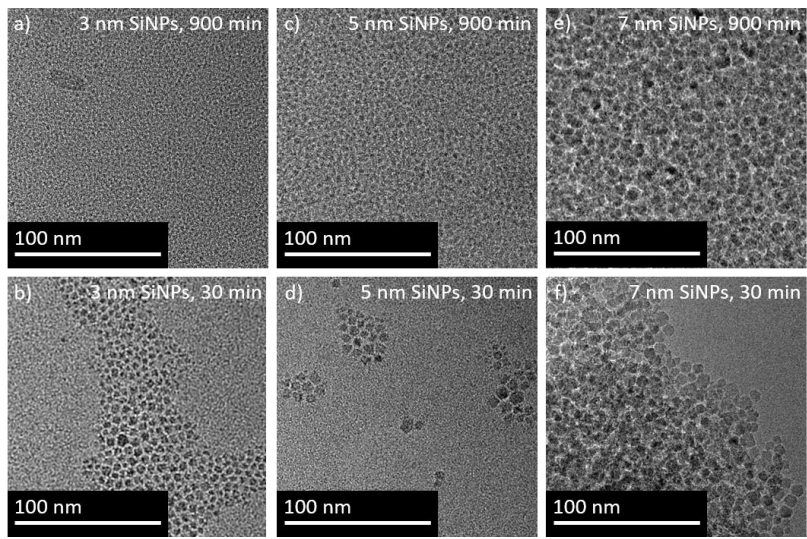


Figure 4-7. Brightfield TEM images showing (a and b) 3, (c and d) 5, and (e and f) 7 nm SiNPs functionalized for (a,c,e) 900 and (b, d, f) 30 min after oxidation.

Size distributions were plotted as average shifted histograms (Figure 4-8).³² The difference in d_{TEM} ($d_{\text{TEM}, 30 \text{ min}} - d_{\text{TEM}, 900 \text{ min}}$) provides an estimate for the change in diameter arising as a result of oxidation; we observe that it is inversely related to the d_{TEM} of particles functionalized for 900 min ($d_{\text{TEM}, 900 \text{ min}}$; Figure 4-9). From this, we conclude that smaller SiNPs grow more than larger SiNPs with upon oxidation.

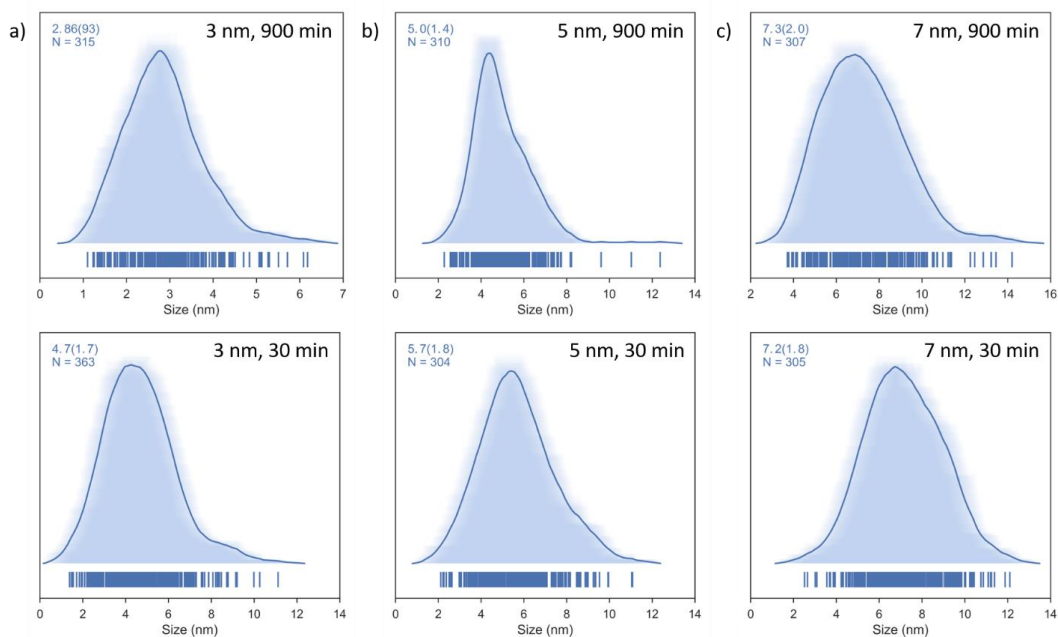


Figure 4-8. Histograms showing the size distribution of a) 3, b) 5, and c) 7 nm SiNPs functionalized for 900 min (top) and for 30 min (bottom). Sizes were determined based on brightfield TEM imaging.

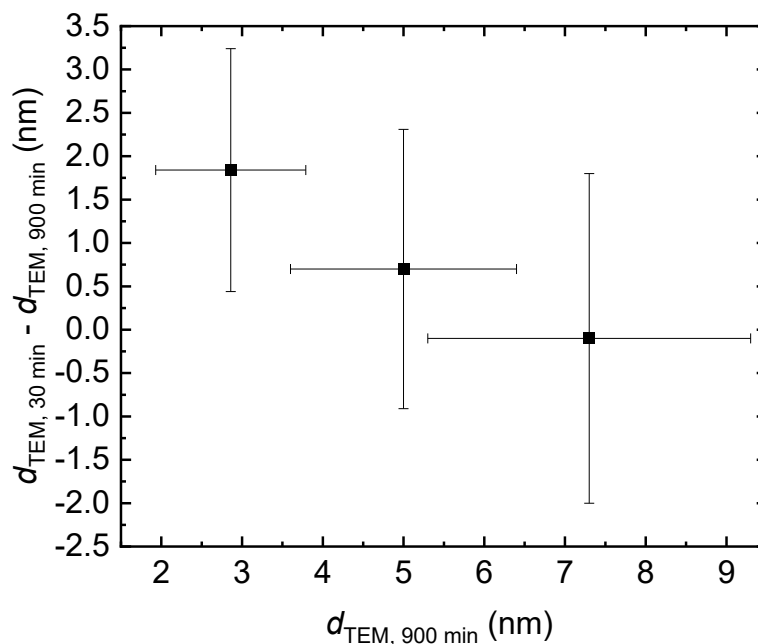


Figure 4-9. A plot showing the difference in d_{TEM} for samples functionalized for 30 min ($d_{TEM, 30 \text{ min}}$) and 900 min ($d_{TEM, 900 \text{ min}}$) as a function of $d_{TEM, 900 \text{ min}}$. Error bars represent standard deviations based on the size distributions.

To complement the TEM size analyses, we also evaluated the crystalline domain using XRD (d_{XRD}). Through refinement of the powder pattern (Figure 4-10), as outlined previously,³⁷ we gained insight into the domain size, associated strain, and lattice parameter for each of the samples. The crystalline domain size decreases with increased oxidation for 3 and 5 nm SiNPs (Figure 4-11a and b). The short-range order ($d_{XRD} = 1.3 \text{ nm}$) virtually disappears ($d_{XRD} = 0.7 \text{ nm}$) for the 3 nm SiNPs, consistent with oxidation disrupting structural order in the small domains. In cases in which a larger domain exists ($d_{XRD} = 3.3 \text{ nm}$), the decrease in crystalline domain size is more pronounced (change in $d_{XRD} = 1.8 \text{ nm}$). The largest SiNPs studied here ($d_{TEM} = 7 \text{ nm}$) do not show a significant change in the size.

XRD can also provide information related to changes in crystal strain, which manifests as broadening of the reflection (non-uniform broadening) and changes in lattice parameter (uniform broadening).³⁸ Falcão et al. showed that unstrained SiNPs synthesized using a nonthermal plasma showed increased compressive strain upon oxidation.²⁸ No similar investigation of SiNPs prepared using the HSQ method has been performed.

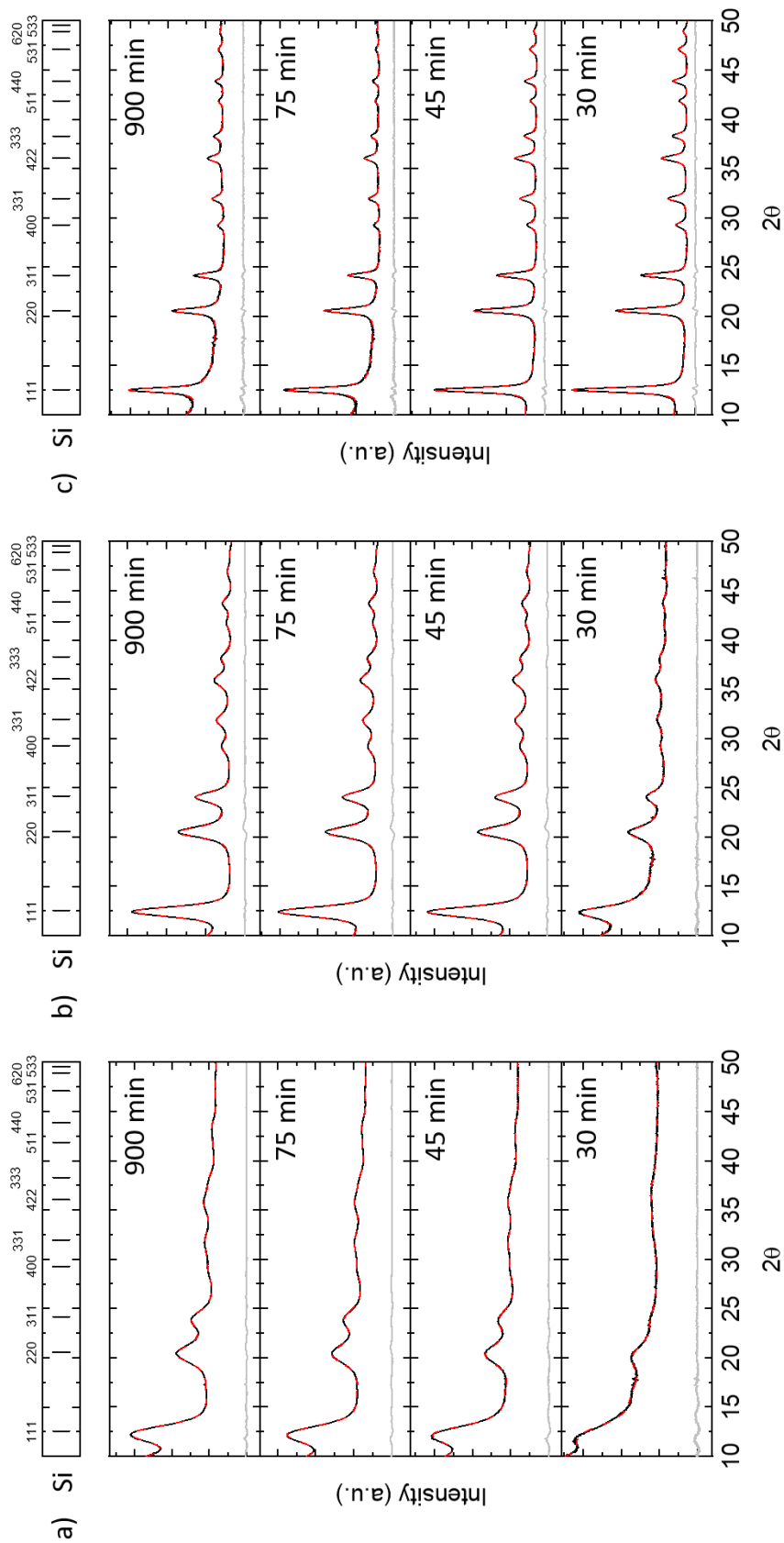


Figure 4-10. XRD patterns for a) 3 nm, b) 5 nm, and c) 7 nm SiNPs (nominally) functionalized for different lengths of time after oxidation, showing the experimental data (black trace), the fit (red, dashed trace), and the difference between the two (gray trace). All samples except the smallest, most oxidized SiNPs show reflections characteristic of crystalline Si (as indexed above the plots).

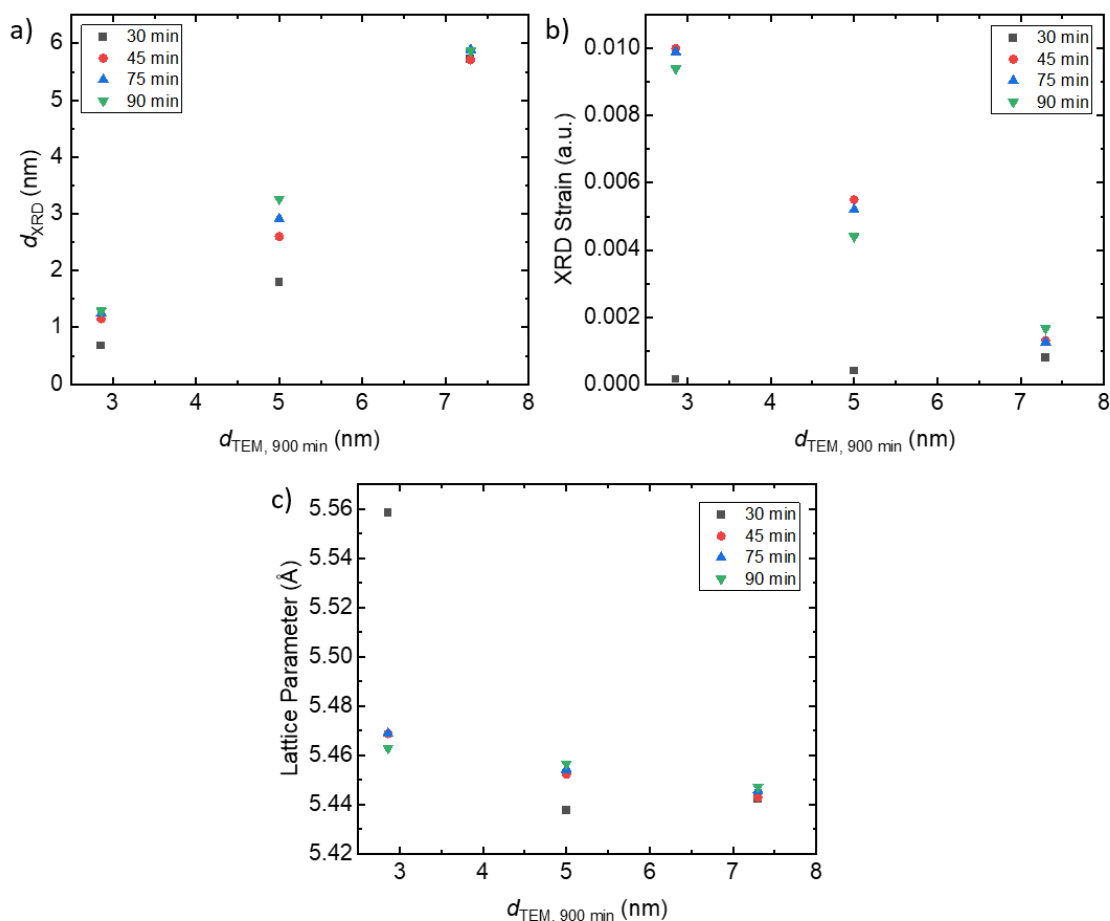


Figure 4-11. Plots comparing the a) size, b) strain, and c) lattice parameter determined from the XRD fitting for the SiNPs functionalized for different amounts of time and different functionalized TEM sizes.

Synchrotron XRD provides more Bragg reflections than what is observed from a lab scale experiment utilizing a Cu K α source. As a result, a more accurate determination of the size and strain of the crystalline domain is possible because these parameters scale with $1/(\cos \theta)$ and $\tan \theta$, respectively. Refinement of the powder pattern provides insight into size and strain induced broadening of the peaks. The fitting showed decreased strain for the most oxidized 3 and 5 nm SiNPs (See: Figure 4-11b). For the 3 nm SiNPs, this likely arises because the crystalline core has largely amorphized. This is evidenced by d_{XRD} (i.e., 0.68 nm) approaching the lattice parameter for bulk silicon (i.e., 0.543 nm), suggesting that little crystalline domain remains, and that the lattice parameter of the crystallite increases compared to bulk crystalline silicon (~ 5.56 vs 5.43 Å; Figure 4-9c), suggesting that the average spacing between atoms is increasing.

For 5 nm SiNPs, a more interesting situation arises. The d_{XRD} corresponds to a few unit cells (i.e., ~ 3 unit cells for $d_{\text{XRD}, 30 \text{ min}}$), and the lattice parameter approaches that observed for crystalline silicon (i.e., $\sim 5.43 \text{ \AA}$). In this sample, lattice parameter shifts toward values that are more consistent with bulk systems as the level of oxidation increases. The widened lattice parameter (5.46 \AA) for samples functionalized for 900 min suggests that tensile (i.e., expansive) strain exists in the less oxidized SiNPs. This suggests atoms are, on average, located further apart from each other. With increased oxidation (and decreased functionalization time), a decrease in the lattice parameter is observed (5.44 \AA), suggesting that the atoms are, on average, closer together. The shift to a less strained system can be attributed to the compressive strain caused by the oxidation of the nanoparticle²⁸ counteracting the tensile strain present in the less oxidized SiNPs. It is unclear how much the change in strain within these systems can be attributed to the oxidation and how much is induced by differing degrees of functionalization.³⁹ For the 7 nm SiNPs, where less strain is observed, the strain within the SiNPs remains largely unchanged, with varying degrees of oxidation. This likely results from a combination of having less strain initially and less oxidation. Further work using variable temperature XRD at the synchrotron would elucidate useful information about the nature of the strain in these systems and allow more accurate quantification.

4.3.2 Impact of Oxidation on the Optical Response of SiNPs

It is well-known that oxidation of freestanding SiNPs impacts their optical properties. The goal of the work described in this chapter was to gain insight into the role of the crystalline domain of oxidized SiNPs in the photoluminescence response; clearly, the present system is exceptionally complex, with contributions from interconnected factors, such as NP size, crystallinity, strain, surface oxidation, among others. We endeavored to prepare and structurally interrogate SiNPs of different sizes and surface chemistry that would lead to differing degrees of oxidation (see above). Subsequently, we evaluated SiNP photoluminescence emission and lifetimes in the context of d_{TEM} and d_{XRD} as well as the amount of surface functionalization.

A blue-shift of the photoluminescence maximum was observed for less functionalized 3 and 5 nm SiNPs after oxidation (Figure 4-12a and b). In contrast, the emission maximum of 7 nm SiNPs remained constant (Figure 4-12c). The shifting photoluminescence seems to correlate with the decrease in d_{XRD} for the samples and be consistent with carrier quantum confinement.

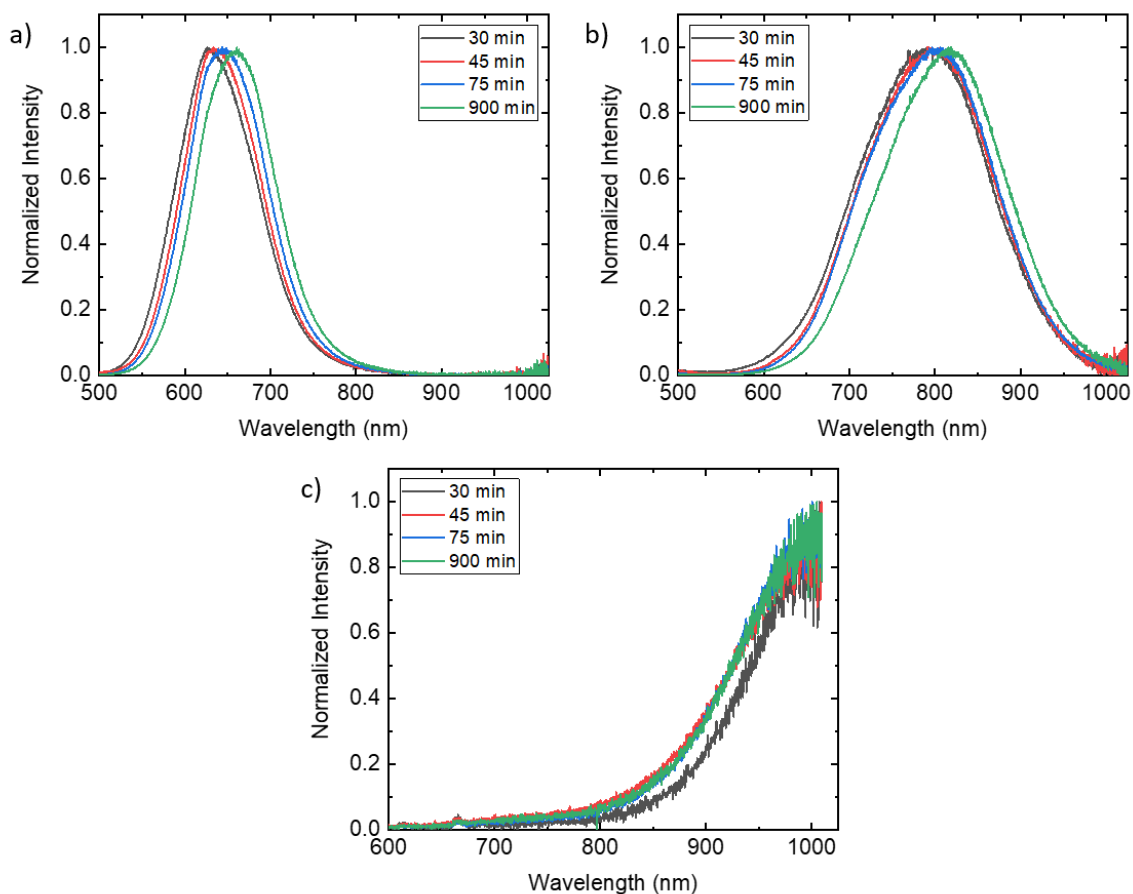


Figure 4-12. Photoluminescence spectra for a) 3 nm, b) 5 nm, and c) 7 nm SiNPs with varying functionalization times after oxidation.

However, when the PL max is compared with d_{XRD} in Figure 4-13a, the changes in d_{XRD} and PL max no longer follow a quantum confinement model. Chapter 3 shows that the PL max trends with d_{XRD} in reasonable agreement with the effective mass approximation, however, SiNPs with $d_{\text{XRD}} < 2.5$ nm do not follow this trend. The PL emission also does not trend towards one high energy trap state (i.e., 2.1 eV) that has been reported previously.¹⁹ Instead, our observations point to more complex interactions between the crystalline core, the disordered silicon shell, and the silicon oxide.

The influence that oxidation imposes on the excited-state lifetimes of SiNPs was evaluated as described in Chapter 3. The 7 nm SiNPs (which showed the least amount of oxidation) showed the largest change in the lifetimes and the smallest samples showed the smallest change in lifetimes (Figure 4-14).

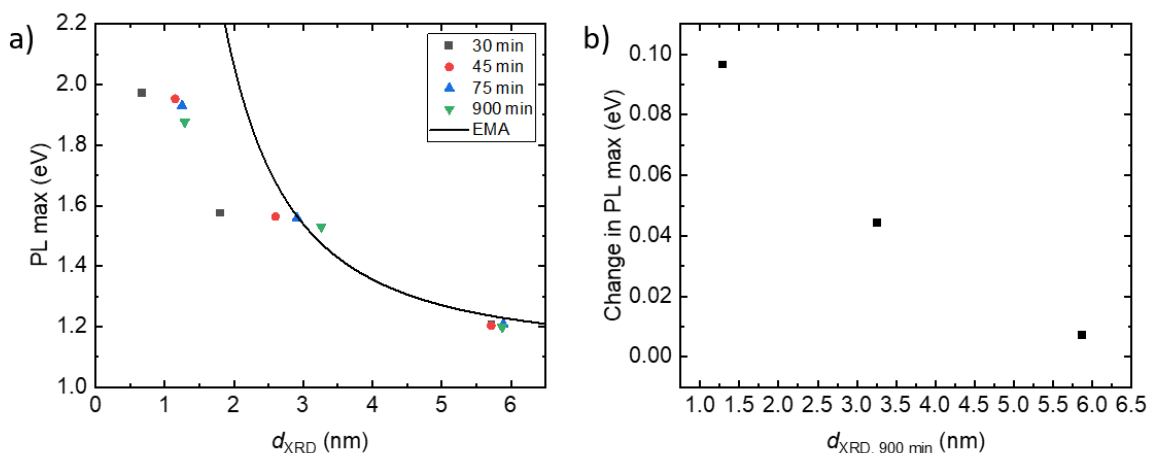


Figure 4-13. Comparing the PL max as a function of a) d_{XRD} for 3, 5, and 7 nm SiNPs with varying degrees of oxidation to the effective mass approximation (black trace: $E_g(r) = 1.12 + 3.77/r^2$). For further understanding, the change in photoluminescence is compared to b) d_{XRD} .

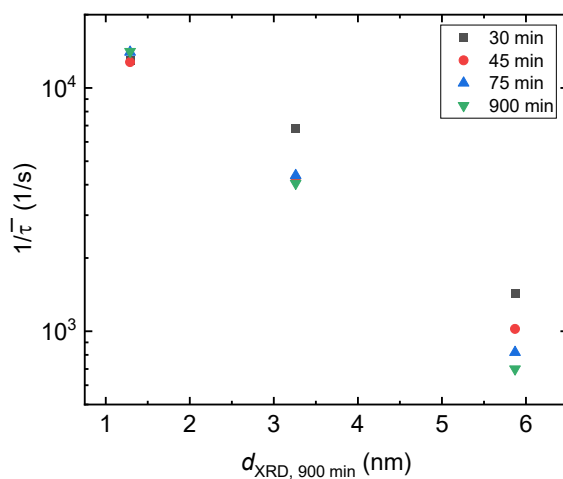


Figure 4-14. A comparison of lifetimes as a function of $d_{XRD, 900 \text{ min}}$ with different functionalization times after oxidation.

4.3.3 Internal Structure Dependent Impact of Oxidation on Structure of SiNPs

Prolonged etching, described in Chapter 3, removes most of the amorphous layer on the surface of SiNPs and results in SiNPs, where d_{XRD} aligns more closely with d_{TEM} . Employing the functionalization procedures described herein, we achieved SiNPs with varied degrees of functionalization and degrees of oxidation. Over etched samples were annealed at 1200 °C and subjected to prolonged etching (over-etched), as shown in Figure 4-15.

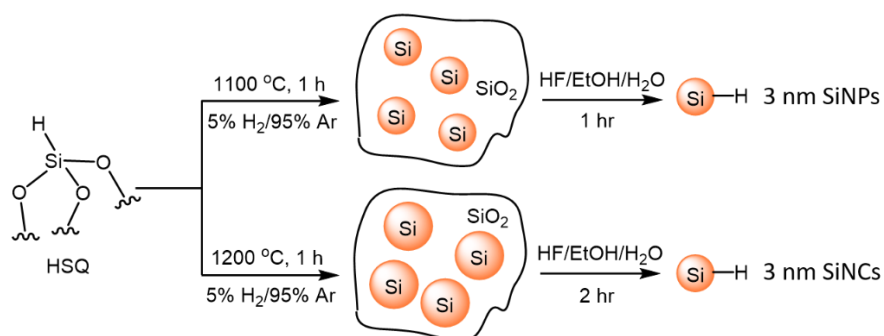


Figure 4-15. Scheme showing the synthesis of hydride-terminated 3 nm SiNPs and 3 nm SiNCs from hydrogen silsesquioxane (HSQ).

From here on, these samples will be referred to as 3 nm SiNCs and compared with the 3 nm SiNPs described above. Referring to the more ordered, over-etched sample as SiNCs serves for nominal differentiation only. For these samples, discussion will focus on the two extremes by looking at material that was functionalized for 30 min and 900 min. Using these materials, we aimed to identify the role of the crystalline component and the particle diameter in the oxidation of SiNPs.

To identify differences in the degree of oxidation, XPS analysis and fitting was performed as described above. The Si 2p XP spectra for 3 nm SiNPs described above is shown in Figure 4-16a, and the spectra for 3 nm SiNCs in Figure 4-16b. Both samples show increased oxidation with decreased functionalization times, similar to that discussed above for 3, 5, and 7 nm SiNPs. More oxidation is observed for 3 nm SiNCs than for 3 nm SiNPs, however, this difference could be a result of more carbonaceous species on the surface.

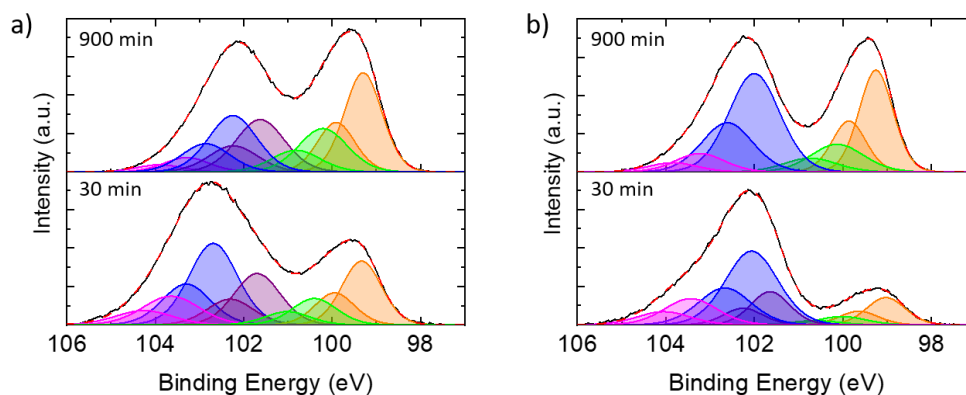


Figure 4-16. High resolution Si 2p spectrum showing the 2p_{3/2} and 2p_{1/2} emissions for oxidized samples of a) 3 nm SiNPs and b) 3 nm SiNCs. The colored traces are: black = experimental data, dashed red = fitting envelope, orange = core Si, green = $\sim\text{SiO}_{0.5}$ or silicon-carbon species, purple = $\sim\text{SiO}$, blue = $\sim\text{SiO}_{1.5}$, and magenta = $\sim\text{SiO}_2$.

To gain further insight into the impact of oxidation on the materials, TEM analysis was performed on the well-functionalized samples as well as the oxidized samples to compare the impact on the size (Figure 4-17). On average, the 3 nm SiNCs exhibited a similar amount of oxide induced growth as was observed for the 3 nm SiNPs (Figure 4-18). The 3 nm SiNCs exhibit a bimodal size distribution, where one portion of the distribution aligns with the functionalized sample and the other shows a significant increase in particle size. There are at least two possible explanations for this observation: 1) the initial functionalization step resulted in two types of particles, one that was well-passivated and one that had no functionalization and oxidized readily or 2) that the internal structure of the particles lead to one set of particles that was more easily oxidized than the other. The first explanation is more likely, as the rate of oxidation is similar for amorphous and crystalline silicon in bulk systems.⁴⁰ It also supports previous theories and studies on the hydrosilylation mechanism. Specifically, it supports that hydrosilylation separates SiNP aggregates during the functionalization process.²⁹ If we assume that the radical propagates across the surfaces after the functionalization has been initiated, then it is reasonable that varying degrees of functionalization would be exaggerated for samples with short functionalization times. Further evaluation of the bimodal distribution may be achieved by exploring the impact of oxidation for hydride-terminated 3 nm SiNCs.

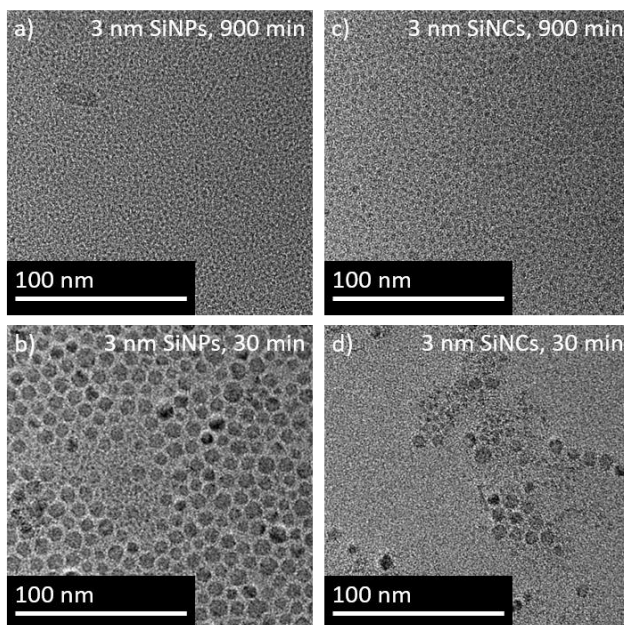


Figure 4-17. TEM images showing (a and b) 3 nm SiNPs and (c and d) 3 nm SiNCs functionalized for (a,c) 900 and (b, d) 30 min after oxidation.

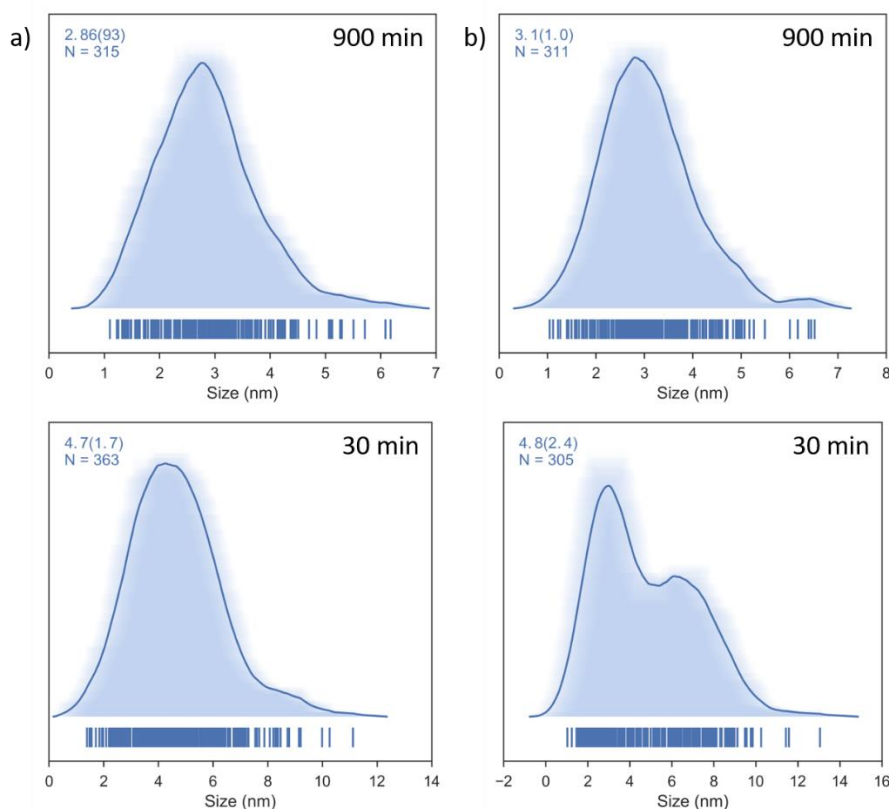


Figure 4-18. Histograms showing the size distribution of a) 3 nm SiNPs, and b) 3 nm SiNCs that were functionalized for 900 min (top) and for 30 min (bottom). Sizes were determined based on TEM imaging of the SiNPs.

The final structural characterization used to probe the 3 nm SiNPs and 3 nm SiNCs was XRD (Figure 4-19). XRD provides insight into the crystalline domains and confirmed that $d_{\text{XRD}, 900 \text{ min}}$ aligns more closely with $d_{\text{TEM}, 900 \text{ min}}$ for 3 nm SiNCs than 3 nm SiNPs. Relative to the 3 nm SiNPs, the change in d_{XRD} with increased oxidation is less for the 3 nm SiNCs. Strain analysis shows similar trends of decreasing strain with increased oxidation for 3 nm SiNPs and 3 nm SiNCs (Table 4-3), but the change in strain is less for 3 nm SiNCs. Contrary to the other samples, little change is observed in the lattice parameter for 3 nm SiNCs with different degrees of oxidation. While the trends in size, strain, and lattice parameter are similar to what is observed for 3, 5, and 7 nm SiNPs, it is unclear if less change is observed because of the internal structure or if, instead, the well-passivated fraction of the SiNCs are dominating the diffraction pattern. Therefore, more work is required to understand the nature of these difference and the role that the internal structure has during oxidation.

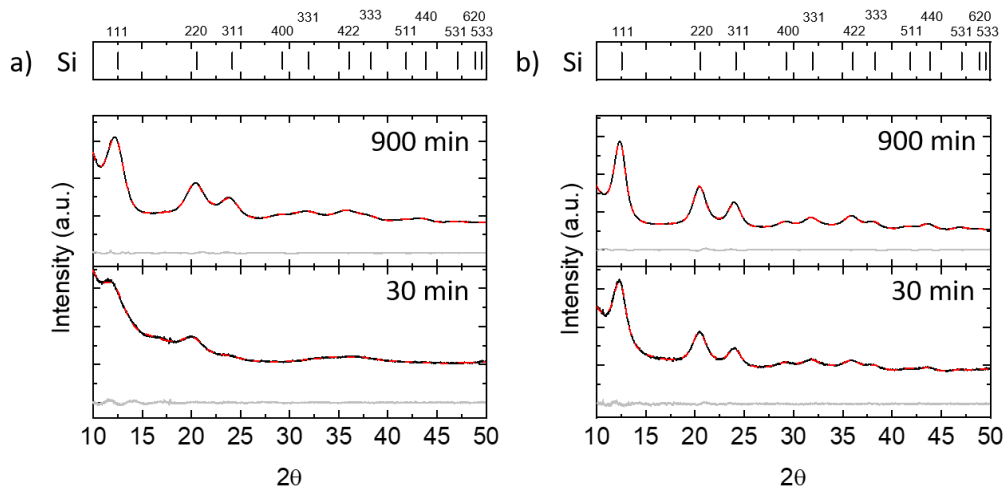


Figure 4-19. XRD patterns for a) 3 nm SiNPs and b) 3 nm SiNCs functionalized for 900 min and for 30 min after oxidation, showing the experimental data (black trace), the fit (red, dashed trace), and the difference between the two (gray trace). The SiNCs show reflections characteristic of crystalline Si.

Table 4-3. Table of d_{TEM} obtained from TEM analysis and d_{XRD} , strain, and lattice parameter, obtained from XRD fitting of 3 nm SiNPs and 3 nm SiNC

	3 nm SiNPs		3 nm SiNCs	
Functionalization time (min)	900	30	900	30
d_{TEM} (nm)	2.86 ± 0.93	4.7 ± 1.7	3.1 ± 1.0	4.8 ± 2.4
d_{XRD} (nm)	1.3	0.7	2.3	1.8
Strain from broadening	0.009	0.000	0.006	0.003
Lattice parameter (Å)	5.46	5.56	5.46	5.46

4.3.4 Influence of Internal Structure on Oxidation-based Changes in Photoluminescence

In addition to the structural changes explored in the previous section, the changes in the photoluminescence (PL) emission for 3 nm SiNPs and 3 nm SiNCs upon oxidation were examined. The goal was to identify the impact of the crystalline core and oxidation on the photoluminescence of SiNPs. The 3 nm SiNPs and 3 nm SiNCs are compared with 5 and 7 nm SiNPs, which have a larger d_{XRD} , to provide more insight into the role of the crystalline core. The 3 nm SiNCs exhibit a blue-shift of the PL max, as discussed above; however, the total shift is smaller for 3 nm SiNCs than for 3 nm SiNPs, but more than for 6 nm SiNPs (Figure 4-20). The increased PL emission energy is associated with a decrease in d_{XRD} , as observed above (Figure 4-21a). While there may be some correlation between the change in PL max and d_{XRD} , 900 min (Figure 4-21b), any detailed analysis would be speculative and requires further understanding of the changes in structure as outlined above and a larger sample size.

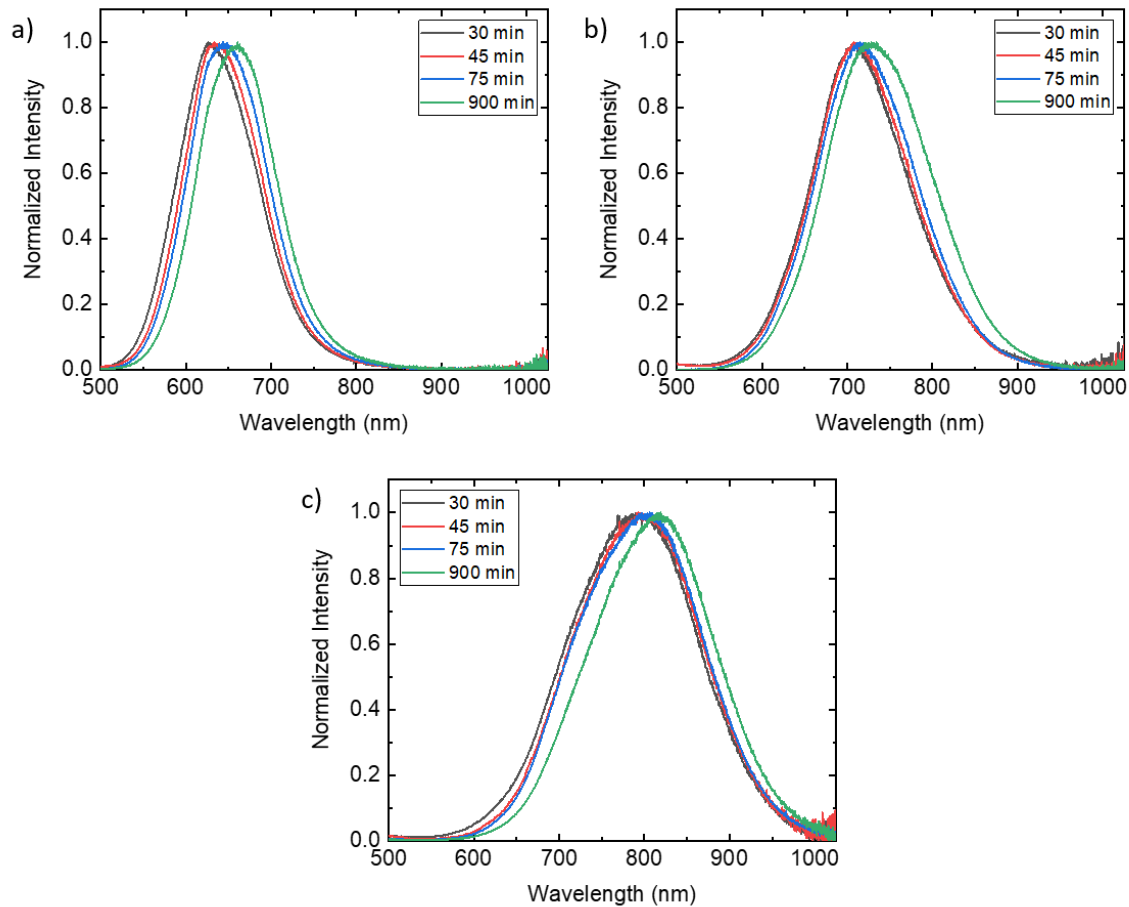


Figure 4-20. Photoluminescence spectra for a) 3 nm SiNPs, b) 3 nm SiNCs, and c) 5 nm SiNPs with varying functionalization times after oxidation.

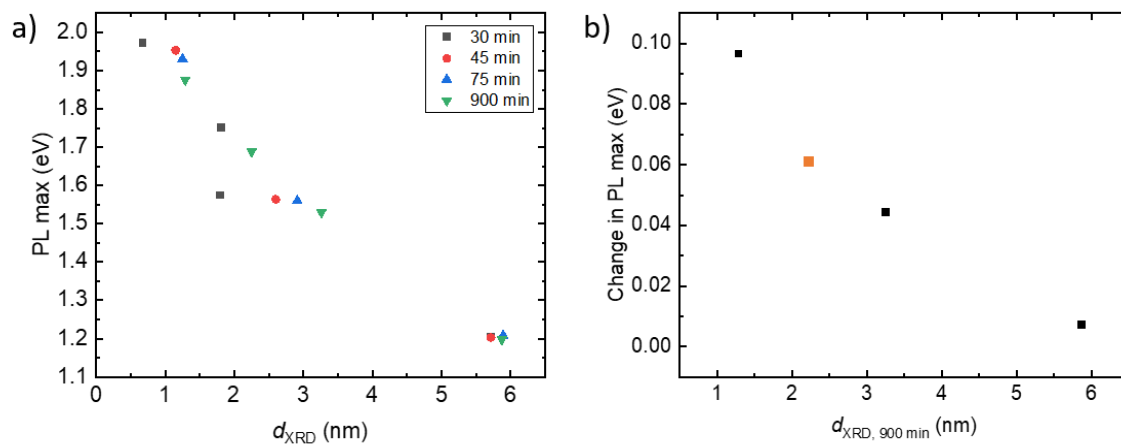


Figure 4-21. a) A plot of the PL max as a function of d_{XRD} for 3, 5, and 7 nm SiNPs, as well as 3 nm SiNCs with varying degrees of oxidation. b) The change in photoluminescence is plotted against $d_{XRD, 900 \text{ min}}$, with the 3 nm SiNCs showed in orange.

4.4 Conclusions and Future Work

This work identifies anticipated structural changes associated with the oxidation of silicon nanoparticles, including an increase in overall particle diameter (d_{TEM}) and a decrease in crystallite size (d_{XRD}). Increased oxidation also corresponds to changes in the strain and lattice parameter of the SiNPs, which can be investigated further using temperature dependent XRD and Raman spectroscopy.²⁸ The change in d_{TEM} and XPS-derived Si to O ratios appear to relate to $d_{\text{TEM}, 900 \text{ min}}$, suggesting that the degree of oxidation is dependent on the overall particle size, and thus, the surface area to volume ratio of the SiNPs. This trend is consistent for 3 nm SiNCs as well as 3, 5, and 7 nm SiNP samples, but the bimodal size distribution observed for 3 nm SiNCs needs to be explored before conclusions can be drawn. While the degree of oxidation appears to be related to $d_{\text{TEM}, 900 \text{ min}}$, changes in d_{XRD} , strain, and lattice parameters appear to be related to $d_{\text{XRD}, 900 \text{ min}}$. However, further work examining samples with a higher $d_{\text{XRD}}:d_{\text{TEM}}$ ratio is required to understand this relationship.

When examining the photoluminescence properties, the PL max of oxidized SiNPs no longer corresponds with d_{XRD} , as shown in Chapter 3, suggesting that more complex mechanisms influence the optical response. This could be related to electron–phonon coupling with the Si-O-Si or donor–acceptor recombination in the oxide shell.^{18, 19} Further investigation into the relationship between d_{TEM} and d_{XRD} and the photoluminescence blue-shift and the change lifetimes is required.

4.5 References

1. Canham, L. T., Silicon quantum wire array fabrication by electrochemical and chemical dissolution of wafers. *Appl Phys Lett* **1990**, *57* (10), 1046-1048.
2. Yu, Y.; Fan, G.; Fermi, A.; Mazzaro, R.; Morandi, V.; Ceroni, P.; Smilgies, D.-M.; Korgel, B. A., Size-Dependent Photoluminescence Efficiency of Silicon Nanocrystal Quantum Dots. *J. Phys. Chem. C* **2017**, *121* (41), 23240-23248.
3. Hessel, C. M.; Henderson, E. J.; Veinot, J. G. C., Hydrogen Silsesquioxane: A Molecular Precursor for Nanocrystalline Si–SiO₂ Composites and Freestanding Hydride-Surface-Terminated Silicon Nanoparticles. *Chem. Mater.* **2006**, *18* (26), 6139-6146.
4. Hessel, C. M.; Reid, D.; Panthani, M. G.; Rasch, M. R.; Goodfellow, B. W.; Wei, J.; Fujii, H.; Akhavan, V.; Korgel, B. A., Synthesis of Ligand-Stabilized Silicon Nanocrystals with Size-Dependent Photoluminescence Spanning Visible to Near-Infrared Wavelengths. *Chem. Mater.* **2012**, *24* (2), 393-401.
5. Erogbogbo, F.; Yong, K.-T.; Roy, I.; Hu, R.; Law, W.-C.; Zhao, W.; Ding, H.; Wu, F.; Kumar, R.; Swihart, M. T.; Prasad, P. N., In Vivo Targeted Cancer Imaging, Sentinel Lymph Node Mapping and Multi-Channel Imaging with Biocompatible Silicon Nanocrystals. *ACS Nano* **2011**, *5* (1), 413-423.

6. Romano, F.; Angeloni, S.; Morselli, G.; Mazzaro, R.; Morandi, V.; Shell, J. R.; Cao, X.; Pogue, B. W.; Ceroni, P., Water-soluble silicon nanocrystals as NIR luminescent probes for time-gated biomedical imaging. *Nanoscale* **2020**, *12* (14), 7921-7926.
7. Gonzalez, C. M.; Iqbal, M.; Dasog, M.; Piercey, D. G.; Lockwood, R.; Klapotke, T. M.; Veinot, J. G. C., Detection of high-energy compounds using photoluminescent silicon nanocrystal paper based sensors. *Nanoscale* **2014**, *6* (5), 2608-2612.
8. Meinardi, F.; Ehrenberg, S.; Dharmo, L.; Carulli, F.; Mauri, M.; Bruni, F.; Simonutti, R.; Kortshagen, U.; Brovelli, S., Highly efficient luminescent solar concentrators based on earth-abundant indirect-bandgap silicon quantum dots. *Nature Photonics* **2017**, *11*, 177-185.
9. Mazzaro, R.; Gradone, A.; Angeloni, S.; Morselli, G.; Cozzi, P. G.; Romano, F.; Vomiero, A.; Ceroni, P., Hybrid Silicon Nanocrystals for Color-Neutral and Transparent Luminescent Solar Concentrators. *ACS Photonics* **2019**, *6* (9), 2303-2311.
10. Liu, X.; Zhao, S.; Gu, W.; Zhang, Y.; Qiao, X.; Ni, Z.; Pi, X.; Yang, D., Light-Emitting Diodes Based on Colloidal Silicon Quantum Dots with Octyl and Phenylpropyl Ligands. *ACS Appl. Mater. Interfaces* **2018**, *10* (6), 5959-5966.
11. Angi, A.; Loch, M.; Sinelnikov, R.; Veinot, J. G. C.; Becherer, M.; Lugli, P.; Rieger, B., The influence of surface functionalization methods on the performance of silicon nanocrystal LEDs. *Nanoscale* **2018**, *10* (22), 10337-10342.
12. Mazzaro, R.; Romano, F.; Ceroni, P., Long-lived luminescence of silicon nanocrystals: from principles to applications. *Phys. Chem. Chem. Phys.* **2017**, *19* (39), 26507-26526.
13. Tsybeskov, L.; Vandyshv, J. V.; Fauchet, P. M., Blue emission in porous silicon: Oxygen-related photoluminescence. *Phys. Rev. B* **1994**, *49* (11), 7821-7824.
14. de Boer, W. D. A. M.; Timmerman, D.; Dohnalová, K.; Yassievich, I. N.; Zhang, H.; Buma, W. J.; Gregorkiewicz, T., Red spectral shift and enhanced quantum efficiency in phonon-free photoluminescence from silicon nanocrystals. *Nature Nanotech.* **2010**, *5*, 878-884.
15. Valenta, J.; Fucikova, A.; Pelant, I.; Kúsová, K.; Dohnalová, K.; Aleknavičius, A.; Cibulka, O.; Fojtík, A.; Kada, G., On the origin of the fast photoluminescence band in small silicon nanoparticles. *New Journal of Physics* **2008**, *10* (7), 073022.
16. Plautz, G. L.; Graff, I. L.; Schreiner, W. H.; Bezerra, A. G., Evolution of size distribution, optical properties, and structure of Si nanoparticles obtained by laser-assisted fragmentation. *Applied Physics A* **2017**, *123*, 359.
17. Gupta, A.; Wiggers, H., Freestanding silicon quantum dots: origin of red and blue luminescence. *Nanotechnology* **2010**, *22* (5), 055707.
18. Botas, A. M. P.; Ferreira, R. A. S.; Pereira, R. N.; Anthony, R. J.; Moura, T.; Rowe, D. J.; Kortshagen, U., High Quantum Yield Dual Emission from Gas-Phase Grown Crystalline Si Nanoparticles. *J. Phys. Chem. C* **2014**, *118* (19), 10375-10383.
19. Martin, J.; Cichos, F.; Huisken, F.; von Borczyskowski, C., Electron-Phonon Coupling and Localization of Excitons in Single Silicon Nanocrystals. *Nano Lett.* **2008**, *8* (2), 656-660.
20. Kang, Z.; Liu, Y.; Tsang, C. H. A.; Ma, D. D. D.; Fan, X.; Wong, N.-B.; Lee, S.-T., Water-Soluble Silicon Quantum Dots with Wavelength-Tunable Photoluminescence. *Adv. Mater.* **2009**, *21* (6), 661-664.
21. Gupta, A.; Swihart, M. T.; Wiggers, H., Luminescent Colloidal Dispersion of Silicon Quantum Dots from Microwave Plasma Synthesis: Exploring the Photoluminescence Behavior Across the Visible Spectrum. *Adv. Funct. Mater.* **2009**, *19* (5), 696-703.
22. Yang, Z.; De los Reyes, G. B.; Titova, L. V.; Sychugov, I.; Dasog, M.; Linnros, J.; Hegmann, F. A.; Veinot, J. G. C., Evolution of the Ultrafast Photoluminescence of Colloidal Silicon Nanocrystals with Changing Surface Chemistry. *ACS Photonics* **2015**, *2* (5), 595-605.

23. Pereira, R. N.; Rowe, D. J.; Anthony, R. J.; Kortshagen, U., Oxidation of freestanding silicon nanocrystals probed with electron spin resonance of interfacial dangling bonds. *Phys. Rev. B* **2011**, *83* (15), 155327.
24. Lockwood, R.; Yang, Z.; Sammynaiken, R.; Veinot, J. G. C.; Meldrum, A., Light-Induced Evolution of Silicon Quantum Dot Surface Chemistry—Implications for Photoluminescence, Sensing, and Reactivity. *Chem. Mater.* **2014**, *26* (19), 5467-5474.
25. Liptak, R. W.; Kortshagen, U.; Campbell, S. A., Surface chemistry dependence of native oxidation formation on silicon nanocrystals. *J. Appl. Phys.* **2009**, *106* (6), 064313.
26. Kúsová, K.; Ondič, L.; Klimešová, E.; Herynková, K.; Pelant, I.; Daniš, S.; Valenta, J.; Gallart, M.; Ziegler, M.; Hönerlage, B.; Gilliot, P., Luminescence of free-standing versus matrix-embedded oxide-passivated silicon nanocrystals: The role of matrix-induced strain. *Appl. Phys. Lett.* **2012**, *101* (14), 143101.
27. Hofmeister, H.; Huisken, F.; Kohn, B. Lattice contraction in nanosized silicon particles produced by laser pyrolysis of silane, In *The European Physical Journal D*; Châtelain, A.; Bonard, J. M., Eds.; Springer: Berlin, Heidelberg; 1999; pp 137-140.
28. Falcão, B. P.; Leitão, J. P.; Soares, M. R.; Ricardo, L.; Águas, H.; Martins, R.; Pereira, R. N., Oxidation and Strain in Free-standing Silicon Nanocrystals. *Phys. Rev. Applied* **2019**, *11* (2), 024054.
29. Kehrlé, J.; Kaiser, S.; Purkait, T. K.; Winnacker, M.; Helbich, T.; Vagin, S.; Veinot, J. G. C.; Rieger, B., In situ IR-spectroscopy as a tool for monitoring the radical hydrosilylation process on silicon nanocrystal surfaces. *Nanoscale* **2017**, *9* (24), 8489-8495.
30. Askar, A. M.; Bernard, G. M.; Wiltshire, B.; Shankar, K.; Michaelis, V. K., Multinuclear Magnetic Resonance Tracking of Hydro, Thermal, and Hydrothermal Decomposition of CH₃NH₃PbI₃. *J. Phys. Chem. C* **2017**, *121*, (2), 1013-1024.
31. Bruker AXS. *TOPAS V4: General Profile and Structure Analysis Software for Powder Diffraction Data. - User's Manual*; Bruker AXS: Karlsruhe, Germany, 2008.
32. Anderson, S. L.; Luber, E. J.; Olsen, B. C.; Buriak, J. M., Substance over Subjectivity: Moving beyond the Histogram. *Chem. Mater.* **2016**, *28* (17), 5973-5975.
33. Yang, Z.; Gonzalez, C. M.; Purkait, T. K.; Iqbal, M.; Meldrum, A.; Veinot, J. G. C., Radical Initiated Hydrosilylation on Silicon Nanocrystal Surfaces: An Evaluation of Functional Group Tolerance and Mechanistic Study. *Langmuir* **2015**, *31* (38), 10540-10548.
34. Purkait, T. K.; Iqbal, M.; Wahl, M. H.; Gottschling, K.; Gonzalez, C. M.; Islam, M. A.; Veinot, J. G. C., Borane-catalyzed room-temperature hydrosilylation of alkenes/alkynes on silicon nanocrystal surfaces. *J. Am. Chem. Soc.* **2014**, *136* (52), 17914-7.
35. Barr, T. L.; Seal, S. Nature of the use of Adventitious Carbon as a Binding Energy Standard. *J. Vac. Sci. Technol., A* **1995**, *13*, 1239– 1246.
36. Hu, M.; Luber, E.; Buriak, J. M., Reconsidering XPS Quantification of Substitution Levels of Monolayers on Unoxidized Silicon Surfaces. ChemRxiv. Preprint, 2020, DOI: 10.26434/chemrxiv.12268325.v1.
37. Thiessen, A. N.; Ha, M.; Hooper, R. W.; Yu, H.; Oliynyk, A. O.; Veinot, J. G. C.; Michaelis, V. K., Silicon Nanoparticles: Are They Crystalline from the Core to the Surface? *Chem. Mater.* **2019**, *31* (3), 678-688.
38. Khorsand Zak, A.; Abd. Majid, W. H.; Abrishami, M. E.; Yousefi, R., X-ray analysis of ZnO nanoparticles by Williamson–Hall and size–strain plot methods. *Solid State Sciences* **2011**, *13* (1), 251-256.
39. Dohnalová, K.; Hapala, P.; Kúsová, K.; Infante, I., Electronic Structure Engineering Achieved via Organic Ligands in Silicon Nanocrystals. *Chem. Mater.* **2020**, DOI:10.1021/acs.chemmater.0c00443.
40. Yang, D. Q.; Meunier, M.; Sacher, E., Room temperature air oxidation of nanostructured Si thin films with varying porosities as studied by x-ray photoelectron spectroscopy. *J. Appl. Phys.* **2006**, *99* (8), 084315.

Chapter 5

Conclusions and Future Directions

5.1 Conclusions

Luminescent silicon nanoparticles (SiNPs) are biologically compatible quantum dots (QDs) that are based upon the second most abundant element in the earth's crust.^{1, 2} They exhibit photoluminescence (PL) and chemical properties that make them well suited for a wide-range of applications.³⁻¹⁰ The structure of SiNPs, which can be controlled during the nanoparticle synthesis and its subsequent functionalization, dominates the desirable properties.¹¹⁻¹⁴ This, in turn, impacts the suitability of the resulting SiNPs for various applications.^{15, 16} The aim of this thesis was to explore the internal structure of SiNPs (Chapter 2 and Chapter 4) and evaluate the influence of that structure on the photoluminescence response (Chapter 3 and Chapter 4).

Chapter 2 employs a combination of complementary techniques to examine the internal structure of hydride-terminated SiNPs (H-SiNPs) of different sizes derived from the thermal annealing of hydrogen silsesquioxane (HSQ). Fourier-transform infrared spectroscopy and X-ray photoelectron spectroscopy indicate the presence of Si-H species and little-to-no oxidation of the SiNPs. Brightfield TEM and XRD analyses indicate that the SiNP overall diameter (d_{TEM}) is consistently larger than the crystalline domain (d_{XRD}). Two ^{29}Si SS NMR pulse sequences were utilized, a Bloch pulse and $^{29}\text{Si}[^1\text{H}]$ cross-polarization, to probe Si atoms in the entire SiNP and near the surface. These techniques were employed for 3, 6, 9, 21, and 64 nm SiNPs (nominal sizes based on d_{TEM}). For the largest SiNPs studied (i.e., 64 nm), a clear graded structure was identified, where the SiNPs exhibit a crystalline core and a disordered surface, bridged by a semi-ordered subsurface (Figure 5-1). The smallest SiNPs studied (i.e., 3 nm) do not exhibit a significant crystalline core ($d_{\text{XRD}} = 1.2$ nm; i.e., \sim two unit cells of diamond-cubic Si). The 3 and 6 nm SiNPs also exhibited strain in the crystalline domain that was not observed for other sizes. The 9 nm SiNPs appear to be the critical size, where long-range order appears for SiNPs made through the HSQ method. This suggests a size-dependence of the graded internal structure of SiNPs, as represented in Figure 5-1.

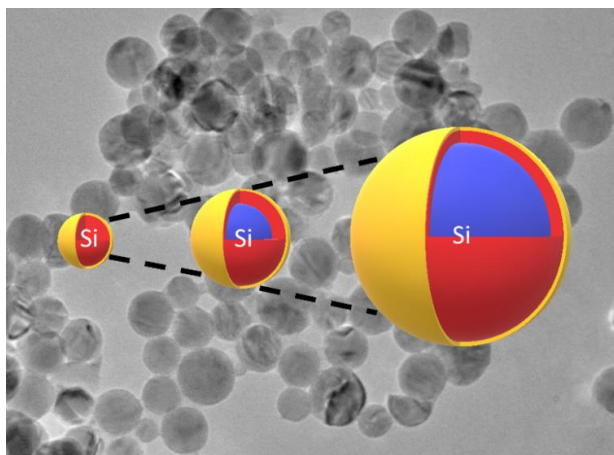


Figure 5-1. A schematic representation of the internal structure of SiNPs of various sizes, as outlined in Chapter 2. Blue represents the crystalline core; red, the semi-ordered subsurface; and yellow, the disordered surface. Reprinted with permission from *Chem. Mater.*, 2019, 31 (3), 679-688.

In Chapter 3, the impact of the internal structure on the photoluminescence properties was evaluated. For this study, HF etching was used to remove the amorphous layer of the SiNPs, resulting in SiNPs where d_{TEM} and d_{XRD} were closer. A detailed study of two SiNPs with the same d_{TEM} and different d_{XRD} showed that the sample with the larger d_{XRD} exhibited longer luminescence lifetimes and a red-shifted PL emission maximum (PL max) relative to the other sample (Figure 5-2). Next, this work was expanded to a series of SiNPs that were categorized by the difference between d_{TEM} and d_{XRD} . The study demonstrated that d_{XRD} better correlates with the PL max and lifetimes than d_{TEM} when the amorphous shell is thick ($d_{\text{TEM}} - d_{\text{XRD}} > 2$ nm) and that both correlate well when the amorphous shell is thin ($d_{\text{TEM}} - d_{\text{XRD}} < 0.8$ nm).

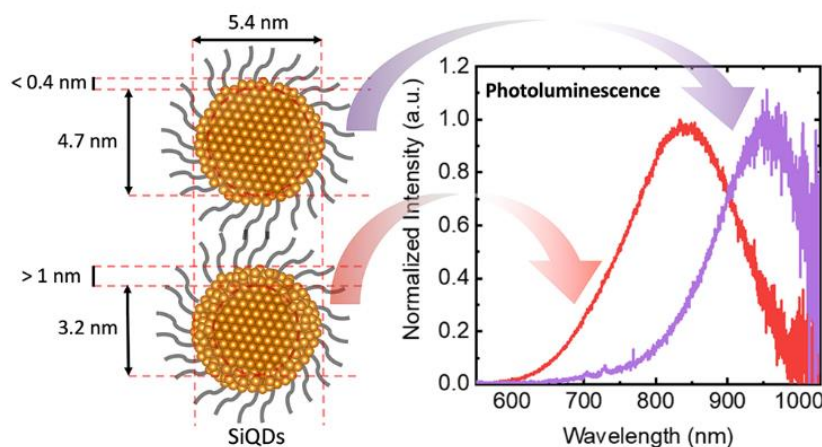


Figure 5-2. An artistic rendering of SiNPs with different amorphous shell thicknesses and a demonstration of the impact on photoluminescence emission for SiNPs of the same d_{TEM} . Reprinted with permission from *Chem. Mater.*, 2020, 32 (16), 6838-6846.

Chapter 4 attempts to understand the impact of oxidation on the internal structure and photoluminescence properties of SiNPs as it relates to the size and initial internal structure of the SiNPs. SiNPs of different sizes ($\sim 3, 5,$ and 7 nm d_{TEM}) were made through the thermal annealing of HSQ. The resulting SiNPs were functionalized with radical-initiated hydrosilylation using varied reaction times to yield SiNPs with different surface coverage. Subsequently, the samples were oxidized to provide SiNPs with varying degrees of oxidation. With increasing oxidation, d_{XRD} decreases and d_{TEM} increases for SiNPs annealed at the same temperature. This corresponds with a blueshift in the PL max. The amount of oxidation appears to correlate with d_{TEM} for the SiNPs with the lowest surface coverage. SiNPs with the same d_{TEM} and different d_{XRD} also were studied. The sample with a larger d_{XRD} exhibited a similar change in d_{TEM} upon oxidation (though a bimodal distribution emerged) and a smaller change in d_{XRD} . Unfortunately, we were unable to determine if this was a result of the ligand surface coverage or the different internal structure. Further work is required to evaluate the observed structural and luminescence changes upon oxidation.

5.2 Future Directions

5.2.1 Expanding Insights into the Structure of SiNPs

Insights into the structure of H-SiNPs are important as they are the closest approximation we have to a “naked” SiNP. However, H-SiNPs rarely are used due to their tendency to oxidize and their limited solution processability. Future studies into SiNPs made through other synthetic techniques and more complicated systems, such as functionalized and oxidized SiNPs, will deepen our understanding of SiNP structure, enabling further insight into the relationships between the structure and properties of these materials.

5.2.1.1 Exploring Oxidation on H-SiNPs

The study described in Chapter 4 was hindered by the application of partially functionalized surfaces. Future work using H-SiNPs will elucidate better the origin of the observed structural changes, based on the size and initial internal structure. To complete these studies, a combination of techniques, like those employed in Chapter 2, would be most beneficial. Further, variable temperature XRD and Raman spectroscopy could be performed to identify the nature of the changing strain and to quantify it accurately.¹⁷⁻¹⁹ When combined with ^{29}Si SS NMR, this can

provide detailed insight into the structural changes that SiNPs undergo during oxidation. Understanding the structural changes that occur may provide insight into the observed photoluminescence changes and is beneficial for understanding the degradation of SiNPs.

5.2.1.2 Impact of Synthetic Methods on Internal Structure of SiNPs

Due to the influence of structure over SiNP properties, understanding the impact of synthetic methods on the structure is important. The internal structure can be influenced by the synthesis of the SiNP core and the functionalization method used to passivate the surface.

The graded internal structure observed for SiNPs made through the thermal disproportionation of HSQ is attributed, at least in part, to the lattice mismatch between the SiO₂ matrix and the crystalline SiNP core.^{20, 21} SiNPs made through the plasma-synthesis method are not oxide embedded and could yield more crystalline SiNPs than the HSQ method.¹¹ A systematic study examining H-SiNPs made from both methods employing the techniques outlined in Chapter 2 would be informative. Further comparison with SiNPs made through other synthetic methods (e.g., CO₂ laser pyrolysis)²² could enable tailoring of SiNPs for the desired application. For example, a more disordered SiNP may be more suited for lithium ion battery (LIB) anode applications.¹⁵

The internal structure of the SiNP also may be impacted by the functionalization method employed. Etchant-based hydrosilylation methods (e.g., XeF₂) isotropically etch the surface of the SiNPs, likely removing the disordered layer, while radical and thermal hydrosilylation methods are anticipated to maintain the internal structure.¹³ To probe this, initial ²⁹Si SS NMR experiments examining 9 nm SiNPs functionalized using XeF₂ and AIBN were performed (Figure 5-3). Brightfield TEM indicates a decrease in d_{TEM} for SiNPs functionalized with XeF₂. The ²⁹Si NMR spectra of XeF₂ functionalized SiNPs is sharper than the spectra of 6 nm H-SiNPs but shifted relative to 9 nm H-SiNPs; this is consistent with the decrease in d_{TEM} (Figure 5-3). The ²⁹Si NMR spectra of AIBN functionalized SiNPs is similar to 9 nm H-SiNPs, with an additional peak around -115 ppm, which is likely due to surface oxidation. Further work evaluating the data and employing other characterization methods (e.g., cross-polarization, XRD, XPS) will help illuminate the structural changes. This work could be extended to other functionalization methods, such as dehydrocoupling or reactions with organolithium reagents, and analyzing the impact of functionalization method on the photodegradation of SiNPs.²³

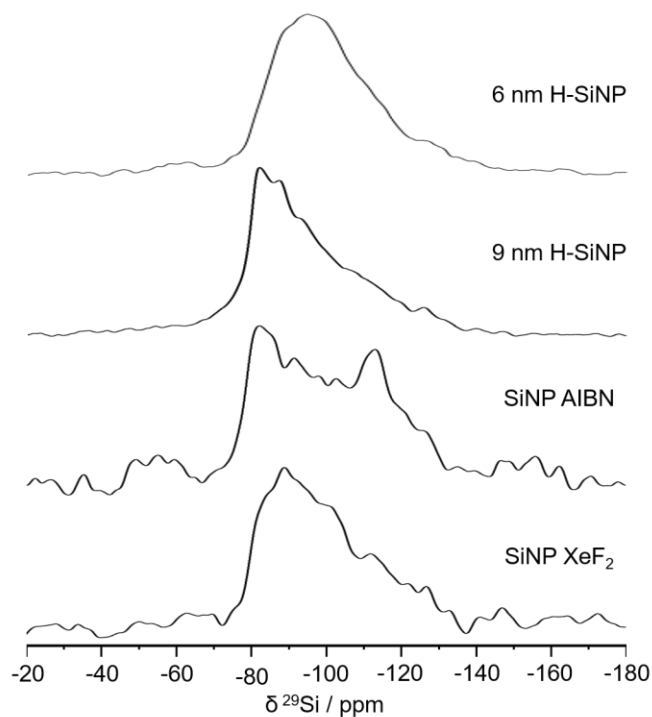


Figure 5-3. ^{29}Si NMR spectra of 9 nm SiNPs functionalized with dodecene using AIBN and XeF_2 as the initiators. The spectra of 6 and 9 nm H-SiNPs are presented for comparison.

5.2.2 Impact of SiNP Internal Structure on Applications

As discussed in Chapter 1, the structure of SiNPs is important for their applications. Now that we have a better understanding of the structure of SiNPs made through the thermal disproportionation of HSQ (Chapter 2) and some control over the internal structure (Chapter 3), we can evaluate the impact that the internal structure has on various applications.

5.2.2.1 Impact of SiNP Internal Structure on Performance of Lithium Ion Battery Anodes

While it has been shown that amorphous SiNPs outperform more crystalline SiNPs as LIB anode materials,¹⁵ further work looking at the effect of a graded shell could be insightful. To do this, SiNPs of similar sizes but varying degrees of crystallinity can be prepared, as outlined in Chapter 3. Comparing the performance of anodes based upon SiNPs of different crystallinity can provide further insight into the impact of the internal structure. This will help with optimization of SiNPs as anode materials for LIBs as these materials begin to move towards commercialization.²⁴

5.2.2.2 Optimization of Structure for Multimodal Imaging

SiNPs are excellent candidates for multimodal imaging as the photoluminescence falls in the near-IR;⁷ the SiNP core is promising for ^{29}Si magnetic resonance imaging (MRI),²⁵ and the

surface ligands can be optimized for other imaging modes (i.e., ^{64}Cu or ^{18}F positron emission tomography (PET) imaging).^{26, 27} The ideal imaging agent based upon SiNPs would have large quantities of radicals in the core to optimize hyperpolarization (i.e., DNP) and long relaxation times so the SiNPs remain polarized for imaging. In a DNP study (follow up from Chapter 2), we found that 6 nm H-SiNPs have a low radical concentration (0.16 and 0.10 mM from two synthetic batches), yielding no DNP enhancement.²⁸ However, oxidation of SiNPs has been shown to increase radical concentration.²⁹ In Chapter 4, it was observed that oxidation of 6 nm SiNPs does not impact the near-IR photoluminescence detrimentally, thus making oxidation of the SiNPs a viable route to increase the radical concentration to improve DNP enhancements. The radical concentration also may be increased by annealing the SiNPs in an inert atmosphere (i.e., Ar) as H_2 is known to passivate unpaired electron defects.²⁰ By capping the resulting SiNPs with a mixed-surface using PEG for water solubility and a fluorinated ligand capable of conversion to ^{18}F for PET imaging (e.g., SiFA),³⁰ it is possible to envision a multimodal imaging agent based upon SiNPs. Bruker's preclinical imaging device, capable of simultaneous PET and MRI, makes multimodal contrast agents such as this practical for real world applications.³¹

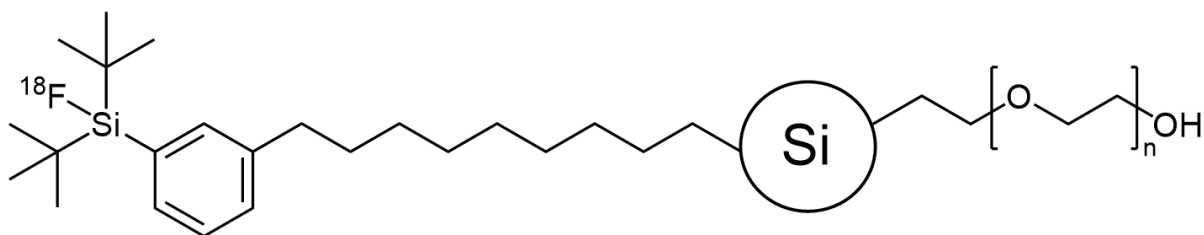


Figure 5-4. Purposed structure for a SiNP-based multimodal imaging agent.

5.2.3 Moving into a New Size Regime

Metamaterials are artificial media that interact with electromagnetic waves due to the structure and composition of the materials.³² The first optical metamaterials used split ring resonators to interact with microwave radiation, demonstrating a negative refractive index.³³ It is highly desirable to push these properties into the visible range for applications such as cloaking devices or super resolution lenses.^{34, 35} Large SiNPs (80–280 nm) offer a high refractive index and low absorption coefficient that are necessary to make low loss meta-atoms (building blocks for metamaterials).³⁶ The optimal SiNPs for meta-atoms are highly crystalline and non-porous, with narrow size distributions and uniform composition.³⁶

In Chapter 2, 64 nm SiNPs were synthesized by annealing HSQ at 1500 °C for 1 h. Since that work, the temperature profile has been expanded up to 1700 °C, resulting in spherical SiNPs 113 ± 35 nm in diameter (Figure 5-5a). The prepared SiNPs are crystalline, with no observable porosity (Figure 5-5 a and b). In a collaboration with Drs. Glenna Drisko and Philippe Barois at the University of Bordeaux, the optical scattering of these promising materials is being investigated. Early scattering experiments show an overlap in the magnetic and electric scattering coefficients that was not anticipated (Figure 5-5c). This effect can be simulated by accounting for the broad size distribution (Figure 5-5d), however, further work examining samples with narrow size distributions and larger sizes is required to provide insight into this response. Once understood, these SiNPs can be employed as meta-atoms for creating new metamaterials operating in the visible spectrum.

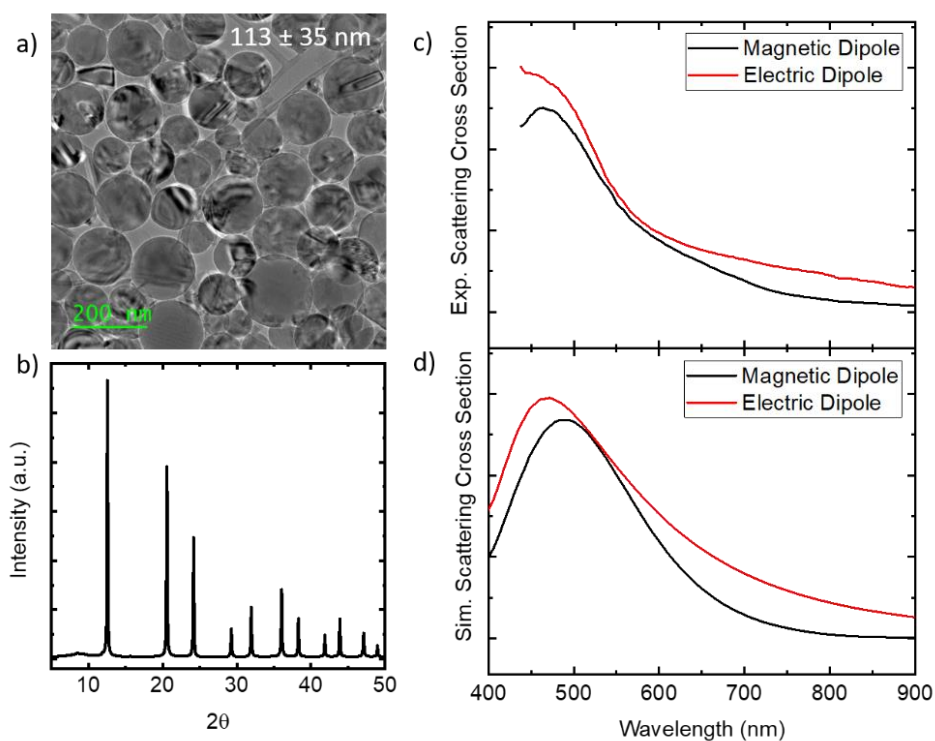


Figure 5-5. a) Bright field TEM image, b) X-ray diffraction pattern, and c) experimental and d) simulated light scattering data for 113 ± 35 nm SiNPs. The bright field TEM image was acquired as outlined in 4.2.2.4 and the diffraction pattern was acquired at the Canadian Light Source (as described in 4.2.2.3). Static light scattering experiments and simulations were performed by Philippe Barois at the University of Bordeaux. Static light scattering experiments were performed using a custom built set-up. Colloidal solutions of the SiNPs were irradiated using a super continuum white source (SuperK EXB-6 with SuperK Split visible filter from NKT Photonics), and the scattered light is collected at 90° using a Minispectrometer (Hamamatsu C10083CA) fed with an optical fiber. Simulations were performed using software that solves the equations of Mie scattering theory (coded in Maple). The software calculates the scattering efficiency of the diagonal elements of the scattering matrix and every individual mode. Size, size distribution, porosity, and crystallinity of the SiNPs are accounted for in the simulations.

5.3 References

1. Islam, M. A.; Sinelnikov, R.; Howlader, M. A.; Faramus, A.; Veinot, J. G. C., Mixed Surface Chemistry: An Approach to Highly Luminescent Biocompatible Amphiphilic Silicon Nanocrystals. *Chem. Mater.* **2018**, *30* (24), 8925-8931.
2. Pramanik, S.; Hill, S. K. E.; Zhi, B.; Hudson-Smith, N. V.; Wu, J. J.; White, J. N.; McIntire, E. A.; Kondeti, V. S. S. K.; Lee, A. L.; Bruggeman, P. J.; Kortshagen, U. R.; Haynes, C. L., Comparative toxicity assessment of novel Si quantum dots and their traditional Cd-based counterparts using bacteria models *Shewanella oneidensis* and *Bacillus subtilis*. *Environ. Sci.: Nano* **2018**, *5* (8), 1890-1901.
3. Su, X.; Wu, Q.; Li, J.; Xiao, X.; Lott, A.; Lu, W.; Sheldon, B. W.; Wu, J., Silicon-Based Nanomaterials for Lithium-Ion Batteries: A Review. *Adv. Energy Mater.* **2014**, *4* (1), 1300882.
4. Choi, J. W.; Aurbach, D., Promise and reality of post-lithium-ion batteries with high energy densities. *Nat. Rev. Mater.* **2016**, *1* (4), 16013.
5. Gonzalez, C. M.; Veinot, J. G. C., Silicon nanocrystals for the development of sensing platforms. *J. Mater. Chem. C* **2016**, *4* (22), 4836-4846.
6. Hill, S. K. E.; Connell, R.; Peterson, C.; Hollinger, J.; Hillmyer, M. A.; Kortshagen, U.; Ferry, V. E., Silicon Quantum Dot–Poly(methyl methacrylate) Nanocomposites with Reduced Light Scattering for Luminescent Solar Concentrators. *ACS Photonics* **2019**, *6* (1), 170-180.
7. Romano, F.; Angeloni, S.; Morselli, G.; Mazzaro, R.; Morandi, V.; Shell, J. R.; Cao, X.; Pogue, B. W.; Ceroni, P., Water-soluble silicon nanocrystals as NIR luminescent probes for time-gated biomedical imaging. *Nanoscale* **2020**, *12* (14), 7921-7926.
8. Meinardi, F.; Ehrenberg, S.; Dharmo, L.; Carulli, F.; Mauri, M.; Bruni, F.; Simonutti, R.; Kortshagen, U.; Brovelli, S., Highly efficient luminescent solar concentrators based on earth-abundant indirect-bandgap silicon quantum dots. *Nature Photon.* **2017**, *11*, 177-185.
9. Maier-Flaig, F.; Rinck, J.; Stephan, M.; Bocksrocker, T.; Bruns, M.; Kübel, C.; Powell, A. K.; Ozin, G. A.; Lemmer, U., Multicolor Silicon Light-Emitting Diodes (SiLEDs). *Nano Lett.* **2013**, *13* (2), 475-480.
10. Angi, A.; Loch, M.; Sinelnikov, R.; Veinot, J. G. C.; Becherer, M.; Lugli, P.; Rieger, B., The influence of surface functionalization methods on the performance of silicon nanocrystal LEDs. *Nanoscale* **2018**, *10* (22), 10337-10342.
11. Mangolini, L.; Thimsen, E.; Kortshagen, U., High-Yield Plasma Synthesis of Luminescent Silicon Nanocrystals. *Nano Lett.* **2005**, *5* (4), 655-659.
12. Anthony, R.; Kortshagen, U., Photoluminescence quantum yields of amorphous and crystalline silicon nanoparticles. *Phys. Rev. B* **2009**, *80* (11), 115407.
13. Mobarok, M. H.; Purkait, T. K.; Islam, M. A.; Miskolzie, M.; Veinot, J. G. C., Instantaneous Functionalization of Chemically Etched Silicon Nanocrystal Surfaces. *Angew. Chem. Int. Ed.* **2017**, *56* (22), 6073-6077.
14. Islam, M. A.; Mobarok, M. H.; Sinelnikov, R.; Purkait, T. K.; Veinot, J. G. C., Phosphorus Pentachloride Initiated Functionalization of Silicon Nanocrystals. *Langmuir* **2017**, *33* (35), 8766-8773.
15. Ko, M.; Chae, S.; Jeong, S.; Oh, P.; Cho, J., Elastic α -Silicon Nanoparticle Backboned Graphene Hybrid as a Self-Compacting Anode for High-Rate Lithium Ion Batteries. *ACS Nano* **2014**, *8* (8), 8591-8599.
16. Dasog, M.; De los Reyes, G. B.; Titova, L. V.; Hegmann, F. A.; Veinot, J. G., Size vs surface: tuning the photoluminescence of freestanding silicon nanocrystals across the visible spectrum via surface groups. *ACS Nano* **2014**, *8* (9), 9636-48.
17. Falcão, B. P.; Leitão, J. P.; Soares, M. R.; Ricardo, L.; Águas, H.; Martins, R.; Pereira, R. N., Oxidation and Strain in Free-standing Silicon Nanocrystals. *Phys. Rev. Appl.* **2019**, *11* (2), 024054.
18. Wu, Y.; Chen, Z.; Nan, P.; Xiong, F.; Lin, S.; Zhang, X.; Chen, Y.; Chen, L.; Ge, B.; Pei, Y., Lattice Strain Advances Thermoelectrics. *Joule* **2019**, *3* (5), 1276-1288.
19. Ouyang, G.; Zhu, W. G.; Sun, C. Q.; Zhu, Z. M.; Liao, S. Z., Atomistic origin of lattice strain on stiffness of nanoparticles. *Phys. Chem. Chem. Phys.* **2010**, *12* (7), 1543-1549.
20. Lee, B. G.; Hiller, D.; Luo, J. W.; Semonin, O. E.; Beard, M. C.; Zacharias, M.; Stradins, P., Strained Interface Defects in Silicon Nanocrystals. *Adv. Funct. Mater.* **2012**, *22* (15), 3223-3232.
21. Kleovoulou, K.; Kelires, P. C., Stress state of embedded Si nanocrystals. *Phys. Rev. B* **2013**, *88*, 085424.
22. Huisken, F.; Ledoux, G.; Guillois, O.; Reynaud, C., Light-Emitting Silicon Nanocrystals from Laser Pyrolysis. *Adv. Mater.* **2002**, *14* (24), 1861-1865.

23. Wu, J. J.; Kortshagen, U. R., Photostability of thermally-hydrosilylated silicon quantum dots. *RSC Adv.* **2015**, *5* (126), 103822-103828.
24. Ross, P. E., Startup Offers a Silicon Solution for Lithium-Ion Batteries. *IEEE Spectrum*, [Online], Dec 13, 2019, <https://spectrum.ieee.org/energywise/green-tech/fuel-cells/startup-advano-silicon-lithium-ion-batteries> (July 10, 2020)
25. Cassidy, M. C.; Chan, H. R.; Ross, B. D.; Bhattacharya, P. K.; Marcus, C. M., In vivo magnetic resonance imaging of hyperpolarized silicon particles. *Nature Nanotech.* **2013**, *8*, 363-368.
26. Tu, C.; Ma, X.; House, A.; Kauzlarich, S. M.; Louie, A. Y., PET Imaging and Biodistribution of Silicon Quantum Dots in Mice. *ACS Med. Chem. Lett.* **2011**, *2* (4), 285-288.
27. Chen, W.; Silverman, D. H. S.; Delaloye, S.; Czernin, J.; Kamdar, N.; Pope, W.; Satyamurthy, N.; Schiepers, C.; Cloughesy, T., 18F-FDOPA PET imaging of brain tumors: comparison study with 18F-FDG PET and evaluation of diagnostic accuracy. *J. Nucl. Med.* **2006**, *47* (6), 904-911.
28. Ha, M.; Thiessen, A. N.; Sergeev, I. V.; Veinot, J. G. C.; Michaelis, V. K., Endogenous dynamic nuclear polarization NMR of hydride-terminated silicon nanoparticles. *Solid State Nucl. Mag.* **2019**, *100*, 77-84.
29. Pereira, R. N.; Rowe, D. J.; Anthony, R. J.; Kortshagen, U., Oxidation of freestanding silicon nanocrystals probed with electron spin resonance of interfacial dangling bonds. *Phys. Rev. B* **2011**, *83* (15), 155327.
30. Wängler, C.; Niedermoser, S.; Chin, J.; Orchowski, K.; Schirmmayer, E.; Jurkschat, K.; Iovkova-Berends, L.; Kostikov, A. P.; Schirmmayer, R.; Wängler, B., One-step 18F-labeling of peptides for positron emission tomography imaging using the SiFA methodology. *Nat. Protoc.* **2012**, *7* (11), 1946-1955.
31. Bruker, PET/MR 3T. https://www.bruker.com/products/preclinical-imaging/nuclear-molecular-imaging/petmr-3t.html?gclid=Cj0KCQjw0YD4BRD2ARIsAHwmKVmnrQ7gxq8Rnzyz_RMQ9cBm2TdsH7HIWFdhymA9q0yBHO3Of9GP9qkaAoIdEALw_wcB (accessed July 10, 2020)
32. Zheludev, N. I., Obtaining optical properties on demand. *Science* **2015**, *348* (6238), 973-974.
33. Shelby, R. A.; Smith, D. R.; Schultz, S., Experimental Verification of a Negative Index of Refraction. *Science* **2001**, *292* (5514), 77-79.
34. Mühlig, S.; Cunningham, A.; Dintinger, J.; Farhat, M.; Hasan, S. B.; Scharf, T.; Bürgi, T.; Lederer, F.; Rockstuhl, C., A self-assembled three-dimensional cloak in the visible. *Sci. Rep.* **2013**, *3* (1), 2328.
35. Haxha, S.; AbdelMalek, F.; Ouerghi, F.; Charlton, M. D. B.; Aggoun, A.; Fang, X., Metamaterial Superlenses Operating at Visible Wavelength for Imaging Applications. *Sci. Rep.* **2018**, *8* (1), 16119.
36. De Marco, M. L.; Semlali, S.; Korgel, B. A.; Barois, P.; Drisko, G. L.; Aymonier, C., Silicon-Based Dielectric Metamaterials: Focus on the Current Synthetic Challenges. *Angew. Chem. Int. Ed.* **2018**, *57* (17), 4478-4498.

Bibliography

Chapter 1

1. National Nanotechnology Institute. What is Nanotechnology? <https://www.nano.gov/nanotech-101/what/definition> (accessed: July 6, 2020).
2. Bayda, S.; Adeel, M.; Tuccinardi, T.; Cordani, M.; Rizzolio, F., The History of Nanoscience and Nanotechnology: From Chemical-Physical Applications to Nanomedicine. *Molecules* **2019**, *25* (1), 112.
3. Nature. Nanoscience and technology. <https://www.nature.com/subjects/nanoscience-and-technology> (accessed: July 6, 2020).
4. Wang, L.-W.; Zunger, A., Dielectric Constants of Silicon Quantum Dots. *Phys. Rev. Lett.* **1994**, *73* (7), 1039-1042.
5. Brus, L. E., Electron–electron and electron-hole interactions in small semiconductor crystallites: The size dependence of the lowest excited electronic state. *J. Chem. Phys.* **1984**, *80* (9), 4403-4409.
6. Bawendi, M. G.; Steigerwald, M. L.; Brus, L. E., The Quantum Mechanics of Larger Semiconductor Clusters ("Quantum Dots"). *Annu. Rev. Phys. Chem.* **1990**, *41* (1), 477-496.
7. Kortan, A. R.; Hull, R.; Opila, R. L.; Bawendi, M. G.; Steigerwald, M. L.; Carroll, P. J.; Brus, L. E., Nucleation and Growth of CdSe on ZnS Quantum Crystallite Seeds, and Vice Versa, in Inverse Micelle Media. *J. Am. Chem. Soc.* **1990**, *112* (4), 1327-1332.
8. Vasudevan, D.; Gaddam, R. R.; Trinchi, A.; Cole, I., Core–shell quantum dots: Properties and applications. *J. Alloys Compd.* **2015**, *636*, 395-404.
9. AbouElhamd, A. R.; Al-Sallal, K. A.; Hassan, A., Review of Core/Shell Quantum Dots Technology Integrated into Building's Glazing. *Energies* **2019**, *12* (6), 1058.
10. Hanifi, D. A.; Bronstein, N. D.; Koscher, B. A.; Nett, Z.; Swabeck, J. K.; Takano, K.; Schwartzberg, A. M.; Maserati, L.; Vandewal, K.; van de Burgt, Y.; Salleo, A.; Alivisatos, A. P., Redefining near-unity luminescence in quantum dots with photothermal threshold quantum yield. *Science* **2019**, *363* (6432), 1199-1202.
11. Pan, Z.; Zhang, H.; Cheng, K.; Hou, Y.; Hua, J.; Zhong, X., Highly Efficient Inverted Type-I CdS/CdSe Core/Shell Structure QD-Sensitized Solar Cells. *ACS Nano* **2012**, *6* (5), 3982-3991.
12. Kim, S.; Fisher, B.; Eisler, H.-J.; Bawendi, M., Type-II Quantum Dots: CdTe/CdSe(Core/Shell) and CdSe/ZnTe(Core/Shell) Heterostructures. *J. Am. Chem. Soc.* **2003**, *125* (38), 11466-11467.
13. Chuang, C.-H.; Lo, S. S.; Scholes, G. D.; Burda, C., Charge Separation and Recombination in CdTe/CdSe Core/Shell Nanocrystals as a Function of Shell Coverage: Probing the Onset of the Quasi Type-II Regime. *J. Phys. Chem. Lett.* **2010**, *1* (17), 2530-2535.
14. Thuy, U. T. D.; Tu, L. A.; Loan, N. T.; Chi, T. T. K.; Liem, N. Q., Comparative photoluminescence properties of type-I and type-II CdTe/CdS core/shell quantum dots. *Opt. Mater.* **2016**, *53*, 34-38.
15. Yarema, M.; Xing, Y.; Lechner, R. T.; Ludescher, L.; Dordevic, N.; Lin, W. M. M.; Yarema, O.; Wood, V., Mapping the Atomistic Structure of Graded Core/Shell Colloidal Nanocrystals. *Sci. Rep.* **2017**, *7*, 11718.
16. Boldt, K.; Bartlett, S.; Kirkwood, N.; Johannessen, B., Quantification of Material Gradients in Core/Shell Nanocrystals Using EXAFS Spectroscopy. *Nano Lett.* **2020**, *20* (2), 1009-1017.
17. Park, Y.-S.; Bae, W. K.; Padilha, L. A.; Pietryga, J. M.; Klimov, V. I., Effect of the Core/Shell Interface on Auger Recombination Evaluated by Single-Quantum-Dot Spectroscopy. *Nano Lett.* **2014**, *14* (2), 396-402.
18. Park, Y.-S.; Lim, J.; Makarov, N. S.; Klimov, V. I., Effect of Interfacial Alloying versus "Volume Scaling" on Auger Recombination in Compositionally Graded Semiconductor Quantum Dots. *Nano Lett.* **2017**, *17* (9), 5607-5613.

19. Walsh, B. R.; Saari, J. I.; Krause, M. M.; Mack, T. G.; Nick, R.; Coe-Sullivan, S.; Kambhampati, P., Interfacial Electronic Structure in Graded Shell Nanocrystals Dictates Their Performance for Optical Gain. *J. Phys. Chem. C* **2016**, *120* (34), 19409-19415.
20. Boldt, K.; Kirkwood, N.; Beane, G. A.; Mulvaney, P., Synthesis of Highly Luminescent and Photo-Stable, Graded Shell CdSe/CdxZn1-xS Nanoparticles by In Situ Alloying. *Chem. Mater.* **2013**, *25* (23), 4731-4738.
21. Beane, G. A.; Gong, K.; Kelley, D. F., Auger and Carrier Trapping Dynamics in Core/Shell Quantum Dots Having Sharp and Alloyed Interfaces. *ACS Nano* **2016**, *10* (3), 3755-3765.
22. Cragg, G. E.; Efros, A. L., Suppression of Auger Processes in Confined Structures. *Nano Lett.* **2010**, *10* (1), 313-317.
23. Pramanik, S.; Hill, S. K. E.; Zhi, B.; Hudson-Smith, N. V.; Wu, J. J.; White, J. N.; McIntire, E. A.; Kondeti, V. S. S. K.; Lee, A. L.; Bruggeman, P. J.; Kortshagen, U. R.; Haynes, C. L., Comparative toxicity assessment of novel Si quantum dots and their traditional Cd-based counterparts using bacteria models *Shewanella oneidensis* and *Bacillus subtilis*. *Environ. Sci.: Nano* **2018**, *5* (8), 1890-1901.
24. Werner, T. T.; Mudd, G. M.; Jowitt, S. M., Indium: key issues in assessing mineral resources and long-term supply from recycling. *Applied Earth Science* **2015**, *124* (4), 213-226.
25. Islam, M. A.; Sinelnikov, R.; Howlader, M. A.; Faramus, A.; Veinot, J. G. C., Mixed Surface Chemistry: An Approach to Highly Luminescent Biocompatible Amphiphilic Silicon Nanocrystals. *Chem. Mater.* **2018**, *30* (24), 8925-8931.
26. Haynes, J. R.; Westphal, W. C., Radiation Resulting from Recombination of Holes and Electrons in Silicon. *Phys. Rev.* **1956**, *101* (6), 1676-1678.
27. Michaelis, W.; Pilkuhn, M. H., Radiative Recombination in Silicon p-n Junctions. *Phys. Status Solidi B* **1969**, *36* (1), 311-319.
28. Canham, L. T., Silicon quantum wire array fabrication by electrochemical and chemical dissolution of wafers. *Appl. Phys. Lett.* **1990**, *57* (10), 1046-1048.
29. Liang, D.; Bowers, J. E., Recent progress in lasers on silicon. *Nature Photon.* **2010**, *4* (8), 511-517.
30. Zelewski, S. J.; Kudrawiec, R., Photoacoustic and modulated reflectance studies of indirect and direct band gap in van der Waals crystals. *Sci. Rep.* **2017**, *7* (1), 15365.
31. Brus, L., Luminescence of Silicon Materials: Chains, Sheets, Nanocrystals, Nanowires, Microcrystals, and Porous Silicon. *J. Phys. Chem.* **1994**, *98* (14), 3575-3581.
32. Hybertsen, M. S., Absorption and emission of light in nanoscale silicon structures. *Phys. Rev. Lett.* **1994**, *72* (10), 1514-1517.
33. Hill, N. A.; Whaley, K. B., A theoretical study of light emission from nanoscale silicon. *J. Electron. Mater.* **1996**, *25* (2), 269-285.
34. Delerue, C.; Allan, G.; Lannoo, M., Electron-phonon coupling and optical transitions for indirect-gap semiconductor nanocrystals. *Phys. Rev. B* **2001**, *64* (19), 193402.
35. Mazzaro, R.; Romano, F.; Ceroni, P., Long-lived luminescence of silicon nanocrystals: from principles to applications. *Phys. Chem. Chem. Phys.* **2017**, *19* (39), 26507-26526.
36. Su, X.; Wu, Q.; Li, J.; Xiao, X.; Lott, A.; Lu, W.; Sheldon, B. W.; Wu, J., Silicon-Based Nanomaterials for Lithium-Ion Batteries: A Review. *Adv. Energy Mater.* **2014**, *4*, (1), 1300882.
37. Canham, L., Introductory lecture: origins and applications of efficient visible photoluminescence from silicon-based nanostructures. *Faraday Discuss.* **2020**, *222*, 10-81.
38. Gonzalez, C. M.; Veinot, J. G. C., Silicon nanocrystals for the development of sensing platforms. *J. Mater. Chem. C* **2016**, *4* (22), 4836-4846.
39. Erogbogbo, F.; Yong, K.-T.; Roy, I.; Xu, G.; Prasad, P. N.; Swihart, M. T., Biocompatible Luminescent Silicon Quantum Dots for Imaging of Cancer Cells. *ACS Nano* **2008**, *2* (5), 873-878.

40. Romano, F.; Angeloni, S.; Morselli, G.; Mazzaro, R.; Morandi, V.; Shell, J. R.; Cao, X.; Pogue, B. W.; Ceroni, P., Water-soluble silicon nanocrystals as NIR luminescent probes for time-gated biomedical imaging. *Nanoscale* **2020**, *12* (14), 7921-7926.
41. Aptekar, J. W.; Cassidy, M. C.; Johnson, A. C.; Barton, R. A.; Lee, M.; Ogier, A. C.; Vo, C.; Anahtar, M. N.; Ren, Y.; Bhatia, S. N.; Ramanathan, C.; Cory, D. G.; Hill, A. L.; Mair, R. W.; Rosen, M. S.; Walsworth, R. L.; Marcus, C. M., Silicon Nanoparticles as Hyperpolarized Magnetic Resonance Imaging Agents. *ACS Nano* **2009**, *3* (12), 4003-4008.
42. Cassidy, M. C.; Chan, H. R.; Ross, B. D.; Bhattacharya, P. K.; Marcus, C. M., In vivo magnetic resonance imaging of hyperpolarized silicon particles. *Nat. Nanotechnol.* **2013**, *8*, 363-368.
43. Gonzalez, C. M.; Iqbal, M.; Dasog, M.; Piercey, D. G.; Lockwood, R.; Klapotke, T. M.; Veinot, J. G. C., Detection of high-energy compounds using photoluminescent silicon nanocrystal paper based sensors. *Nanoscale* **2014**, *6* (5), 2608-2612.
44. Robidillo, C. J. T.; Wandelt, S.; Dalangin, R.; Zhang, L.; Yu, H.; Meldrum, A.; Campbell, R. E.; Veinot, J. G. C., Ratiometric Detection of Nerve Agents by Coupling Complementary Properties of Silicon-Based Quantum Dots and Green Fluorescent Protein. *ACS Appl. Mater. Interfaces* **2019**, *11* (36), 33478-33488.
45. Meinardi, F.; Ehrenberg, S.; Dharmo, L.; Carulli, F.; Mauri, M.; Bruni, F.; Simonutti, R.; Kortshagen, U.; Brovelli, S., Highly efficient luminescent solar concentrators based on earth-abundant indirect-bandgap silicon quantum dots. *Nature Photon.* **2017**, *11*, 177-185.
46. Hill, S. K. E.; Connell, R.; Peterson, C.; Hollinger, J.; Hillmyer, M. A.; Kortshagen, U.; Ferry, V. E., Silicon Quantum Dot–Poly(methyl methacrylate) Nanocomposites with Reduced Light Scattering for Luminescent Solar Concentrators. *ACS Photonics* **2019**, *6* (1), 170-180.
47. Cheng, K.-Y.; Anthony, R.; Kortshagen, U. R.; Holmes, R. J., High-Efficiency Silicon Nanocrystal Light-Emitting Devices. *Nano Lett.* **2011**, *11* (5), 1952-1956.
48. Liu, X.; Zhao, S.; Gu, W.; Zhang, Y.; Qiao, X.; Ni, Z.; Pi, X.; Yang, D., Light-Emitting Diodes Based on Colloidal Silicon Quantum Dots with Octyl and Phenylpropyl Ligands. *ACS Appl. Mater. Interfaces* **2018**, *10* (6), 5959-5966.
49. Choi, J. W.; Aurbach, D., Promise and reality of post-lithium-ion batteries with high energy densities. *Nat. Rev. Mater.* **2016**, *1* (4), 16013.
50. Li, Z. F.; Ruckenstein, E., Water-Soluble Poly(acrylic acid) Grafted Luminescent Silicon Nanoparticles and Their Use as Fluorescent Biological Staining Labels. *Nano Lett.* **2004**, *4* (8), 1463-1467.
51. Warner, J. H.; Hoshino, A.; Yamamoto, K.; Tilley, R. D., Water-soluble photoluminescent silicon quantum dots. *Angew. Chem. Int. Ed.* **2005**, *44* (29), 4550-4.
52. Sato, S.; Swihart, M. T., Propionic-Acid-Terminated Silicon Nanoparticles: Synthesis and Optical Characterization. *Chem. Mater.* **2006**, *18* (17), 4083-4088.
53. Cheng, X.; Lowe, S. B.; Ciampi, S.; Magenau, A.; Gaus, K.; Reece, P. J.; Gooding, J. J., Versatile “Click Chemistry” Approach to Functionalizing Silicon Quantum Dots: Applications toward Fluorescent Cellular Imaging. *Langmuir* **2014**, *30* (18), 5209-5216.
54. Erogbogbo, F.; Yong, K.-T.; Roy, I.; Hu, R.; Law, W.-C.; Zhao, W.; Ding, H.; Wu, F.; Kumar, R.; Swihart, M. T.; Prasad, P. N., In Vivo Targeted Cancer Imaging, Sentinel Lymph Node Mapping and Multi-Channel Imaging with Biocompatible Silicon Nanocrystals. *ACS Nano* **2011**, *5* (1), 413-423.
55. Erogbogbo, F.; Yong, K.-T.; Hu, R.; Law, W.-C.; Ding, H.; Chang, C.-W.; Prasad, P. N.; Swihart, M. T., Biocompatible Magnetofluorescent Probes: Luminescent Silicon Quantum Dots Coupled with Superparamagnetic Iron(III) Oxide. *ACS Nano* **2010**, *4* (9), 5131-5138.
56. Joo, J.; Liu, X.; Kotamraju, V. R.; Ruoslahti, E.; Nam, Y.; Sailor, M. J., Gated Luminescence Imaging of Silicon Nanoparticles. *ACS Nano* **2015**, *9* (6), 6233-6241.

57. Gu, L.; Hall, D. J.; Qin, Z.; Anglin, E.; Joo, J.; Mooney, D. J.; Howell, S. B.; Sailor, M. J., In vivo time-gated fluorescence imaging with biodegradable luminescent porous silicon nanoparticles. *Nat. Commun.* **2013**, *4* (1), 2326.
58. Tu, C.-C.; Awasthi, K.; Chen, K.-P.; Lin, C.-H.; Hamada, M.; Ohta, N.; Li, Y.-K., Time-Gated Imaging on Live Cancer Cells Using Silicon Quantum Dot Nanoparticles with Long-Lived Fluorescence. *ACS Photonics* **2017**, *4* (6), 1306-1315.
59. Yang, W.; Srivastava, P. K.; Han, S.; Jing, L.; Tu, C.-C.; Chen, S.-L., Optomechanical Time-Gated Fluorescence Imaging Using Long-Lived Silicon Quantum Dot Nanoparticles. *Anal. Chem.* **2019**, *91* (9), 5499-5503.
60. Uhlig, F., ²⁹Si NMR Spectroscopy. In *Organosilicon Compounds*; Lee, V. Y., Ed. Academic Press: 2017; Chapter 2, pp 59-77.
61. Ha, M.; Michaelis, V. K., High-Frequency Dynamic Nuclear Polarization NMR for Solids: Part 1 – An Introduction. In *Modern Magnetic Resonance*, Webb, G. A., Ed. Springer International Publishing: 2017; pp 1-24.
62. Hooper, R. W.; Klein, B. A.; Michaelis, V. K., Dynamic Nuclear Polarization (DNP) 101: A New Era for Materials. *Chem. Mater.* **2020**, *32* (11), 4425-4430.
63. Hu, J.; Whiting, N.; Bhattacharya, P., Hyperpolarization of Silicon Nanoparticles with TEMPO Radicals. *J. Phys. Chem. C* **2018**, *122* (19), 10575-10581.
64. Atkins, T. M.; Cassidy, M. C.; Lee, M.; Ganguly, S.; Marcus, C. M.; Kauzlarich, S. M., Synthesis of Long T₁ Silicon Nanoparticles for Hyperpolarized ²⁹Si Magnetic Resonance Imaging. *ACS Nano* **2013**, *7* (2), 1609-1617.
65. Tu, C.; Ma, X.; Pantazis, P.; Kauzlarich, S. M.; Louie, A. Y., Paramagnetic, Silicon Quantum Dots for Magnetic Resonance and Two-Photon Imaging of Macrophages. *J. Am. Chem. Soc.* **2010**, *132* (6), 2016-2023.
66. Tu, C.; Ma, X.; House, A.; Kauzlarich, S. M.; Louie, A. Y., PET Imaging and Biodistribution of Silicon Quantum Dots in Mice. *ACS Med. Chem. Lett.* **2011**, *2* (4), 285-288.
67. Singh, M. P.; Atkins, T. M.; Muthuswamy, E.; Kamali, S.; Tu, C.; Louie, A. Y.; Kauzlarich, S. M., Development of Iron-Doped Silicon Nanoparticles As Bimodal Imaging Agents. *ACS Nano* **2012**, *6* (6), 5596-5604.
68. Ban, R.; Zheng, F.; Zhang, J., A highly sensitive fluorescence assay for 2,4,6-trinitrotoluene using amine-capped silicon quantum dots as a probe. *Anal. Methods* **2015**, *7* (5), 1732-1737.
69. Zhang, J.; Yu, S.-H., Highly photoluminescent silicon nanocrystals for rapid, label-free and recyclable detection of mercuric ions. *Nanoscale* **2014**, *6* (8), 4096-4101.
70. Liao, B.; Wang, W.; Deng, X.; He, B.; Zeng, W.; Tang, Z.; Liu, Q., A facile one-step synthesis of fluorescent silicon quantum dots and their application for detecting Cu²⁺. *RSC Adv.* **2016**, *6* (18), 14465-14467.
71. Campos, B. B.; Algarra, M.; Alonso, B.; Casado, C. M.; Jiménez-Jiménez, J.; Rodríguez-Castellón, E.; Esteves da Silva, J. C. G., Fluorescent sensor for Cr(VI) based in functionalized silicon quantum dots with dendrimers. *Talanta* **2015**, *144*, 862-867.
72. Yi, Y.; Deng, J.; Zhang, Y.; Li, H.; Yao, S., Label-free Si quantum dots as photoluminescence probes for glucose detection. *Chem. Commun.* **2013**, *49* (6), 612-614.
73. Chen, Q.; Liu, M.; Zhao, J.; Peng, X.; Chen, X.; Mi, N.; Yin, B.; Li, H.; Zhang, Y.; Yao, S., Water-dispersible silicon dots as a peroxidase mimetic for the highly-sensitive colorimetric detection of glucose. *Chem. Commun.* **2014**, *50* (51), 6771-6774.
74. Zhang, X.; Chen, X.; Kai, S.; Wang, H.-Y.; Yang, J.; Wu, F.-G.; Chen, Z., Highly Sensitive and Selective Detection of Dopamine Using One-Pot Synthesized Highly Photoluminescent Silicon Nanoparticles. *Anal. Chem.* **2015**, *87* (6), 3360-3365.
75. Zhang, Z. H.; Lockwood, R.; Veinot, J. G. C.; Meldrum, A., Detection of ethanol and water vapor with silicon quantum dots coupled to an optical fiber. *Sensor. Actuat. B: Chem.* **2013**, *181*, 523-528.
76. Yi, Y.; Zhu, G.; Liu, C.; Huang, Y.; Zhang, Y.; Li, H.; Zhao, J.; Yao, S., A Label-Free Silicon Quantum Dots-Based Photoluminescence Sensor for Ultrasensitive Detection of Pesticides. *Anal. Chem.* **2013**, *85* (23), 11464-11470.

77. Hill, S. K. E.; Connell, R.; Held, J.; Peterson, C.; Francis, L.; Hillmyer, M. A.; Ferry, V. E.; Kortshagen, U., Poly(methyl methacrylate) Films with High Concentrations of Silicon Quantum Dots for Visibly Transparent Luminescent Solar Concentrators. *ACS Appl. Mater. Interfaces* **2020**, *12* (4), 4572-4578.
78. Mazzaro, R.; Gradone, A.; Angeloni, S.; Morselli, G.; Cozzi, P. G.; Romano, F.; Vomiero, A.; Ceroni, P., Hybrid Silicon Nanocrystals for Color-Neutral and Transparent Luminescent Solar Concentrators. *ACS Photonics* **2019**, *6* (9), 2303-2311.
79. Union, T. E., Ed. *Publications Office of the European Union: Official Journal of the European Union*, 2017; Vol. 2017/1975, p 3.
80. Jang, E.; Kim, Y.; Won, Y.-H.; Jang, H.; Choi, S.-M., Environmentally Friendly InP-Based Quantum Dots for Efficient Wide Color Gamut Displays. *ACS Energy Lett.* **2020**, *5* (4), 1316-1327.
81. Maier-Flaig, F.; Rinck, J.; Stephan, M.; Bocksrocker, T.; Bruns, M.; Kübel, C.; Powell, A. K.; Ozin, G. A.; Lemmer, U., Multicolor Silicon Light-Emitting Diodes (SiLEDs). *Nano Lett.* **2013**, *13* (2), 475-480.
82. Wu, H.; Cui, Y., Designing nanostructured Si anodes for high energy lithium ion batteries. *Nano Today* **2012**, *7* (5), 414-429.
83. Aghajamali, M.; Xie, H.; Javadi, M.; Kalisvaart, W. P.; Buriak, J. M.; Veinot, J. G. C., Size and Surface Effects of Silicon Nanocrystals in Graphene Aerogel Composite Anodes for Lithium Ion Batteries. *Chem. Mater.* **2018**, *30* (21), 7782-7792.
84. Jiang, S.; Hu, B.; Sahore, R.; Liu, H.; Pach, G. F.; Carroll, G. M.; Zhang, L.; Zhao, B.; Neale, N. R.; Zhang, Z., Tailoring the Surface of Silicon Nanoparticles for Enhanced Chemical and Electrochemical Stability for Li-Ion Batteries. *ACS Appl. Energy Mater.* **2019**, *2* (9), 6176-6183.
85. Shen, T. D.; Koch, C. C.; McCormick, T. L.; Nemanich, R. J.; Huang, J. Y.; Huang, J. G., The structure and property characteristics of amorphous/nanocrystalline silicon produced by ball milling. *J. Mater. Res.* **1995**, *10* (1), 139-148.
86. Chaudhary, A.-L.; Sheppard, D. A.; Paskevicius, M.; Saunders, M.; Buckley, C. E., Mechanochemical synthesis of amorphous silicon nanoparticles. *RSC Adv.* **2014**, *4* (42), 21979-21983.
87. Tan, D.; Ma, Z.; Xu, B.; Dai, Y.; Ma, G.; He, M.; Jin, Z.; Qiu, J., Surface passivated silicon nanocrystals with stable luminescence synthesized by femtosecond laser ablation in solution. *Phys. Chem. Chem. Phys.* **2011**, *13* (45), 20255-20261.
88. Murthy, T. U. M. S.; Miyamoto, N.; Shimbo, M.; Nishizawa, J., Gas-phase nucleation during the thermal decomposition of silane in hydrogen. *J. Cryst. Growth* **1976**, *33* (1), 1-7.
89. Hofmeister, H.; Huisken, F.; Kohn, B. Lattice contraction in nanosized silicon particles produced by laser pyrolysis of silane. In *The European Physical Journal D*; Châtelain, A., Bonard, J. M., Eds.; Springer Berlin Heidelberg: 1999; pp 137-140.
90. Li, X.; He, Y.; Talukdar, S. S.; Swihart, M. T., Preparation of luminescent silicon nanoparticles by photothermal aerosol synthesis followed by acid etching. *Phase Transit.* **2004**, *77*, 131-137.
91. Huisken, F.; Ledoux, G.; Guillois, O.; Reynaud, C., Light-Emitting Silicon Nanocrystals from Laser Pyrolysis. *Adv. Mater.* **2002**, *14* (24), 1861-1865.
92. Li, X.; He, Y.; Talukdar, S. S.; Swihart, M. T., Process for Preparing Macroscopic Quantities of Brightly Photoluminescent Silicon Nanoparticles with Emission Spanning the Visible Spectrum. *Langmuir* **2003**, *19* (20), 8490-8496.
93. Li, X.; He, Y.; Swihart, M. T., Surface Functionalization of Silicon Nanoparticles Produced by Laser-Driven Pyrolysis of Silane followed by HF-HNO₃ Etching. *Langmuir* **2004**, *20* (11), 4720-4727.
94. Kortshagen, U. R.; Sankaran, R. M.; Pereira, R. N.; Girshick, S. L.; Wu, J. J.; Aydil, E. S., Nonthermal Plasma Synthesis of Nanocrystals: Fundamental Principles, Materials, and Applications. *Chem. Rev.* **2016**, *116* (18), 11061-11127.

95. Gorla, C. R.; Liang, S.; Tompa, G. S.; Mayo, W. E.; Lu, Y., Silicon and germanium nanoparticle formation in an inductively coupled plasma reactor. *J. Vac. Sci. Technol. A* **1997**, *15* (3), 860-864.
96. Mangolini, L.; Thimsen, E.; Kortshagen, U., High-Yield Plasma Synthesis of Luminescent Silicon Nanocrystals. *Nano Lett.* **2005**, *5* (4), 655-659.
97. So, K.-S.; Lee, H.; Kim, T.-H.; Choi, S.; Park, D.-W., Synthesis of silicon nanopowder from silane gas by RF thermal plasma. *Phys. Status Solidi A* **2014**, *211*, 310-315.
98. Gupta, A.; Swihart, M. T.; Wiggers, H., Luminescent Colloidal Dispersion of Silicon Quantum Dots from Microwave Plasma Synthesis: Exploring the Photoluminescence Behavior Across the Visible Spectrum. *Adv. Funct. Mater.* **2009**, *19* (5), 696-703.
99. Mangolini, L.; Kortshagen, U., Plasma-assisted synthesis of silicon nanocrystal inks. *Adv. Mater.* **2007**, *19* (18), 2513-2519.
100. Anthony, R.; Kortshagen, U., Photoluminescence quantum yields of amorphous and crystalline silicon nanoparticles. *Phys. Rev. B* **2009**, *80* (11), 115407.
101. Pi, X. D.; Liptak, R. W.; Deneen Nowak, J.; Wells, N. P.; Carter, C. B.; Campbell, S. A.; Kortshagen, U., Air-stable full-visible-spectrum emission from silicon nanocrystals synthesized by an all-gas-phase plasma approach. *Nanotechnology* **2008**, *19* (24), 245603.
102. Liptak, R. W.; Yang, J.; Kramer, N. J.; Kortshagen, U.; Campbell, S. A., Environmental photostability of SF₆-etched silicon nanocrystals. *Nanotechnology* **2012**, *23* (39), 395205.
103. Pringle, T. A.; Hunter, K. I.; Brumberg, A.; Anderson, K. J.; Fagan, J. A.; Thomas, S. A.; Petersen, R. J.; Sefannaser, M.; Han, Y.; Brown, S. L.; Kilin, D. S.; Schaller, R. D.; Kortshagen, U. R.; Boudjouk, P. R.; Hobbie, E. K., Bright Silicon Nanocrystals from a Liquid Precursor: Quasi-Direct Recombination with High Quantum Yield. *ACS Nano* **2020**, *14* (4), 3858-3867.
104. Yasar-Inceoglu, O.; Lopez, T.; Farshihagro, E.; Mangolini, L., Silicon nanocrystal production through non-thermal plasma synthesis: a comparative study between silicon tetrachloride and silane precursors. *Nanotechnology* **2012**, *23* (25), 255604.
105. Dasog, M.; Yang, Z. Y.; Regli, S.; Atkins, T. M.; Faramus, A.; Singh, M. P.; Muthuswamy, E.; Kauzlarich, S. M.; Tilley, R. D.; Veinot, J. G. C., Chemical Insight into the Origin of Red and Blue Photoluminescence Arising from Freestanding Silicon Nanocrystals. *ACS Nano* **2013**, *7* (3), 2676-2685.
106. Rosso-Vasic, M.; Spruijt, E.; van Lagen, B.; De Cola, L.; Zuilhof, H., Alkyl-functionalized oxide-free silicon nanoparticles: synthesis and optical properties. *Small* **2008**, *4* (10), 1835-1841.
107. Tilley, R. D.; Warner, J. H.; Yamamoto, K.; Matsui, I.; Fujimori, H., Micro-emulsion synthesis of monodisperse surface stabilized silicon nanocrystals. *Chem. Commun.* **2005**, *14*, 1833-1835.
108. Baldwin, R. K.; Pettigrew, K. A.; Ratai, E.; Augustine, M. P.; Kauzlarich, S. M., Solution reduction synthesis of surface stabilized silicon nanoparticles. *Chem. Commun.* **2002**, *17*, 1822-1823.
109. Zou, J.; Baldwin, R. K.; Pettigrew, K. A.; Kauzlarich, S. M., Solution synthesis of ultrastable luminescent siloxane-coated silicon nanoparticles. *Nano Lett.* **2004**, *4* (7), 1181-1186.
110. Heath, J. R., A liquid-solution-phase synthesis of crystalline silicon. *Science* **1992**, *258* (5085), 1131-1133.
111. Janka, O.; Kauzlarich, S. M. Zintl Compounds. In *Encyclopedia of Inorganic and Bioinorganic Chemistry*; Scott, R. A., Ed.; John Wiley & Sons: 2014; pp 1-14.
112. Bley, R. A.; Kauzlarich, S. M., A Low-Temperature Solution Phase Route for the Synthesis of Silicon Nanoclusters. *J. Am. Chem. Soc.* **1996**, *118* (49), 12461-12462.
113. Yang, C.-S.; Bley, R. A.; Kauzlarich, S. M.; Lee, H. W. H.; Delgado, G. R., Synthesis of Alkyl-Terminated Silicon Nanoclusters by a Solution Route. *J. Am. Chem. Soc.* **1999**, *121* (22), 5191-5195.
114. Mayeri, D.; Phillips, B. L.; Augustine, M. P.; Kauzlarich, S. M., NMR Study of the Synthesis of Alkyl-Terminated Silicon Nanoparticles from the Reaction of SiCl₄ with the Zintl Salt, NaSi. *Chem. Mater.* **2001**, *13* (3), 765-770.

115. Pettigrew, K. A.; Liu, Q.; Power, P. P.; Kauzlarich, S. M., Solution Synthesis of Alkyl- and Alkyl/Alkoxy-Capped Silicon Nanoparticles via Oxidation of Mg₂Si. *Chem. Mater.* **2003**, *15* (21), 4005-4011.
116. Zhang, X.; Neiner, D.; Wang, S.; Louie, A. Y.; Kauzlarich, S. M., A new solution route to hydrogen-terminated silicon nanoparticles: synthesis, functionalization and water stability. *Nanotechnology* **2007**, *18* (9), 095601.
117. Nesheva, D.; Raptis, C.; Perakis, A.; Bineva, I.; Aneva, Z.; Levi, Z.; Alexandrova, S.; Hofmeister, H., Raman scattering and photoluminescence from Si nanoparticles in annealed SiO_x thin films. *J. Appl. Phys.* **2002**, *92* (8), 4678-4683.
118. Hao, X. J.; Podhorodecki, A. P.; Shen, Y. S.; Zatoryb, G.; Misiewicz, J.; Green, M. A., Effects of Si-rich oxide layer stoichiometry on the structural and optical properties of Si QD/SiO₂ multilayer films. *Nanotechnology* **2009**, *20* (48), 485703.
119. Sun, W.; Qian, C.; Cui, X. S.; Wang, L.; Wei, M.; Casillas, G.; Helmy, A. S.; Ozin, G. A., Silicon monoxide – a convenient precursor for large scale synthesis of near infrared emitting monodisperse silicon nanocrystals. *Nanoscale* **2016**, *8*, (6), 3678-3684.
120. Liu, S.-M.; Yang; Sato, S.; Kimura, K., Enhanced Photoluminescence from Si Nano-organosols by Functionalization with Alkenes and Their Size Evolution. *Chem. Mater.* **2006**, *18* (3), 637-642.
121. Hessel, C. M.; Henderson, E. J.; Veinot, J. G. C., Hydrogen Silsesquioxane: A Molecular Precursor for Nanocrystalline Si–SiO₂ Composites and Freestanding Hydride-Surface-Terminated Silicon Nanoparticles. *Chem. Mater.* **2006**, *18* (26), 6139-6146.
122. Clark, R. J.; Aghajamali, M.; Gonzalez, C. M.; Hadidi, L.; Islam, M. A.; Javadi, M.; Mobarok, M. H.; Purkait, T. K.; Robidillo, C. J. T.; Sinelnikov, R.; Thiessen, A. N.; Washington, J.; Yu, H.; Veinot, J. G. C., From Hydrogen Silsesquioxane to Functionalized Silicon Nanocrystals. *Chem. Mater.* **2017**, *29* (1), 80-89.
123. Wilkinson, A. R.; Elliman, R. G., The effect of annealing environment on the luminescence of silicon nanocrystals in silica. *J. Appl. Phys.* **2004**, *96* (7), 4018-4020.
124. Hessel, C. M.; Reid, D.; Panthani, M. G.; Rasch, M. R.; Goodfellow, B. W.; Wei, J.; Fujii, H.; Akhavan, V.; Korgel, B. A., Synthesis of Ligand-Stabilized Silicon Nanocrystals with Size-Dependent Photoluminescence Spanning Visible to Near-Infrared Wavelengths. *Chem. Mater.* **2012**, *24* (2), 393-401.
125. Yang, Z.; Dobbie, A. R.; Veinot, J. G. C., Shape Evolution of Faceted Silicon Nanocrystals upon Thermal Annealing in an Oxide Matrix. *MRS Proceedings* **2013**, *1536*, 207-212.
126. Yang, Z.; Dobbie, A. R.; Cui, K.; Veinot, J. G. C., A Convenient Method for Preparing Alkyl-Functionalized Silicon Nanocubes. *J. Am. Chem. Soc.* **2012**, *134* (34), 13958-13961.
127. Yu, Y.; Lu, X.; Guillaussier, A.; Voggu, V. R.; Pineros, W.; de la Mata, M.; Arbiol, J.; Smilgies, D.-M.; Truskett, T. M.; Korgel, B. A., Orientationally Ordered Silicon Nanocrystal Cuboctahedra in Superlattices. *Nano Lett.* **2016**, *16* (12), 7814-7821.
128. Pereira, R. N.; Rowe, D. J.; Anthony, R. J.; Kortshagen, U., Oxidation of freestanding silicon nanocrystals probed with electron spin resonance of interfacial dangling bonds. *Phys. Rev. B* **2011**, *83* (15), 155327.
129. Rinck, J.; Schray, D.; Kübel, C.; Powell, A. K.; Ozin, G. A., Size-Dependent Oxidation of Monodisperse Silicon Nanocrystals with Allylphenylsulfide Surfaces. *Small* **2015**, *11* (3), 335-340.
130. Purkait, T. K.; Iqbal, M.; Wahl, M. H.; Gottschling, K.; Gonzalez, C. M.; Islam, M. A.; Veinot, J. G. C., Borane-catalyzed room-temperature hydrosilylation of alkenes/alkynes on silicon nanocrystal surfaces. *J. Am. Chem. Soc.* **2014**, *136* (52), 17914-17917.
131. Ghosh, B.; Masuda, Y.; Wakayama, Y.; Imanaka, Y.; Inoue, J.-i.; Hashi, K.; Deguchi, K.; Yamada, H.; Sakka, Y.; Ohki, S.; Shimizu, T.; Shirahata, N., Hybrid White Light Emitting Diode Based on Silicon Nanocrystals. *Adv. Funct. Mater.* **2014**, *24* (45), 7151-7160.
132. Islam, M. A.; Mobarok, M. H.; Sinelnikov, R.; Purkait, T. K.; Veinot, J. G. C., Phosphorus Pentachloride Initiated Functionalization of Silicon Nanocrystals. *Langmuir* **2017**, *33* (35), 8766-8773.

133. Mobarok, M. H.; Purkait, T. K.; Islam, M. A.; Miskolzie, M.; Veinot, J. G. C., Instantaneous Functionalization of Chemically Etched Silicon Nanocrystal Surfaces. *Angew. Chem. Int. Ed.* **2017**, *56* (22), 6073-6077.
134. Purkait, T. K.; Iqbal, M.; Islam, M. A.; Mobarok, M. H.; Gonzalez, C. M.; Hadidi, L.; Veinot, J. G. C., Alkoxy-Terminated Si Surfaces: A New Reactive Platform for the Functionalization and Derivatization of Silicon Quantum Dots. *J. Am. Chem. Soc.* **2016**, *138* (22), 7114-7120.
135. Kelly, J. A.; Shukaliak, A. M.; Fleischauer, M. D.; Veinot, J. G. C., Size-dependent reactivity in hydrosilylation of silicon nanocrystals. *J. Am. Chem. Soc.* **2011**, *133* (24), 9564-9571.
136. Buriak, J. M., Illuminating Silicon Surface Hydrosilylation: An Unexpected Plurality of Mechanisms. *Chem. Mater.* **2014**, *26* (1), 763-772.
137. Holm, J.; Roberts, J. T., Thermally Induced Hydrosilylation at Deuterium-Terminated Silicon Nanoparticles: An Investigation of the Radical Chain Propagation Mechanism. *Langmuir* **2009**, *25* (12), 7050-7056.
138. Yang, Z.; Iqbal, M.; Dobbie, A. R.; Veinot, J. G. C., Surface-Induced Alkene Oligomerization: Does Thermal Hydrosilylation Really Lead to Monolayer Protected Silicon Nanocrystals? *J. Am. Chem. Soc.* **2013**, *135* (46), 17595-17601.
139. Rosso-Vasic, M.; Spruijt, E.; van Lagen, B.; De Cola, L.; Zuilhof, H., Alkyl-Functionalized Oxide-Free Silicon Nanoparticles: Synthesis and Optical Properties. *Small* **2008**, *4* (10), 1835-1841.
140. Kelly, J. A.; Veinot, J. G. C., An Investigation into Near-UV Hydrosilylation of Freestanding Silicon Nanocrystals. *ACS Nano* **2010**, *4* (8), 4645-4656.
141. Huck, L. A.; Buriak, J. M., Toward a mechanistic understanding of exciton-mediated hydrosilylation on nanocrystalline silicon. *J. Am. Chem. Soc.* **2012**, *134* (1), 489-497.
142. Hohlein, I. M.; Kehrlé, J.; Helbich, T.; Yang, Z.; Veinot, J. G.; Rieger, B., Diazonium salts as grafting agents and efficient radical-hydrosilylation initiators for freestanding photoluminescent silicon nanocrystals. *Chem. Eur. J.* **2014**, *20* (15), 4212-4216.
143. Yang, Z.; Gonzalez, C. M.; Purkait, T. K.; Iqbal, M.; Meldrum, A.; Veinot, J. G. C., Radical Initiated Hydrosilylation on Silicon Nanocrystal Surfaces: An Evaluation of Functional Group Tolerance and Mechanistic Study. *Langmuir* **2015**, *31* (38), 10540-10548.
144. Sun, W.; Qian, C.; Mastronardi, M. L.; Wei, M.; Ozin, G. A., Hydrosilylation kinetics of silicon nanocrystals. *Chem. Commun.* **2013**, *49* (97), 11361-11363.
145. Wheeler, L. M.; Anderson, N. C.; Palomaki, P. K. B.; Blackburn, J. L.; Johnson, J. C.; Neale, N. R., Silyl Radical Abstraction in the Functionalization of Plasma-Synthesized Silicon Nanocrystals. *Chem. Mater.* **2015**, *27* (19), 6869-6878.
146. Rogozhina, E. V.; Eckhoff, D. A.; Gratton, E.; Braun, P. V., Carboxyl functionalization of ultrasmall luminescent silicon nanoparticles through thermal hydrosilylation. *J. Mater. Chem.* **2006**, *16* (15), 1421-1430.
147. Yang, Z. Y.; Dasog, M.; Dobbie, A. R.; Lockwood, R.; Zhi, Y. Y.; Meldrum, A.; Veinot, J. G. C., Highly Luminescent Covalently Linked Silicon Nanocrystal/Polystyrene Hybrid Functional Materials: Synthesis, Properties, and Processability. *Adv. Funct. Mater.* **2014**, *24* (10), 1345-1353.
148. Hua, F.; Swihart, M. T.; Ruckenstein, E., Efficient surface grafting of luminescent silicon quantum dots by photoinitiated hydrosilylation. *Langmuir* **2005**, *21* (13), 6054-62.
149. Stewart, M. P.; Buriak, J. M., Exciton-mediated hydrosilylation on photoluminescent nanocrystalline silicon. *J. Am. Chem. Soc.* **2001**, *123* (32), 7821-7830.
150. Calder, S.; Boies, A.; Lei, P. Y.; Girshick, S.; Roberts, J., Photo-Assisted Hydrosilylation of Silicon Nanoparticles: Dependence of Particle Size on Grafting Chemistry. *Chem. Mater.* **2011**, *23* (11), 2917-2921.
151. Wu, Y.-D.; Wong, C.-L., Substituent Effect on the Dissociation Energy of the Si-H Bond: A Density Functional Study. *J. Org. Chem.* **1995**, *60* (4), 821-828.

152. Yang, Z.; De los Reyes, G. B.; Titova, L. V.; Sychugov, I.; Dasog, M.; Linnros, J.; Hegmann, F. A.; Veinot, J. G. C., Evolution of the Ultrafast Photoluminescence of Colloidal Silicon Nanocrystals with Changing Surface Chemistry. *ACS Photonics* **2015**, *2* (5), 595-605.
153. Shiohara, A.; Prabakar, S.; Faramus, A.; Hsu, C. Y.; Lai, P. S.; Northcote, P. T.; Tilley, R. D., Sized controlled synthesis, purification, and cell studies with silicon quantum dots. *Nanoscale* **2011**, *3* (8), 3364-3370.
154. Helbich, T.; Kloberg, M. J.; Sinelnikov, R.; Lyuleeva, A.; Veinot, J. G. C.; Rieger, B., Diaryliodonium salts as hydrosilylation initiators for the surface functionalization of silicon nanomaterials and their collaborative effect as ring opening polymerization initiators. *Nanoscale* **2017**, *9* (23), 7739-7744.
155. Kehrlé, J.; Kaiser, S.; Purkait, T. K.; Winnacker, M.; Helbich, T.; Vagin, S.; Veinot, J. G. C.; Rieger, B., In situ IR-spectroscopy as a tool for monitoring the radical hydrosilylation process on silicon nanocrystal surfaces. *Nanoscale* **2017**, *9* (24), 8489-8495.
156. Hohlein, I. M.; Angi, A.; Sinelnikov, R.; Veinot, J. G.; Rieger, B., Functionalization of Hydride Terminated Photoluminescent Silicon Nanocrystals with Organolithium Reagents. *Chem. Eur. J.* **2015**, *21* (7), 2755-2758.
157. Song, J. H.; Sailor, M. J., Functionalization of Nanocrystalline Porous Silicon Surfaces with Aryllithium Reagents: Formation of Silicon–Carbon Bonds by Cleavage of Silicon–Silicon Bonds. *J. Am. Chem. Soc.* **1998**, *120* (10), 2376-2381.
158. Angi, A.; Sinelnikov, R.; Heenen, H. H.; Meldrum, A.; Veinot, J. G. C.; Scheurer, C.; Reuter, K.; Ashkenazy, O.; Azulay, D.; Balberg, I.; Millo, O.; Rieger, B., The influence of conjugated alkynyl(aryl) surface groups on the optical properties of silicon nanocrystals: photoluminescence through in-gap states. *Nanotechnology* **2018**, *29* (35), 355705.
159. Kim, D.; Joo, J.; Pan, Y.; Boarino, A.; Jun, Y. W.; Ahn, K. H.; Arkles, B.; Sailor, M. J., Thermally Induced Silane Dehydrocoupling on Silicon Nanostructures. *Angew. Chem. Int. Ed.* **2016**, *55* (22), 6423-6427.
160. Yang, Z.; Wahl, M. H.; Veinot, J. G. C., Size-independent organosilane functionalization of silicon nanocrystals using Wilkinson's catalyst. *Can. J. Chem.* **2014**, *92* (10), 951-957.
161. Holland, J. M.; Stewart, M. P.; Allen, M. J.; Buriak, J. M., Metal Mediated Reactions on Porous Silicon Surfaces. *J. Solid State Chem.* **1999**, *147* (1), 251-258.
162. Dasog, M.; Veinot, J. G. C., Size independent blue luminescence in nitrogen passivated silicon nanocrystals. *Phys. Status Solidi A* **2012**, *209* (10), 1844-1846.
163. Dasog, M.; Bader, K.; Veinot, J. G. C., Influence of Halides on the Optical Properties of Silicon Quantum Dots. *Chem. Mater.* **2015**, *27* (4), 1153-1156.
164. Wang, R.; Pi, X.; Yang, D., Surface modification of chlorine-passivated silicon nanocrystals. *Phys. Chem. Chem. Phys.* **2013**, *15* (6), 1815-1820.
165. Zhai, Y.; Dasog, M.; Snitynsky, R. B.; Purkait, T. K.; Aghajamali, M.; Hahn, A. H.; Sturdy, C. B.; Lowary, T. L.; Veinot, J. G. C., Water-soluble photoluminescent d-mannose and l-alanine functionalized silicon nanocrystals and their application to cancer cell imaging. *J. Mater. Chem. B* **2014**, *2* (47), 8427-8433.
166. Baldwin, R. K.; Pettigrew, K. A.; Ratai, E.; Augustine, M. P.; Kauzlarich, S. M., Solution reduction synthesis of surface stabilized silicon nanoparticles. *Chem. Commun.* **2002**, *17*, 1822-1823.
167. Dasog, M.; De los Reyes, G. B.; Titova, L. V.; Hegmann, F. A.; Veinot, J. G., Size vs surface: tuning the photoluminescence of freestanding silicon nanocrystals across the visible spectrum via surface groups. *ACS Nano* **2014**, *8* (9), 9636-9648.
168. El-Demellawi, J. K.; Holt, C. R.; Abou-Hamad, E.; Al-Talla, Z. A.; Saih, Y.; Chaieb, S., Room-Temperature Reactivity Of Silicon Nanocrystals With Solvents: The Case Of Ketone And Hydrogen Production From Secondary Alcohols: Catalysis? *ACS Appl. Mater. Interfaces* **2015**, *7* (25), 13794-13800.
169. Dasog, M.; Thompson, J. R.; Lewis, N. S., Oxidant-Activated Reactions of Nucleophiles with Silicon Nanocrystals. *Chem. Mater.s* **2017**, *29* (16), 7002-7013.

170. Yu, Y.; Rowland, C. E.; Schaller, R. D.; Korgel, B. A., Synthesis and Ligand Exchange of Thiol-Capped Silicon Nanocrystals. *Langmuir* **2015**, *31* (24), 6886-6893.
171. Hessel, C. M.; Henderson, E. J.; Veinot, J. G. C., An Investigation of the Formation and Growth of Oxide-Embedded Silicon Nanocrystals in Hydrogen Silsesquioxane-Derived Nanocomposites. *J. Phys. Chem. C* **2007**, *111* (19), 6956-6961.
172. Hannah, D. C.; Yang, J.; Kramer, N. J.; Schatz, G. C.; Kortshagen, U. R.; Schaller, R. D., Ultrafast Photoluminescence in Quantum-Confined Silicon Nanocrystals Arises from an Amorphous Surface Layer. *ACS Photonics* **2014**, *1* (10), 960-967.
173. Petkov, V.; Hessel, C. M.; Ovtchinnikov, J.; Guillaussier, A.; Korgel, B. A.; Liu, X.; Giordano, C., Structure-Properties Correlation in Si Nanoparticles by Total Scattering and Computer Simulations. *Chem. Mater.* **2013**, *25* (11), 2365-2371.
174. Yu, Y.; Fan, G.; Fermi, A.; Mazzaro, R.; Morandi, V.; Ceroni, P.; Smilgies, D.-M.; Korgel, B. A., Size-Dependent Photoluminescence Efficiency of Silicon Nanocrystal Quantum Dots. *J. Phys. Chem. C* **2017**, *121* (41), 23240-23248.
175. Vatan Meidanshahi, R.; Bowden, S.; Goodnick, S. M., Electronic structure and localized states in amorphous Si and hydrogenated amorphous Si. *Phys. Chem. Chem. Phys.* **2019**, *21* (24), 13248-13257.
176. Jarolimek, K.; Hazrati, E.; de Groot, R. A.; de Wijs, G. A., Band Offsets at the Interface between Crystalline and Amorphous Silicon from First Principles. *Phys. Rev. Appl.* **2017**, *8* (1), 014026.
177. Park, N.-M.; Kim, T.-S.; Park, S.-J., Band gap engineering of amorphous silicon quantum dots for light-emitting diodes. *Appl. Phys. Lett.* **2001**, *78* (17), 2575-2577.
178. Park, N.-M.; Choi, C.-J.; Seong, T.-Y.; Park, S.-J., Quantum Confinement in Amorphous Silicon Quantum Dots Embedded in Silicon Nitride. *Phys. Rev. Lett.* **2001**, *86* (7), 1355-1357.
179. Askari, S.; Svrcek, V.; Maguire, P.; Mariotti, D., The Interplay of Quantum Confinement and Hydrogenation in Amorphous Silicon Quantum Dots. *Adv. Mater.* **2015**, *27* (48), 8011-8016.
180. Guo, Y.; Wang, Q.; Kawazoe, Y.; Jena, P., A New Silicon Phase with Direct Band Gap and Novel Optoelectronic Properties. *Sci. Rep.* **2015**, *5* (1), 14342.
181. Wang, Q.; Xu, B.; Sun, J.; Liu, H.; Zhao, Z.; Yu, D.; Fan, C.; He, J., Direct Band Gap Silicon Allotropes. *J. Am. Chem. Soc.* **2014**, *136* (28), 9826-9829.
182. Hannah, D. C.; Yang, J.; Podsiadlo, P.; Chan, M. K. Y.; Demortière, A.; Gosztola, D. J.; Prakapenka, V. B.; Schatz, G. C.; Kortshagen, U.; Schaller, R. D., On the Origin of Photoluminescence in Silicon Nanocrystals: Pressure-Dependent Structural and Optical Studies. *Nano Lett.* **2012**, *12* (8), 4200-4205.
183. Kůsová, K.; Hapala, P.; Valenta, J.; Jelínek, P.; Cibulka, O.; Ondič, L.; Pelant, I., Direct Bandgap Silicon: Tensile-Strained Silicon Nanocrystals. *Adv. Mater. Interfaces* **2014**, *1* (2), 1300042.
184. Kůsová, K.; Ondič, L.; Pelant, I., Comment on "Ultrafast Photoluminescence in Quantum-Confined Silicon Nanocrystals Arises from an Amorphous Surface Layer". *ACS Photonics* **2015**, *2*, (3), 454-455.
185. Hannah, D. C.; Yang, J.; Kramer, N. J.; Schatz, G. C.; Kortshagen, U. R.; Schaller, R. D., Reply to "Comment on 'Ultrafast Photoluminescence in Quantum-Confined Silicon Nanocrystals Arises from an Amorphous Surface Layer'". *ACS Photonics* **2015**, *2* (3), 456-458.
186. Kim, H.; Seo, M.; Park, M. H.; Cho, J., A critical size of silicon nano-anodes for lithium rechargeable batteries. *Angew. Chem. Int. Ed.* **2010**, *49* (12), 2146-2149.
187. Chan, C. K.; Peng, H. L.; Liu, G.; McIlwrath, K.; Zhang, X. F.; Huggins, R. A.; Cui, Y., High-performance lithium battery anodes using silicon nanowires. *Nat. Nanotechnol.* **2008**, *3* (1), 31-35.
188. Ko, M.; Chae, S.; Jeong, S.; Oh, P.; Cho, J., Elastic a-Silicon Nanoparticle Backboned Graphene Hybrid as a Self-Compacting Anode for High-Rate Lithium Ion Batteries. *ACS Nano* **2014**, *8* (8), 8591-8599.

189. Lockwood, R.; Yang, Z.; Sammynaiken, R.; Veinot, J. G. C.; Meldrum, A., Light-Induced Evolution of Silicon Quantum Dot Surface Chemistry—Implications for Photoluminescence, Sensing, and Reactivity. *Chem. Mater.* **2014**, *26* (19), 5467-5474.
190. Aghajamali, M.; Iqbal, M.; Purkait, T. K.; Hadidi, L.; Sinelnikov, R.; Veinot, J. G. C., Synthesis and Properties of Luminescent Silicon Nanocrystal/Silica Aerogel Hybrid Materials. *Chem. Mater.* **2016**, *28* (11), 3877-3886.
191. DeBenedetti, W. J. I.; Chiu, S.-K.; Radlinger, C. M.; Ellison, R. J.; Manhat, B. A.; Zhang, J. Z.; Shi, J.; Goforth, A. M., Conversion from Red to Blue Photoluminescence in Alcohol Dispersions of Alkyl-Capped Silicon Nanoparticles: Insight into the Origins of Visible Photoluminescence in Colloidal Nanocrystalline Silicon. *J. Phys. Chem. C* **2015**, *119* (17), 9595-9608.
192. Sinelnikov, R.; Dasog, M.; Beamish, J.; Meldrum, A.; Veinot, J. G. C., Revisiting an Ongoing Debate: What Role Do Surface Groups Play in Silicon Nanocrystal Photoluminescence? *ACS Photonics* **2017**, *4* (8), 1920-1929.
193. Kang, Z.; Liu, Y.; Tsang, C. H. A.; Ma, D. D. D.; Fan, X.; Wong, N.-B.; Lee, S.-T., Water-Soluble Silicon Quantum Dots with Wavelength-Tunable Photoluminescence. *Adv. Mater.* **2009**, *21* (6), 661-664.
194. Martin, J.; Cichos, F.; Huisken, F.; von Borczyskowski, C., Electron-Phonon Coupling and Localization of Excitons in Single Silicon Nanocrystals. *Nano Lett.* **2008**, *8* (2), 656-660.
195. Botas, A. M. P.; Ferreira, R. A. S.; Pereira, R. N.; Anthony, R. J.; Moura, T.; Rowe, D. J.; Kortshagen, U., High Quantum Yield Dual Emission from Gas-Phase Grown Crystalline Si Nanoparticles. *J. Phys. Chem. C* **2014**, *118* (19), 10375-10383.
196. Reboredo, F. A.; Galli, G., Theory of Alkyl-Terminated Silicon Quantum Dots. *J. Phys. Chem. B* **2005**, *109* (3), 1072-1078.
197. Angi, A.; Sinelnikov, R.; Meldrum, A.; Veinot, J. G. C.; Balberg, I.; Azulay, D.; Millo, O.; Rieger, B., Photoluminescence through in-gap states in phenylacetylene functionalized silicon nanocrystals. *Nanoscale* **2016**, *8* (15), 7849-7853.
198. Valenta, J.; Fucikova, A.; Pelant, I.; Kůsová, K.; Dohnalová, K.; Aleknavičius, A.; Cibulka, O.; Fojtík, A.; Kada, G., On the origin of the fast photoluminescence band in small silicon nanoparticles. *New J. Phys.* **2008**, *10* (7), 073022.
199. Yang, S.; Li, W.; Cao, B.; Zeng, H.; Cai, W., Origin of Blue Emission from Silicon Nanoparticles: Direct Transition and Interface Recombination. *J. Phys. Chem. C* **2011**, *115* (43), 21056-21062.
200. Gupta, A.; Wiggers, H., Freestanding silicon quantum dots: origin of red and blue luminescence. *Nanotechnology* **2010**, *22* (5), 055707.
201. Uchino, T.; Kurumoto, N.; Sagawa, N., Structure and formation mechanism of blue-light-emitting centers in silicon and silica-based nanostructured materials. *Phys. Rev. B* **2006**, *73* (23), 233203.
202. Loni, A.; Simons, A. J.; Calcott, P. D. J.; Canham, L. T., Blue photoluminescence from rapid thermally oxidized porous silicon following storage in ambient air. *J. Appl. Phys.* **1995**, *77* (7), 3557-3559.
203. Ddungu, J. L. Z.; Silvestrini, S.; Tassoni, A.; De Cola, L., Shedding light on the aqueous synthesis of silicon nanoparticles by reduction of silanes with citrates. *Faraday Discuss.* **2020**, *222*, 350-361.
204. Wilbrink, Jonathan L.; Huang, C.-C.; Dohnalova, K.; Paulusse, J. M. J., Critical assessment of wet-chemical oxidation synthesis of silicon quantum dots. *Faraday Discuss.* **2020**, *222*, 149-165.
205. Oliinyk, B. V.; Korytko, D.; Lysenko, V.; Alekseev, S., Are Fluorescent Silicon Nanoparticles Formed in a One-Pot Aqueous Synthesis? *Chem. Mater.* **2019**, *31* (18), 7167-7172.
206. Angi, A.; Loch, M.; Sinelnikov, R.; Veinot, J. G. C.; Becherer, M.; Lugli, P.; Rieger, B., The influence of surface functionalization methods on the performance of silicon nanocrystal LEDs. *Nanoscale* **2018**, *10* (22), 10337-10342.
207. Yang, S.; Li, G.; Zhu, Q.; Pan, Q., Covalent binding of Si nanoparticles to graphene sheets and its influence on lithium storage properties of Si negative electrode. *J. Mater. Chem.* **2012**, *22* (8), 3420-3425.
208. Lee, J. K.; Smith, K. B.; Hayner, C. M.; Kung, H. H., Silicon nanoparticles-graphene paper composites for Li ion battery anodes. *Chem. Commun.* **2010**, *46* (12), 2025-2027.

Chapter 2

1. Union, T. E., Ed. Publications Office of the European Union: Official Journal of the European Union, 2017; Vol. 2017/1975, p 3.
2. Liu, J.; Erogbogbo, F.; Yong, K.-T.; Ye, L.; Liu, J.; Hu, R.; Chen, H.; Hu, Y.; Yang, Y.; Yang, J.; Roy, I.; Karker, N. A.; Swihart, M. T.; Prasad, P. N., Assessing Clinical Prospects of Silicon Quantum Dots: Studies in Mice and Monkeys. *ACS Nano* **2013**, *7*, 7303-7310.
3. Park, J. H.; Gu, L.; von Maltzahn, G.; Ruoslahti, E.; Bhatia, S. N.; Sailor, M. J., Biodegradable Luminescent Porous Silicon Nanoparticles for in vivo Applications. *Nature Mater* **2009**, *8*, 331-6.
4. Mobarok, M. H.; Purkait, T. K.; Islam, M. A.; Miskolzie, M.; Veinot, J. G. C., Instantaneous Functionalization of Chemically Etched Silicon Nanocrystal Surfaces. *Angew. Chem., Int. Ed.* **2017**, *56*, 6073-6077.
5. Islam, M. A.; Mobarok, M. H.; Sinelnikov, R.; Purkait, T. K.; Veinot, J. G. C., Phosphorus Pentachloride Initiated Functionalization of Silicon Nanocrystals. *Langmuir* **2017**, *33*, 8766-8773.
6. Mastronardi, M. L.; Maier-Flaig, F.; Faulkner, D.; Henderson, E. J.; Kübel, C.; Lemmer, U.; Ozin, G. A., Size-Dependent Absolute Quantum Yields for Size-Separated Colloidally-Stable Silicon Nanocrystals. *Nano Lett* **2012**, *12*, 337-342.
7. Bhattacharjee, S.; Rietjens, I. M. C. M.; Singh, M. P.; Atkins, T. M.; Purkait, T. K.; Xu, Z.; Regli, S.; Shukaliak, A.; Clark, R. J.; Mitchell, B. S.; Alink, G. M.; Marcelis, A. T. M.; Fink, M. J.; Veinot, J. G. C.; Kauzlarich, S. M.; Zuillhof, H., Cytotoxicity of Surface-Functionalized Silicon and Germanium Nanoparticles: The Dominant Role of Surface Charges. *Nanoscale* **2013**, *5*, 4870-4883.
8. Erogbogbo, F.; Yong, K.-T.; Roy, I.; Hu, R.; Law, W.-C.; Zhao, W.; Ding, H.; Wu, F.; Kumar, R.; Swihart, M. T.; Prasad, P. N., In vivo Targeted Cancer Imaging, Sentinel Lymph Node Mapping and Multi-Channel Imaging with Biocompatible Silicon Nanocrystals. *ACS Nano* **2011**, *5*, 413-423.
9. Cassidy, M. C.; Chan, H. R.; Ross, B. D.; Bhattacharya, P. K.; Marcus, C. M., In vivo Magnetic Resonance Imaging of Hyperpolarized Silicon Particles. *Nature Nanotechnol.* **2013**, *8*, 363.
10. Tu, C.; Ma, X.; House, A.; Kauzlarich, S. M.; Louie, A. Y., PET Imaging and Biodistribution of Silicon Quantum Dots in Mice. *ACS Med. Chem. Lett.* **2011**, *2*, 285-288.
11. Liu, X.; Zhao, S.; Gu, W.; Zhang, Y.; Qiao, X.; Ni, Z.; Pi, X.; Yang, D., Light-Emitting Diodes Based on Colloidal Silicon Quantum Dots with Octyl and Phenylpropyl Ligands. *ACS Appl. Mater. Interfaces* **2018**, *10*, 5959-5966.
12. Dutta, M.; Thirugnanam, L.; Van Trinh, P.; Fukata, N., High Efficiency Hybrid Solar Cells Using Nanocrystalline Si Quantum Dots and Si Nanowires. *ACS Nano* **2015**, *9*, 6891-6899.
13. Svrcek, V.; McDonald, C.; Lozac'h, M.; Tayagaki, T.; Koganezawa, T.; Miyadera, T.; Mariotti, D.; Matsubara, K., Stable Ultrathin Surfactant-Free Surface-Engineered Silicon Nanocrystal Solar Cells Deposited at Room Temperature. *Energy Sci. Eng.* **2017**, *5*, 184-193.
14. Zhao, S.; Pi, X., Colloidal Silicon Quantum Dots and Solar Cells. In *Handbook of Photovoltaic Silicon*, Yang, D., Ed. Springer Berlin Heidelberg: Berlin, Heidelberg, 2017; pp 1-27.
15. Gonzalez, C. M.; Veinot, J. G. C., Silicon Nanocrystals for the Development of Sensing Platforms. *J. Mater. Chem. C* **2016**, *4*, 4836-4846.
16. Meinardi, F.; Ehrenberg, S.; Dharmo, L.; Carulli, F.; Mauri, M.; Bruni, F.; Simonutti, R.; Kortshagen, U.; Brovelli, S., Highly Efficient Luminescent Solar Concentrators based on Earth-Abundant Indirect-Bandgap Silicon Quantum Dots. *Nature Photonics* **2017**, *11*, 177.
17. Chan, C. K.; Peng, H. L.; Liu, G.; McIlwrath, K.; Zhang, X. F.; Huggins, R. A.; Cui, Y., High-Performance Lithium Battery Anodes using Silicon Nanowires. *Nature Nanotechnol* **2008**, *3*, 31-35.
18. Kim, H.; Seo, M.; Park, M. H.; Cho, J., A Critical Size of Silicon Nano-Anodes for Lithium Rechargeable Batteries. *Angew. Chem., Int. Ed.* **2010**, *49*, 2146-9.
19. Su, X.; Wu, Q.; Li, J.; Xiao, X.; Lott, A.; Lu, W.; Sheldon Brian, W.; Wu, J., Silicon-Based Nanomaterials for Lithium-Ion Batteries: A Review. *Adv. Energy Mater.* **2014**, *4*, 1300882.
20. Dohnalova, K.; Gregorkiewicz, T.; Kusova, K., Silicon Quantum Dots: Surface Matters. *J Phys Condens Matter* **2014**, *26*, 173201.
21. Chan, C. K.; Ruffo, R.; Hong, S. S.; Cui, Y., Surface Chemistry and Morphology of the Solid Electrolyte Interphase on Silicon Nanowire Lithium-ion Battery Anodes. *J Power Sources* **2009**, *189*, 1132-1140.

22. Dasog, M.; Yang, Z. Y.; Regli, S.; Atkins, T. M.; Faramus, A.; Singh, M. P.; Muthuswamy, E.; Kauzlarich, S. M.; Tilley, R. D.; Veinot, J. G. C., Chemical Insight into the Origin of Red and Blue Photoluminescence Arising from Freestanding Silicon Nanocrystals. *ACS Nano* **2013**, *7*, 2676-2685.
23. Dasog, M.; De los Reyes, G. B.; Titova, L. V.; Hegmann, F. A.; Veinot, J. G., Size vs Surface: Tuning the Photoluminescence of Freestanding Silicon Nanocrystals across the Visible Spectrum via Surface Groups. *ACS Nano* **2014**, *8*, 9636-48.
24. Dasog, M.; Bader, K.; Veinot, J. G. C., Influence of Halides on the Optical Properties of Silicon Quantum Dots. *Chem. Mater.* **2015**, *27*, 1153-1156.
25. Wheeler, L. M.; Anderson, N. C.; Palomaki, P. K. B.; Blackburn, J. L.; Johnson, J. C.; Neale, N. R., Silyl Radical Abstraction in the Functionalization of Plasma-Synthesized Silicon Nanocrystals. *Chem. Mater.* **2015**, *27*, 6869-6878.
26. Lee, B. G.; Hiller, D.; Luo, J. W.; Semonin, O. E.; Beard, M. C.; Zacharias, M.; Stradins, P., Strained Interface Defects in Silicon Nanocrystals. *Adv. Funct. Mater.* **2012**, *22*, 3223-3232.
27. Kleovoulou, K.; Kelires, P. C., Stress State of Embedded Si Nanocrystals. *Phys. Rev. B* **2013**, *88*, 085424.
28. Zhou, Z. Y.; Brus, L.; Friesner, R., Electronic Structure and Luminescence of 1.1- and 1.4-nm Silicon Nanocrystals: Oxide Shell Versus Hydrogen Passivation. *Nano Lett.* **2003**, *3*, 163-167.
29. Shu, Y. N.; Kortshagen, U. R.; Levine, B. G.; Anthony, R. J., Surface Structure and Silicon Nanocrystal Photoluminescence: The Role of Hypervalent Silyl Groups. *J. Phys. Chem. C* **2015**, *119*, 26683-26691.
30. Veprek, S.; Sarott, F.; Iqbal, Z., Effect of Grain Boundaries on the Raman Spectra, Optical Absorption, and Elastic Light Scattering in Nanometer-sized Crystalline Silicon. *Phys. Rev. B Condens. Matter* **1987**, *36*, 3344-3350.
31. Nikitin, T.; Khriachtchev, L., Optical and Structural Properties of Si Nanocrystals in SiO₂ Films. *Nanomaterials* **2015**, *5*, 614-655.
32. Yogi, P.; Tanwar, M.; Saxena, S. K.; Mishra, S.; Pathak, D. K.; Chaudhary, A.; Sagdeo, P. R.; Kumar, R., Quantifying the Short-Range Order in Amorphous Silicon by Raman Scattering. *Anal. Chem.* **2018**, *90*, 8123-8129.
33. Marra, D. C.; Edelberg, E. A.; Naone, R. L.; Aydil, E. S., Silicon Hydride Composition of Plasma-Deposited Hydrogenated Amorphous and Nanocrystalline Silicon Films and Surfaces. *J. Vac. Sci. Technol. A* **1998**, *16*, 3199-3210.
34. Mangolini, L.; Kortshagen, U., Plasma-Assisted Synthesis of Silicon Nanocrystal Inks. *Adv. Mater.* **2007**, *19*, 2513-2519.
35. Jariwala, B. N.; Kramer, N. J.; Petcu, M. C.; Bobela, D. C.; Sanden, M. C. M. v. d.; Stradins, P.; Ciobanu, C. V.; Agarwal, S., Surface Hydride Composition of Plasma-Synthesized Si Nanoparticles. *J. Phys. Chem. C* **2011**, *115*, 20375-20379.
36. Zipoli, F.; Bernasconi, M., Ab initio Simulation of the Grafting of Phenylacetylene on Hydrogenated Surfaces of Crystalline Silicon Catalyzed by a Lewis Acid. *J. Phys. Chem. B* **2006**, *110*, 23403-23409.
37. Hua, F.; Swihart, M. T.; Ruckenstein, E., Efficient Surface Grafting of Luminescent Silicon Quantum Dots by Photoinitiated Hydrosilylation. *Langmuir* **2005**, *21*, 6054-6062.
38. Hua, F.; Erogbogbo, F.; Swihart, M. T.; Ruckenstein, E., Organically Capped Silicon Nanoparticles with Blue Photoluminescence Prepared by Hydrosilylation Followed by Oxidation. *Langmuir* **2006**, *22*, 4363-4370.
39. Giuliani, J. R.; Harley, S. J.; Carter, R. S.; Power, P. P.; Augustine, M. P., Using Liquid and Solid-State NMR and Photoluminescence to Study the Synthesis and Solubility Properties of Amine Capped Silicon Nanoparticles. *Solid State Nucl. Magnet. Reson.* **2007**, *32*, 1-10.
40. Shiohara, A.; Prabakar, S.; Faramus, A.; Hsu, C. Y.; Lai, P. S.; Northcote, P. T.; Tilley, R. D., Sized Controlled Synthesis, Purification, and Cell Studies with Silicon Quantum Dots. *Nanoscale* **2011**, *3*, 3364-3370.
41. Zou, J.; Kauzlarich, S. M., Functionalization of Silicon Nanoparticles via Silanization: Alkyl, Halide and Ester. *J. Cluster Sci.* **2008**, *19*, 341-355.
42. Ahire, J. H.; Wang, Q.; Coxon, P. R.; Malhotra, G.; Brydson, R.; Chen, R.; Chao, Y., Highly Luminescent and Nontoxic Amine-Capped Nanoparticles from Porous Silicon: Synthesis and their use in Biomedical Imaging. *ACS Applied Mater. & Inter.* **2012**, *4*, 3285-3292.
43. Biesta, W.; van Lagen, B.; Gevaert, V. S.; Marcelis, A. T. M.; Paulusse, J. M. J.; Nielen, M. W. F.; Zuilhof, H., Preparation, Characterization, and Surface Modification of Trifluoroethyl Ester-Terminated Silicon Nanoparticles. *Chem. Mater.* **2012**, *24*, 4311-4318.
44. Mayeri, D.; Phillips, B. L.; Augustine, M. P.; Kauzlarich, S. M., NMR Study of the Synthesis of Alkyl-Terminated Silicon Nanoparticles from the Reaction of SiCl₄ with the Zintl Salt, NaSi. *Chem. Mater.* **2001**, *13*, 765-770.

45. Baldwin, R. K.; Pettigrew, K. A.; Ratai, E.; Augustine, M. P.; Kauzlarich, S. M., Solution Reduction Synthesis of Surface Stabilized Silicon Nanoparticles. *Chem. Commun.* **2002**, *17*, 1822-1823.
46. Carter, R. S.; Harley, S. J.; Power, P. P.; Augustine, M. P., Use of NMR Spectroscopy in the Synthesis and Characterization of Air- and Water-Stable Silicon Nanoparticles from Porous Silicon. *Chem. Mater.* **2005**, *17*, 2932-2939.
47. Yesinowski, J. P., Solid-State NMR of Inorganic Semiconductors. In *Solid State NMR*, Chan, J. C. C., Ed. Springer Berlin Heidelberg: Berlin, Heidelberg, 2012; pp 229-312.
48. Atkins, T. M.; Cassidy, M. C.; Lee, M.; Ganguly, S.; Marcus, C. M.; Kauzlarich, S. M., Synthesis of Long T₁ Silicon Nanoparticles for Hyperpolarized ²⁹Si Magnetic Resonance Imaging. *ACS Nano* **2013**, *7*, (2), 1609-1617.
49. Neiner, D.; Kauzlarich, S. M., Hydrogen-Capped Silicon Nanoparticles as a Potential Hydrogen Storage Material: Synthesis, Characterization, and Hydrogen Release. *Chem. Mater.* **2010**, *22*, (2), 487-493.
50. El-Demellawi, J. K.; Holt, C. R.; Abou-Hamad, E.; Al-Talla, Z. A.; Saih, Y.; Chaieb, S., Room-Temperature Reactivity Of Silicon Nanocrystals With Solvents: The Case of Ketone and Hydrogen Production From Secondary Alcohols: Catalysis? *ACS Applied Mater. Inter.* **2015**, *7*, 13794-13800.
51. Kravitz, K.; Kamyshny, A.; Gedanken, A.; Magdassi, S., Solid State Synthesis of Water-Dispersible Silicon Nanoparticles from Silica Nanoparticles. *J. Solid State Chem.* **2010**, *183*, 1442-1447.
52. Kolyagin, Y. G.; Zakharov, V. N.; Yatsenko, A. V.; Aslanov, L. A., Studies of Silicon Nanocluster Ligand Coating by Solid-State NMR. *Russian Chem. Bulle.* **2015**, *64*, 1829-1832.
53. Aptekar, J. W.; Cassidy, M. C.; Johnson, A. C.; Barton, R. A.; Lee, M.; Ogier, A. C.; Vo, C.; Anahtar, M. N.; Ren, Y.; Bhatia, S. N.; Ramanathan, C.; Cory, D. G.; Hill, A. L.; Mair, R. W.; Rosen, M. S.; Walsworth, R. L.; Marcus, C. M., Silicon Nanoparticles as Hyperpolarized Magnetic Resonance Imaging Agents. *ACS Nano* **2009**, *3*, 4003-4008.
54. Faulkner, A. R.; DiVerdi, A. J.; Yang, Y.; Kobayashi, T.; Maciel, E. G., The Surface of Nanoparticle Silicon as Studied by Solid-State NMR. *Materials* **2013**, *6*, 18-46.
55. Lee, D.; Kaushik, M.; Coustel, R.; Chenavier, Y.; Chanal, M.; Bardet, M.; Dubois, L.; Okuno, H.; Rochat, N.; Duclairoir, F.; Mouesca, J. M.; De Paëpe, G., Solid-State NMR and DFT Combined for the Surface Study of Functionalized Silicon Nanoparticles. *Chemistry – A European Journal* **2015**, *21*, 16047-16058.
56. Hanrahan, M. P.; Fought, E. L.; Windus, T. L.; Wheeler, L. M.; Anderson, N. C.; Neale, N. R.; Rossini, A. J., Characterization of Silicon Nanocrystal Surfaces by Multidimensional Solid-State NMR Spectroscopy. *Chem. Mater.* **2017**, *29*, 10339-10351.
57. Coleman, N. R. B.; Morris, M. A.; Spalding, T. R.; Holmes, J. D., The Formation of Dimensionally Ordered Silicon Nanowires within Mesoporous Silica. *J. Amer. Chem. Soc.* **2001**, *123*, 187-188.
58. Davidowski, S. K.; Holland, G. P., Solid-State NMR Characterization of Mixed Phosphonic Acid Ligand Binding and Organization on Silica Nanoparticles. *Langmuir* **2016**, *32*, 3253-3261.
59. Lafon, O.; Thankamony, A. S. L.; Kobayashi, T.; Carnevale, D.; Vitzthum, V.; Slowing, I. I.; Kandel, K.; Vezin, H.; Amoureux, J.-P.; Bodenhausen, G.; Pruski, M., Mesoporous Silica Nanoparticles Loaded with Surfactant: Low Temperature Magic Angle Spinning ¹³C and ²⁹Si NMR Enhanced by Dynamic Nuclear Polarization. *J. Phys. Chem. C* **2013**, *117*, 1375-1382.
60. Sugiyama, Y.; Okamoto, H.; Mitsuoka, T.; Morikawa, T.; Nakanishi, K.; Ohta, T.; Nakano, H., Synthesis and Optical Properties of Monolayer Organosilicon Nanosheets. *J. Amer. Chem. Soc.* **2010**, *132*, 5946-5947.
61. Helbich, T.; Lyuleeva, A.; Höhle, I. M. D.; Marx, P.; Scherf, L. M.; Kehrle, J.; Fässler, T. F.; Lugli, P.; Rieger, B., Radical-Induced Hydrosilylation Reactions for the Functionalization of Two-Dimensional Hydride Terminated Silicon Nanosheets. *Chem. – A Euro. J.* **2016**, *22*, 6194-6198.
62. Mackenzie, K.; Smith, M., Chapter 4 - ²⁹Si NMR. In *Pergamon Materials Series*, MacKenzie, K. J. D.; Smith, M. E., Eds. Pergamon: 2002; Vol. 6, pp 201-268.
63. Takeuchi, Y.; Takayama, T., ²⁹Si NMR Spectroscopy of Organosilicon Compounds. In *The Chemistry of Organic Silicon Compounds*, 2003; pp 267-354.
64. Wrackmeyer, B., Applications of ²⁹Si NMR Parameters. In *Annual Reports on NMR Spectroscopy*, Webb, G. A., Ed. Academic Press: 2006; Vol. 57, pp 1-49.
65. Harris, R. K.; Kimber, B. J., ²⁹Si NMR as a Tool for Studying Silicones. *Applied Spectroscopy Reviews* **2007**, *10*, 117-137.
66. Collins, W. T. F., C. L. Condensed Soluble Hydrogensilsesquioxane Resin. US3615272A, 1971.

67. Hessel, C. M.; Henderson, E. J.; Veinot, J. G. C., Hydrogen Silsesquioxane: A Molecular Precursor for Nanocrystalline Si–SiO₂ Composites and Freestanding Hydride-Surface-Terminated Silicon Nanoparticles. *Chem. Mater.* **2006**, *18*, (26), 6139-6146.
68. Barr, T. L.; Seal, S., Nature of the use of Adventitious Carbon as a Binding Energy Standard. *J. Vac. Sci. Tech. A* **1995**, *13*, 1239-1246.
69. Payne, B. P.; Biesinger, M. C.; McIntyre, N. S., The Study of Polycrystalline Nickel Metal Oxidation by Water Vapour. *J. Elec. Spectros. Rel. Phen.* **2009**, *175*, 55-65.
70. Sublemontier, O.; Nicolas, C.; Aureau, D.; Patanen, M.; Kintz, H.; Liu, X.; Gaveau, M.-A.; Le Garrec, J.-L.; Robert, E.; Barreda, F.-A.; Etcheberry, A.; Reynaud, C.; Mitchell, J. B.; Miron, C., X-Ray Photoelectron Spectroscopy of Isolated Nanoparticles. *J. Phys. Chem. Lett.* **2014**, *5*, 3399-3403.
71. Plymale, N. T.; Dasog, M.; Brunshwig, B. S.; Lewis, N. S., A Mechanistic Study of the Oxidative Reaction of Hydrogen-Terminated Si(111) Surfaces with Liquid Methanol. *J. Phys. Chem. C* **2017**, *121*, 4270-4282.
72. Yang, Z. Y.; Iqbal, M.; Dobbie, A. R.; Veinot, J. G. C., Surface-Induced Alkene Oligomerization: Does Thermal Hydrosilylation Really Lead to Monolayer Protected Silicon Nanocrystals? *J. Amer. Chem. Soc.* **2013**, *135*, 17595-17601.
73. Bruker AXS (2008): TOPAS V4: General Profile and Structure Analysis Software for Powder Diffraction Data. - User's Manual, Bruker AXS, Karlsruhe, Germany.
74. Bennett, A. E.; Rienstra, C. M.; Auger, M.; Lakshmi, K. V.; Griffin, R. G., Heteronuclear Decoupling in Rotating Solids. *J. Chem. Phys.* **1995**, *103*, 6951-6958.
75. Hayashi, S.; Hayamizu, K., Chemical Shift Standards in High-Resolution Solid-State NMR ¹³C, ²⁹Si, and ¹H Nuclei. *Bull. Chem. Soc. Japan* **1991**, *64*, 685-687.
76. Bloch, F., Nuclear Induction. *Phys. Rev.* **1946**, *70*, 460-474.
77. Pines, A.; Gibby, M. G.; Waugh, J. S., Proton-Enhanced Nuclear Induction Spectroscopy. A Method for High Resolution NMR of Dilute Spins in Solids. *J. Chem. Phys.* **1972**, *56*, 1776-1777.
78. Freeman, R.; Hill, H. D. W., Fourier Transform Study of NMR Spin–Lattice Relaxation by “Progressive Saturation”. *J. Chem. Phys.* **1971**, *54*, 3367-3377.
79. Hessel, C. M.; Reid, D.; Panthani, M. G.; Rasch, M. R.; Goodfellow, B. W.; Wei, J.; Fujii, H.; Akhavan, V.; Korgel, B. A., Synthesis of Ligand-Stabilized Silicon Nanocrystals with Size-Dependent Photoluminescence Spanning Visible to Near-Infrared Wavelengths. *Chem. Mater.* **2012**, *24*, 393-401.
80. Yu, Y.; Hessel, C. M.; Bogart, T. D.; Panthani, M. G.; Rasch, M. R.; Korgel, B. A., Room Temperature Hydrosilylation of Silicon Nanocrystals with Bifunctional Terminal Alkenes. *Langmuir* **2013**, *29*, 1533-1540.
81. Buriak, J. M., Illuminating Silicon Surface Hydrosilylation: An Unexpected Plurality of Mechanisms. *Chem. Mater.* **2014**, *26*, 763-772.
82. Weeks, S. L.; Macco, B.; van de Sanden, M. C.; Agarwal, S., Gas-phase Hydrosilylation of Plasma-synthesized Silicon Nanocrystals with Short- and Long-chain Alkynes. *Langmuir* **2012**, *28*, 17295-301.
83. Nelles, J.; Sendor, D.; Ebbers, A.; Petrat, F. M.; Wiggers, H.; Schulz, C.; Simon, U., Functionalization of Silicon Nanoparticles via Hydrosilylation with 1-Alkenes. *Colloid. Poly. Sci.* **2007**, *285*, 729-736.
84. Hohlein, I. M.; Kehrle, J.; Helbich, T.; Yang, Z.; Veinot, J. G.; Rieger, B., Diazonium Salts as Grafting Agents and Efficient Radical-Hydrosilylation Initiators for Freestanding Photoluminescent Silicon Nanocrystals. *Chem. Eur. J.* **2014**, *20*, 4212-6.
85. Purkait, T. K.; Iqbal, M.; Wahl, M. H.; Gottschling, K.; Gonzalez, C. M.; Islam, M. A.; Veinot, J. G., Borane-Catalyzed Room-Temperature Hydrosilylation of Alkenes/Alkynes on Silicon Nanocrystal Surfaces. *J. Am. Chem. Soc.* **2014**, *136*, 17914-7.
86. Balzar, D.; Audebrand, N.; Daymond, M. R.; Fitch, A.; Hewat, A.; Langford, J. I.; Le Bail, A.; Louer, D.; Masson, O.; McCowan, C. N.; Popa, N. C.; Stephens, P. W.; Toby, B. H., Size-Strain Line-Broadening Analysis of the Ceria Round-Robin Sample. *J. Appl. Cryst.* **2004**, *37*, 911-924.
87. Hartman, J. S.; Richardson, M. F.; Sherriff, B. L.; Winsborrow, B. G., Magic Angle Spinning NMR Studies of Silicon Carbide: Polytypes, Impurities, and Highly Inefficient Spin-Lattice Relaxation. *J. Amer. Chem. Soc.* **1987**, *109*, 6059-6067.
88. Holzman, G. R.; Lauterbur, P. C.; Anderson, J. H.; Koth, W., Nuclear Magnetic Resonance Field Shifts of Si-29 in Various Materials. *J. Chem. Phys.* **1956**, *25*, 172-173.
89. Reimer, J. A.; Dubois Murphy, P.; Gerstein, B. C.; Knights, J. C., Silicon-29 Cross-Polarization Magic-Angle Sample Spinning Spectra in Amorphous Silicon-Hydrogen Films. *J. Chem. Phys.* **1981**, *74*, 1501.

90. Shao, W.-L.; Shinar, J.; Gerstein, B. C.; Li, F.; Lannin, J. S., Magic-Angle Spinning ^{29}Si NMR Study of Short-Range Order in a-Si. *Phys Rev B* **1990**, *41*, 9491-9494.
91. Bercier, J. J.; Jirousek, M.; Graetzel, M.; Klink, J. J. v. d., Evidence from NMR for Temperature-Dependent Bardeen-Friedel Oscillations in Nanometre-Sized Silver Particles. *J. Phys.: Condens. Matter* **1993**, *5*, L571.
92. Charles, R. J.; Harrison, W. A., Size Effect in Nuclear Magnetic Resonance. *Phys. Rev. Lett.* **1963**, *11*, 75-77.
93. Terskikh, V. V.; Moudrakovski, I. L.; Ratcliffe, C. I.; Ripmeester, J. A.; Reinhold, C. J.; Anderson, P. A.; Edwards, P. P., Size Effects on the Nuclear Magnetic Resonance of Sodium Metal Confined in Controlled Pore Glasses. In *Magnetic Resonance in Colloid and Interface Science*, Fraissard, J.; Lapina, O., Eds. Springer Netherlands: Dordrecht, 2002; pp 469-475.
94. Javadi, M.; Michaelis, V. K.; Veinot, J. G. C., Thermally-Induced Evolution of 'Ge(OH)₂': Controlling the Formation of Oxide-Embedded Ge Nanocrystals. *J. Phys. Chem. C* **2018**, *122*, 17518-17525.
95. Cadars, S.; Smith, B. J.; Epping, J. D.; Acharya, S.; Belman, N.; Golan, Y.; Chmelka, B. F., Atomic Positional Versus Electronic Order in Semiconducting ZnSe Nanoparticles. *Phys. Rev. Lett.* **2009**, *103*, 136802.
96. Mobarok, M. H.; Lubber, E. J.; Bernard, G. M.; Peng, L.; Wasylshen, R. E.; Buriak, J. M., Phase-Pure Crystalline Zinc Phosphide Nanoparticles: Synthetic Approaches and Characterization. *Chem. Mater.* **2014**, *26*, 1925-1935.
97. Ratcliffe, C. I.; Yu, K.; Ripmeester, J. A.; Badruz Zaman, M.; Badarau, C.; Singh, S., Solid State NMR Studies of Photoluminescent Cadmium Chalcogenide Nanoparticles. *Phys. Chem. Chem. Phys.* **2006**, *8*, 3510-3519.
98. Tomaselli, M.; Yarger, J. L.; Bruchez, M.; Havlin, R. H.; deGraw, D.; Pines, A.; Alivisatos, A. P., NMR Study of InP Quantum Dots: Surface Structure and Size Effects. *J. Chem. Phys.* **1999**, *110*, 8861-8864.
99. Marbella, L. E.; Millstone, J. E., NMR Techniques for Noble Metal Nanoparticles. *Chem. Mater.* **2015**, *27*, 2721-2739.
100. Maciel, G. E.; Sindorf, D. W., Silicon-29 NMR Study of the Surface of Silica Gel by Cross Polarization and Magic-Angle Spinning. *J. Amer. Chem. Soc.* **1980**, *102*, 7606-7607.
101. Hayashi, S.; Hayamizu, K.; Yamasaki, S.; Matsuda, A.; Tanaka, K., Interpretation of ^{29}Si Nuclear Magnetic Resonance Spectra of Amorphous Hydrogenated Silicon. *J. Appl. Phys.* **1986**, *60*, 1839-1841.
102. Hayashi, S.; Hayamizu, K.; Yamasaki, S.; Matsuda, A.; Tanaka, K., ^{29}Si Nuclear Magnetic Resonance of Amorphous Hydrogenated Silicon and Amorphous Microcrystalline Mixed-Phase Hydrogenated Silicon. *Phys. Rev. B* **1987**, *35*, 4581-4590.
103. Pietraß, T.; Bifone, A.; Roth, R. D.; Koch, V. P.; Alivisatos, A. P.; Pines, A., ^{29}Si High Resolution Solid State Nuclear Magnetic Resonance Spectroscopy of Porous Silicon. *J. Non-Cryst. Solids* **1996**, *202*, 68-76.
104. Shigenobu, H.; Kikuko, H.; Satoshi, Y.; Akihisa, M.; Kazunobu, T., Silicon-29 Nuclear Magnetic Resonance Study of Amorphous-Microcrystalline Mixed-Phase Hydrogenated Silicon. *Japanese J. Applied Phys.* **1986**, *25*, L313.
105. Smith, J. V.; Blackwell, C. S., Nuclear Magnetic Resonance of Silica Polymorphs. *Nature* **1983**, *303*, 223-225.
106. Wang, M.; Wu, X.-P.; Zheng, S.; Zhao, L.; Li, L.; Shen, L.; Gao, Y.; Xue, N.; Guo, X.; Huang, W.; Gan, Z.; Blanc, F.; Yu, Z.; Ke, X.; Ding, W.; Gong, X.-Q.; Grey, C. P.; Peng, L., Identification of Different Oxygen Species in Oxide Nanostructures with ^{17}O Solid-State NMR Spectroscopy. *Sci. Advances* **2015**, *1*, e1400133.
107. Jameson, C. J.; Gutowsky, H. S., Calculation of Chemical Shifts. I. General Formulation and the Z Dependence. *J. Chem. Phys.* **1964**, *40*, 1714-1724.
108. Ramsey, N. F., Magnetic Shielding of Nuclei in Molecules. *Phys. Rev.* **1950**, *78*, 699-703.
109. Thayer, A. M.; Steigerwald, M. L.; Duncan, T. M.; Douglass, D. C., NMR Study of Semiconductor Molecular Clusters. *Phys. Rev. Lett.* **1988**, *60*, 2673-2676.
110. Bawendi, M. G.; Carroll, P. J.; Wilson, W. L.; Brus, L. E., Luminescence Properties of CdSe Quantum Crystallites: Resonance Between Interior and Surface Localized States. *J. Chem. Phys.* **1992**, *96*, 946-954.
111. Colvin, V. L.; Alivisatos, A. P.; Tobin, J. G., Valence-Band Photoemission from a Quantum-Dot System. *Phys. Rev. Lett.* **1991**, *66*, 2786-2789.
112. Comedi, D.; Zalloum, O. H. Y.; Irving, E. A.; Wojcik, J.; Roschuk, T.; Flynn, M. J.; Mascher, P., X-Ray Diffraction Study of Crystalline Si Nanocluster Formation in Annealed Silicon-Rich Silicon Oxides. *J. Appl. Phys.* **2006**, *99*, 023518.
113. Zhao, Y.; Kim, Y.-H.; Du, M.-H.; Zhang, S. B., First-Principles Prediction of Icosahedral Quantum Dots for Tetravalent Semiconductors. *Phys. Rev. Lett.* **2004**, *93*, 015502.

114. Avramov, P. V. F., D. G.; Sorokin, P. B.; Chernozatonskii, L. A.; Gordon, M. S., New Symmetric Families of Silicon Quantum Dots and Their Conglomerates as a Tunable Source of Photoluminescence in Nanodevices. *Los Alamos Natl. Lab, Prepr. Arch., Condens. Matter* **2007**, 1-19.
115. Okada, Y.; Tokumaru, Y., Precise Determination of Lattice Parameter and Thermal Expansion Coefficient of Silicon Between 300 and 1500 K. *J Appl Phys* **1984**, 56, 314-320.

Chapter 3

1. Samsung Newsroom. [NEXT for QLED] Part 1: Samsung Dominates the Large Screen TV Market. <https://news.samsung.com/global/next-for-qled-part-1-samsung-dominates-the-large-screen-tv-market> (01/02),
2. Halford, B., Quantum dot LEDs go cadmium-free. In American Chemical Society: Chemical and Engineering News, 2019; Vol. 97.
3. Union, T. E., Ed. *Publications Office of the European Union: Official Journal of the European Union*, 2017; Vol. 2017/1975, p 3.
4. Program, N. T. *NTP Technical Report on the Toxicology and Carcinogenesis Studies of Indium Phosphide in F344/N Rats and B6C3F1 Mice (Inhalation Studies)*; U.S. Department of Health and Human Services: July 2001, 2001.
5. Nanoco <https://www.nanocotechnologies.com/> (01/02),
6. Veinot, J. G. C., Synthesis, surface functionalization, and properties of freestanding silicon nanocrystals. *Chem. Commun.* **2006**, 40, 4160-4168.
7. Mangolini, L.; Kortshagen, U., Plasma-assisted synthesis of silicon nanocrystal inks. *Adv. Mater.* **2007**, 19 (18), 2513-2519.
8. Tilley, R. D.; Warner, J. H.; Yamamoto, K.; Matsui, I.; Fujimori, H., Micro-emulsion synthesis of monodisperse surface stabilized silicon nanocrystals. *Chem. Commun.* **2005**, 14, 1833-1835.
9. Baldwin, R. K.; Pettigrew, K. A.; Ratai, E.; Augustine, M. P.; Kauzlarich, S. M., Solution reduction synthesis of surface stabilized silicon nanoparticles. *Chem. Commun.* **2002**, 17, 1822-1823.
10. Zou, J.; Kauzlarich, S. M., Functionalization of Silicon Nanoparticles via Silanization: Alkyl, Halide and Ester. *J. Clust. Sci.* **2008**, 19 (2), 341-355.
11. Yang, Z.; Gonzalez, C. M.; Purkait, T. K.; Iqbal, M.; Meldrum, A.; Veinot, J. G., Radical Initiated Hydrosilylation on Silicon Nanocrystal Surfaces: An Evaluation of Functional Group Tolerance and Mechanistic Study. *Langmuir* **2015**, 31 (38), 10540-10548.
12. Liu, X.; Zhao, S.; Gu, W.; Zhang, Y.; Qiao, X.; Ni, Z.; Pi, X.; Yang, D., Light-Emitting Diodes Based on Colloidal Silicon Quantum Dots with Octyl and Phenylpropyl Ligands. *ACS Appl. Mater. Interfaces* **2018**, 10 (6), 5959-5966.
13. Meinardi, F.; Ehrenberg, S.; Dharmo, L.; Carulli, F.; Mauri, M.; Bruni, F.; Simonutti, R.; Kortshagen, U.; Brovelli, S., Highly efficient luminescent solar concentrators based on earth-abundant indirect-bandgap silicon quantum dots. *Nature Photon.* **2017**, 11, 177-185.
14. Mazzaro, R.; Gradone, A.; Angeloni, S.; Morselli, G.; Cozzi, P. G.; Romano, F.; Vomiero, A.; Ceroni, P., Hybrid Silicon Nanocrystals for Color-Neutral and Transparent Luminescent Solar Concentrators. *ACS Photonics* **2019**, 6 (9), 2303-2311.
15. Erogbogbo, F.; Yong, K.-T.; Roy, I.; Hu, R.; Law, W.-C.; Zhao, W.; Ding, H.; Wu, F.; Kumar, R.; Swihart, M. T.; Prasad, P. N., In Vivo Targeted Cancer Imaging, Sentinel Lymph Node Mapping and Multi-Channel Imaging with Biocompatible Silicon Nanocrystals. *ACS Nano* **2011**, 5 (1), 413-423.
16. Tu, C.; Ma, X.; House, A.; Kauzlarich, S. M.; Louie, A. Y., PET Imaging and Biodistribution of Silicon Quantum Dots in Mice. *ACS Med. Chem. Lett.* **2011**, 2 (4), 285-288.
17. Gonzalez, C. M.; Iqbal, M.; Dasog, M.; Piercey, D. G.; Lockwood, R.; Klapotke, T. M.; Veinot, J. G. C., Detection of high-energy compounds using photoluminescent silicon nanocrystal paper based sensors. *Nanoscale* **2014**, 6 (5), 2608-2612.
18. Gonzalez, C.M.; Veinot, J. G. C., Silicon nanocrystals for the development of sensing platforms. *J. Mater. Chem. C* **2016**, 4 (22), 4836-4846.
19. Kim, H.; Seo, M.; Park, M. H.; Cho, J., A critical size of silicon nano-anodes for lithium rechargeable batteries. *Angew. Chem. Int. Ed.* **2010**, 49 (12), 2146-2149.
20. Su, X.; Wu, Q.; Li, J.; Xiao, X.; Lott, A.; Lu, W.; Sheldon Brian, W.; Wu, J., Silicon-Based Nanomaterials for Lithium-Ion Batteries: A Review. *Adv. Energy Mater.* **2014**, 4 (1), 1300882.

21. Dasog, M.; De los Reyes, G. B.; Titova, L. V.; Hegmann, F. A.; Veinot, J. G. C., Size vs surface: tuning the photoluminescence of freestanding silicon nanocrystals across the visible spectrum via surface groups. *ACS Nano* **2014**, *8* (9), 9636-48.
22. Mobarok, M. H.; Purkait, T. K.; Islam, M. A.; Miskolzie, M.; Veinot, J. G. C., Instantaneous Functionalization of Chemically Etched Silicon Nanocrystal Surfaces. *Angew. Chem. Int. Ed.* **2017**, *56* (22), 6073-6077.
23. Islam, M. A.; Mobarok, M. H.; Sinelnikov, R.; Purkait, T. K.; Veinot, J. G. C., Phosphorus Pentachloride Initiated Functionalization of Silicon Nanocrystals. *Langmuir* **2017**, *33* (35), 8766-8773.
24. Sangghaleh, F.; Sychugov, I.; Yang, Z.; Veinot, J. G. C.; Linnros, J., Near-Unity Internal Quantum Efficiency of Luminescent Silicon Nanocrystals with Ligand Passivation. *ACS Nano* **2015**, *9* (7), 7097-7104.
25. Jurbergs, D.; Rogojina, E.; Mangolini, L.; Kortshagen, U., Silicon nanocrystals with ensemble quantum yields exceeding 60%. *Appl. Phys. Lett.* **2006**, *88* (23), 233116.
26. Wheeler, L. M.; Anderson, N. C.; Palomaki, P. K. B.; Blackburn, J. L.; Johnson, J. C.; Neale, N. R., Silyl Radical Abstraction in the Functionalization of Plasma-Synthesized Silicon Nanocrystals. *Chem. Mater.* **2015**, *27* (19), 6869-6878.
27. Ddungu, J. L. Z.; Silvestrini, S.; Tassoni, A.; De Cola, L., Shedding Light on the Aqueous Synthesis of Silicon Nanoparticles by Reduction of Silanes with Citrates. *Faraday Discussions* **2020**. Accepted Manuscript DOI:10.1039/C9FD00127A
28. Dasog, M.; Yang, Z. Y.; Regli, S.; Atkins, T. M.; Faramus, A.; Singh, M. P.; Muthuswamy, E.; Kauzlarich, S. M.; Tilley, R. D.; Veinot, J. G. C., Chemical Insight into the Origin of Red and Blue Photoluminescence Arising from Freestanding Silicon Nanocrystals. *ACS Nano* **2013**, *7* (3), 2676-2685.
29. Sinelnikov, R.; Dasog, M.; Beamish, J.; Meldrum, A.; Veinot, J. G. C., Revisiting an Ongoing Debate: What Role Do Surface Groups Play in Silicon Nanocrystal Photoluminescence? *ACS Photonics* **2017**, *4* (8), 1920-1929.
30. Rodríguez, J. A.; Vásquez-Agustín, M. A.; Morales-Sánchez, A.; Aceves-Mijares, M., Emission Mechanisms of Si Nanocrystals and Defects in SiO₂ Materials. *J. Nanomater.* **2014**, *2014*, 409482.
31. Canham, L. T., Luminescence Bands and their Proposed Origins In Highly Porous Silicon. *phys. stat. sol. (b)* **1995**, *190*, 9-14.
32. Lee, B. G.; Luo, J.-W.; Neale, N. R.; Beard, M. C.; Hiller, D.; Zacharias, M.; Stradins, P.; Zunger, A., Quasi-Direct Optical Transitions in Silicon Nanocrystals with Intensity Exceeding the Bulk. *Nano Lett.* **2016**, *16* (3), 1583-1589.
33. Mazzaro, R.; Romano, F.; Ceroni, P., Long-lived Luminescence of Silicon Nanocrystals: From Principles to Applications. *Phys. Chem. Chem. Phys.* **2017**, *19* (39), 26507-26526.
34. DeBenedetti, W. J. I.; Chiu, S.-K.; Radlinger, C. M.; Ellison, R. J.; Manhat, B. A.; Zhang, J. Z.; Shi, J.; Goforth, A. M., Conversion from Red to Blue Photoluminescence in Alcohol Dispersions of Alkyl-Capped Silicon Nanoparticles: Insight into the Origins of Visible Photoluminescence in Colloidal Nanocrystalline Silicon. *J. Phys. Chem. C* **2015**, *119* (17), 9595-9608.
35. Dasog, M.; Bader, K.; Veinot, J. G. C., Influence of Halides on the Optical Properties of Silicon Quantum Dots. *Chem. Mater.* **2015**, *27* (4), 1153-1156.
36. Li, X.; He, Y.; Talukdar, S. S.; Swihart, M. T., Process for Preparing Macroscopic Quantities of Brightly Photoluminescent Silicon Nanoparticles with Emission Spanning the Visible Spectrum. *Langmuir* **2003**, *19* (20), 8490-8496.
37. Hessel, C. M.; Reid, D.; Panthani, M. G.; Rasch, M. R.; Goodfellow, B. W.; Wei, J.; Fujii, H.; Akhavan, V.; Korgel, B. A., Synthesis of Ligand-Stabilized Silicon Nanocrystals with Size-Dependent Photoluminescence Spanning Visible to Near-Infrared Wavelengths. *Chem. Mater.* **2012**, *24* (2), 393-401.
38. Niquet, Y. M.; Delerue, C.; Allan, G.; Lannoo, M., Method for Tight-binding Parametrization: Application to Silicon Nanostructures. *Phys. Rev. B* **2000**, *62* (8), 5109-5116.
39. Yu, Y.; Fan, G.; Fermi, A.; Mazzaro, R.; Morandi, V.; Ceroni, P.; Smilgies, D.-M.; Korgel, B. A., Size-Dependent Photoluminescence Efficiency of Silicon Nanocrystal Quantum Dots. *J. Phys. Chem. C* **2017**, *121* (41), 23240-23248.
40. Jia, X.; Zhang, P.; Lin, Z.; Anthony, R.; Kortshagen, U.; Huang, S.; Puthen-Veetil, B.; Conibeer, G.; Perez-Wurfl, I., Accurate Determination of the Size Distribution of Si Nanocrystals from PL Spectra. *RSC Adv.* **2015**, *5* (68), 55119-55125.

41. de Boer, W. D. A. M.; Timmerman, D.; Dohnalová, K.; Yassievich, I. N.; Zhang, H.; Buma, W. J.; Gregorkiewicz, T., Red Spectral Shift and Enhanced Quantum Efficiency in Phonon-Free Photoluminescence from Silicon Nanocrystals. *Nat. Nanotechnol.* **2010**, *5* (12), 878-884.
42. Delerue, C.; Allan, G.; Lannoo, M., Theoretical Aspects of the Luminescence of Porous Silicon. *Phys. Rev. B* **1993**, *48* (15), 11024-11036.
43. Wang, L. W.; Zunger, A., Electronic Structure Pseudopotential Calculations of Large (.apprx.1000 Atoms) Si Quantum Dots. *J. Phys. Chem.* **1994**, *98* (8), 2158-2165.
44. Hill, N. A.; Whaley, K. B., Size Dependence of Excitons in Silicon Nanocrystals. *Phys. Rev. Lett.* **1995**, *75* (6), 1130-1133.
45. Hill, N. A.; Whaley, K. B., A Theoretical Study of Light Emission from Nanoscale Silicon. *J. Electron. Mater.* **1996**, *25* (2), 269-285.
46. Ögüt, S.; Chelikowsky, J. R.; Louie, S. G., Quantum Confinement and Optical Gaps in Si Nanocrystals. *Phys. Rev. Lett.* **1997**, *79* (9), 1770-1773.
47. Hannah, D. C.; Yang, J.; Kramer, N. J.; Schatz, G. C.; Kortshagen, U. R.; Schaller, R. D., Ultrafast Photoluminescence in Quantum-Confined Silicon Nanocrystals Arises from an Amorphous Surface Layer. *ACS Photonics* **2014**, *1*, (10), 960-967.
48. Kúsová, K.; Ondič, L.; Pelant, I., Comment on “Ultrafast Photoluminescence in Quantum-Confined Silicon Nanocrystals Arises from an Amorphous Surface Layer”. *ACS Photonics* **2015**, *2* (3), 454-455.
49. Hannah, D. C.; Yang, J.; Kramer, N. J.; Schatz, G. C.; Kortshagen, U. R.; Schaller, R. D., Reply to “Comment on ‘Ultrafast Photoluminescence in Quantum-Confined Silicon Nanocrystals Arises from an Amorphous Surface Layer’”. *ACS Photonics* **2015**, *2* (3), 456-458.
50. Brown, S. L.; Miller, J. B.; Anthony, R. J.; Kortshagen, U. R.; Kryjevski, A.; Hobbie, E. K., Abrupt Size Partitioning of Multimodal Photoluminescence Relaxation in Monodisperse Silicon Nanocrystals. *ACS Nano* **2017**, *11* (2), 1597-1603.
51. Thiessen, A. N.; Ha, M.; Hooper, R. W.; Yu, H.; Oliynyk, A. O.; Veinot, J. G. C.; Michaelis, V. K., Silicon Nanoparticles: Are They Crystalline from the Core to the Surface? *Chem. Mater.* **2019**, *31* (3), 678-688.
52. Liu, S.-M.; Yang; Sato, S.; Kimura, K., Enhanced Photoluminescence from Si Nano-organosols by Functionalization with Alkenes and Their Size Evolution. *Chem. Mater.* **2006**, *18* (3), 637-642.
53. Mastronardi, M. L.; Maier-Flaig, F.; Faulkner, D.; Henderson, E. J.; Kübel, C.; Lemmer, U.; Ozin, G. A., Size-Dependent Absolute Quantum Yields for Size-Separated Colloidally-Stable Silicon Nanocrystals. *Nano Lett.* **2012**, *12* (1), 337-342.
54. Hannah, D. C.; Yang, J.; Podsiadlo, P.; Chan, M. K. Y.; Demortière, A.; Gosztola, D. J.; Prakapenka, V. B.; Schatz, G. C.; Kortshagen, U.; Schaller, R. D., On the Origin of Photoluminescence in Silicon Nanocrystals: Pressure-Dependent Structural and Optical Studies. *Nano Lett.* **2012**, *12* (8), 4200-4205.
55. Wen, X.; Zhang, P.; Smith, T. A.; Anthony, R. J.; Kortshagen, U. R.; Yu, P.; Feng, Y.; Shrestha, S.; Coniber, G.; Huang, S., Tunability Limit of Photoluminescence in Colloidal Silicon Nanocrystals. *Sci. Rep.* **2015**, *5* (1), 12469.
56. Jakob, M.; Javadi, M.; Veinot, J. G. C.; Meldrum, A.; Kartouzian, A.; Heiz, U., Ensemble Effects in the Temperature-Dependent Photoluminescence of Silicon Nanocrystals. *Chem. Eur. J.* **2019**, *25* (12), 3061-3067.
57. Breitenacker, M.; Sexl, R.; Thirring, W., On the effective mass approximation. *Z. Physik* **1964**, *182* (2), 123-129.
58. Jarolimek, K.; Hazrati, E.; de Groot, R. A.; de Wijs, G. A., Band Offsets at the Interface between Crystalline and Amorphous Silicon from First Principles. *Phys. Rev. Applied* **2017**, *8* (1), 014026.
59. Anderson, S. L.; Luber, E. J.; Olsen, B. C.; Buriak, J. M., Substance over Subjectivity: Moving beyond the Histogram. *Chem. Mater.* **2016**, *28* (17), 5973-5975.
60. Kilaas, R., Optimal and near-optimal filters in high-resolution electron microscopy. *Journal of Microscopy* **1998**, *190*, 45-51.
61. Hessel, C. M.; Henderson, E. J.; Veinot, J. G. C., Hydrogen Silsesquioxane: A Molecular Precursor for Nanocrystalline Si-SiO₂ Composites and Freestanding Hydride-Surface-Terminated Silicon Nanoparticles. *Chem. Mater.* **2006**, *18* (26), 6139-6146.
62. Hessel, C. M.; Henderson, E. J.; Veinot, J. G. C., An Investigation of the Formation and Growth of Oxide-Embedded Silicon Nanocrystals in Hydrogen Silsesquioxane-Derived Nanocomposites. *J. Phys. Chem. C* **2007**, *111* (19), 6956-6961.

63. Clark, R. J.; Aghajamali, M.; Gonzalez, C. M.; Hadidi, L.; Islam, M. A.; Javadi, M.; Mobarok, M. H.; Purkait, T. K.; Robidillo, C. J. T.; Sinelnikov, R.; Thiessen, A. N.; Washington, J.; Yu, H.; Veinot, J. G. C., From Hydrogen Silsesquioxane to Functionalized Silicon Nanocrystals. *Chem. Mater.* **2017**, *29* (1), 80-89.
64. Dohnalova, K.; Gregorkiewicz, T.; Kusova, K., Silicon quantum dots: surface matters. *J. Phys. Condens. Matter* **2014**, *26* (17), 173201.
65. Balzar, D.; Audebrand, N.; Daymond, M. R.; Fitch, A.; Hewat, A.; Langford, J. I.; Le Bail, A.; Louër, D.; Masson, O.; McCowan, C. N.; Popa, N. C.; Stephens, P. W.; Toby, B. H., Size-strain line-broadening analysis of the ceria round-robin sample. *J. Appl. Cryst.* **2004**, *37* (6), 911-924.
66. Jakob, M.; Aissiou, A.; Morrish, W.; Marsiglio, F.; Islam, M.; Kartouzian, A.; Meldrum, A., Reappraising the Luminescence Lifetime Distributions in Silicon Nanocrystals. *Nanoscale Res. Lett.* **2018**, *13* (1), 383.
67. Dabbousi, B. O.; Rodriguez-Viejo, J.; Mikulec, F. V.; Heine, J. R.; Mattoussi, H.; Ober, R.; Jensen, K. F.; Bawendi, M. G., (CdSe)ZnS Core-Shell Quantum Dots: Synthesis and Characterization of a Size Series of Highly Luminescent Nanocrystallites. *J. Phys. Chem. B* **1997**, *101* (46), 9463-9475.
68. Lee, B. G.; Hiller, D.; Luo, J. W.; Semonin, O. E.; Beard, M. C.; Zacharias, M.; Stradins, P., Strained Interface Defects in Silicon Nanocrystals. *Adv. Funct. Mater.* **2012**, *22* (15), 3223-3232.
69. Kleovoulou, K.; Kelires, P. C., Stress state of embedded Si nanocrystals. *Phys. Rev. B* **2013**, *88*, 085424.
70. Miller, J. B.; Van Sickle, A. R.; Anthony, R. J.; Kroll, D. M.; Kortshagen, U. R.; Hobbie, E. K., Ensemble Brightening and Enhanced Quantum Yield in Size-Purified Silicon Nanocrystals. *ACS Nano* **2012**, *6* (8), 7389-7396.
71. Huisken, F.; Ledoux, G.; Guillois, O.; Reynaud, C., Light-Emitting Silicon Nanocrystals from Laser Pyrolysis. *Adv. Mater.* **2002**, *14* (24), 1861-1865.
72. Delerue, C.; Allan, G.; Reynaud, C.; Guillois, O.; Ledoux, G.; Huisken, F., Multiexponential Photoluminescence Decay in Indirect-Gap Semiconductor Nanocrystals. *Phys. Rev. B* **2006**, *73* (23), 235318.
73. Belyakov, V. A.; Burdov, V. A.; Gaponova, D. M.; Mikhaylov, A. N.; Tetelbaum, D. I.; Trushin, S. A., Phonon-Assisted Radiative Electron-Hole Recombination in Silicon Quantum Dots. *Phys. Solid State* **2004**, *46*, 27-31.
74. Belyakov, V. A.; Burdov, V. A.; Lockwood, R.; Meldrum, A., Silicon Nanocrystals: Fundamental Theory and Implications for Stimulated Emission. *Adv. Opt. Technol.* **2008**, *2008*, 279502.
75. Lannoo, M.; Delerue, C.; Allan, G., Nonradiative Recombination on Dangling Bonds in Silicon Crystallites. *J. Lumin.* **1993**, *57* (1), 243-247.
76. Bae, W. K.; Padilha, L. A.; Park, Y.-S.; McDaniel, H.; Robel, I.; Pietryga, J. M.; Klimov, V. I., Controlled Alloying of the Core-Shell Interface in CdSe/CdS Quantum Dots for Suppression of Auger Recombination. *ACS Nano* **2013**, *7* (4), 3411-3419.

Chapter 4

1. Canham, L. T., Silicon quantum wire array fabrication by electrochemical and chemical dissolution of wafers. *Appl Phys Lett* **1990**, *57* (10), 1046-1048.
2. Yu, Y.; Fan, G.; Fermi, A.; Mazzaro, R.; Morandi, V.; Ceroni, P.; Smilgies, D.-M.; Korgel, B. A., Size-Dependent Photoluminescence Efficiency of Silicon Nanocrystal Quantum Dots. *J. Phys. Chem. C* **2017**, *121* (41), 23240-23248.
3. Hessel, C. M.; Henderson, E. J.; Veinot, J. G. C., Hydrogen Silsesquioxane: A Molecular Precursor for Nanocrystalline Si-SiO₂ Composites and Freestanding Hydride-Surface-Terminated Silicon Nanoparticles. *Chem. Mater.* **2006**, *18* (26), 6139-6146.
4. Hessel, C. M.; Reid, D.; Panthani, M. G.; Rasch, M. R.; Goodfellow, B. W.; Wei, J.; Fujii, H.; Akhavan, V.; Korgel, B. A., Synthesis of Ligand-Stabilized Silicon Nanocrystals with Size-Dependent Photoluminescence Spanning Visible to Near-Infrared Wavelengths. *Chem. Mater.* **2012**, *24* (2), 393-401.
5. Erogbogbo, F.; Yong, K.-T.; Roy, I.; Hu, R.; Law, W.-C.; Zhao, W.; Ding, H.; Wu, F.; Kumar, R.; Swihart, M. T.; Prasad, P. N., In Vivo Targeted Cancer Imaging, Sentinel Lymph Node Mapping and Multi-Channel Imaging with Biocompatible Silicon Nanocrystals. *ACS Nano* **2011**, *5* (1), 413-423.
6. Romano, F.; Angeloni, S.; Morselli, G.; Mazzaro, R.; Morandi, V.; Shell, J. R.; Cao, X.; Pogue, B. W.; Ceroni, P., Water-soluble silicon nanocrystals as NIR luminescent probes for time-gated biomedical imaging. *Nanoscale* **2020**, *12* (14), 7921-7926.

7. Gonzalez, C. M.; Iqbal, M.; Dasog, M.; Piercey, D. G.; Lockwood, R.; Klapotke, T. M.; Veinot, J. G. C., Detection of high-energy compounds using photoluminescent silicon nanocrystal paper based sensors. *Nanoscale* **2014**, *6* (5), 2608-2612.
8. Meinardi, F.; Ehrenberg, S.; Dharmo, L.; Carulli, F.; Mauri, M.; Bruni, F.; Simonutti, R.; Kortshagen, U.; Brovelli, S., Highly efficient luminescent solar concentrators based on earth-abundant indirect-bandgap silicon quantum dots. *Nature Photonics* **2017**, *11*, 177-185.
9. Mazzaro, R.; Gradone, A.; Angeloni, S.; Morselli, G.; Cozzi, P. G.; Romano, F.; Vomiero, A.; Ceroni, P., Hybrid Silicon Nanocrystals for Color-Neutral and Transparent Luminescent Solar Concentrators. *ACS Photonics* **2019**, *6* (9), 2303-2311.
10. Liu, X.; Zhao, S.; Gu, W.; Zhang, Y.; Qiao, X.; Ni, Z.; Pi, X.; Yang, D., Light-Emitting Diodes Based on Colloidal Silicon Quantum Dots with Octyl and Phenylpropyl Ligands. *ACS Appl. Mater. Interfaces* **2018**, *10* (6), 5959-5966.
11. Angl, A.; Loch, M.; Sinelnikov, R.; Veinot, J. G. C.; Becherer, M.; Lugli, P.; Rieger, B., The influence of surface functionalization methods on the performance of silicon nanocrystal LEDs. *Nanoscale* **2018**, *10* (22), 10337-10342.
12. Mazzaro, R.; Romano, F.; Ceroni, P., Long-lived luminescence of silicon nanocrystals: from principles to applications. *Phys. Chem. Chem. Phys.* **2017**, *19* (39), 26507-26526.
13. Tsybeskov, L.; Vandyshev, J. V.; Fauchet, P. M., Blue emission in porous silicon: Oxygen-related photoluminescence. *Phys. Rev. B* **1994**, *49* (11), 7821-7824.
14. de Boer, W. D. A. M.; Timmerman, D.; Dohnalová, K.; Yassievich, I. N.; Zhang, H.; Buma, W. J.; Gregorkiewicz, T., Red spectral shift and enhanced quantum efficiency in phonon-free photoluminescence from silicon nanocrystals. *Nature Nanotech.* **2010**, *5*, 878-884.
15. Valenta, J.; Fucikova, A.; Pelant, I.; Kůsová, K.; Dohnalová, K.; Aleknavičius, A.; Cibulka, O.; Fojtík, A.; Kada, G., On the origin of the fast photoluminescence band in small silicon nanoparticles. *New Journal of Physics* **2008**, *10* (7), 073022.
16. Plautz, G. L.; Graff, I. L.; Schreiner, W. H.; Bezerra, A. G., Evolution of size distribution, optical properties, and structure of Si nanoparticles obtained by laser-assisted fragmentation. *Applied Physics A* **2017**, *123*, 359.
17. Gupta, A.; Wiggers, H., Freestanding silicon quantum dots: origin of red and blue luminescence. *Nanotechnology* **2010**, *22* (5), 055707.
18. Botas, A. M. P.; Ferreira, R. A. S.; Pereira, R. N.; Anthony, R. J.; Moura, T.; Rowe, D. J.; Kortshagen, U., High Quantum Yield Dual Emission from Gas-Phase Grown Crystalline Si Nanoparticles. *J. Phys. Chem. C* **2014**, *118* (19), 10375-10383.
19. Martin, J.; Cichos, F.; Huisken, F.; von Borczyskowski, C., Electron-Phonon Coupling and Localization of Excitons in Single Silicon Nanocrystals. *Nano Lett.* **2008**, *8* (2), 656-660.
20. Kang, Z.; Liu, Y.; Tsang, C. H. A.; Ma, D. D. D.; Fan, X.; Wong, N.-B.; Lee, S.-T., Water-Soluble Silicon Quantum Dots with Wavelength-Tunable Photoluminescence. *Adv. Mater.* **2009**, *21* (6), 661-664.
21. Gupta, A.; Swihart, M. T.; Wiggers, H., Luminescent Colloidal Dispersion of Silicon Quantum Dots from Microwave Plasma Synthesis: Exploring the Photoluminescence Behavior Across the Visible Spectrum. *Adv. Funct. Mater.* **2009**, *19* (5), 696-703.
22. Yang, Z.; De los Reyes, G. B.; Titova, L. V.; Sychugov, I.; Dasog, M.; Linnros, J.; Hegmann, F. A.; Veinot, J. G. C., Evolution of the Ultrafast Photoluminescence of Colloidal Silicon Nanocrystals with Changing Surface Chemistry. *ACS Photonics* **2015**, *2* (5), 595-605.
23. Pereira, R. N.; Rowe, D. J.; Anthony, R. J.; Kortshagen, U., Oxidation of freestanding silicon nanocrystals probed with electron spin resonance of interfacial dangling bonds. *Phys. Rev. B* **2011**, *83* (15), 155327.
24. Lockwood, R.; Yang, Z.; Sammynaiken, R.; Veinot, J. G. C.; Meldrum, A., Light-Induced Evolution of Silicon Quantum Dot Surface Chemistry—Implications for Photoluminescence, Sensing, and Reactivity. *Chem. Mater.* **2014**, *26* (19), 5467-5474.
25. Liptak, R. W.; Kortshagen, U.; Campbell, S. A., Surface chemistry dependence of native oxidation formation on silicon nanocrystals. *J. Appl. Phys.* **2009**, *106* (6), 064313.
26. Kůsová, K.; Ondič, L.; Klimešová, E.; Herynková, K.; Pelant, I.; Daniš, S.; Valenta, J.; Gallart, M.; Ziegler, M.; Hönerlage, B.; Gilliot, P., Luminescence of free-standing versus matrix-embedded oxide-passivated silicon nanocrystals: The role of matrix-induced strain. *Appl. Phys. Lett.* **2012**, *101* (14), 143101.

27. Hofmeister, H.; Huisken, F.; Kohn, B. Lattice contraction in nanosized silicon particles produced by laser pyrolysis of silane, In *The European Physical Journal D*; Châtelain, A.; Bonard, J. M., Eds.; Springer: Berlin, Heidelberg; 1999; pp 137-140.
28. Falcão, B. P.; Leitão, J. P.; Soares, M. R.; Ricardo, L.; Águas, H.; Martins, R.; Pereira, R. N., Oxidation and Strain in Free-standing Silicon Nanocrystals. *Phys. Rev. Applied* **2019**, *11* (2), 024054.
29. Kehrlé, J.; Kaiser, S.; Purkait, T. K.; Winnacker, M.; Helbich, T.; Vagin, S.; Veinot, J. G. C.; Rieger, B., In situ IR-spectroscopy as a tool for monitoring the radical hydrosilylation process on silicon nanocrystal surfaces. *Nanoscale* **2017**, *9* (24), 8489-8495.
30. Askar, A. M.; Bernard, G. M.; Wiltshire, B.; Shankar, K.; Michaelis, V. K., Multinuclear Magnetic Resonance Tracking of Hydro, Thermal, and Hydrothermal Decomposition of CH₃NH₃PbI₃. *J. Phys. Chem. C* **2017**, *121*, (2), 1013-1024.
31. Bruker AXS. *TOPAS V4: General Profile and Structure Analysis Software for Powder Diffraction Data. - User's Manual*; Bruker AXS: Karlsruhe, Germany, 2008.
32. Anderson, S. L.; Luber, E. J.; Olsen, B. C.; Buriak, J. M., Substance over Subjectivity: Moving beyond the Histogram. *Chem. Mater.* **2016**, *28* (17), 5973-5975.
33. Yang, Z.; Gonzalez, C. M.; Purkait, T. K.; Iqbal, M.; Meldrum, A.; Veinot, J. G. C., Radical Initiated Hydrosilylation on Silicon Nanocrystal Surfaces: An Evaluation of Functional Group Tolerance and Mechanistic Study. *Langmuir* **2015**, *31* (38), 10540-10548.
34. Purkait, T. K.; Iqbal, M.; Wahl, M. H.; Gottschling, K.; Gonzalez, C. M.; Islam, M. A.; Veinot, J. G. C., Borane-catalyzed room-temperature hydrosilylation of alkenes/alkynes on silicon nanocrystal surfaces. *J. Am. Chem. Soc.* **2014**, *136* (52), 17914-7.
35. Barr, T. L.; Seal, S. Nature of the use of Adventitious Carbon as a Binding Energy Standard. *J. Vac. Sci. Technol., A* **1995**, *13*, 1239-1246.
36. Hu, M.; Luber, E.; Buriak, J. M., Reconsidering XPS Quantification of Substitution Levels of Monolayers on Unoxidized Silicon Surfaces. ChemRxiv. Preprint, 2020, DOI: 10.26434/chemrxiv.12268325.v1.
37. Thiessen, A. N.; Ha, M.; Hooper, R. W.; Yu, H.; Oliynyk, A. O.; Veinot, J. G. C.; Michaelis, V. K., Silicon Nanoparticles: Are They Crystalline from the Core to the Surface? *Chem. Mater.* **2019**, *31* (3), 678-688.
38. Khorsand Zak, A.; Abd. Majid, W. H.; Abrishami, M. E.; Yousefi, R., X-ray analysis of ZnO nanoparticles by Williamson–Hall and size–strain plot methods. *Solid State Sciences* **2011**, *13* (1), 251-256.
39. Dohnalová, K.; Hapala, P.; Kůsová, K.; Infante, I., Electronic Structure Engineering Achieved via Organic Ligands in Silicon Nanocrystals. *Chem. Mater.* **2020**, DOI:10.1021/acs.chemmater.0c00443.
40. Yang, D. Q.; Meunier, M.; Sacher, E., Room temperature air oxidation of nanostructured Si thin films with varying porosities as studied by x-ray photoelectron spectroscopy. *J. Appl. Phys.* **2006**, *99* (8), 084315.

Chapter 5

1. Islam, M. A.; Sinelnikov, R.; Howlader, M. A.; Faramus, A.; Veinot, J. G. C., Mixed Surface Chemistry: An Approach to Highly Luminescent Biocompatible Amphiphilic Silicon Nanocrystals. *Chem. Mater.* **2018**, *30* (24), 8925-8931.
2. Pramanik, S.; Hill, S. K. E.; Zhi, B.; Hudson-Smith, N. V.; Wu, J. J.; White, J. N.; McIntire, E. A.; Kondeti, V. S. S. K.; Lee, A. L.; Bruggeman, P. J.; Kortshagen, U. R.; Haynes, C. L., Comparative toxicity assessment of novel Si quantum dots and their traditional Cd-based counterparts using bacteria models *Shewanella oneidensis* and *Bacillus subtilis*. *Environ. Sci.: Nano* **2018**, *5* (8), 1890-1901.
3. Su, X.; Wu, Q.; Li, J.; Xiao, X.; Lott, A.; Lu, W.; Sheldon, B. W.; Wu, J., Silicon-Based Nanomaterials for Lithium-Ion Batteries: A Review. *Adv. Energy Mater.* **2014**, *4* (1), 1300882.
4. Choi, J. W.; Aurbach, D., Promise and reality of post-lithium-ion batteries with high energy densities. *Nat. Rev. Mater.* **2016**, *1* (4), 16013.
5. Gonzalez, C. M.; Veinot, J. G. C., Silicon nanocrystals for the development of sensing platforms. *J. Mater. Chem. C* **2016**, *4* (22), 4836-4846.
6. Hill, S. K. E.; Connell, R.; Peterson, C.; Hollinger, J.; Hillmyer, M. A.; Kortshagen, U.; Ferry, V. E., Silicon Quantum Dot–Poly(methyl methacrylate) Nanocomposites with Reduced Light Scattering for Luminescent Solar Concentrators. *ACS Photonics* **2019**, *6* (1), 170-180.

7. Romano, F.; Angeloni, S.; Morselli, G.; Mazzaro, R.; Morandi, V.; Shell, J. R.; Cao, X.; Pogue, B. W.; Ceroni, P., Water-soluble silicon nanocrystals as NIR luminescent probes for time-gated biomedical imaging. *Nanoscale* **2020**, *12* (14), 7921-7926.
8. Meinardi, F.; Ehrenberg, S.; Dharmo, L.; Carulli, F.; Mauri, M.; Bruni, F.; Simonutti, R.; Kortshagen, U.; Brovelli, S., Highly efficient luminescent solar concentrators based on earth-abundant indirect-bandgap silicon quantum dots. *Nature Photon.* **2017**, *11*, 177-185.
9. Maier-Flaig, F.; Rinck, J.; Stephan, M.; Bocksrocker, T.; Bruns, M.; Kübel, C.; Powell, A. K.; Ozin, G. A.; Lemmer, U., Multicolor Silicon Light-Emitting Diodes (SiLEDs). *Nano Lett.* **2013**, *13* (2), 475-480.
10. Angl, A.; Loch, M.; Sinelnikov, R.; Veinot, J. G. C.; Becherer, M.; Lugli, P.; Rieger, B., The influence of surface functionalization methods on the performance of silicon nanocrystal LEDs. *Nanoscale* **2018**, *10* (22), 10337-10342.
11. Mangolini, L.; Thimsen, E.; Kortshagen, U., High-Yield Plasma Synthesis of Luminescent Silicon Nanocrystals. *Nano Lett.* **2005**, *5* (4), 655-659.
12. Anthony, R.; Kortshagen, U., Photoluminescence quantum yields of amorphous and crystalline silicon nanoparticles. *Phys. Rev. B* **2009**, *80* (11), 115407.
13. Mobarok, M. H.; Purkait, T. K.; Islam, M. A.; Miskolzie, M.; Veinot, J. G. C., Instantaneous Functionalization of Chemically Etched Silicon Nanocrystal Surfaces. *Angew. Chem. Int. Ed.* **2017**, *56* (22), 6073-6077.
14. Islam, M. A.; Mobarok, M. H.; Sinelnikov, R.; Purkait, T. K.; Veinot, J. G. C., Phosphorus Pentachloride Initiated Functionalization of Silicon Nanocrystals. *Langmuir* **2017**, *33* (35), 8766-8773.
15. Ko, M.; Chae, S.; Jeong, S.; Oh, P.; Cho, J., Elastic α -Silicon Nanoparticle Backboned Graphene Hybrid as a Self-Compacting Anode for High-Rate Lithium Ion Batteries. *ACS Nano* **2014**, *8* (8), 8591-8599.
16. Dasog, M.; De los Reyes, G. B.; Titova, L. V.; Hegmann, F. A.; Veinot, J. G., Size vs surface: tuning the photoluminescence of freestanding silicon nanocrystals across the visible spectrum via surface groups. *ACS Nano* **2014**, *8* (9), 9636-48.
17. Falcão, B. P.; Leitão, J. P.; Soares, M. R.; Ricardo, L.; Águas, H.; Martins, R.; Pereira, R. N., Oxidation and Strain in Free-standing Silicon Nanocrystals. *Phys. Rev. Appl.* **2019**, *11* (2), 024054.
18. Wu, Y.; Chen, Z.; Nan, P.; Xiong, F.; Lin, S.; Zhang, X.; Chen, Y.; Chen, L.; Ge, B.; Pei, Y., Lattice Strain Advances Thermoelectrics. *Joule* **2019**, *3* (5), 1276-1288.
19. Ouyang, G.; Zhu, W. G.; Sun, C. Q.; Zhu, Z. M.; Liao, S. Z., Atomistic origin of lattice strain on stiffness of nanoparticles. *Phys. Chem. Chem. Phys.* **2010**, *12* (7), 1543-1549.
20. Lee, B. G.; Hiller, D.; Luo, J. W.; Semonin, O. E.; Beard, M. C.; Zacharias, M.; Stradins, P., Strained Interface Defects in Silicon Nanocrystals. *Adv. Funct. Mater.* **2012**, *22* (15), 3223-3232.
21. Kleovoulou, K.; Kelires, P. C., Stress state of embedded Si nanocrystals. *Phys. Rev. B* **2013**, *88*, 085424.
22. Huysken, F.; Ledoux, G.; Guillois, O.; Reynaud, C., Light-Emitting Silicon Nanocrystals from Laser Pyrolysis. *Adv. Mater.* **2002**, *14* (24), 1861-1865.
23. Wu, J. J.; Kortshagen, U. R., Photostability of thermally-hydrosilylated silicon quantum dots. *RSC Adv.* **2015**, *5* (126), 103822-103828.
24. Ross, P. E., Startup Offers a Silicon Solution for Lithium-Ion Batteries. *IEEE Spectrum*, [Online], Dec 13, 2019, <https://spectrum.ieee.org/energywise/green-tech/fuel-cells/startup-advano-silicon-lithium-ion-batteries> (July 10, 2020)
25. Cassidy, M. C.; Chan, H. R.; Ross, B. D.; Bhattacharya, P. K.; Marcus, C. M., In vivo magnetic resonance imaging of hyperpolarized silicon particles. *Nature Nanotech.* **2013**, *8*, 363-368.
26. Tu, C.; Ma, X.; House, A.; Kauzlarich, S. M.; Louie, A. Y., PET Imaging and Biodistribution of Silicon Quantum Dots in Mice. *ACS Med. Chem. Lett.* **2011**, *2* (4), 285-288.
27. Chen, W.; Silverman, D. H. S.; Delaloye, S.; Czernin, J.; Kamdar, N.; Pope, W.; Satyamurthy, N.; Schiepers, C.; Cloughesy, T., ¹⁸F-FDOPA PET imaging of brain tumors: comparison study with ¹⁸F-FDG PET and evaluation of diagnostic accuracy. *J. Nucl. Med.* **2006**, *47* (6), 904-911.
28. Ha, M.; Thiessen, A. N.; Sergeyev, I. V.; Veinot, J. G. C.; Michaelis, V. K., Endogenous dynamic nuclear polarization NMR of hydride-terminated silicon nanoparticles. *Solid State Nucl. Mag.* **2019**, *100*, 77-84.
29. Pereira, R. N.; Rowe, D. J.; Anthony, R. J.; Kortshagen, U., Oxidation of freestanding silicon nanocrystals probed with electron spin resonance of interfacial dangling bonds. *Phys. Rev. B* **2011**, *83* (15), 155327.

30. Wängler, C.; Niedermoser, S.; Chin, J.; Orchowski, K.; Schirrmacher, E.; Jurkschat, K.; Iovkova-Berends, L.; Kostikov, A. P.; Schirrmacher, R.; Wängler, B., One-step ¹⁸F-labeling of peptides for positron emission tomography imaging using the SiFA methodology. *Nat. Protoc.* **2012**, *7* (11), 1946-1955.
31. Bruker, PET/MR 3T. https://www.bruker.com/products/preclinical-imaging/nuclear-molecular-imaging/petmr-3t.html?gclid=Cj0KCQjw0YD4BRD2ARIsAHwmKVmnrQ7gxq8Rnzyz_RMQ9cBm2TdsH7HIWFdhymA9q0yBHO3Of9GP9qkaAoIdEALw_wcB (accessed July 10, 2020)
32. Zheludev, N. I., Obtaining optical properties on demand. *Science* **2015**, *348* (6238), 973-974.
33. Shelby, R. A.; Smith, D. R.; Schultz, S., Experimental Verification of a Negative Index of Refraction. *Science* **2001**, *292* (5514), 77-79.
34. Mühlig, S.; Cunningham, A.; Dintinger, J.; Farhat, M.; Hasan, S. B.; Scharf, T.; Bürgi, T.; Lederer, F.; Rockstuhl, C., A self-assembled three-dimensional cloak in the visible. *Sci. Rep.* **2013**, *3* (1), 2328.
35. Haxha, S.; AbdelMalek, F.; Ouerghi, F.; Charlton, M. D. B.; Aggoun, A.; Fang, X., Metamaterial Superlenses Operating at Visible Wavelength for Imaging Applications. *Sci. Rep.* **2018**, *8* (1), 16119.
36. De Marco, M. L.; Semlali, S.; Korgel, B. A.; Barois, P.; Drisko, G. L.; Aymonier, C., Silicon-Based Dielectric Metamaterials: Focus on the Current Synthetic Challenges. *Angew. Chem. Int. Ed.* **2018**, *57* (17), 4478-4498.

Appendix A

Lewis Acid Protection: A Method Towards Synthesizing Phase Transferable Luminescent Silicon Nanocrystals^a

A.1 Introduction

Quantum dots have been the subject of intense investigation due to their promising optoelectronic properties and potential for biological imaging and sensing.¹ Photoluminescent silicon-based quantum dots, in particular, have been explored for biological imaging due to their relatively low toxicity compared to their CdSe counterparts.²⁻⁶ Silicon nanocrystals (SiNCs) also exhibit photoluminescence lifetimes on the microsecond timescale that can be useful in time-gated imaging and red photoluminescence that optically stands out from the background luminescence in cells.⁷ However, when the silicon nanocrystals are exposed to even trace amounts of nitrogen, the photoluminescence becomes blue.⁸ While the specific chemical nature of the blue emitter is still unknown, it is established that it exhibits faster decay times that are likely caused by surface trap states.⁸ For biological applications, this blue emission is undesirable because it falls within the same spectral window as the background fluorescence of the cells.

Introducing a nitrogen-containing chemical functionality terminal to the surface of the SiNCs, while maintaining the bandgap-based photoluminescence, is desirable to access a new scope of reactivity. One method of achieving this is to “protect” the lone pair electrons on the nitrogen atom with a Lewis acid, such as borane. This general approach has been employed previously to protect the nitrogen in the pyridine for the synthesis of vitronectin,⁹ however, it never has been extended to SiNC surface chemistry. Coordinating the lone pair on the pyridinic nitrogen prevents the cyclization of (3-bromopropyl)(pyridin-2-yl)amine in the presence of a base, allowing subsequent base-catalyzed reaction of the bromine.⁹ Once this protecting group has been removed, the pyridinic nitrogen retains its original reactivity.

^a The contents of this chapter have been adapted with permission from the following publication: Thiessen, A. N.; Purkait, T. K.; Faramus, A.; Veinot, J. G. C., Lewis acid protection: a method towards synthesizing phase transferable luminescent silicon nanocrystals. *Phys. Status Solidi A*. **2018**, *215*, 1700620. Copyright © 2017 WILEY-VCH Verlag GmbH & Co. kGaA, Weinheim.

It is reasonable that this approach can be employed to introduce nitrogen containing functional groups terminal to the SiNC surface by protecting the lone pairs. Introducing nitrogen-containing functionalities terminal to the SiNC surface, while maintaining red photoluminescence, would serve to expand the repertoire of surface chemistry that can be done with these materials.

Amidines are nitrogen-containing chemical moieties that exhibit switchable hydrophilicity properties, which can be controlled via a defined exposure to dissolved CO₂.^{10,11} By rendering the solution slightly acidic, one of the nitrogen atoms becomes protonated and becomes hydrophilic (as shown in Figure A-1). Upon purging with argon or nitrogen gas, the ligand is deprotonated and hydrophobicity returns. Utilizing CO₂ as the trigger for the conversion is advantageous as it is benign, inexpensive, and abundant. CO₂ responsive materials have found applications as surfactants¹⁰ and drying agents¹² and are suitable for drug release¹³ as well as polymer self-assembly.¹⁴ With all these diverse potential applications of CO₂ responsive materials, it is desirable to combine these ligand properties with nanomaterials to control their solubility. Pocoví-Martínez et al. demonstrated that by interdigitating N'-oleyl-N,N-dimethylacetamide with oleylamine capped gold nanoparticles, they were able to control the solubility properties of the nanoparticles.¹⁵ However, covalent attachment is desirable to prevent ligand displacement.

In this work, BH₃ was used as a protecting group to synthesize amidine functionalized SiNCs with the nitrogen containing group distal to the surface while maintaining desirable photoluminescence properties. The reactive properties of the surface are maintained during the synthesis, and hydrophilicity switchable, photoluminescent SiNCs were produced. These nanocrystals could act as removable sensors or controlled targeting agents for imaging different tissues in biological systems. By covalently linking the amidine to the surface of the particle, instead of interdigitating it as has been done previously, the surface is more accessible for sensing applications of the material, and displacement is less likely to occur.

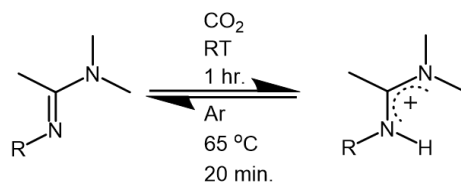


Figure A-1. Scheme showing amidine switching hydrophilicity in the presence of CO₂.

A.2 Experimental Section

A.2.1 Materials

A.2.1.1 Starting Materials

Hydrogen silsesquioxane (HSQ, trade name Fox-17) was purchased from Dow Corning, and the solvent was removed to yield a white solid that was used directly. Hydrofluoric acid (Electronic grade, 48–50%) and hydrochloric acid (36.5–38%) were purchased from Fischer Scientific. 1-Amino-10-undecene (97%) was purchased from GFS Chemicals. Azobisisobutyronitrile (AIBN, 98%), $\text{BH}_3 \cdot \text{THF}$ complex (1 M solution in THF), and dimethylacetamide dimethyl acetal (90%) were purchased from Sigma Aldrich. All reagents were used as received, unless otherwise specified. All solvents were reagent grade and used as received. Toluene was collected from a Pure-Solv purification system immediately prior to use.

A.2.1.2 Preparation of N'-undec-10-enyl-N,N-dimethylacetamide

The N'-undec-10-enyl-N,N-dimethylacetamide was synthesized using the method developed by Jessop and coworkers.¹⁰ 1-amino-10-undecene was added to dimethylacetamide dimethyl acetal in equimolar amounts and heated without solvent at 65 °C for 30 min. The methanol byproduct was removed using rotary evaporation under high vacuum. The crude mixture was used without further purification. ^1H NMR (CDCl_3): 1.22 (m, 12 H, C_6H_{12}), 1.37 (quintet, $J=6.0$ Hz, 2 H, N-C- CH_2), 1.74 (singlet, 3 H, C- CH_3), 1.91 (sextet, $J=5.6$ Hz, 2H, =C- CH_2), 2.74 (singlet, 6 H, $\text{N}(\text{CH}_3)_2$), 3.05 (triplet, $J=6.0$ Hz 2 H, NCH_2), 4.82 (m, 2 H, C= CH_2), 5.67 (m, 1 H, C= CH) ^{13}C NMR (CDCl_3): 12.3, 27.5, 28.9, 29.0, 29.4, 29.5, 32.3, 33.7, 37.9, 50.1, 114.0, 139.0, 158.6. IR (neat): 722 (w), 909 (m), 1007 (w), 1139 (w), 1188 (w), 1261 (w), 1343 (m), 1385 (m), 1408 (w), 1438 (m), 1464 (m), 1629 (s), 1686 (w), 2854 (s), 2925 (s) 2975 (w), 3002 (w), 3076 (w).

A.2.1.3 Preparation of the H-SiNCs

Hydride-terminated SiNCs (H-SiNCs) were prepared via previously reported procedures.¹⁶ Approximately 5 g of hydrogen silsesquioxane (HSQ) were annealed for 1 h at 1100 °C under a slightly reducing atmosphere (flowing 5% H_2 /95% Ar). The resulting SiNCs are embedded in an SiO_2 matrix. The SiNC/ SiO_2 composite was ground using an agate mortar

and pestle for 30 min, before adding to a shaker flask equipped with borosilicate glass beads and shaken on a wrist action shaker for ca. 7 h.

H-SiNCs were liberated from the SiO₂ matrix upon HF etching: 500 mg of the SiNC/SiO₂ powder were mixed with 5 mL H₂O, 5 mL ethanol, and 5 mL 48% HF in a PET beaker. The etching mixture was stirred at room temperature for 50 min. The resulting H-SiNCs were extracted with toluene and isolated via centrifugation at 3000 rpm.

A.2.1.4 Synthesis of Amidine Functionalized SiNCs

H-SiNCs (25 mg) were dispersed in 15 mL of dry toluene containing 0.48 mmol of azobisisobutyronitrile (AIBN) in a Schlenk flask, and N'-undec-10-enyl-N,N-dimethylacetamide (10 mmol) was added to a second Schlenk flask.¹⁷ The contents of both flasks were subjected to three freeze-pump-thaw cycles. Then, 12 mL of 1M BH₃·THF adduct was added to the amidine and allowed to stir for 15 min. The amidine/borane mixture was transferred to the Schlenk flask containing the SiNCs, causing the mixture to change colour from yellow-orange to brown. The reaction mixture was heated to 70 °C and stirred overnight (15 h) to yield an orange reaction mixture that contained some dark brown solid.

The functionalized SiNCs were removed from the reaction mixture by centrifugation at 3000 rpm, and the supernatant was decanted and discarded. The recovered solid pellet was redispersed in toluene (5 mL), and aqueous HCl (1 mL) was added to the mixture, rendering the particles dispersible in H₂O. Methanol (5 mL) was added to the solution, and the SiNCs were centrifuged again at 3000 rpm. The SiNCs were washed once more with methanol and once with toluene to remove any unreacted amidine. The purified SiNCs were stored as a toluene solution (ca. 5 mL).

A.2.2 Characterization

Fourier transform infrared spectroscopy (FT-IR) was performed on a Nicolet Magna 750 IR spectrophotometer by drop casting SiNCs from toluene solutions. Nuclear magnetic resonance (NMR) spectra were collected using an Agilent/Varian VNMRS two-channel 500 MHz spectrometer at 27.0 °C. X-ray photoelectron spectroscopy (XPS) was measured using a Kratos Axis Ultra X-Ray photoelectron spectrometer operated in energy spectrum mode at 210 W. XPS samples were prepared by drop-coating a toluene dispersion of SiNCs

onto a copper foil. Spectra were calibrated to the C 1s (284.8 eV) and fitted to appropriate spin-orbit pairs using CasaXPS (VAMAS) software with a Shirley-type background. To fit the Si 2p high resolution spectrum, the doublet area ratio was fixed at 2:1, and the separation was set at 0.6. Transmission electron microscopy (TEM) was performed on a JEOL-2010 (LaB6 filament) electron microscope, with an accelerating voltage of 200 kV using SiNCs drop-coated from a toluene solution onto a carbon-coated copper grid. The SiNC size was determined by averaging the size of 300 particles using ImageJ software (version 1.51j8). Photoluminescence emission measurements were collected on a Cary Eclipse spectrophotometer, with an excitation wavelength of 350 nm.

A.2.3 Hydrophilicity Switch Experiments

Functionalized SiNCs (ca. 2 mg) were dispersed in a test tube containing additional toluene (ca. 2 mL), water (ca. 4 mL) was added, and the tube was capped with a septum equipped with a venting needle. To track the location of the SiNCs, their photoluminescence was qualitatively evaluated using a handheld UV light (365 nm). CO₂ was bubbled through the SiNC mixture for 1 h at room temperature (20 °C) to acidify the water and remove the toluene. Following this procedure, the previously hydrophobic SiNCs were dispersed readily in the water phase. Addition of fresh toluene (4 mL), followed by vigorous bubbling with Ar and heating to 65 °C for 1 h, rendered the SiNCs hydrophobic, causing them to partition into the toluene phase.

A.3 Results and Discussion

A.3.1 Synthesis of Amidine Functionalized SiNCs

Lewis acid mediated surface hydrosilylation of SiNCs using BH₃·THF has been reported.¹⁸ For the present reaction involving alkene/amidine bifunctional substrates, this approach would require at least 3 molar equivalents of BH₃·THF to achieve the desired surface modification; the first 2 equivalents coordinate to the nitrogen atoms, and the third drives the hydrosilylation reaction. Unfortunately, removal of excess boric acid byproducts can compromise material properties and be challenging to remove. In this regard, we investigated a hybrid procedure involving Lewis acid protection of the amidine functionality, the radical initiated hydrosilylation followed by deprotection.

Amidine-terminated SiNCs were prepared upon reaction of hydride-terminated SiNCs with a BH_3 protected N'-undec-10-enyl-N,N-dimethylacetamide (Figure A-2). It is reasonable that the Lewis acid coordinates to the most basic nitrogen of the amidine functionality, limiting its reactivity with the H-Si surface. This leaves the terminal alkene to participate in radical initiated hydrosilylation and the formation of a Si—C surface linkage. The BH_3 protecting group can be removed readily upon exposure to aqueous HCl, recovering the original amidine functionality. Throughout the procedure the integrity of the SiNC core (Figure A-3a, 2.85 ± 0.67 nm) and its photoluminescent (PL) properties are maintained (Figure A-3b).

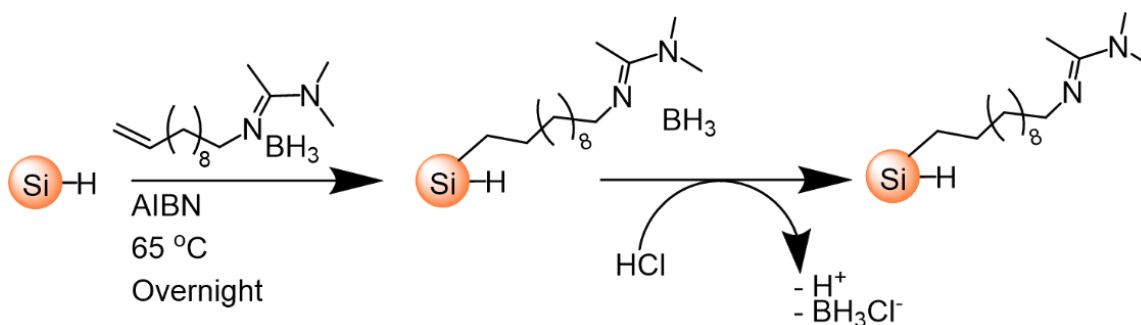


Figure A-2. Scheme showing the functionalization of SiNCs with a terminal amidine group using radical initiated hydrosilylation, followed by deprotection using HCl.

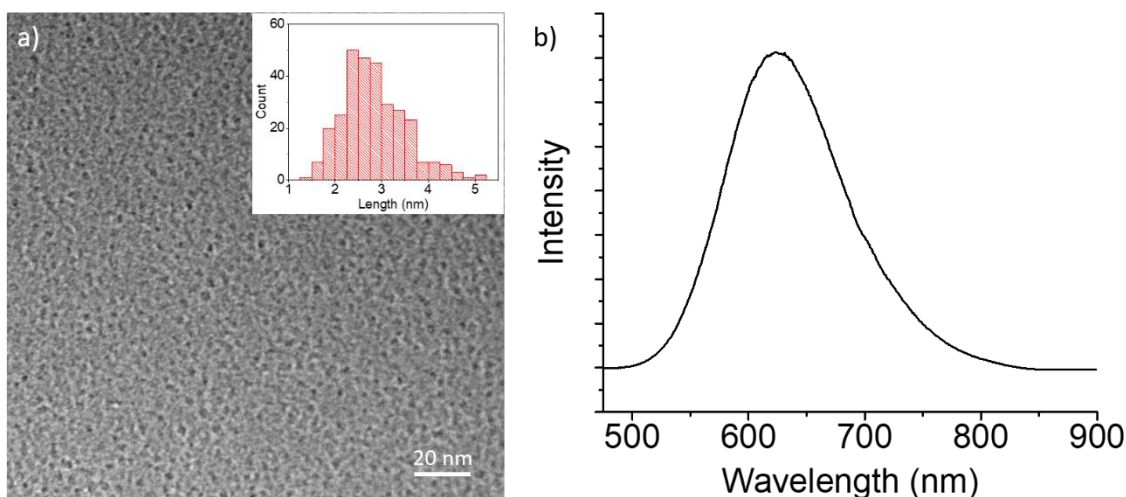


Figure A-3. a) Brightfield TEM image and b) photoluminescence emission spectrum of the amidine-functionalized SiNCs. Inset: Histogram depicting measured SiNC size.

Information about the surface chemistry of the SiNCs investigated here can be gained by comparing their IR spectra (Figure A-4). As expected, the spectrum of hydride-terminated SiNCs (Figure A-4, blue trace) shows absorptions associated with Si-H_x (*x* = 1, 2, 3) at 2100 cm⁻¹. The spectrum of the amidine (Figure A-4, red trace) shows characteristic features associated with N at 1627 cm⁻¹, alkyl C-H stretching at 2900 cm⁻¹, as well as the alkene C-H at 3076 cm⁻¹ and C=C at 1685 cm⁻¹. The isolated functionalized particles show a composite spectrum of these components (Figure A-4, black trace). The Si-H region (i.e., 2000–2250 cm⁻¹) has evolved and now shows features at 2243 cm⁻¹ associated with back-bonded to Si-O; this evolution is consistent with the appearance of Si-O features at 1100 cm⁻¹ resulting from partial surface oxidation. Similar surface oxidation has been noted when comparatively large surface groups have been tethered to SiNC surfaces, and they have been attributed to work-up induced oxidation; however, exposure to water during liberation of the amidine functionality is likely also responsible. Further confirming the presence of N'-undec-10-enyl-N,N-dimethylacetamide, we note characteristic spectral features related to the C-H and C=N stretches at 2900 and 1629 cm⁻¹, respectively, suggesting that the amidine ligand is present and the C=N is maintained. In addition, the “tell-tale” C=C alkene features at 3079 cm⁻¹ and 1685 cm⁻¹ are absent, consistent with successful hydrosilylation.

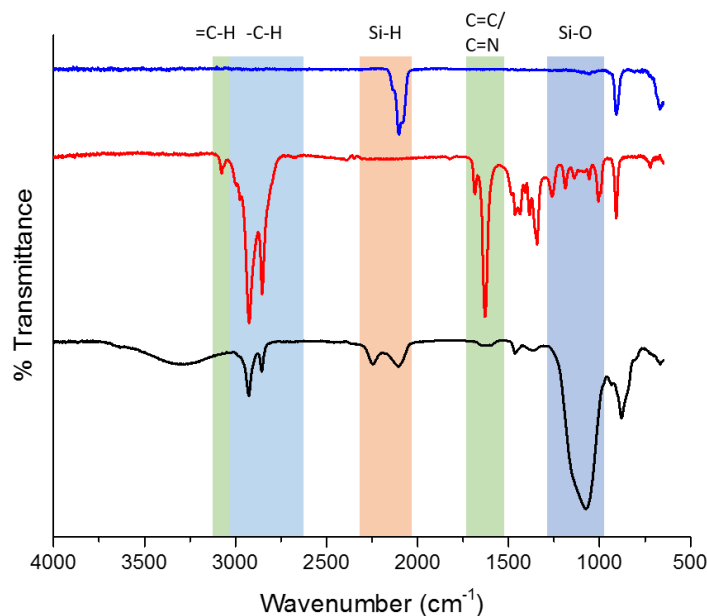


Figure A-4. FTIR spectra highlighting the chemical functionalities of hydride-terminated SiNCs (blue), N'-undec-10-enyl-N,N-dimethylacetamide (red), and the amidine-functionalized SiNCs (black).

XPS provides information about oxidation of the SiNC as well as further indication of amidine surface modification and insight into surface bonding. The survey XP spectrum (not shown) indicates the presence of carbon (41 atm%), nitrogen (2 atm%), oxygen (30 atm%), silicon (26 atm%), fluorine (1 atm%), and copper (from the copper foil). The high-resolution Si 2p XP spectrum (Figure A-5a) shows features associated with an elemental silicon core as well as oxidized silicon consistent with Si-O-Si species observed IR (Figure A-4). Figure A-5b shows the high-resolution N 1s XP spectrum. There are two noticeably distinct nitrogen species, consistent with the presence of the amidine surface group. Furthermore, no evidence of Si-N species at 397 eV is noted.⁸

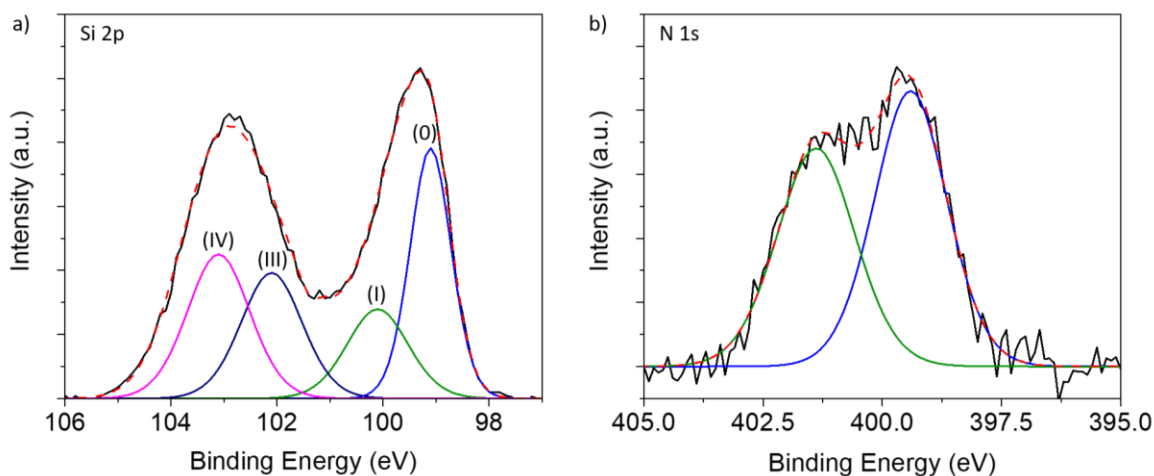


Figure A-5. High resolution X-ray photoelectron spectroscopy (XPS) of the a) Si 2p and b) N 1s. The black trace is the experimental spectra and the red dashed line is the fit. For clarity, only the Si 2p_{3/2} are shown.

A.3.2 Hydrophilicity Switch Experiments

The amidine functional group has previously been shown to exhibit switchable hydrophilicity by taking advantage of its acid-base chemistry.¹⁰ The phase transfer occurs as a result of the protonation of the nitrogen, which induces a positive charge on the otherwise hydrophobic molecule (Figure A-1). Having prepared amidine-terminated SiNCs, we endeavoured to investigate their phase-transferability between hydrophilic and hydrophobic environments.

The present amidine modified SiNCs preferentially disperse in hydrophobic toluene (note: these particles do not fully solubilize in hydrophobic media). To investigate the acid induced phase transfer properties of these SiNCs, toluene dispersions of the SiNCs were added into a test tube, followed by addition of water. The organic phase containing amidine-

terminated SiNCs maintained their bright orange photoluminescence (Figure A-6b). The test tube subsequently was capped with a septum, and CO₂ was bubbled through the mixture at room temperature for 1 h to induce acidification and protonate the amidine. After protonation, amidine modified SiNCs preferentially partition into water, as shown in Figure A-6c. This partitioning process does not shift the photoluminescence of the SiNCs (Figure A-7) that typically is observed during oxidation of SiNCs.¹⁹ However, the photoluminescence intensity is diminished severely.

To investigate the reversibility of the CO₂ induced hydrophilicity, additional toluene was added to the test tube, and the mixture was saturated with Ar upon bubbling at 65 °C for 30 min. The resulting decrease in acidity shifts the acid/base equilibrium, shown in Figure A-1, to the left, reforming the hydrophobic amidine surface. Figure A-6d shows that the material has partitioned back into the toluene phase, however, almost all of the photoluminescence intensity is lost. This large decrease in photoluminescence intensity can be observed also in the photoluminescence spectrum shown in Figure A-7.

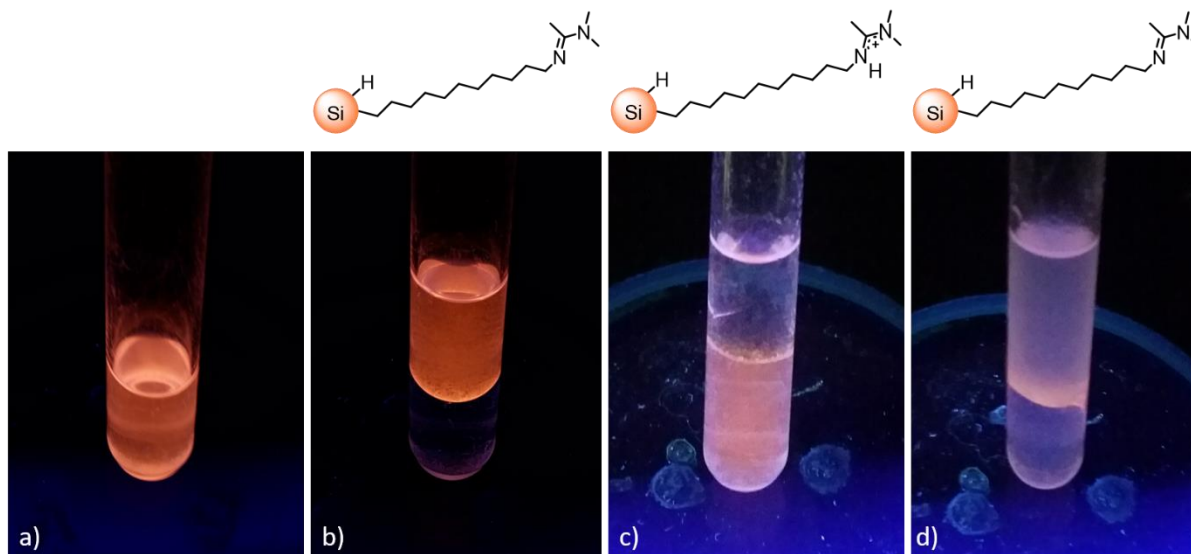


Figure A-6. Photographs depicting the hydrophilicity switch of the material irradiated under 365 nm light depicting the photoluminescence of the SiNCs a) in toluene before switching, b) after adding water, c) after bubbling through CO₂ for 1 h, and d) after bubbling Ar through the sample for 30 min at 65 °C.

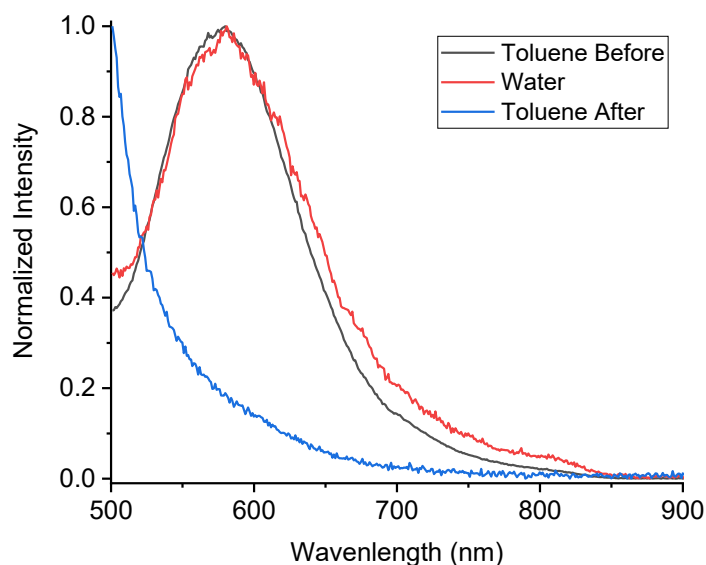


Figure A-7. Comparison of normalized photoluminescence spectra of SiNCs in toluene before the switch (black), water after bubbling CO₂ at room temperature for 1 h (red), and toluene after bubbling Ar through the sample for 30 min at 65 °C.

A.4 Conclusions

A Lewis acid protecting group has been used to prepare amidine-terminated SiNCs exhibiting orange PL and having hydrophilicity switchable properties that can be employed to make the material phase transferable. The resulting material was characterized using TEM, IR, XPS, and PL emission to confirm the presence of the amidines and that surface bonding did not occur through the nitrogen atoms (within the sensitivity of the techniques). Once this was confirmed, hydrophilicity control was demonstrated, and the SiNCs were transferred successfully into and out of the water, based on the presence of CO₂, though significant degradation occurred. Future work will look into improving the solubility of the material in both phases and limiting oxidation of the material during the phase transfer process to improve cyclability.

A.5 References

1. Erogbogbo, F.; Yong, K.-T.; Roy, I.; Hu, R.; Law, W.-C.; Zhao, W.; Ding, H.; Wu, F.; Kumar, R.; Swihart, M. T.; Prasad, P. N., In Vivo Targeted Cancer Imaging, Sentinel Lymph Node Mapping and Multi-Channel Imaging with Biocompatible Silicon Nanocrystals. *ACS Nano*, **2011**, *5*, 413-423.
2. Erogbogbo, F.; Yong, K.-T.; Roy, I.; Xu, G.; Prasad, P. N.; Swihart, M. T., Biocompatible Luminescent Silicon Quantum Dots for Imaging of Cancer Cells. *ACS Nano*, **2008**, *2*, 873-878.
3. McVey, B. F. P.; Tilley, R. D., Solution Synthesis, Optical Properties, and Bioimaging Applications of Silicon Nanocrystals. *Acc. Chem. Res.*, **2014**, *47*, 3045-3051.

4. Zhai, Y.; Dasog, M.; Snitynsky, R. B.; Purkait, T. K.; Aghajamali, M.; Hahn, A. H.; Sturday, C. B.; Lowary, T. L.; Veinot, J. G. C., Water-soluble photoluminescent d-mannose and l-alanine functionalized silicon nanocrystals and their application to cancer cell imaging. *J. Mater. Chem. B*, **2014**, *2*, 8427-8433.
5. Kirchner, C.; Liedl, T.; Kudera, S.; Pellegrino, T.; Javier, A. M.; Gaub, H. E.; Stölzle, S.; Fertig, N.; Parak, W. J., Cytotoxicity of Colloidal CdSe and CdSe/ZnS Nanoparticles. *Nano Lett.*, **2005**, *5*(2), 331-338.
6. Bhattacharjee, S.; Rietjens, I. M. C. M.; Singh, M. P.; Atkins, T. M.; Purkait, T. K.; Xu, Z.; Regli, S.; Shukaliak, A.; Clark, R. J.; Michell, B. S.; Alink, G. M.; Marcelis, A. T. M.; Fink, M. J.; Veinot, J. G. C.; Kauzlarich, S. M.; Zuillhof, H., Cytotoxicity of surface-functionalized silicon and germanium nanoparticles: the dominant role of surface charges. *Nanoscale*, **2013**, *5*, 4870-4883.
7. Gu, L.; Hall, D. J.; Qin, Z.; Anglin, E.; Joo, J.; Mooney, D. J.; Howell, S. B.; Sailor, M. J., In vivo time-gated fluorescence imaging with biodegradable luminescent porous silicon nanoparticles. *Nat. Commun.*, **2013**, *4*, 2326.
8. Dasog, M.; Yang, Z.; Regli, S.; Atkins, T. M.; Faramus, A.; Singh, M. P.; Muthuswamy, E.; Kauzlarich, S. M.; Tilley, R. D.; Veinot, J. G. C., Chemical Insight into the Origin of Red and Blue Photoluminescence Arising from Freestanding Silicon Nanocrystals. *ACS Nano*, **2013**, *7*(3), 2676-2685.
9. Zajac, M. A., An Application of Borane as a Protecting Group for Pyridine. *J. Org. Chem.*, **2008**, *73*, 6899-6901.
10. Liu, Y.; Jessop, P. G.; Cunningham, M.; Eckert, C. A.; Liotta, C. L., Switchable Surfactants. *Science*, **2006**, *313*, 958-960.
11. Alshamrani, A. K.; Vanderveen, J. R.; Jessop, P. G., A guide to the selection of switchable functional groups for CO₂-switchable compounds. *Phys. Chem. Chem. Phys.*, **2016**, *18*, 19276-19288.
12. Boniface, K. J.; Dykeman, R. R.; Cormier, A.; Wang, H.-B.; Mercer, S. M.; Liu, G.; Cunningham, M. F.; Jessop, P. G., CO₂-switchable drying agents. *Green Chem.*, **2016**, *18*, 208-213.
13. Che, H.; Huo, M.; Peng, L.; Ye, Q.; Guo, J.; Wang, K.; Wei, Y.; Yuan, J., CO₂-switchable drug release from magneto-polymeric nanohybrids. *Polym. Chem.*, **2015**, *6*, 2319-2326.
14. Darabi, A.; Jessop, P. G.; Cunningham, M. F., CO₂-responsive polymeric materials: synthesis, self-assembly, and functional applications. *Chem. Soc. Rev.*, **2016**, *45*, 4391-4436.
15. Pociví-Martínez, S.; Francés-Soriano, L.; Zaballos-García, E.; Scaiano, J. C.; González-Béjar, M.; Pérez-Prieto, J., CO₂ switchable nanoparticles: reversible water/organic-phase exchange of gold nanoparticles by gas bubbling. *RSC Adv.*, **2013**, *3*, 4867-4871.
16. Hessel, C. M.; Henderson, E. J.; Veinot, J. G. C., Hydrogen Silsesquioxane: A Molecular Precursor for Nanocrystalline Si-SiO₂ Composites and Freestanding Hydride-Surface-Terminated Silicon Nanoparticles. *Chem. Mater.*, **2006**, *18*(26), 6139-6146.
17. Yang, Z.; Gonzalez, C. M.; Purkait, T. K.; Iqbal, M.; Meldrum, A.; Veinot, J. G., Radical Initiated Hydrosilylation on Silicon Nanocrystal Surfaces: An Evaluation of Functional Group Tolerance and Mechanistic Study. *Langmuir*, **2015**, *31*(38), 10540-10548.
18. Purkait, T. K.; Iqbal, M.; Wahl, M. H.; Gottschling, K.; Gonzalez, C. M.; Islam, M. A.; Veinot, J. G. C., Borane-Catalyzed Room-Temperature Hydrosilylation of Alkenes/Alkynes on Silicon Nanocrystal Surfaces. *J. Am. Chem. Soc.*, **2014**, *136*(52), 17914-17917.
19. Sinelnikov, R.; Dasog, M.; Beamish, J.; Meldrum, A.; Veinot, J. G. C., Revisiting an Ongoing Debate: What Role Do Surface Groups Play in Silicon Nanocrystal Photoluminescence? *ACS Photonics*, **2017**, *4*(8), 1920-1929.

Appendix B

Calculation of Surface Coverage from TGA

In Chapter 4, surface coverage of silicon nanoparticles (SiNPs) was estimated using thermogravimetric analysis (TGA).^{1, 2} The calculation uses the % weight loss determined by TGA measurement and requires the number of Si atoms in the SiNP and on the surface.

The number of Si atoms in an SiNP was calculated using the volume of one unit cell of Si (0.16 nm³), which is comprised of eight Si atoms. To estimate the number of surface atoms, an atomic density of 8.06 atoms/nm² was used, which is the average of the 100, 110, and 111 faces of Si. The calculations are based on an icosahedral shape, where the length of one edge (*a*) is approximately 0.809x the radius of the particle.

$$\text{SiNP volume} = \frac{5(3 + \sqrt{5})}{12} a^3$$

$$\text{Si atoms per SiNP} = \frac{\text{SiNP volume}}{0.16} \times 8$$

$$\text{SiNP surface area} = 5\sqrt{3}a^2$$

$$\text{Si surface atoms per SiNP} = \text{SiNP surface area} \times 8.06$$

For a 3.5 nm SiNP, this yields 1102 Si atoms and 327 surface Si atoms, which is close to the 1100 Si atoms and 300 surface Si atoms previously calculated.^{3, 4} This method is efficient for calculating Si atoms and Si surface atoms for SiNPs of different diameters for use in the surface coverage calculations outlined below.

$$\% \text{ mole ligand} = \frac{\% \text{ wt loss}}{\text{molecular weight ligand (g/mol)}}$$

$$\% \text{ mole Si atoms} = \frac{100 - \% \text{ mole of ligand}}{\text{weight silicon (g/mol)}}$$

$$\text{number of ligands per SiNP} = \frac{\% \text{ mole of ligand}}{\% \text{ mole of Si atoms}} \times \text{Si atoms per SiNP}$$

$$\% \text{ surface coverage} = \frac{\text{number of ligands per SiNP}}{\text{Si surface atoms per SiNP}} \times 100$$

References

1. Yang, Z.; Gonzalez, C. M.; Purkait, T. K.; Iqbal, M.; Meldrum, A.; Veinot, J. G., Radical Initiated Hydrosilylation on Silicon Nanocrystal Surfaces: An Evaluation of Functional Group Tolerance and Mechanistic Study. *Langmuir* **2015**, *31* (38), 10540-10548.
2. Purkait, T. K.; Iqbal, M.; Wahl, M. H.; Gottschling, K.; Gonzalez, C. M.; Islam, M. A.; Veinot, J. G., Borane-catalyzed room-temperature hydrosilylation of alkenes/alkynes on silicon nanocrystal surfaces. *J. Am. Chem. Soc.* **2014**, *136* (52), 17914-17917.
3. Avramov, P. V. F., D. G.; Sorokin, P. B.; Chernozatonskii, L. A.; Gordon, M. S. , New symmetric families of silicon quantum dots and their conglomerates as a tunable source of photoluminescence in nanodevices. *Los Alamos Natl. Lab, Prepr. Arch., Condens. Matter* **2007**, 1-19.
4. Zhao, Y.; Kim, Y.-H.; Du, M.-H.; Zhang, S. B., First-Principles Prediction of Icosahedral Quantum Dots for Tetravalent Semiconductors. *Phys. Rev. Lett.* **2004**, *93* (1), 015502.

Appendix C

Calculation of Si:O Ratio From High Binding Energy Components of High Resolution Si 2p XP Spectrum

The relative ratio of Si and O in the oxidized SiNPs, discussed in Chapter 4, was calculated by the following equation:¹

$$\text{O : Si ratio} = \frac{0.5(I_{\text{Si(I)}}) + I_{\text{Si(II)}} + 1.5(I_{\text{Si(III)}}) + 2(I_{\text{Si(IV)}})}{I_{\text{Total}}}$$

Where I_{Total} is the total intensity of the fitted Si 2p XP spectrum, $I_{\text{Si(I)}}$ is the intensity of the Si(I) component of the Si 2p XP spectrum, $I_{\text{Si(II)}}$ is the intensity of the Si(II) component, and so on. Calculation of the O content using this method will provide an overestimate because not all higher binding energy Si is bound to O and the attenuation length of the photoelectrons was not accounted for in the calculation.

References

1. Liebhaber, M.; Mews, M.; Schulze, T. F.; Korte, L.; Rech, B.; Lips, K., Valence band offset in heterojunctions between crystalline silicon and amorphous silicon (sub)oxides (a-SiO_x:H, 0 < x < 2). *Appl. Phys. Lett.* **2015**, *106* (3), 031601.